

# Scanning Tunneling Spectroscopy on $\text{Bi}_2\text{Sr}_2\text{CaCu}_2\text{O}_{8+\delta}$ and $\text{Bi}_2\text{Sr}_2\text{Ca}_2\text{Cu}_3\text{O}_{10+\delta}$ compounds

THÈSE

*présentée à la Faculté des Sciences  
de l'Université de Genève  
pour obtenir le grade de Docteur ès sciences,  
Mention Physique*

par

Francisco Giorgio LEVY DE CASTRO

de

Neuquén (*Argentine*)

*Thèse n° 3860*

GENÈVE

*Atelier de reproduction de la Section de physique  
2007*



**UNIVERSITÉ  
DE GENÈVE**

FACULTÉ DES SCIENCES

**Doctorat ès sciences  
mention physique**

Thèse de *Monsieur Francisco Giorgio LEVY de CASTRO*

intitulée :

**"Scanning Tunneling Spectroscopy on  $\text{Bi}_2\text{Sr}_2\text{CaCu}_2\text{O}_{8+\delta}$   
and  $\text{Bi}_2\text{Sr}_2\text{Ca}_2\text{Cu}_3\text{O}_{10+\delta}$  Compounds "**

La Faculté des sciences, sur le préavis de Messieurs Ø. FISCHER, professeur ordinaire et directeur de thèse (Département de physique de la matière condensée), D. VAN DER MAREL, professeur ordinaire (Département de physique de la matière condensée), I. MAGGIO-APRILE, docteur (Département de physique de la matière condensée), J. MESOT, professeur (Eidgenössische Technische Hochschule Zürich, Paul Scherer Institut, Labor für Neutronenstreuung, Villigen, Suisse) et D. RODITCHEV, docteur (Institut des NanoSciences de Paris, Dispositifs quantiques contrôlés : nanofabrication et propriétés électroniques, Paris, France), autorise l'impression de la présente thèse, sans exprimer d'opinion sur les propositions qui y sont énoncées.

Genève, le 15 juin 2007

Thèse - 3860 -

Le Doyen, Pierre SPIERER

# Contents

<b>Contents</b>	<b>i</b>
<b>Résumé en français</b>	<b>1</b>
<b>Introduction</b>	<b>15</b>
<b>1 The Scanning Tunneling Microscopy Technique</b>	<b>17</b>
1.1 Introduction . . . . .	17
1.2 Experimental setup . . . . .	18
1.2.1 General Setup . . . . .	18
1.2.2 STM unit . . . . .	19
1.2.3 Cryogenic unit . . . . .	20
1.2.4 UHV unit . . . . .	23
1.2.5 Electronic equipment and acquisition software . . . . .	24
1.3 Experimental Methods . . . . .	26
<b>2 Theory</b>	<b>29</b>
2.1 Introduction . . . . .	29
2.2 STM and LDOS . . . . .	30
2.3 Theoretical calculation of LDOS . . . . .	37
2.3.1 BCS . . . . .	38
2.3.2 Coupling to a collective mode . . . . .	39
2.4 Discussion and interpretation . . . . .	41
2.4.1 Electron tunneling process in superconductors . . . . .	41

2.4.2	Gap symmetry in a free electron model . . . . .	42
2.4.3	Effects of band-structure . . . . .	43
2.4.4	Collective mode coupling . . . . .	45
<b>3</b>	<b>High-Temperature superconductors</b>	<b>49</b>
3.1	Introduction . . . . .	49
3.2	The Bi-family of high $T_c$ superconductors . . . . .	50
3.3	Phase diagram and spectroscopy . . . . .	52
3.4	Spatial variations of the STM spectra . . . . .	55
3.4.1	Spatial gap distribution . . . . .	55
3.4.2	Quasiparticle interference . . . . .	56
3.4.3	Non-dispersive electronic modulations . . . . .	57
<b>4</b>	<b>Vortex core Spectroscopy in <math>\text{Bi}_2\text{Sr}_2\text{CaCu}_2\text{O}_{8+\delta}</math></b>	<b>59</b>
4.1	Introduction . . . . .	59
4.2	Zero Field Characterization . . . . .	60
4.3	Vortex core spectroscopy . . . . .	62
4.4	Square modulation . . . . .	65
4.5	Spatial variation of core states . . . . .	65
4.6	Discussion and Conclusion . . . . .	68
<b>5</b>	<b>Low Temperature Spectroscopy in <math>\text{Bi}_2\text{Sr}_2\text{CaCu}_2\text{O}_{8+\delta}</math></b>	<b>71</b>
5.1	Introduction . . . . .	71
5.2	Characterization . . . . .	72
5.3	Nanoscale spectral variations . . . . .	74
5.4	Atomic variations of the spectra . . . . .	78
<b>6</b>	<b>Low Temperature Spectroscopy in <math>\text{Bi}_2\text{Sr}_2\text{Ca}_2\text{Cu}_3\text{O}_{10+\delta}</math></b>	<b>85</b>
6.1	Introduction . . . . .	85
6.2	General Sample Characteristics . . . . .	86
6.3	Zero-Field Spectroscopy . . . . .	86
6.3.1	Tunnel junction characterization . . . . .	86

---

6.3.2	Correlation between transition widths and inhomogeneity . . . . .	88
6.3.3	Doping evolution of the spectra . . . . .	89
6.4	Nanoscale variations of the spectra . . . . .	93
6.5	Tunneling spectra in a magnetic field . . . . .	96
<b>7</b>	<b>Spectral Form</b>	<b>99</b>
7.1	Form of the spectra in $\text{Bi}_2\text{Sr}_2\text{CaCu}_2\text{O}_{8+\delta}$ . . . . .	99
7.2	Form of the spectra in $\text{Bi}_2\text{Sr}_2\text{Ca}_2\text{Cu}_3\text{O}_{10+\delta}$ . . . . .	105
<b>8</b>	<b>Scanning Tunneling Spectra on HTS: The interplay of the gap, the bosonic mode and the van Hove singularity</b>	<b>111</b>
8.1	Introduction . . . . .	111
8.2	Accurate fit to an experimental spectrum . . . . .	112
8.3	Effects of the different parameters . . . . .	115
8.4	Fitting program . . . . .	118
8.5	Fits to the spectra . . . . .	121
<b>9</b>	<b>Conclusion and Perspectives</b>	<b>125</b>
<b>Appendix A</b>	<b>Evaluation of the Function <math>B(\omega, E)</math></b>	<b>127</b>
<b>Appendix B</b>	<b>Cross-correlation definition</b>	<b>129</b>
<b>Appendix C</b>	<b>Fourier Transform definitions and convention</b>	<b>131</b>
<b>Bibliography</b>		<b>143</b>
<b>Acknowledgements</b>		<b>147</b>
<b>Index</b>		<b>149</b>



# List of Figures

1	Spectre tunnel mesuré dans le composé $\text{Bi}_2\text{Sr}_2\text{Ca}_2\text{Cu}_3\text{O}_{10+\delta}$ . . . . .	3
2	Diagramme de phase schématique pour les matériaux à haute température critique . . . . .	4
3	États dans le cœur de vortex en Bi2212. . . . .	6
4	Transformé de Fourier des états de cœur en Bi2212. . . . .	8
5	Systématique de la pente du background et de la position en energy de creux. . . . .	10
6	Ajustement d'un spectre tunnel typique avec trois modèles. . . . .	12
1.2.1	STM Unit. . . . .	19
1.2.2	Experimental cryogenic setup. . . . .	21
1.2.3	Schematic UHV setup. . . . .	23
1.2.4	Schematic electronic setup. . . . .	25
1.2.5	Snapshot of the data acquisition software. . . . .	26
1.3.1	Example of topography, spectral map and trace acquisition. . . . .	28
2.2.1	Tunnel configuration. . . . .	30
2.2.2	STM configuration. . . . .	31
2.2.3	Normalization of spectra to the tunnel resistance. . . . .	36
2.4.1	Tunnel into superconductors. . . . .	41
2.4.2	<i>s</i> - and <i>d</i> -wave gap symmetry. . . . .	43
2.4.3	<i>d</i> -wave gap in BCS theory settled in a tight-binding band. . . . .	44
2.4.4	Model spectrum and trends with parameters. . . . .	46
3.2.1	Unit cell structure for the Bi-based HTS. . . . .	50
3.2.2	Schematic atomic positions in the $\text{CuO}_2$ plane. . . . .	51

3.3.1	Schematic phase diagram of cuprate oxides HTS. . . . .	52
3.3.2	Tunneling spectra on Bi2223. . . . .	53
4.2.1	Topographic image of Bi2212 and analysis. . . . .	61
4.3.1	Vortex core in Bi2212. . . . .	62
4.4.1	Core states in Bi2212. . . . .	64
4.4.2	Spatial variation of core states. . . . .	66
4.5.1	Fourier analysis of the tunneling conductance inside the vortex cores in Bi2212. . . . .	67
4.6.1	Simulation of the vortex modulation. . . . .	69
5.2.1	Zero-field STM characterization in Bi2212. . . . .	73
5.3.1	Nanometer spectra variation in Bi2212 and gap map. . . . .	76
5.3.2	Spatial dependence of the coherence peaks. . . . .	77
5.4.1	Spatial dependence of the coherence peaks. . . . .	79
5.4.2	Trace along 2 atoms. . . . .	81
5.4.3	Atomic variations of the spectra. . . . .	82
6.3.1	Topography Bi2223. . . . .	87
6.3.2	Spectral normalization in Bi2223. . . . .	88
6.3.3	Apparent barrier height measured in Bi2223. . . . .	89
6.3.4	Spectral traces in Bi2223. . . . .	90
6.3.5	Gap Distribution in Bi2223. . . . .	91
6.3.6	Comparison of Spectra between Bi2212 and Bi2223. . . . .	91
6.3.7	Averaged spectra in Bi2223. . . . .	92
6.4.1	Nanometer spectra variation in Bi2223 and gap map. . . . .	95
6.5.1	Spectra taken at 2K and 6T in Bi2223. . . . .	96
7.1.1	Traces on Bi2212. . . . .	101
7.1.2	Single spectrum of Bi2212 with $\Delta_p = 36$ meV. . . . .	102
7.1.3	Averaged spectra of Bi2212 with $\Delta_p = 36$ meV. . . . .	103
7.1.4	Slope and Dip systematics on Bi2212. . . . .	104
7.2.1	Mean spectra on Bi2223. . . . .	105

---

7.2.2	Spectra with the same gap magnitude in Bi2223. . . . .	106
7.2.3	Slope and dip energy systematics on Bi2223. . . . .	107
7.2.4	Comparison of spectra in Bi2212 and Bi2223 systems. . . . .	109
8.2.1	Fit of the tunneling conductance using three models. . . . .	113
8.3.1	High-resolution calculation of the density of states in HTS. . . . .	116
8.3.2	Evolution of the theoretical conductance with model's parameters. . . . .	117
8.3.3	Averaged tunneling conductance spectra of Bi2223. . . . .	119
8.5.1	Fits of the averaged tunneling conductance spectra. . . . .	122
8.5.2	Evolution of the fitted parameters upon the superconducting gap. . . . .	123



# List of Tables

8.5.1	Values of the model's parameters obtained from fits to the spectra. . . . .	121
-------	---	-----



# Abbreviations

ARPES	Angle-resolved photoemission spectroscopy
BCS	Bardeen - Copper - Schrieffer
BZ	Brillouin zone
Bi2201	$\text{Bi}_2\text{Sr}_2\text{CuO}_6 + \delta$
Bi2212	$\text{Bi}_2\text{Sr}_2\text{CaCu}_2\text{O}_{8+\delta}$
Bi2223	$\text{Bi}_2\text{Sr}_2\text{Ca}_2\text{Cu}_3\text{O}_{10+\delta}$
CITS	Current-imaging tunneling spectroscopy
DOS	Density of states
FT	Fourier transform
HTS	High $T_c$ superconductors
ILDOS	Integrated local density of states
INS	Inelastic neutron scattering
LDOS	Local density of states
STM	Scanning tunneling microscope
OVC	Outer vacuum chamber
STS	Scanning tunneling spectroscopy
SIN	Superconductor - insulator - metal junction
SIS	Superconductor - insulator - superconductor junction
UHV	Ultra high vacuum
VHS	Van Hove singularity
YBCO	$\text{YBa}_2\text{Cu}_3\text{O}_{7-\delta}$



# Résumé: Mesures au microscope à effet tunnel dans les composés $\text{Bi}_2\text{Sr}_2\text{CaCu}_2\text{O}_{8+\delta}$ et $\text{Bi}_2\text{Sr}_2\text{Ca}_2\text{Cu}_3\text{O}_{10+\delta}$ .

## • Le microscope à effet tunnel

En 1981, une révolution technique a eu lieu quand Binnig et Rohrer [1,2] inventèrent le microscope à effet tunnel (en anglais scanning tunneling microscope ou STM). Le STM est composé basiquement d'une pointe métallique qui se trouve à quelques Ångströms d'un échantillon conducteur. Quand une différence de potentiel est appliquée entre la pointe et l'échantillon, un courant tunnel apparaît à cause du tunnel quantique. Le courant tunnel est sensible aux propriétés électroniques locales de l'échantillon et il dépend exponentiellement de la distance entre la pointe et l'échantillon. Si on balaye la pointe parallèlement à la surface de l'échantillon (dans le plan  $x - y$ ) et si on mesure simultanément le courant tunnel, on détermine les propriétés spatiales de l'échantillon. Pendant une mesure STM, on contrôle les quatre paramètres suivants : la position de la pointe dans les directions  $x, y$  et  $z$  par rapport à la surface de l'échantillon, la différence de potentiel  $V_s$  et le courant tunnel  $I$  à travers le vide entre la pointe et l'échantillon. De cette façon, on peut obtenir des informations topographiques ou spectroscopiques en fonction des paramètres contrôlés quand le courant tunnel est mesuré.

Dans ce travail, nous utilisons un STM conçu à Genève. Il fonctionne à des températures entre 275 mK et la température ambiante, dans un champ magnétique jusqu'à 14 Tesla et dans une chambre à ultra haut vide (UHV) avec la possibilité de manipuler l'échantillon et la pointe *in situ*. Le système, d'une architecture non-conventionnelle, est basée sur un cryostat qui se charge par le bas et qui est monté au dessus de la chambre UHV. Ce design permet un système compact donnant un accès facile au STM et des temps courts pour le changement de pointe et d'échantillon. Au centre du cryostat, se trouve "la canne de mesure" dotée d'un insert avec un réfrigérateur d' $^3\text{He}$ . Ce réfrigérateur ne fonctionne pas en circulation continue, mais par cycles successifs (*single shot*). Le contrôle en température de l'échantillon est réalisé par les réfrigérateurs de  $^3\text{He}$  et  $^4\text{He}$

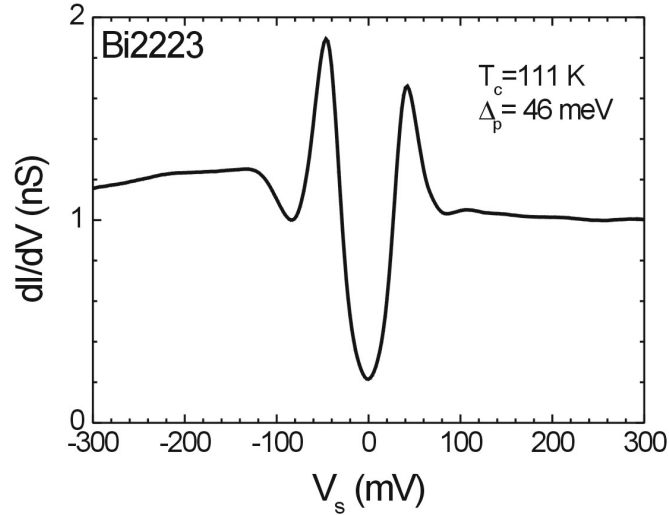
avec chauffages résistifs. A l'extrémité de l'insert se trouve la tête du STM. La configuration STM utilisée à Genève [3, 4] consiste en deux tubes piézo-électriques concentriques : les mouvements de la pointe sont gouvernés par le tube intérieur et le tube extérieur contrôle les mouvements de l'échantillon. Avec cet instrument, on peut réaliser des études dans une région de  $\sim 1 \mu\text{m}^2$  à une température de 2 K. Par le mouvement de l'insert, le STM peut être déplacé de sa position de mesure, au centre de l'aimant supraconducteur, jusqu'à sa position de sortie dans la chambre UHV où on peut changer *in situ* l'échantillon et la pointe.

Un feedback électronique est utilisé pour stabiliser de façon dynamique la pointe au-dessus de l'échantillon pendant le balayage. La pointe est connectée à la terre et l'échantillon est mis au potentiel  $V_s$ . Comme le courant tunnel est mesuré entre l'échantillon et la pointe, on mesure un courant positif quand une différence de potentiel positive est appliquée. Dans cette configuration, les états vides sont testés pour des potentiels positifs et les états occupés pour  $V_s < 0$ . Dans ce mode de courant constant, on mesure les variations de la position verticale de la pointe (la coordonnée  $z$ ) au cours du balayage afin d'obtenir une image topographique de la surface à un potentiel donné.

Si on maintient la coordonnée  $z$  de la pointe fixée à une distance donnée de l'échantillon et que le potentiel est varié pendant qu'on mesure le courant tunnel on obtient l'information spectroscopique locale. On définit la conductance tunnel différentielle comme la dérivée du courant tunnel par rapport au potentiel  $V_s$ . Dans la configuration STM, cette conductance tunnel différentielle est proportionnelle à la densité locale des états. Dans ce travail, elle est directement mesurée par une technique lock-in, où une petite modulation alternative  $V_{ac} \cos(\omega t)$  est additionnée au potentiel, laquelle induit une modulation du courant tunnel. L'amplitude de cette modulation induite est mesurée comme un signal DC est proportionnel à la première dérivée du courant si l'amplificateur est en phase avec la première harmonique de la modulation appliquée. La première dérivée du courant est par définition la conductance tunnel différentielle.

Une carte spectroscopique peut être obtenue si on combine sa résolution spatiale avec la possibilité de mesurer les propriétés spectroscopiques locales de l'échantillon. Une carte spectroscopique représente les variations de la conductance tunnel différentielle mesurée à un potentiel donné et dans une certaine région. Dans cette région, on définit une matrice régulière des points équidistants qui nous permet d'obtenir une carte topographique de cette région. En chaque point de cette matrice, deux relevés sont successivement effectués. Un relevé topographique est établi à la tension  $V_t$  (feedback enclenché). Puis le feedback est interrompu, et une mesure spectroscopique de la conductance différentielle  $dI/dV$  est effectuée, à une ou plusieurs tensions  $V_s$ . La tension initiale  $V_t$  est rétablie, le feedback réenclenché et on déplace la pointe au prochain point défini. A la fin de la mesure, une carte spectroscopique à énergie  $eV_s$  et une carte topographique mesurée au potentiel  $V_t$  sont obtenues. Une série de données spectroscopiques mesurées sur une ligne peut être obtenue et ils définissent une trace spectroscopique. Un exemple de spectre est montré dans la Figure 1 qui correspond à un spectre mesuré sur la surface

(001) du composé  $\text{Bi}_2\text{Sr}_2\text{Ca}_2\text{Cu}_3\text{O}_{10+\delta}$  à  $T = 2 \text{ K}$  et  $H = 0 \text{ T}$ .



## • Les supraconducteurs à haute température critique

En 1986, une autre révolution ébranla le monde de la physique avec la découverte des nouveaux matériaux supraconducteurs par Bednorz et Müller [5]. Ces matériaux présentent les températures critiques les plus élevées et ils possèdent tous des plans d'oxyde de cuivre  $\text{CuO}_2$ . Ces plans sont séparés par des plans de blocage qui se comportent comme des réservoirs de charge. On estime que les excitations à basse énergie dans les supraconducteurs à haute température critique (HTS) sont déterminées principalement par les interactions dans les plans de  $\text{CuO}_2$ . L'état de valence du cuivre peut être varié si on change la composition chimique des plans de blocage, ce qui équivaut à doper les plans de  $\text{CuO}_2$ . Dans ce qui suit, on considérera uniquement le diagramme de phase température-dopage pour les matériaux dopés avec des trous.

Le composé avec un électron par maille unitaire est un isolant. L'incorporation des trous supprime graduellement l'ordre antiferromagnétique initial (région AF dans la Fig. 2). A un dopage de  $x \approx 0.02 - 0.04$  trous par maille unitaire, le composé devient d'abord métallique puis supraconducteur en dessous de la température critique  $T_c$ . La variation de la température critique avec le dopage détermine une parabole inversée qui délimite la phase supraconductrice (région SC dans la Fig. 2). Le  $T_c$  maximal définit la concentration

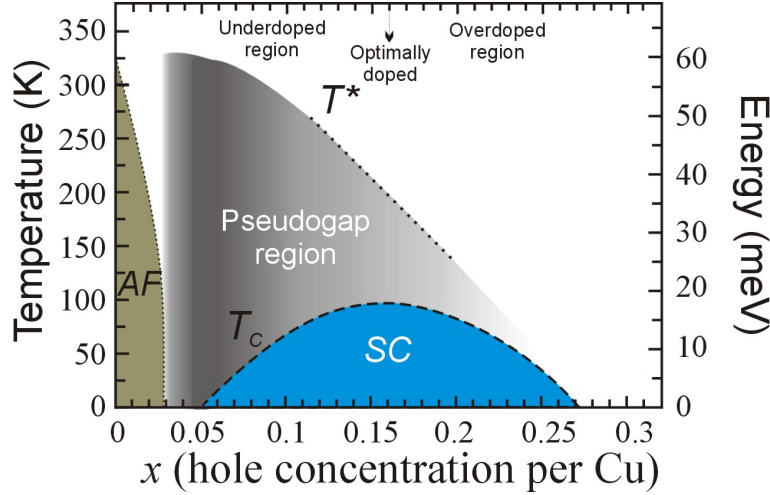


Figure 2: Diagramme de phase schématisé pour les matériaux à haute température critique.

optimale des trous et détermine deux régions dans le diagramme de phase: la région sous-dopée correspondant aux  $x < x^{opt}$  et la région sur-dopée pour  $x > x^{opt}$ . La dépendance de la température critique avec le dopage fut donnée de façon empirique par Presland *et al.* [6]:

$$T_c(x) = T_c^{max} \left[ 1 - 82.6 (x - x^{opt})^2 \right],$$

où  $T_c^{max}$  est la température critique maximale au dopage optimal.

Le STM nous permet de déterminer les caractéristiques spectroscopiques des HTS dans différentes régions du diagramme de phase. Un exemple de spectre dans le composé à trois plans  $\text{Bi}_2\text{Sr}_2\text{Ca}_2\text{Cu}_3\text{O}_{10+\delta}$ , à dopage optimal ( $T_c = 111$  K) mesuré à 1.8 K est montré dans la Fig. 1. Il présente une forme en V à basses énergies avec des grands pics à  $\pm 46$  mV et une structure asymétrique caractérisée d'abord par un creux et ensuite par une bosse autour de 80 mV. A plus hautes énergies ( $E > 150$  mV), il présente un fond de conductance asymétrique assez plat. Comme les spectres de conductance tunnel différentielle sont proportionnels à la densité d'états à une particule  $N(\omega)$  [7, 8], les caractéristiques du spectre de la Fig. 1 peuvent être compris par une densité d'états modélisée qui inclut des quasi particules de Bogoliubov dans une symétrie  $d$  et qui possèdent un gap d'énergie  $\Delta_{\mathbf{k}}$ . Ces quasi-particules sont excitées dans une bande électronique d'énergie  $\xi_{\mathbf{k}}$  et couplées à un mode collectif d'excitations à travers un terme de self-énergie  $\hat{\Sigma}(\mathbf{k}, \omega)$ . De cette façon, on peut relier les caractéristiques spectroscopiques du spectre montrées dans la Fig. 1 avec les paramètres de la densité d'états modélisée. Sa forme en V à basses énergies ( $E \sim 0$ ) mV correspond à la supraconductivité à symétrie  $d$ , les grands pics sont interprétés comme les pics de cohérence supraconducteurs et leurs positions nous permettent d'estimer le gap d'énergie  $\Delta_p$ , dans ce cas  $\Delta_p = 46$  mV. La structure creux-bosse est associée à un effet de couplage fort [9]. Finalement, les variations dans l'asymétrie du

fond de la conductance pour  $|E| > 150$  meV sont normalement reliées aux corrélations fortes présentes dans ces matériaux [10, 11, 12].

## • Spectroscopie dans le cœur de vortex dans le composé $\text{Bi}_2\text{Sr}_2\text{CaCu}_2\text{O}_{8+\delta}$

Une étude spectroscopique détaillée du cœur de vortex d'un échantillon sur-dopé de  $\text{Bi}_2\text{Sr}_2\text{CaCu}_2\text{O}_{8+\delta}$  a été réalisée. Dans le cœur, une modulation de la densité d'états avec une symétrie quatre a été observée. Cette modulation présente une période de  $(4.3 \pm 0.3)a$  qui est indépendante de l'énergie et on démontre qu'elle est reliée aux états dans le cœur de vortex localisé à  $\pm 6$  meV. Comme l'énergie des états de cœur est proportionnelle au gap supraconducteur  $\Delta_p$ , nos résultats indiquent l'existence d'une relation directe entre les états supraconducteurs et les modulations électroniques locales aux cœurs de vortex.

La spectroscopie tunnel des cœurs de vortex dans le  $\text{Bi}_2\text{Sr}_2\text{CaCu}_2\text{O}_{8+\delta}$  a montré que le spectre pseudogap apparaît dans le cœur de vortex avec deux pics additionnels. Ces pics demeurent à une énergie constante plus petite que le gap et cette énergie ne dépend pas de la distance du centre de vortex [13, 14, 15]. L'énergie de ces états localisés est autour de  $0.3\Delta_p$ , où  $\Delta_p$  est la position des pics de cohérence dans l'état supraconducteur.

Hoffman *et al.* ont aussi observé une modulation spatiale de la conductance tunnel à basse énergie dans le cœur de vortex. Ces modulations présentent une période de  $4a$  [16] (où  $a = 3.8 \text{ \AA}$  est la distance entre les ions de cuivre). Plus tard, des modulations similaires ont été observées en l'absence d'un champ magnétique [17, 18]. Hoffman *et al.* ont remarqué que la longueur d'onde de ces modulations présente une dispersion en énergie et ils ont proposé d'expliquer cet effet par une interférence entre les quasi-particules à cause de la diffusion avec les impuretés et autres inhomogénéités [17, 19]. Par contre, certaines modulations périodiques reportées par Howald *et al.* [18] n'ont pas de dispersion pas en énergie, et une explication en termes de stripes statiques fut invoquée. Plus récemment, Vershinin *et al.* [20] ont étudié la dépendance spatiale de la conductance tunnel dans la région pseudogap, juste au dessus de la température critique. Ils ont observé un réseau carré incommensurable avec une période  $(4.7 \pm 0.2)a$  et pas de dispersion pas en énergie. Ces observations permettent de conclure que ces modulations sont différentes de celles observées dans l'état supraconducteur. Un pattern non-dispersif a été observé aussi à basse températures dans des échantillons fortement sous-dopés de Bi2212 [21] et  $\text{Ca}_{2-x}\text{Na}_x\text{CuO}_2\text{Cl}_2$  (NCCOC) [22] caractérisés par des spectres semblables au spectre du pseudogap. On peut donc relier le pseudogap au pattern carré avec une longueur d'onde non dispersive. Par contre dans l'état supraconducteur, des modulations dispersives sont principalement observées, probablement à cause des interférences entre quasi-particules.

La Figure 3a montre une carte de conductance obtenue à  $V_s = -25$  mV où on voit clairement la position du cœur de vortex. Sa taille et sa forme irrégulière correspondent aux études préalables [23, 24]. Une carte spectroscopique à  $V_s = +6$  mV est montrée sur la Fig. 3. Cette énergie, 6 meV, correspond à l'énergie des états dans le cœur de vortex.

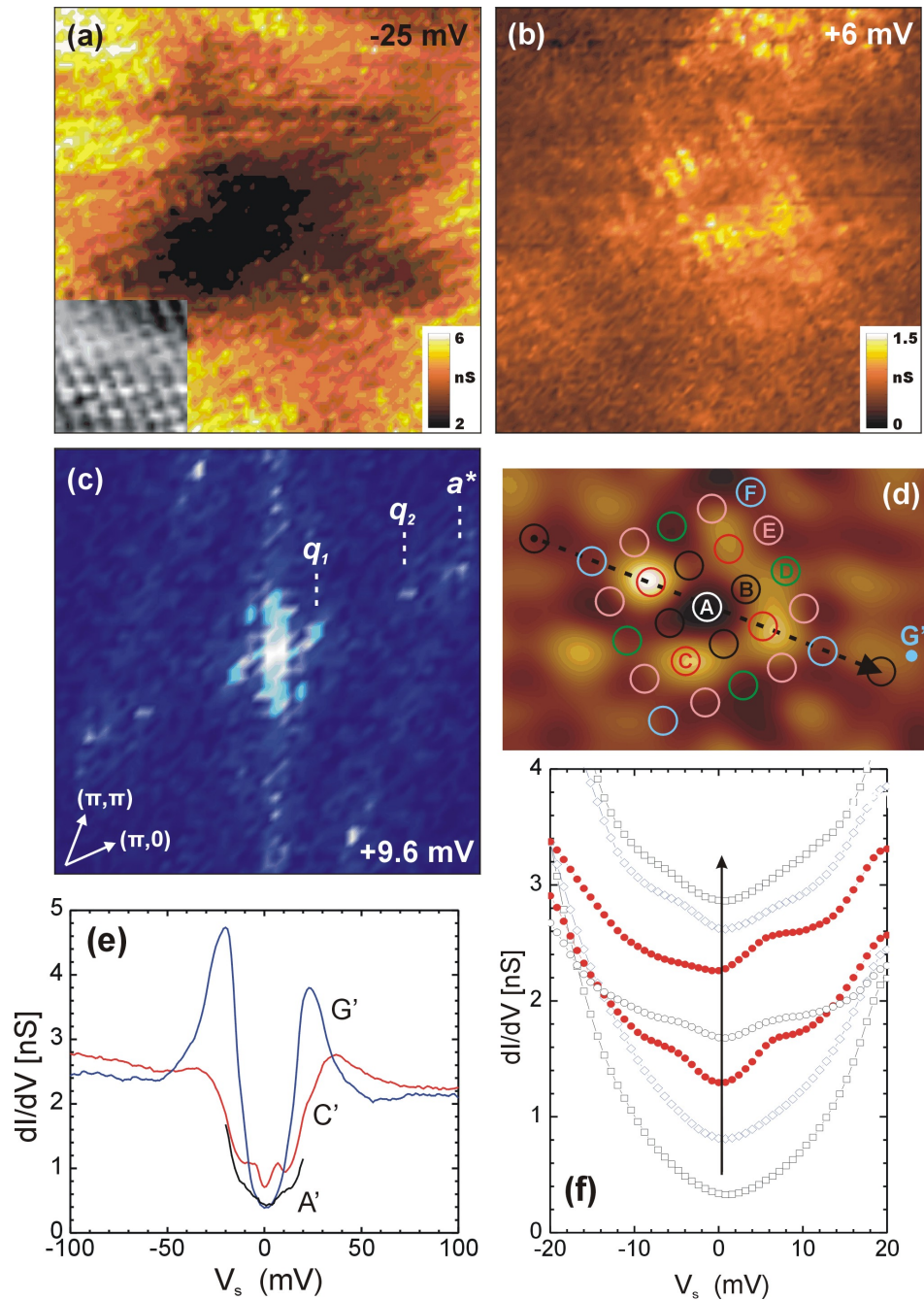


Figure 3: (a)  $8.7 \times 8.7$  nm<sup>2</sup> carte de la conductance à  $V_s = -25$  mV. L'“inset” montre la topographie mesurée en même temps et à la même échelle que la carte de conductance. (b) Carte de la conductance dans la même région que (a) à  $V_s = +6$  mV. (c) Image résultante après une transformation de Fourier appliquée à une carte de conductance mesurée à  $V_s = +9.6$  mV. (d) Région centrale d'une image filtrée par transformation de Fourier d'une carte à  $V_s = +6$  mV. Le filtre appliqué sélectionne la région entre deux cercles de rayons  $q[2\pi/a] \sim 0.17$  et  $\sim 0.32$ , ce qui inclut les pics les plus proches du centre. (e) Spectre mesuré au centre du cœur de vortex ( $A'$ ), dans un maximum du réseau carré ( $C'$ ) et à l'extérieur du cœur. (f) Spectre moyenné dans les sept cercles à travers la flèche sur la figure (d). Les spectres ont été déplacés verticalement pour plus de clarté.

Dans le cœur, une structure carrée formée par quatre régions claires est observée, similaire aux observations précédentes réalisées par Hoffman *et al.* [16]. Afin d'analyser de façon quantitative cette structure, on a appliqué une transformation de Fourier (FT) aux cartes spectroscopiques mesurées à différentes énergies. A part le pic correspondant au réseau atomique, il y a deux structures qui sont clairement observées. D'abord, il y a quatre pics à  $q_1 \simeq 0.25\pi/a$  qui correspondent à une période incommensurable de  $(4.3 \pm 0.3)a$  orientés parallèlement à la liaison Cu-O. Ces maxima sont clairement observés dans toutes les transformées de Fourier des cartes spectroscopiques mesurées entre 4 et 12 mV, et entre -8 et -12 mV, avec une intensité de l'ordre de  $2/3$  plus petite pour les états occupés ( $V_s < 0$ ) que pour les états vides. Ensuite, il y a deux maxima à  $q_2 \simeq 0.75\pi/a$  qui apparaissent uniquement dans la direction  $(\pm\pi, 0)$ . On remarque que les pics  $q_1$  sont légèrement tournés par rapport à la structure atomique, par contre les pics correspondant à la réflexion  $q_2$  ne le sont pas.

Afin d'étudier la variation spatiale de la densité d'états locale dans le cœur de vortex, on a sélectionné 27 zones circulaires dans les images spectroscopiques, chacune avec 21 pixels qui sont montrées dans la Fig. 3d. Pour plus de clarté, l'image filtrée et inversée de la transformée de Fourier est utilisée pour définir ces positions. Trois spectres caractéristiques sont montrés dans la Fig. 3e : A' et C' ont été obtenus au centre des régions A et C, respectivement, et le spectre G' au point G à une distance de 3.4 nm du centre du réseau carré. Le spectre G' est similaire au spectre mesuré en absence de champ magnétique, par contre les spectres A' et C' sont très différents. Les états de cœur apparaissent clairement dans le spectre C' mesuré à un maximum du réseau carré, par contre le spectre correspondant au point A' ne présente presque aucune signature d'états de cœur. Donc, il apparaît que le pattern carré représente la variation spatiale des états localisés. Afin de étudier avec plus de détails cette relation et pour extraire des caractéristiques plus fiables, on a moyenné les spectres dans chaque cercle de la Fig. 3d. Les spectres moyennés qui suivent la flèche indiquée dans la Fig. 3d sont montrés dans la Fig. 3f. Les états de cœur apparaissent clairement dans les deux cercles localisés au maximums du pattern carré (rouge). Au centre A, une faible signature d'états localisés est observée, et cette signature disparaît quand on se déplace à l'extérieur du pattern carré.

Toutes ces observations nous permettent de conclure que les états de cœur de vortex sont étroitement reliés au pattern carré. La Fig. 4a montre une coupe réalisée dans les transformées de Fourier le long de la direction  $(\pi, 0)$  pour différentes énergies. Le pic à  $q_1$  et qui correspond à une période  $\sim 4a$  ne présente pas de dispersion en énergie dans la marge d'erreur de nos mesures. Une faible dispersion aux longueurs d'ondes plus grandes ne peut pas être exclue étant donnée la résolution en énergie. Cependant, cette possible dispersion serait dans le sens opposé à celles observées à travers la direction  $(\pi, 0)$  dans l'état supraconducteur et qui ont été attribuées aux interférences de quasi-particules [17]. Il faut rappeler également que les pics  $q_2$  qui correspondent à une longueur d'onde de  $(4/3)a$  sont uniquement présents dans la direction  $(\pi, 0)$  et pas dans la direction  $(0, \pi)$ .

La figure 4b montre les intensités des trois pics dominants en fonction de l'énergie.

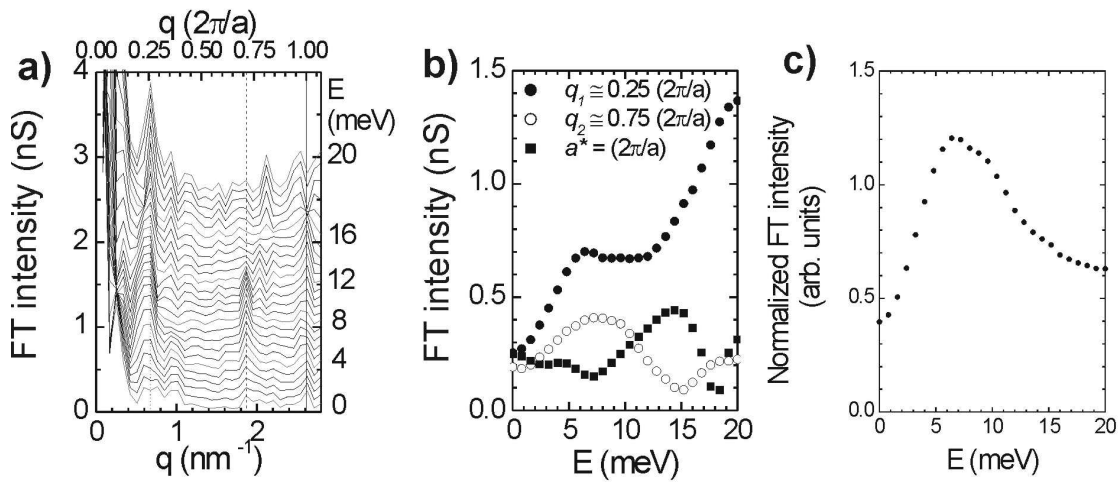


Figure 4: (a) Conductance tunnel différentielle aux énergies entre 0 et 16 meV mesurées le long de la direction  $(\pi, 0)$ . (b) Intensité de la transformée de Fourier pour  $q_0 = 2\pi/a$  correspondant au réseau atomique,  $q_1 \simeq 0.25(2\pi/a)$  correspondant au pattern carré dans le cœur de vortex, et  $q_2 \simeq 0.75(2\pi/a)$  qui apparaît uniquement dans les directions  $(\pm\pi, 0)$ . Les intensités ont été mesurées aux positions des pics indiquées dans la Fig. 3c. (c) Variation en énergie de l'intensité de la transformée de Fourier normalisée correspondant au pic  $q_1 \simeq 0.25(2\pi/a)$ . La normalisation correspond à la valeur moyenne de la carte spectroscopique après que la transformée de Fourier ait été appliquée à chaque énergie.

L'intensité du pic  $q_1$  possède un maximum à l'énergie de l'état localisé. L'augmentation près de 20 meV n'est pas significative, puisqu'il y a une augmentation générale de l'intensité à plus haute énergie. (voir Fig. 3c).

En comparant nos résultats avec les observations de Vershinin *et al.* [20] réalisées dans le pseudogap au-dessus de la température critique, on trouve que l'ordre dans le cœur de vortex est très similaire à l'ordre dans le pseudogap. La structure de base est une modulation carrée sans dispersion et orientée dans la direction de la liaison Cu-O. La période  $(4.7 \pm 0.2)a$  trouvée dans le cœur de vortex à 2 K est légèrement plus petite que la période  $(4.7 \pm 0.2)a$  correspondant au pseudogap à 100 K. Ils ont trouvé que l'intensité du pic dans la transformé de Fourier est plus grande et indépendante de l'énergie au dessous de 20 meV. Par contre, nous avons trouvé que la dépendance en énergie ressemble à la conductance tunnel. Cette différence peut être reliée à un élargissement dû à la température de 100 K. Une autre différence est qu'on a trouvé une modulation  $(4/3)a$  dans une seule direction. Ce type d'ordre a été aussi vu par Hanaguri *et al.* [22] à basse température dans le composé  $\text{Ca}_{2-x}\text{Na}_x\text{CuO}_2\text{Cl}_2$  avec un période principale de  $4a$ .

### • Spectroscopie tunnel a basse temperature dans les composés $\text{Bi}_2\text{Sr}_2\text{CaCu}_2\text{O}_{8+\delta}$ (Bi2212) et $\text{Bi}_2\text{Sr}_2\text{Ca}_2\text{Cu}_3\text{O}_{10+\delta}$ (Bi2223)

Nous avons étudié en détail la forme des spectres tunnel dans les systèmes Bi2212 et Bi2223 mesurés à  $\sim 2$  K et sans champ magnétique appliqué. Il est possible d'obtenir des échantillons homogènes, au moins dans la région sur-dopé. Ces échantillons sont identifiés par une transition supraconductrice étroite  $\Delta T_c/T_c \leq 1\%$ . Dans les échantillons inhomogènes, les spectres varient dans une région d'un nanomètre. En utilisant la dépendance en dopage du gap et le fond de la conductance dans le composé Bi2212 comme référence, on a estimé de façon qualitative le niveau du dopage dans les échantillons de Bi2223. Pour les deux systèmes, on observe une évolution systématique des caractéristiques spectroscopiques quand le gap augmente :

- La hauteur des pics de cohérence diminue.
- La largeur des pics de cohérence semble rester constante.
- La symétrie de la hauteur des pics de cohérence change, ils sont presque symétriques pour des gaps correspondant au dopage optimal.
- La profondeur du creux à voltage négatif diminue en suivant apparemment la diminution en hauteur des pics de cohérence.
- La pente du fond de la conductance dépend linéairement de la largeur du gap.
- Autour du dopage optimal, il y a un changement de signe dans la pente du background de conductance: positive pour gaps plus petits.

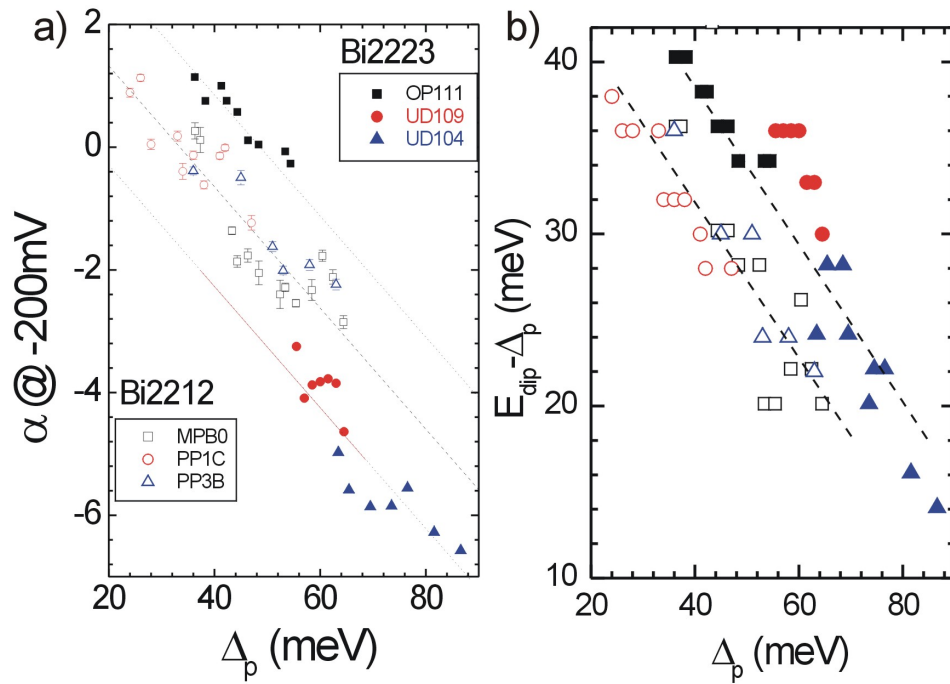


Figure 5: (a) Pente du fond  $\alpha$  déterminé à  $V_s = -200$  mV en fonction du gap d'énergie  $\Delta_p$ . (b) Position absolue en énergie du creux par rapport au gap  $E_{dip} - \Delta_p$  en fonction de  $\Delta_p$ . Les symboles fermés (ouverts) correspondent aux valeurs déterminés des spectres moyennés pour le composé Bi2223 (Bi2212). Chaque spectre a été normalisé à 1 à  $V_s = 300$  mV.

La Fig. 5a montre une évolution presque linéaire de la pente du background  $\alpha$  en fonction du gap pour tous les échantillons mesurés. La position en énergie du creux par rapport aux pics de cohérence  $E_{dip} - \Delta_p$  en fonction de  $\Delta_p$  est montrée dans la Fig. 5b. Ces comportements ont été déterminés pour les échantillons des composés Bi2212 et Bi2223. Un comportement linéaire est observé pour les deux systèmes avec la même pente, c.f. Fig. 5b.

Finalement, dans le spectre tunnel du composé Bi2212, une structure avec des doubles pics est fréquemment observée sur les pics de cohérence. Les deux pics sont normalement séparés par  $\sim 12$  meV et leurs intensités relatives varient à l'échelle atomique.

## • Spectroscopie tunnel sur les supraconducteurs à haute température critique : effet spectroscopique de la singularité de Van Hove, du gap, et du couplage avec un mode collectif

Il a été mentionné ci-avant que les spectres tunnel des supraconducteurs à haute température critique peuvent être compris par une densité des états modélisée  $N(\omega)$  qui inclut les quasi-particules de Bogoliubov avec un gap  $\Delta_k$  de symétrie  $d$ . Ces quasi-particules sont excitées dans une bande électronique avec une relation de dispersion  $\xi_k$  et couplées à un mode bosonique d'excitations à travers un terme de self-énergie  $\hat{\Sigma}(\mathbf{k}, \omega)$ . On présentera dans ce qui suit un ajustement ("fit") des spectres tunnel en utilisant ce modèle qui nous permet de déterminer de façon non ambiguë les paramètres du modèle à partir du fit.

On a utilisé le composé à trois plans  $\text{Bi}_2\text{Sr}_2\text{Ca}_2\text{Cu}_3\text{O}_{8+\delta}$  (Bi2223) qui possède la plus grande température critique dans la famille des composés basés sur le bismuth. La conductance tunnel différentielle mesurée sous ultra haut vide dans un échantillon dopé de façon optimale est montrée dans la Fig. 6. Le spectre présente le comportement en  $V$  caractéristique d'un supraconducteur à symétrie  $d$  et une structure asymétrique de creux-bosse. On a choisi de façon délibérée un échantillon avec un dopage optimal qui montre un fond de la conductance assez plat dans la conductance jusqu'à des énergies élevées (voir "inset" dans la Fig. 6). Pour les échantillon sous-dopés, les spectres montrent un background asymétrique relié aux effets des corrélations fortes [10, 11, 12], qui peut dissimuler d'autres asymétries intrinsèques. Choisir un échantillon avec un dopage optimal et sans background asymétrique nous permet d'exclure les fortes corrélations comme cause des asymétries observés.

Pour illustration, on montre dans la Fig. 6 la prédiction par un modèle à électrons libres qui interagissent selon une interaction BCS avec symétrie  $d$  (courbe définie par l'aire grisée) [25, 26]. Ce modèle reproduit bien les données expérimentales à basse énergie ( $\lesssim \Delta_p/2$ ), mais il ne reproduit pas les données à plus hautes énergies, en particulier l'asymétrie dans la hauteur des pics de cohérence. Une description meilleure de la hauteur

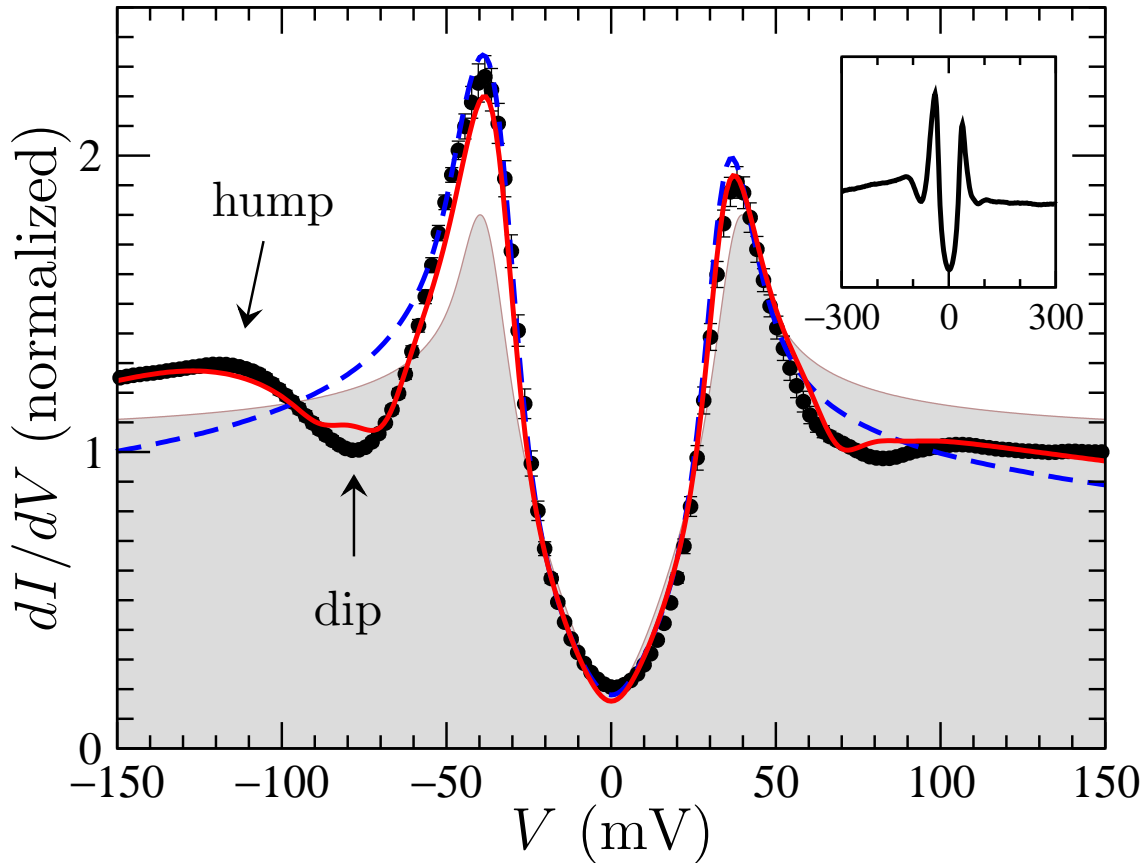


Figure 6: Conductance tunnel typique pour le composé Bi2223 ( $T_c = 111$  K) à  $T = 2$  K (points). Le spectre expérimental est une moyenne de plusieurs spectres mesurés à des positions différentes sur le même échantillon et avec le même gap  $\Delta_p = 38$  meV. Les barres d'erreur donnent les déviations standard de cette moyenne. L'“inset” montre le spectre dans une échelle d'énergie plus grande. On montre aussi les spectres prédits par trois modèles (voir texte) : électrons libres avec une interaction BCS et avec une symétrie  $d$  (grisé), modèle BCS avec symétrie  $d$  qui inclut une dispersion de bande avec une singularité de van Hove (VHS) (ligne en traits tiré), et modèle BCS avec symétrie  $d$  incluant VHS et couplé à un mode magnétique résonant (ligne continue). Le poids spectral total dans la gamme d'énergie de la figure est le même pour toutes les courbes.

des pics de cohérence, de leur largeur et de l'asymétrie est obtenue si on considère la structure de bande électronique. Aux énergies plus petites que 200 meV, un modèle à une seule bande est suffisant pour améliorer les ajustements du spectre. On considère un modèle de réseau à deux dimensions  $\xi_{\mathbf{k}} = 2t_1(\cos k_x + \cos k_y) + 4t_2 \cos k_x \cos k_y + 2t_3(\cos 2k_x + \cos 2k_y) - \mu$  où les  $t_i$  représentent les  $i$ -èmes énergies de hopping entre voisins. Pour cette dispersion la singularité de van Hove (VHS) se trouve à une énergie  $\xi_M = -4(t_2 - t_3) - \mu$  correspondant au point de selle  $\mathbf{k} = (\pi, 0) \equiv M$ . Les paramètres de la bande sont déterminés par un ajustement du minimum carré de tout le spectre qui est montré dans l'“inset” de la Fig. 8.2.1. Cet ajustement donne les valeurs suivantes:  $t_1 = -882$ ,  $t_2 = 239$ ,  $t_3 = -14$ , and  $\xi_M = -26$  meV, avec  $\Delta_0 = 34.1$  meV comme gap de symétrie  $d$ . Ces valeurs déterminées uniquement à partir de la conductance tunnel donnent une surface de Fermi en accord semi-quantitatif avec les mesures de photoémission [27], ce qui est très encourageant. En particulier, la VHS se trouve au-dessus de l'énergie de Fermi comme attendu pour un matériau dopé avec des trous. La courbe théorique résultante (Fig. 6, ligne trait tirés) est très similaire au modèle des électrons libres pour les énergies plus petites que le gap, mais il suit la courbe expérimentale jusqu'à des énergies légèrement plus grandes que les pics de cohérence. L'effet principal de la VHS est d'ajouter du poids spectral additionnel au dessous du niveau de Fermi et en conséquence d'augmenter la hauteur des pics de cohérence pour des potentiels négatifs. On remarque qu'en absence des facteurs d'élargissement [26] la VHS apparaîtra comme un deuxième pic à coté du pic de cohérence principal.

Le modèle “BCS plus VHS” n'est pas satisfaisant aux énergies supérieures à  $2\Delta_p$ , où il échoue à reproduire le transfert significatif de poids spectral du creux à la bosse et qui est plus fort aux potentiels négatifs dans le spectre expérimental. Typiquement, ces transferts signalent un couplage fort des quasi-particules avec une excitation collective. Ce couplage augmente l'amortissement des quasi-particules dans une gamme d'énergie et en même temps il produit une renormalisation dans sa dispersion. Dans les supraconducteurs conventionnels, le couplage électron-phonon induit des effets similaires dans le spectre tunnel, bien que moins prononcés, aux énergies reliées à la fréquence des phonons [28, 29, 30]. Une interprétation de la structure creux-bosse basée sur les phonons a été récemment utilisée [31, 32, 33, 34, 35, 36]. Un autre possible candidat est l'excitation magnétique à  $(\pi, \pi)$  [37, 38, 9], connue normalement comme “la résonance à 41 meV” — bien que son énergie change d'un matériau à un autre et varie aussi avec le dopage [39]. Le couplage des quasi-particules avec ce mode collectif change la self-énergie des électrons et peut être exprimé en termes de susceptibilité du spin  $\chi_s(\mathbf{q}, \omega)$  [38]. En utilisant une expression de  $\chi_s$  obtenue pour reproduire les données de la diffusion inélastique des neutrons, Hoogenboom *et al.* ont montré que ce modèle fournit une très bonne description du spectre tunnel du composé Bi2212 à des dopages différents [40]. En plus des paramètres de la structure de bande  $t_i$ ,  $\mu$  et  $\Delta_0$ , ce modèle contient trois paramètres additionnels qui sont l'énergie de la résonance  $\Omega_s$ , la longueur caractéristique  $\xi_s \sim 2a$  qui représente l'extension du mode autour du point  $\mathbf{q} = (\pi, \pi)$  [38], et une constante de couplage  $g$ .

Afin d'estimer ces paramètres, on a réalisé un autre ajustement aux moindres carrés

de tout le spectre qui est montré dans le “inset” de la Fig. 8.2.1, mais cette fois-ci on a fixé les paramètres  $t_i$  aux valeurs déterminées précédemment. Cette procédure donne  $\Delta_0 = 33.9$  meV,  $\xi_M = -42.4$  meV et  $\Omega_s = 34.4$  meV, avec un accord raisonnable avec les propriétés magnétiques de la résonance mesurées dans le composé Bi2223 [41]. Le spectre théorique résultant suit la courbe expérimentale avec une excellente précision (Fig. 8.2.1, ligne complète). En particulier, le modèle reproduit toutes les asymétries se trouvant expérimentalement entre les énergies positives et négatives. Il est important de remarquer que ces asymétries ne peuvent pas être comprises dans des modèles qui négligent la structure de bande (Refs [35] et [42]). Des spectres théoriques de qualités similaires ont été obtenus par ajustement de spectres avec des gaps entre  $\Delta_p = 36$  et 54 meV.

# Introduction

Superconductivity was discovered by Kamerling Onnes and Gilles Holst in 1911 by cooling mercury to temperatures below 4 K. After its discovery, a complete experimental characterization of this new phenomena followed. During this period, new theoretical ideas were developed which were setting the foundations for a theoretical understanding of superconductivity. After considerably efforts, a theory of superconductivity was developed in 1957, the BCS theory [43], after 46 years of research. This theory explains the general physical properties of superconductors known until that date. It gave full description of the superconducting ground state as well as its low-energy excitations. It brought also a fundamental basis to the hypothesis developed by London that the ground state of a superconductor is a manifestation of a macroscopic quantum state.

In 1986, a revolution came with the discovery of superconductivity in the transition-metal oxide  $\text{La}_{2-x}\text{Ba}_x\text{CuO}_4$  with a  $T_c = 30$  K by Bednorz and Muller [5]. Since its discovery, a race started to find a material with the highest  $T_c$ , which up to now the record is kept by  $\text{HgBa}_2\text{Ca}_2\text{Cu}_3\text{O}_{8-\delta}$  with  $T_c = 133$  K discovered by Schilling *et al.* [44]. These materials are usually referred as high  $T_c$  superconductors (HTS) and they created new excitement in condensed matter physics for its fundamental properties as well as its possible applications to industry. Contrary to previous superconductors which have a  $s$ -wave pairing symmetry and could be fully understood by BCS theory, the high- $T_c$  materials have a  $d$ -wave pairing symmetry and BCS theory can not fully account for the diversity of phenomena that they present. At the moment, the microscopic origin of superconductivity in these materials is not known albeit they are the most extensively studied materials. This is due to the presence of a whole new physics phenomena which makes these materials different. They are also complex materials since their carrier concentration can be smoothly changed by doping. By this process, the material can be tuned from an antiferromagnet insulating phase to a metallic superconductor. Between these two phases a number of interesting phenomena appears that makes difficult a general explanation.

Another technical revolution came in 1981 when Binning and Rohrer [1,2] invented the scanning tunneling microscope (STM). This instrument allows to measure the spectroscopic properties of conducting materials with sub-nanometer spatial resolution. It is an ideal tool to study the different electronic orders that appears in metals and semiconductors like charge density waves or superconductivity. Since its discovery, the STM evolved from an exploration tool to a manipulating technique.

A STM is basically composed of a sharp metallic tip at a few Åströms [45] distance of a conducting sample. When a bias voltage is applied between the tip and the sample a tunnel current flows due to quantum tunnelling. The tunneling current is sensitive to the local electronic properties of the sample and it is exponentially dependent of the tip - sample separation. These two phenomena allow to monitor the charge distribution on the sample surface by scanning the tip over it.

In this work, we use a STM to study the spatial dependence of the spectroscopic properties in high-temperature superconductors (HTS). The STM system is presented in chapter 1 where we discuss the experimental information that can be obtained. In order to interpret the data, we relate the differential tunneling conductance measurements ( $dI/dV(V)$ ) to the local density of states (LDOS) which is done in the first part of chapter 2. In the second part, we calculate a realistic form for the LDOS of HTS. The physical properties of HTS are reviewed in chapter 3 where we have focused on the spectroscopic information that STM can obtain on these materials. As we have performed measurements in the Bi-family of HTS, this chapter ends with a brief description of these compounds. The experimental results are discussed in the following chapters. We start by presenting in chapter 4 a detail study of vortex core spectroscopy in  $\text{Bi}_2\text{Sr}_2\text{CaCu}_2\text{O}_{8+\delta}$  system. A link between the four-fold modulation inside the core and the core states was found. Usually, the spectra of this material varies spatially with different characteristic scales. Chapter 5 shows the spectral changes at nanometer and sub-atomic scales. To obtain general properties, it is important to perform similar measurements in different materials. First STM measurements in the trilayer compound  $\text{Bi}_2\text{Sr}_2\text{Ca}_2\text{Cu}_3\text{O}_{10+\delta}$  are shown in chapter 6 where we discuss the doping variation of the spectra in this material and its similarities with the parent compound  $\text{Bi}_2\text{Sr}_2\text{CaCu}_2\text{O}_{8+\delta}$ . A detailed analysis of the spectral form in  $\text{Bi}_2\text{Sr}_2\text{CaCu}_2\text{O}_{8+\delta}$  and  $\text{Bi}_2\text{Sr}_2\text{Ca}_2\text{Cu}_3\text{O}_{10+\delta}$  systems is presented in Chapter 7. There, we also compare the spectra in both systems and their trends with increasing gap. The role of the Van Hove singularity on the spectra is investigated in Chapter 8. This is performed through fits of the tunneling spectra with the modelled density of states presented in Chapter 2. Finally, the conclusions and perspectives of this work are presented in Chapter 9.

# Chapter 1

## The Scanning Tunneling Microscopy Technique

In this work we use a home-built scanning tunneling microscope (STM). We start describing the experimental setup to later discuss the operational modes. We finish the chapter by showing the different experimental measurements that can be performed with a STM.

### 1.1 Introduction

The scanning tunneling microscope (STM) was invented by Binnig and Rohrer [1,2]. In its early days, the STM was used to reveal the surface arrangement of atoms on different crystals, e.g., the atomic reconstruction in the Si(111) surface. Later on, its spectroscopic capabilities were developed which allowed to observe the spatial distribution of electronic states also in the surface of Si(111) [46]. Therefore, the STM became an ideal exploratory technique to study the spatial variations of local spectroscopic properties due to the combination of the atomic resolution in real-space and meV resolution in energy. Its possibilities were beautifully demonstrated by Hess *et al.* [47]. These authors were able to image individual Abrikosov vortex cores in the superconducting phase of NbSe<sub>2</sub>. Furthermore, they were the first to confirm the existence of electronic bound states on the cores at energies below the gap, as it was predicted by Caroli *et al.* [48]. Actually, the STM has been successfully applied to study a wide variety of phenomena: atomic surface reconstructions [49], charge density waves [50] and quantum interference oscillations around impurities [51]. Nowadays it is not only used as an exploration tool but also to perform changes by manipulating atoms [52], generating chemical reactions [53] and exciting vibrational molecular modes [54].

In this work the STM is used as an exploratory technique to study the spectroscopic properties of high- $T_c$  superconductors in an atomic scale. A STM is composed basically

of a sharp metallic tip which is scanned over a conducting sample with sub-nanometer precision. It allows to obtain topographic and spectroscopic information by measuring the tunneling current when a bias voltage is applied between the tip and the sample. Furthermore, spectroscopic information is obtained by measuring the differential conductance using a lock-in amplifier.

## 1.2 Experimental setup

We use a home-built STM which operates in a temperature range between 275 mK and room temperature in magnetic fields up to 14 Tesla and in a Ultra High Vacuum (UHV) chamber with *in situ* capabilities for sample manipulation. Since its extreme sensibility to tip-sample distance, the STM requires a good vibration isolation to stabilize the vacuum tunnel junction. To diminish the propagation of mechanical vibrations, the entire system rests on a concrete block of 4 tons independent of the building walls, supported by a frame standing on three legs filled with sand. In order to avoid the excitation of the natural vibrational frequencies of the system, we have kept its center of mass as low as possible whilst maintaining a comfortable access for manipulation.

I will briefly describe below the general setup of the system as well as its different components: the STM unit, the cryogenic unit, the UHV unit and the total electronics. The system was assembled by Martin Kugler and a detailed description of the system can be found in his PhD thesis [55].

### 1.2.1 General Setup

The system design is unconventional since the cryostat is above the UHV chamber in a bottom loading configuration. This design allows a compact system with an easy access to the STM and a short turn-around time. At the center of the cryostat there is an insert with a single-shot  $^3\text{He}$  refrigerator. The STM head unit is located at the end of the insert and can be moved from its upper measuring position at the center of the superconducting magnet to a lower position inside a UHV chamber attached to the cryostat. When the STM is inside the UHV chamber, tips and samples can be exchanged *in situ*.

Due to the whole system dimensions ( $\sim 2$  m height), the system has been installed in a specifically adapted building where a hole has been drilled between the basement and the ground floor. In the basement the system rests together with all the UHV pumps. On the ground floor all the electronic equipment has been installed. The top of the cryostat is at the same level as the ground floor. Finally, a pulley suspended from the ceiling allows us to load the cryostat and remove the insert [56].

### 1.2.2 STM unit

The sub-nanometer control of the tip-sample distance is achieved using piezoelectric materials. The STM configuration developed in Geneva [3, 4] consists of two concentric piezoelectric tubes: The XYZ movement of the tip is governed by the inner tube (scanner), the outer tube (translator) controls the sample movements. Each piezoelectric tube has four outer quadrant gold electrodes for the XY-movement and an inner gold electrode for Z-motion.

A spring-loaded tip holder sits at the center of the scanner and tips are soldered with indium into the holder. The scanner is loaded inside the translator (see Fig. 1.2.1). Attached to the translator are two sapphire rods in mechanical contact with an inertial slider. The sample holder is laterally spring loaded in the inertial slider. By applying a cycloid signal to the translator, the inertial slider steps up or down the rails by stick-slip motion. The magnitude of the frictional forces controlling the stick-slip motion are adjusted by springs holding the inertial slider onto the sapphire rods. On the inertial slider a commercial calibrated Cernox thermometer [57] is glued about 5 mm from the sample. Finally, the whole STM unit hangs on a spring with a resonance frequency of 2 Hz in UHV. This constitutes the final stage of vibrational isolation .

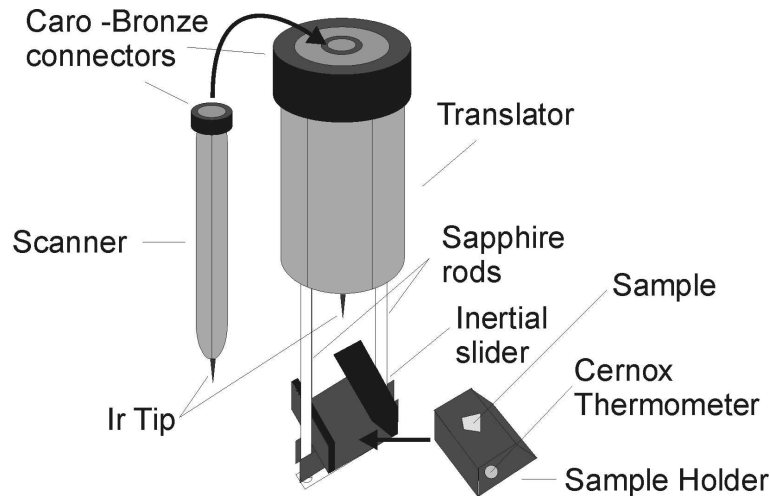


Figure 1.2.1: Schematic STM Unit.

The STM is built from UHV compatible non-magnetic materials with a high thermal conductivity, in order to meet the constraints imposed by its working environment. The home-made pieces of the STM (the inertial slider, sample holder and tip holder) are made from Caro-Bronze alloy [58]. The STM was assembled using two different epoxy glues: Epo-Tek 417 for electrical contacts and Epo-Tek H70E for electrically insulating but thermally conducting contacts [59]. A more complete description of the choice of materials can be found in Ref. [55] .

The tips used are prepared from high purity iridium wire [60]. The wire is electro-

chemically etched in a  $\text{CaCl}_2 + \text{HCl} + \text{H}_2\text{O}$  solution with a carbon rod as the cathode. The process takes 15 minutes using a potential difference of 30 V and a 0.3 A current. A detailed description of the tip preparation process is done in reference [61].

At 2 K this STM can perform spatial scans of  $\sim 1 \mu\text{m}^2$  on a sample surface. To improve this spatial range further, a recently developed XY-table [62] could be incorporated directly into the STM. This table controls the position of the tip on the sample with nanometric precision, allowing a spatial study beyond the conventional maximum piezoelectric elongation.

### 1.2.3 Cryogenic unit

The working temperature of the STM extends from 275 mK to room temperature. We use a  $^3\text{He}$  refrigerator to control the temperature in this range. I will describe the cryogenic equipment and the working procedure used in some detail which are important for obtaining a thermally stable tunnel junction. The basic concepts and a deeper discussion of the temperature control below 1K can be found in Refs [55, 63].

We use a bottom-loading cryostat design and an insert with a single-shot  $^3\text{He}$  refrigerator; both were developed by *Oxford Instruments* in collaboration with Ø. Fischer's group. The bottom-loading design allows the STM to be accessed in a UHV atmosphere, thus achieving a sample turn-around time of  $\sim 10$  hours which is much shorter than top-loading cryostats. The bottom-loading cryostat and all its diverse components are shown in Fig. 1.2.2. The cryostat is made of stainless steel to avoid heat conduction. The heat transport through convection is suppressed by vacuum isolation in the outer vacuum chamber (OVC). Using a turbo pump, a pressure in the OVC of  $10^{-8}$  mbar can be obtained. This pressure is reduced by more than one order of magnitude by cryopumping. Inside the OVC chamber, a 63 litre  $\text{N}_2$  bath screens a 67 litre  $^4\text{He}$  bath from heat radiation. The  $^4\text{He}$  level is measured by a resistive level detector. The OVC is separated from the ultra high vacuum chamber at the bottom of the cryostat (UHV) by large bellows which compensate the thermal stress produced between the cryogenic baths and the UHV chamber at room temperature. Inside the  $^4\text{He}$  bath there is a NbTi/Nb<sub>3</sub>Sn superconducting magnet. It has a clear bore diameter of 64 mm and allows us to reach 12 Tesla at 4.2 K (which is the condensation temperature of  $^4\text{He}$ ) and 14 Tesla at 2.2 K (slightly above the superfluid transition of  $^4\text{He}$ ) by pumping on a  $\lambda$ -plate just above the magnet. At the bottom of the cryostat, two copper baffles are connected to the  $\text{N}_2$  bath. These act as a 77 K radiation shield to the  $^4\text{He}$  bath from the room temperature UHV chamber.

The insert incorporates a continuously operating  $^4\text{He}$  evaporation refrigerator. Here,  $^4\text{He}$  is taken in through a pick-up in the bottom of the  $^4\text{He}$  bath and then flows through a flow impedance into a small vessel called the 1K pot. Its volume load is controlled by an automated needle valve. The  $^4\text{He}$  in the 1K pot is pumped with a 63 m<sup>3</sup>/hr rotary pump, isenthalpically expanding the liquid from the bath through the needle valve. In this way a reference temperature of 1.8 K at the 1K pot is obtained.

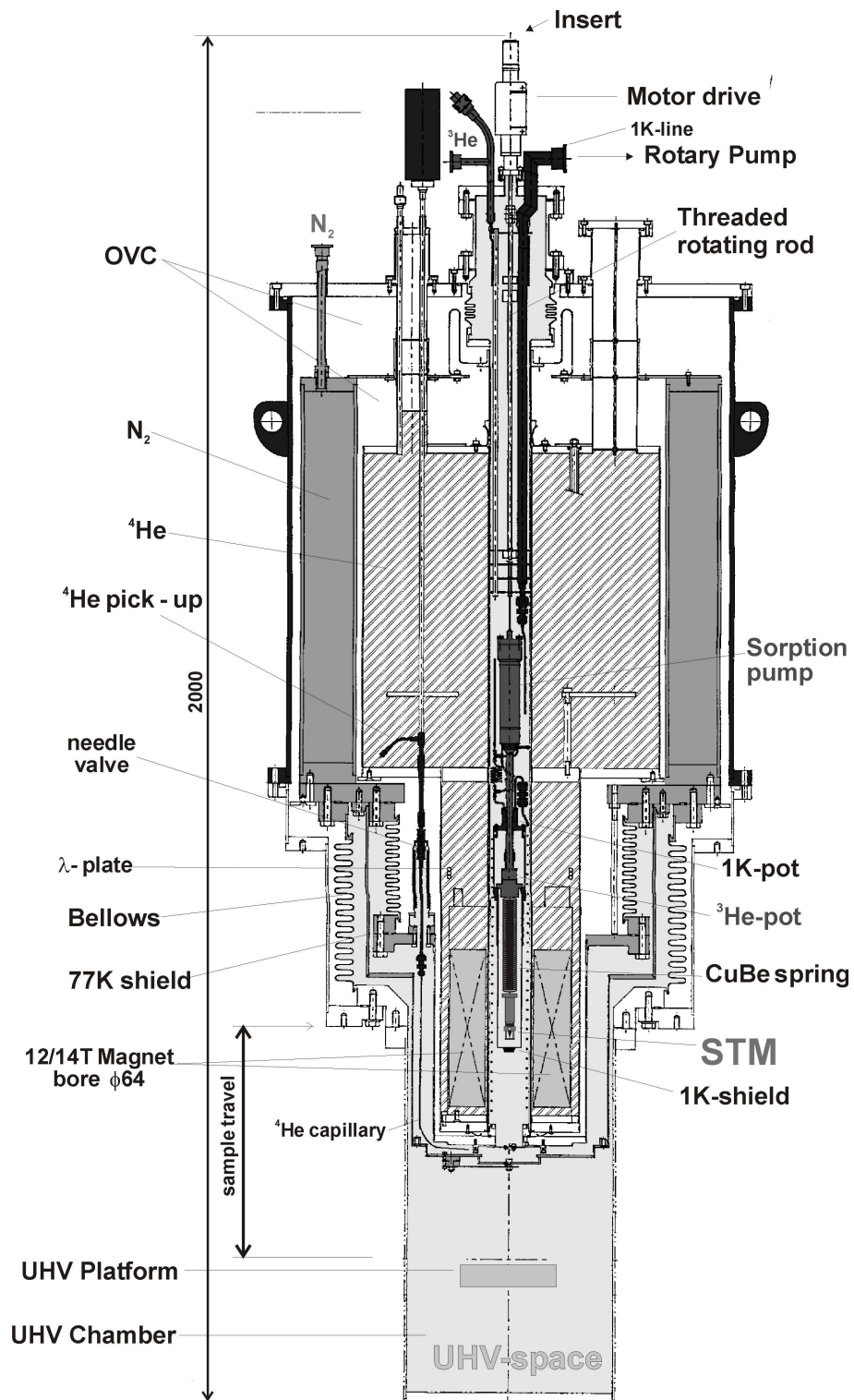


Figure 1.2.2: Experimental cryogenic setup showing the cryostat with the insert.

The insert also includes a single-shot  $^3\text{He}$  refrigerator with an internal sorption pump. The  $^3\text{He}$  refrigerator consists of a  $^3\text{He}$  pot in which the  $^3\text{He}$  condensates and a charcoal sorption pump. The sorption pump adsorbs the  $^3\text{He}$  gas if its temperature is below 20 K and releases it above 25 K; thus by controlling the temperature of the pump the  $^3\text{He}$  can then be condensed. Its temperature can be regulated by the flow rate in the  $^4\text{He}$  line and a 200- $\Omega$  resistive heater at the base of the sorption pump. Between the sorption pump and the  $^3\text{He}$  pot lies the 1K pot which is in thermal contact with the  $^3\text{He}$  system. When the sorption pump is warmed up above 25 K, it releases  $^3\text{He}$  gas that will enter thermal contact with the 1K pot at 1.8 K. As the critical temperature of  $^3\text{He}$  is 3.3 K, it will condense on surfaces below this temperature if the pressure is above its critical pressure  $P_c = 1.15$  bar. The released  $^3\text{He}$  therefore condenses and eventually drips down to the  $^3\text{He}$  pot where liquid  $^3\text{He}$  accumulates. During the formation of the liquid phase, the  $^3\text{He}$  pressure decreases until reaching a steady minimum, implying that the sorption pump has released all the gas adsorbed. Once all the  $^3\text{He}$  is in the  $^3\text{He}$  pot, the sorption pump is cooled down below 20 K and starts to adsorb the  $^3\text{He}$  gas above the liquid, thus reducing the liquid  $^3\text{He}$  temperature by evaporation cooling. In this way, the temperature at the  $^3\text{He}$  pot can be regulated between  $\sim 0.3$  and 1.8 K by the pumping speed of the sorption pump which is regulated by controlling the sorption temperature. The time duration for which the  $^3\text{He}$  pot stays at this temperature is known as hold-time and is about 20 h.

Until now I have discussed how the temperature is controlled below 1.8 K. Next, I discuss how it is controlled above this point. The precise temperature control of the sample allows us to perform details study of its different thermodynamic phases. The temperature control above 1.8 K is performed by the flow of  $^4\text{He}$  and by a 200- $\Omega$  resistive heater located on the  $^3\text{He}$  pot. First we warm up the sorption pump above 25 K (nominally 30 K) in order to release the  $^3\text{He}$  gas adsorbed. This increases the pressure in the  $^3\text{He}$  refrigerator which expands the  $^3\text{He}$  bellow and presses the  $^3\text{He}$  pot against the 1K shield. This mechanical contact acts as a thermal bypass to the heat transport of the  $^3\text{He}$  gas convection between the 1K pot and the  $^3\text{He}$  pot. The cooling power is supplied by the  $^4\text{He}$  flow through the 1K pot and the  $^3\text{He}$  pot and by the convection of  $^3\text{He}$  gas in the  $^3\text{He}$  refrigerator. The 200- $\Omega$  resistor heats the  $^3\text{He}$  pot to the desired temperature. This allows to actively regulate the temperature in the  $^3\text{He}$  pot which is sensed by a calibrated Carbon-Glass thermometer [64]. The temperature is also sensed in the 1K pot by a Generic  $\text{RuO}_2$  thermometer [65]. An *Oxford Instruments* ITC503 temperature controller allows to regulate the temperature with a 1% stability.

For storing the  $^3\text{He}$  gas when warming up the system the sorption pump is connected to a storage vessel through a coiled tube. Another coil connects the 1K pot to the rotary pump. These coils allow the vertical motion of the insert necessary to access the STM in the UHV chamber. This is performed by the vertical motion of the bottom part of the insert, where the 1K pot and the  $^3\text{He}$  refrigerator are located. The vertical displacement of the insert is obtained by a rotating threaded rod controlled by a motor at the top of the cryostat.

The electrical wires must be thermalized before reaching the STM to prevent any heat transport from room temperature. To do so, all the electrical connections passing through the top of the cryostat are thermally anchored on the 1K pot before reaching the  $^3\text{He}$  pot. From there, copper wires descend to the STM. This copper wiring together with the CuBe spring provides the thermal contact between the STM and  $^3\text{He}$  pot. To reduce the heat load on the STM and  $^3\text{He}$  pot, both are enclosed by a radiation shield screwed onto the 1K pot referred to as the 1K shield.

### 1.2.4 UHV unit

The UHV unit consists of several facilities for *in situ* sample and tip exchange. The various components installed for these tasks as well as a complete description of the sample and tip exchange procedure have been described elsewhere [55]. Here I will describe the UHV components and the procedure to attain a base pressure of  $10^{-9}$  mbar. It is important to remark that the final pressure in the STM must be around  $10^{-11}$  mbar if we account for cryopumping and the adsorption power of the charcoal situated at the bottom of the 1K shield.

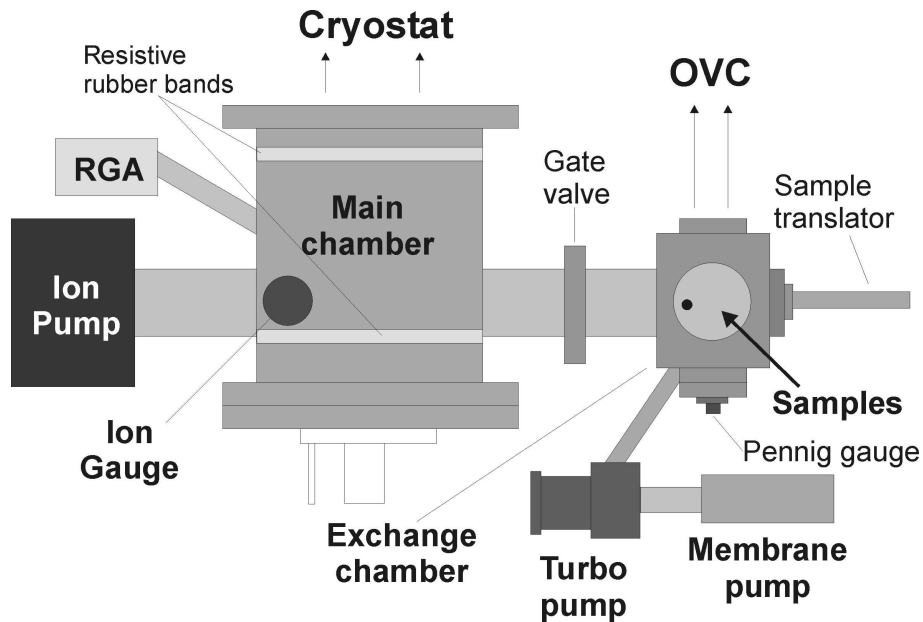


Figure 1.2.3: Schematic UHV setup.

The main component of the UHV unit is a cylindrical stainless steel main chamber that fits at the bottom of the cryostat. As shown in Fig. 1.2.3, an exchange chamber connected to the main chamber allows sample and tip exchange without leaving the UHV environment. A 300 l/s ion pump continuously maintains the pressure around  $10^{-9}$  mbar. In order to produce a UHV environment starting from atmospheric pressure, the main

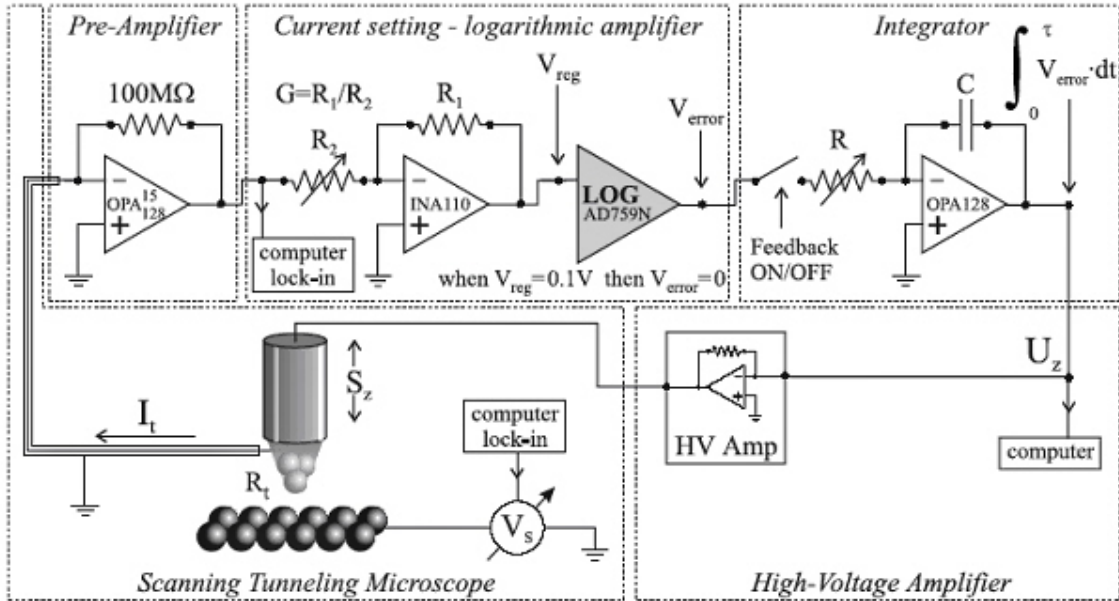
chamber is initially connected to the OVC through the exchange chamber. After that, a membrane pump is switched on; this is the primary pump for a 300 l/s turbo pump connected to the exchange chamber. When the pressure between the membrane pump and the turbo pump is 1.8 mbar, the turbo pump is switched on. After four days a pressure of  $2 \times 10^{-7}$  mbar is obtained. This is measured at the bottom of the exchange chamber by a Pennig gauge. A RGA gas analyzer allows to measure the gas composition of the chamber. At this stage the chamber gas is mostly composed of water (70 % H<sub>2</sub>O, 13 % N<sub>2</sub>, 16 % H<sub>2</sub>).

Next, to eliminate the water, we heat the main chamber at least for three days. Two resistive rubber bands surround the main chamber allowing to bake the system to 100 °C maximum. However several components in the system can not be heated to this temperature: the superconducting magnet (see Section 1.2.3) and the Cernox thermometer located in the STM-slider (see Section 1.2.2). Therefore a cold flow of N<sub>2</sub> is introduced through the <sup>4</sup>He chamber to prevent the magnet from reaching its maximum temperature of 40 °C. Also to avoid that the Cernox thermometer is heated above 60 °C, the STM is raised to its measuring position at the core of the magnet during the whole baking process, with the 77 K radiation baffles at the bottom of the cryostat open (see Fig. 1.2.2). During the baking, the temperature and the pressure of the main chamber are sensed: the temperature is sensed with one thermocouple at its bottom and another at its top; an ion gauge senses the pressure. After seven days of baking with the ion pump turned on, we reach a  $7 \times 10^{-9}$  mbar pressure inside the main chamber, with 66 % of N<sub>2</sub>, 30 % of <sup>4</sup>He and <sup>3</sup>He, the rest 1 % of H<sub>2</sub>O, O<sub>2</sub> and CO<sub>2</sub>. When the system is at 4.2 K and the gate valve is closed, a pressure of  $10^{-9}$  mbar in the main chamber is obtained.

In the present thesis we have studied high- $T_c$  superconducting materials which present highly reactive surfaces. The latter are easily degraded in air which explains the need of a UHV environment. Pristine surfaces are obtained by cleaving these layered materials *in situ* at room temperature.

### 1.2.5 Electronic equipment and acquisition software

A negative feedback setup is used to dynamically stabilize the tip over the sample surface through the vacuum gap during scanning. The electronic circuit used is schematically shown in Fig. 1.2.4 where we observe that the tip is connected to the ground and the sample is biased to a potential  $V_s$ . The tunnel current is measured from sample to tip, therefore at positive bias voltages ( $V_s > 0$ ) a positive tunnel current is measured. In this way, empty sample states are probed for positive bias and occupied states for  $V_s < 0$ . During our research typical bias potentials range between 0.1 and 0.9 V and typical tunnel currents between 0.2 and 1 nA. The tunnel current is carried from the cryostat by a coaxial cable. The current is amplified in a pre-amplification stage located at the top of the cryostat. The amplified output signal is used as an input signal of a logarithmic amplifier which linearizes the exponential dependence of the tunnel current on the tip-sample dis-



Schematic block diagram of the analog feedback regulation circuitry.

Figure 1.2.4: Schematic electronic setup.

tance (see Section 2.2). An output  $V_{error}$  signal is set to zero when the voltage regulation signal is 0.1 V. The signal  $V_{error}$  allows to keep the tunnel current constant into a desired set value: It is different from zero when the measured tunnel current is different from its set value. The integrated  $V_{error}$  signal is amplified and fed back to the scanner piezoelectric. In this way the tip-sample distance is dynamically adjusted in order to maintain the tunnel current constant.

Several electronic components have been improved during this thesis. Newly developed components intended to reduce the electronic noise below 1 mV peak-to-peak have been implemented and tested in order to increase the stability of the STM during scanning. A real-time MicroStar acquisition 16-bit card [66] together with different analogical and digital input and output expansion boards [67] have been installed. A new control software has been implemented to pilot the STM based on this real-time acquisition card. This software was developed in a Labview interface [68] working under the Windows operating system. This platform provides a user-friendly interface to data acquisition and data analysis including Fourier transforms, 3D data rendering, numerical derivatives and a database. Fig. 1.2.5 shows a snapshot of the acquisition software developed.

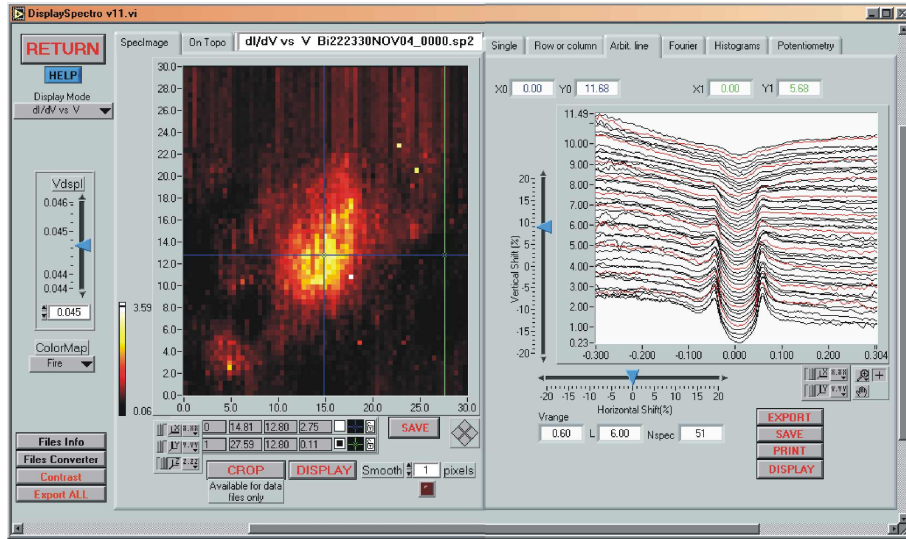


Figure 1.2.5: A snapshot of the data acquisition software showing a spectral map taken at 45 meV and 1.8 K in a  $\text{Bi}_2\text{Sr}_2\text{Ca}_2\text{Cu}_3\text{O}_{10+\delta}$  sample (left) together with a trace of spectra (right) (see Section 1.3).

### 1.3 Experimental Methods

The working physical principle of STM is the quantum mechanical tunnel of electrons between two conductive materials through a thin isolating barrier. When these materials are submitted to a potential difference, a current flows between them. The current is called tunnel current and diminishes with the electrodes distance due to the exponential decay of the electronic waves in the insulating barrier. In STM experiment, one conductive material is a sharp metallic tip which is used to study the electronic properties of the other material named sample. If we move the tip parallel to the sample surface (along the  $x$ - $y$  axis) and measure at the same time the tunnel current we spatially scan the electronic properties of the sample. The spatial resolution of the STM depends on the physical configuration of the tip at its extreme. During a STM experiment we control four of the following parameters: the  $x$ ,  $y$  and  $z$  coordinates of the tip with respect to the sample surface, the potential difference (bias potential)  $V_s$  and the tunnel current  $I$  through the vacuum gap between the tip and the sample. Different information can be obtained depending on which parameter is measured and which are fixed. In the following I will discuss the different operational modes of STM and the information obtained in each mode.

In vacuum tunneling and for a given tunnel current and a bias potential, the exact distance between the tip and the sample depends on the potential barrier between both materials through which electrons tunnel. The potential barrier is determined by the apparent barrier height  $\Phi_A$  between both materials [69] and can be measured by registering the tunnel current as the tip-sample distance is varied. The apparent barrier height is the minimum energy needed to extract an electron from one conductive material and inject

it in the other solid. It is smaller than the work function which is the minimum energy needed to extract an electron from the material surface in contact with vacuum. Typical work-function values for metals range from 2 and 5 eV. We expect to be in a true tunneling regime if the measured apparent barrier height is much bigger than the bias potential applied, so that electrons cannot be excited to energy levels above the apparent barrier height. A schematic diagram of the tunneling junction is shown in Fig. 2.2.1.

In the constant-current mode, the tunnel current is kept constant and the tip-to-sample distance is adjusted through the inverse feedback loop electronics (see Section 1.2.5). In this mode, we measure the vertical position of the tip ( $z$  coordinate), its magnitude being of a few Å. To obtain a topographic image of the surface at a given bias potential, the tip is scanned over the sample and the  $z$  coordinate variation is recorded which is usually represented in a color scheme plot.

In the constant height topographic mode, the  $z$  coordinate of the tip is kept constant and the variations of the tunnel current are measured. The constant-height mode is faster than the constant-current mode since the electronic feedback loop is not used. However since the tip-sample distance is not controlled, there is a risk that the tip enters in mechanical contact with the sample resulting in a change of the microscopic structure or even destruction of the tip. Therefore, the constant height mode is used only when the corrugations of the surface are smaller than the tip height chosen. In this study we have only used the constant-current mode to obtain topographic images of the surfaces since the tip would not crash into any surface protrusion in this operational mode.

Local spectroscopic information is obtained by recording the tunnel current variations when the bias potential is changed at a given point on the surface with the  $z$ -coordinate of the tip fixed. The derivative of the tunnel current  $I$  vs. the bias potential  $V$  is the differential tunnel conductance and in the STM configuration is proportional to the local density of states. The differential tunneling conductance can be obtained either by numerical differentiation of  $I$  vs.  $V$  curves, or by the lock-in technique. In the lock-in technique, a small  $ac$ -voltage modulation  $V_{ac} \cos(\omega t)$  is superimposed to the bias potential. This potential modulation induces a modulation in the tunneling current whose amplitude is measured by a lock-in amplifier. If the lock-in amplifier is in phase with the first harmonic of the modulation, its output DC signal is proportional to the first derivative of the tunneling current giving the differential tunneling conductance. The sample frequency  $\omega$  in the lock-in is typically  $\sim 300$  Hz which is outside the frequency domain of mechanical vibrations  $\omega < 100$  Hz or electronic noise  $\omega > 1$  kHz, considerably enhancing the measurement sensitivity. More details of the lock-in technique can be found in Refs. [55,70].

By combining the spatial resolution performances of the STM with its local spectroscopic capabilities, scanning tunneling spectroscopy (STS) measurements can be made. Hamers *et al.* [46] realized one of the first applications of STS in silicon, using a current-imaging tunneling spectroscopy (CITS) mode. In this mode, spectral maps, i.e. maps of the differential tunneling conductance at a fixed potential can be obtained. In the CITS mode, the tip is scanned over the surface where a regular matrix of points has been dis-

tributed over a predefined area. The bias voltage is fixed to  $V_t$  during scanning and the electronic feedback adjusts continuously the  $z$ -coordinate of the tip maintaining constant the tunneling current  $I$ . In this way, a topographic image is obtained by recording the  $z$ -coordinate variations of the tip at each point. The spectroscopy information is obtained by interrupting the electronic feedback after the tip position has been adjusted. This allows to freeze the tip position and to sweep the bias voltage in order to measure the tunnel conductance  $dI/dV$  at a single value  $V_s$ . After this, the bias voltage is then set back to  $V_t$ , the feedback is turned on and the tip is moved to the next point. At the end of the measurement, we get a spectral map at a given energy and a topographic image measured at  $V_t$ . Also, instead of measuring the spectroscopic properties at a given energy, we can measure the whole spectrum ( $dI/dV$  vs.  $V_s$  curve) at each point by ramping the bias voltage when the electronic feedback loop is disabled. Series of spectra taken at discrete sequential points along a line can be extracted defining a spectral trace.

As an example, Fig. 1.3.1 shows STS measurements performed in the vortex core of a  $\text{Bi}_2\text{Sr}_2\text{CaCu}_2\text{O}_{8+\delta}$  single crystal using the CITS mode. A topography image showing atomic resolution in the  $\text{Bi}_2\text{Sr}_2\text{CaCu}_2\text{O}_{8+\delta}$  (001) surface is presented in Fig. 1.3.1a. Fig. 1.3.1b shows the spectral map acquired simultaneously with the topography indicating the spatial distribution of the vortex core. The images are composed of  $80 \times 80$  equidistant points. A spectral trace of 129 spectra along 8.7 nm through the core is shown in Fig. 1.3.1c where two spectra are highlighted: one outside and another inside the core. These data will be discussed in detail in Chapter 4.

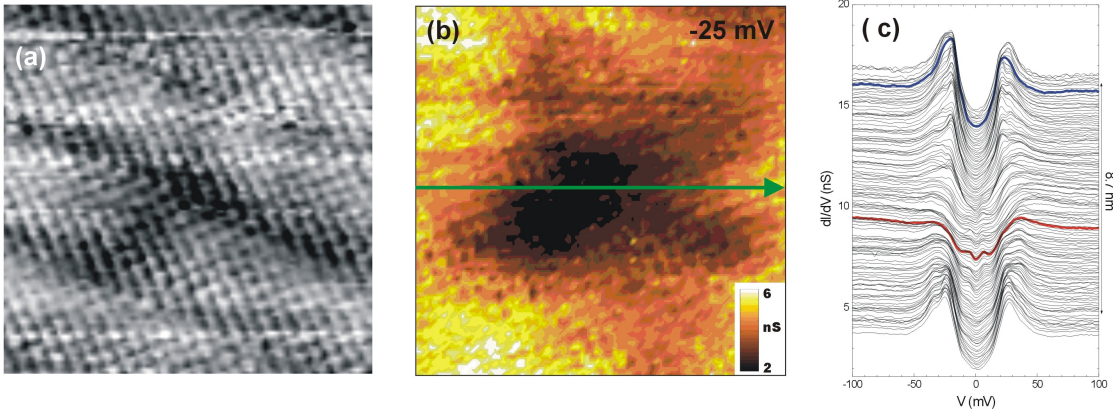


Figure 1.3.1: (a)  $8.7 \times 8.7 \text{ nm}^2$  topography measured at 2 K and 6 T between the  $\text{Bi}_2\text{Sr}_2\text{CaCu}_2\text{O}_{8+\delta}$  (001) surface and an Ir tip. The tunnel conditions are  $I = 0.8 \text{ nA}$  and  $V_t = 0.6 \text{ V}$ . (b) Spectral map acquired at the same time than the topography shown in (a) taken at  $V_s = -25 \text{ mV}$ . (c) A spectral trace performed along the line shown in (b).

# Chapter 2

## Theory

We derive a relation between the differential tunneling conductance and the local density of states. This relation is the basis to interpret the STM spectra. After that, we describe a model that reproduces the local density of states in high  $T_c$  superconductors. This allows us to relate the features of the tunneling spectra to physical parameters.

### 2.1 Introduction

Superconductors were first studied with the tunneling technique by Giaever [71]. He measured the tunneling current in a superconductor-insulator-metal (SIN) planar junction as a function of bias potential  $V$  and interpreted the  $dI/dV$  vs.  $V$  curves as the spectrum of single-particle excitations of the superconducting ground state. Later, a theoretical model for this tunneling junction [72, 73] showed the proportionality between the  $dI/dV(V)$  measurements and the superconducting density of states. This work triggered an effort to understand all known superconductors by correlating theory and experiments. The determination of the phonon density of states and its coupling to the electrons in strong coupling superconductors through a detailed analysis of their tunneling spectrum [30] is perhaps the most remarkable success resulting from this cooperation.

The important relation between the tunneling current measured with a STM and the local density of states (LDOS) was first obtained by Tersoff and Hamman [7] where they applied Bardeen's tunneling theory [74] to the STM symmetry. This reduces the problem to the determination of the LDOS. Using this approach, Hoogenboom *et al.* [40] calculated the LDOS of HTS using different models. They conclude that a model including Bogoliubov quasiparticles coupled to a bosonic mode plus the existence of a van Hove singularity (VHS) in the band structure is able to reproduce the experimental spectra. We will develop this model in the second part of this chapter which will allow us to relate the different features of the experimental spectra to physical parameters. However, we start first by establishing the relation between the differential conductance and the LDOS.

## 2.2 STM and LDOS

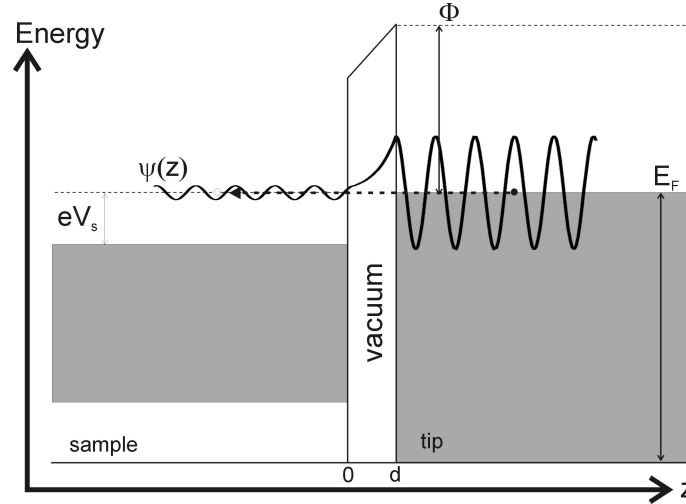


Figure 2.2.1: Schematic representation of the tunnel junction. The electron wave function  $\psi(z)$  decays exponentially in the vacuum barrier.

Here, we describe the theoretical foundations of electron tunneling applied to the STM configuration. The important result is the proportionality of the  $dI/dV$  curves to the local density of states (LDOS). I will start by describing the tunneling formalism and then I will apply it to the STM. At the end, I will discuss the interplay of the tip-sample distance and the LDOS in the tunneling current and in the differential tunneling conductance measurements.

But first, we make some remarks about the theory that accounts for the tunneling phenomena. The tunneling of electrons is an out of equilibrium process where a steady current exists through the junction. There is not a general theory that completely describes the tunneling process. A theory that accounts for the tunneling experiments under certain assumptions was developed by Bardeen [74]. The main assumption on this theory is that the quantum states of the different electrodes are not affected by the presence of the tunneling junction. This assumption is not *a priori* justified but it allows to obtain a simple expression for the tunneling current. Furthermore, this expression correlates with the experimental measurements giving an empirical basis for the theory.

On general grounds, the tunneling current depends on the initial and final states occupied by the tunneling electron, on the strength and width of the potential barrier and on the potential difference between both electrodes. In principle it is possible to fully determine the tunnel current [75] taking into account the continuity of the wave-function and its first derivative across the potential barrier. However this method is cumbersome and is only feasible in idealized junctions with a simple geometry. Another approach to compute the tunneling current is the tunneling Hamiltonian formalism [74] which was first applied to

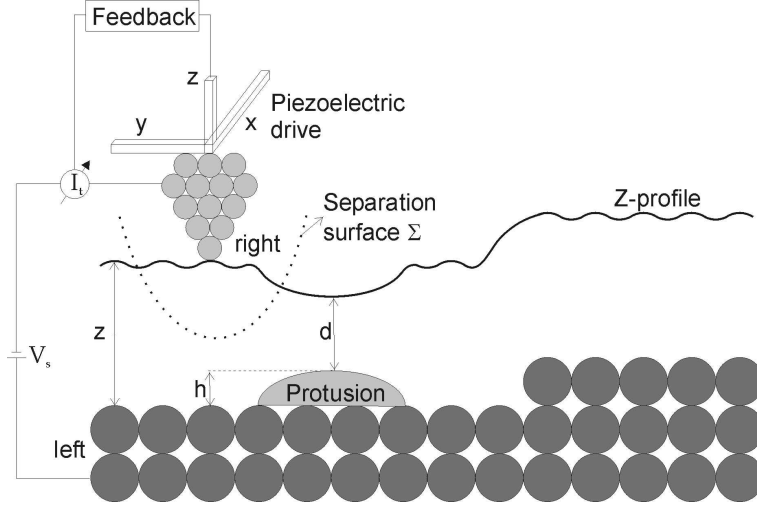


Figure 2.2.2: Schematic STM configuration.

the STM configuration by Tersoff and Hamman [7, 76]. In the tunneling Hamiltonian formalism the two electrodes are considered as quantum mechanically independent systems and the tunneling process is described by a phenomenological Hamiltonian

$$\mathcal{H}_T = \sum_{\lambda, \rho} T_{\lambda\rho} c_\rho^\dagger c_\lambda + T_{\lambda\rho}^* c_\lambda^\dagger c_\rho, \quad (2.2.1)$$

where  $c_\rho^\dagger$  is the creation operator of an electron in the state  $\phi_\rho(\mathbf{r})$  in the right material and  $c_\lambda$  is the destruction operator of an electron in the state  $\phi_\lambda(\mathbf{l})$  in the left material.  $T_{\lambda\rho}$  is the tunneling matrix element between the initial state  $|\phi_\lambda\rangle$  and the final state  $|\phi_\rho\rangle$ . Following Fischer *et al.* [70] we use the real space representation of the tunneling matrix element  $T(\mathbf{l}, \mathbf{r})$  to determine the tunneling current.  $T(\mathbf{l}, \mathbf{r})$  represents the matrix element for an electron to tunnel from a point  $\mathbf{l}$  in the left system to a point  $\mathbf{r}$  in the right system. It is related to  $T_{\lambda\rho}$  through

$$T(\mathbf{l}, \mathbf{r}) = \sum_{\lambda\rho} \phi_\lambda^*(\mathbf{l}) T_{\lambda\rho} \phi_\rho(\mathbf{r}). \quad (2.2.2)$$

In this formalism the tunneling current  $I$  for voltages  $V \ll \Phi_A$  is expressed as [7, 70]

$$I = \frac{2\pi e}{\hbar} \int d\omega [f(\omega - eV) - f(\omega)] \int d\mathbf{l}_1 d\mathbf{r}_1 d\mathbf{r}_2 T(\mathbf{l}_1, \mathbf{r}_1) T^*(\mathbf{l}_2, \mathbf{r}_2) \times A(\mathbf{l}_1, \mathbf{l}_2, \omega) A(\mathbf{r}_2, \mathbf{r}_1, \omega - eV), \quad (2.2.3)$$

where  $f(\omega)$  is the Fermi occupation function and  $A(\mathbf{l}_1, \mathbf{l}_2, \omega)$  [ $A(\mathbf{r}_2, \mathbf{r}_1, \omega)$ ] is the spectral function of the left [right] system. To fix ideas we will assume that the sample is on the left and the tip on the right as in 2.2.1.

According to Bardeen's tunneling theory [74], the tunneling matrix element can be expressed as a surface integral on the separation surface  $\Sigma$  (see Fig. 2.2.2) between the tip and the sample:

$$T_{\lambda\rho} = \frac{\hbar^2}{2m} \int_{\Sigma} (\phi_{\rho}^* \nabla \phi_{\lambda} - \phi_{\lambda} \nabla \phi_{\rho}^*) \cdot d\mathbf{S}, \quad (2.2.4)$$

where  $\phi_{\lambda}$  is the samples wave function,  $\phi_{\rho}$  is the tip wave function and  $d\mathbf{S}$  is the surface element on  $\Sigma$ .

In the vacuum region, the tip and sample wave functions satisfy Schrödinger's equation for states at the Fermi energy

$$(\nabla^2 - \kappa^2)\phi(\mathbf{r}) = 0, \quad \Phi_A = \frac{\hbar^2 \kappa^2}{2m}, \quad (2.2.5)$$

where  $\Phi_A$  is the apparent barrier height. Below, we will solve this equation only for the tip wave functions. Following Chen's procedure [77], we solve Eq. 2.2.5 for the tip state by projecting  $\phi_{\rho}(\mathbf{r})$  on spherical harmonics  $Y_{lm}(\theta, \phi)$ :

$$\phi_{\rho}(\mathbf{r}) = \sum_{l,m} C_{lm} k_l(\kappa|\mathbf{r} - \mathbf{r}_0|) Y_{lm}(\theta, \phi), \quad (2.2.6)$$

where  $\mathbf{r}_0$  is the center of the tip apex and  $k_l(u)$  are the spherical Bessel functions of the second kind. In the following we will keep only the  $s$ -wave solution ( $l = m = 0$ ) for the tip which we denote as  $\phi_{\rho,s}(\mathbf{r})$ .

$$\begin{aligned} \phi_{\rho,s}(\mathbf{r}) &= C k_0(\kappa|\mathbf{r} - \mathbf{r}_0|) Y_{00}(\theta, \phi), \\ &= C \frac{e^{-\kappa|\mathbf{r} - \mathbf{r}_0|}}{\kappa|\mathbf{r} - \mathbf{r}_0|}. \end{aligned} \quad (2.2.7)$$

As pointed out by Chen, the evaluation of  $T_{\lambda\rho}$  in Eq. 2.2.4 is easier if one uses the Green's function of the Schrödinger's equation (Eq. 2.2.5) defined as

$$(\nabla^2 - \kappa^2)G(\mathbf{r} - \mathbf{r}_0) = -\delta(\mathbf{r} - \mathbf{r}_0). \quad (2.2.8)$$

The tip  $s$ -wave solution of Eq. 2.2.8 which is regular at  $|\mathbf{r} - \mathbf{r}_0| \rightarrow \infty$  is

$$\begin{aligned} G(\mathbf{r} - \mathbf{r}_0) &= \frac{e^{-\kappa|\mathbf{r} - \mathbf{r}_0|}}{4\pi|\mathbf{r} - \mathbf{r}_0|}, \\ &= \frac{\kappa}{4\pi} k_0(\kappa|\mathbf{r} - \mathbf{r}_0|), \end{aligned} \quad (2.2.9)$$

and we thus see that the  $s$ -wave tip wave function is simply related to the Green's function through

$$\phi_{\rho,s}(\mathbf{r}) = \frac{4\pi C}{\kappa} G(\mathbf{r} - \mathbf{r}_0). \quad (2.2.10)$$

Inserting this into Bardeen's formula, Eq. 2.2.4, we find

$$T_{\lambda\rho} = \frac{2\pi C\hbar^2}{\kappa m} \int_{\Sigma} [G(\mathbf{r} - \mathbf{r}_0)\nabla\phi_{\lambda} - \phi_{\lambda}\nabla G(\mathbf{r} - \mathbf{r}_0)] \cdot d\mathbf{S}. \quad (2.2.11)$$

Using Green's theorem, the surface integral can now be converted into a volume integral over the space  $\Omega$  to the right of the separation surface  $\Sigma$  (see Fig. 2.2.2):

$$\begin{aligned} T_{\lambda\rho} &= \frac{2\pi C\hbar^2}{\kappa m} \int_{\Omega} [G(\mathbf{r} - \mathbf{r}_0)\nabla^2\phi_{\lambda} - \phi_{\lambda}\nabla^2 G(\mathbf{r} - \mathbf{r}_0)] d\mathbf{r} \\ &= \frac{2\pi C\hbar^2}{\kappa m} \int_{\Omega} [G(\mathbf{r} - \mathbf{r}_0)\kappa^2\phi_{\lambda} - \phi_{\lambda}[\kappa^2 G(\mathbf{r} - \mathbf{r}_0) - \delta(\mathbf{r} - \mathbf{r}_0)]] d\mathbf{r} \\ &= \frac{2\pi C\hbar^2}{\kappa m} \phi_{\lambda}(\mathbf{r}_0), \end{aligned} \quad (2.2.12)$$

where we have used Eq. 2.2.5 valid for the sample wave function in the volume  $\Omega$ . This result was first obtained by Tersoff and Hamman using a different method [7].

In real space, the tunneling matrix element therefore becomes

$$\begin{aligned} T(\mathbf{l}, \mathbf{r}) &= \frac{2\pi C\hbar^2}{\kappa m} \sum_{\lambda\rho} \phi_{\lambda}^*(\mathbf{l})\phi_{\lambda}(\mathbf{r}_0)\phi_{\rho}(\mathbf{r}), \\ &= \frac{2\pi C\hbar^2}{\kappa m} \delta(\mathbf{l} - \mathbf{r}_0) \sum_{\rho} \phi_{\rho}(\mathbf{r}), \end{aligned} \quad (2.2.13)$$

where we have used the completeness relation for the wave function  $\phi_{\lambda}(\mathbf{r})$ .

If the tip is a simple metal described as independent electrons then its spectral function takes the form

$$A(\mathbf{r}_2, \mathbf{r}_1, \omega) = \sum_{\rho} \phi_{\rho}^*(\mathbf{r}_1)\phi_{\rho}(\mathbf{r}_2)\delta(\omega - \epsilon_{\rho}). \quad (2.2.14)$$

Using this spectral function for the tip the tunneling current is:

$$\begin{aligned}
I &= \frac{2\pi e}{\hbar} \left( \frac{2\pi C \hbar^2}{\kappa m} \right)^2 \int d\omega [f(\omega - eV) - f(\omega)] \\
&\quad \int d\mathbf{l}_1 d\mathbf{l}_2 d\mathbf{r}_1 d\mathbf{r}_2 \left( \delta(\mathbf{l}_1 - \mathbf{r}_0) \sum_{\rho} \phi_{\rho}(\mathbf{r}_1) \right) \left( \delta(\mathbf{l}_2 - \mathbf{r}_0) \sum_{\rho'} \phi_{\rho'}^*(\mathbf{r}_2) \right) \\
&\quad A(\mathbf{l}_1, \mathbf{l}_2, \omega) A(\mathbf{r}_2, \mathbf{r}_1, \omega - eV) \\
&= \frac{2\pi e}{\hbar} \left( \frac{2\pi C \hbar^2}{\kappa m} \right)^2 \int d\omega [f(\omega - eV) - f(\omega)] \int d\mathbf{r}_1 d\mathbf{r}_2 \sum_{\rho\rho'} \phi_{\rho}(\mathbf{r}_1) \phi_{\rho'}^*(\mathbf{r}_2) \\
&\quad A(\mathbf{r}_0, \mathbf{r}_0, \omega) \sum_{\rho''} \phi_{\rho''}(\mathbf{r}_2) \phi_{\rho''}^*(\mathbf{r}_1) \delta(\omega - eV - \epsilon_{\rho''}), \tag{2.2.15}
\end{aligned}$$

and using the orthogonality property of the wave functions  $\int d\mathbf{r} \phi_{\rho}^*(\mathbf{r}) \phi_{\rho'}(\mathbf{r}) = \delta_{\rho\rho'}$ , we obtain

$$\begin{aligned}
I &= \frac{2\pi e}{\hbar} \left( \frac{2\pi C \hbar^2}{\kappa m} \right)^2 \int d\omega [f(\omega - eV) - f(\omega)] A(\mathbf{r}_0, \mathbf{r}_0, \omega) \sum_{\rho} \delta(\omega - eV - \epsilon_{\rho}), \\
&= \frac{2\pi e}{\hbar} \left( \frac{2\pi C \hbar^2}{\kappa m} \right)^2 \int d\omega [f(\omega - eV) - f(\omega)] A(\mathbf{r}_0, \mathbf{r}_0, \omega) N_R(\omega - eV), \\
&\propto \int d\omega [f(\omega - eV) - f(\omega)] N_L(\mathbf{r}_0, \omega) N_R(\omega - eV), \tag{2.2.16}
\end{aligned}$$

where  $N_L(\mathbf{r}_0, \omega)$  and  $N_R(\omega - eV)$  are the local density of states (LDOS) of the respective left and right systems and we have used independent electrons for the tip density of states

$$N_R(\omega - eV) = \sum_{\rho} \delta(\omega - eV - \epsilon_{\rho}).$$

Replacing the constant pre-factors in the tunnel current by a constant value "C" and supposing a constant density of states for the tip in the energy range under study, we obtain the following tunneling current measured at the point  $\mathbf{r}_0$

$$I = CN_R \int d\omega [f(\omega - eV) - f(\omega)] N_L(\mathbf{r}_0, \omega), \tag{2.2.17}$$

and the following differential tunnel conductance expression

$$\begin{aligned}
\sigma(\mathbf{r}, V) \equiv \frac{\partial I}{\partial V} &= \frac{\partial}{\partial V} \left[ CN_R \int d\omega [f(\omega - eV) - f(\omega)] N_L(\mathbf{r}_0, \omega) \right] \\
&= CN_R \int d\omega [-f'(\omega - eV)] N_L(\mathbf{r}_0, \omega). \tag{2.2.18}
\end{aligned}$$

Eqs 2.2.17 and 2.2.18 do not show explicitly the exponential dependence of the current on the tip-sample distance. In fact this dependence is contained in the LDOS  $N_L(\mathbf{r}_0, \omega)$ , since the sample wave functions which make up  $N_L(\mathbf{r}_0, \omega)$  all decay exponentially outside the sample surface in the direction of the tip. The sample LDOS  $N_L(\mathbf{r}_0, \omega)$  is therefore evaluated at the tip position giving by the three dimensional vector  $\mathbf{r}_0$ .

We can make this idea more explicit by assuming that the sample wave functions can be factorized in the form

$$\phi_\lambda(\mathbf{1}) = \phi_\lambda^\parallel(x, y)\phi_\lambda^\perp(z)$$

with energy  $\epsilon_\lambda = \epsilon_\lambda^\parallel + \epsilon_\lambda^\perp$ . In the vacuum the functions  $\phi_\lambda^\perp(z)$  decay like free waves so that  $\phi_\lambda^\perp(z) = A_\lambda e^{-\kappa_\lambda z}$ . For simplicity we further assume that there is no dispersion of the quantum momentum along the  $z$ -coordinate, which is a good approximation for quasi-two dimensional materials like the high- $T_c$  superconductors and we neglect the  $\lambda$ -dependence of  $A_\lambda$ . Hence, setting  $\epsilon_\lambda^\perp \equiv 0$  and denoting  $\kappa_\lambda = \kappa_0$  by  $\kappa$ , we find

$$\begin{aligned} N_L(\mathbf{r}_0, \omega) &= \sum_\lambda |\phi_\lambda(\mathbf{r}_0)|^2 \delta(\omega - \epsilon_\lambda) \\ &\propto e^{-2\kappa z_0} \sum_\lambda |\phi_\lambda^\parallel(x_0, y_0)|^2 \delta(\omega - \epsilon_\lambda^\parallel) \\ &= e^{-2\kappa z_0} N_L^\parallel(x_0, y_0, \omega). \end{aligned} \quad (2.2.19)$$

Replacing Eq. 2.2.19 into Eqs 2.2.17 and 2.2.18 we obtain the exponential dependence of the tunneling current and conductance on the tip-sample separation:

$$I \propto e^{-2\kappa z_0} \int d\omega [f(\omega - eV) - f(\omega)] N_L^\parallel(x_0, y_0, \omega) \quad (2.2.20)$$

$$\sigma \propto e^{-2\kappa z_0} \int d\omega [-f'(\omega - eV)] N_L^\parallel(x_0, y_0, \omega). \quad (2.2.21)$$

To obtain Eqs 2.2.17 and 2.2.18, we made a certain number of suppositions which we resume next. We assumed that the tip is a simple metal with constant DOS close to the Fermi energy. We only consider it contributes with  $s$ -wave states in the matrix tunneling element. We can only calculate the matrix tunneling element for  $V = 0$ . Therefore, we assume it does not change with the bias voltage  $V$  neglecting its effect on the tunneling junction. This is justified as long as the bias voltage is much smaller than the apparent barrier height  $V \ll \Phi_A$ . Using a simple approximation we obtain an exponential dependence decay of the sample wave functions into vacuum. This allows us to establish that the the tunneling current is exponentially dependent on the tip-sample distance which is used to develop a criteria for a clean tunneling vacuum condition. A clean vacuum tunneling junction is indicated by a scaling of the spectra with the tip-sample distance . In

each STM measurement we perform, we check if this condition is satisfied in our measurements. An example of this verification is shown in Fig. 2.2.3 where in (a) a series of spectra measured in the CITS mode are shown. Each spectrum has different tunneling conditions ( $I$  and  $V_t$ ) used to stabilize the tip over the sample. If we normalize the different spectra to its tunnel resistance (equivalent to a tip-sample distance normalization) all spectra should collapse into a same curve under the assumption that a vacuum tunnel junction is formed. The good scaling showed in Fig. 2.2.3b suggests that Eq. 2.2.20 is appropriate to analyze the results and provides a method to compare measurements acquired in different samples and different tunnel conditions.

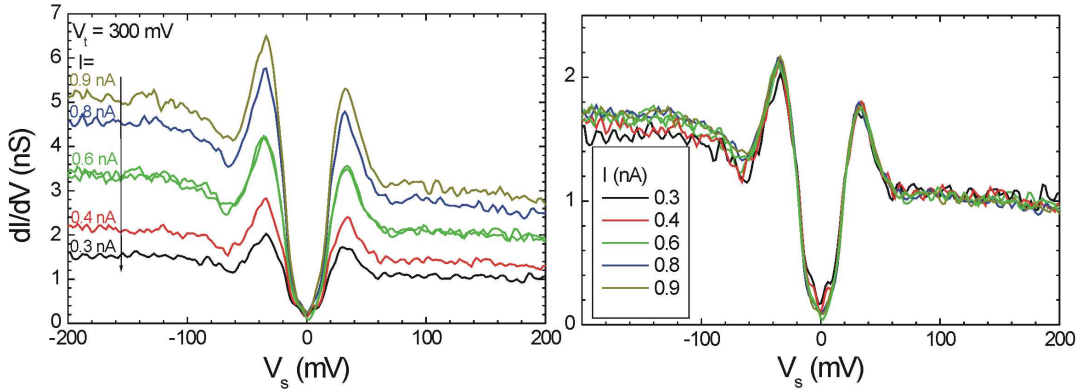


Figure 2.2.3: (a) Tunnel conductance of Bi2212 at  $V_s = 300$  mV and different tunnel currents. (b) Normalized spectra to its corresponding tunnel resistances.

Finally, Eq. 2.2.20 shows that topography images acquired in CITS mode include topographic and spectroscopic information since the vertical variations of the tip can not only be due to relief variations of the sample but also to LDOS variations. During scanning in CITS mode, the  $z$ -coordinate of the tip follows the sample relief if the integrated local density of states (ILDOS) is constant. However, when the ILDOS varies, the tip-sample distance is adjusted to maintain the tunneling current constant during scanning  $I$ . Therefore, the vertical position of the tip can vary due to the sample relief of ILDOS inhomogeneities, *i. e.* if there is a region where the ILDOS is lower, the tip would approach to the sample. This case is shown schematically in Fig. 2.2.2 where we have drawn a protrusion of height  $h$  located in the sample surface. We suppose that the ILDOS in this protrusion is lower than in the rest of the sample, so when the tip moves towards the protrusion, it approaches the sample in order to keep  $I$  constant. Since STM measures relative variations of the tip position, the protrusion appears as a hole in the topography. A simple observation of this phenomena is seen in the adsorption of CO molecules in metallic surfaces [78]. Therefore, we conclude that the variations of the ILDOS are visible in topography images acquired in constant current mode.

## 2.3 Theoretical calculation of LDOS

In this section, we determine the single-particle density of states (DOS) of a BCS superconductor. Furthermore, we couple the Bogoliubov quasiparticles to a collective mode. Following Eschrig and Norman [38] and Hoogenboom *et al.* [40], we use Green's functions formalism to determine the DOS. In the Green's function formalism the propagation of a single electron in a many-body system is described by the time-ordered one-electron Green's function  $G(\mathbf{r}, \mathbf{r}', \tau)$ , defined by

$$G(\mathbf{r}, \mathbf{r}', \tau) = \langle T\psi(\mathbf{r}, \tau), \psi^\dagger(\mathbf{r}', 0) \rangle, \quad (2.3.1)$$

where  $T$  is the time-ordering operator and  $\langle \dots \rangle$  represents a thermodynamic average. The Green's function  $G(\mathbf{r}, \mathbf{r}', \tau)$  can be interpreted as the probability amplitude to remove an electron at position  $\mathbf{r}$  and time  $\tau$  when it was added at the position  $\mathbf{r}'$  and time zero. By taking the time Fourier transform,  $G(\mathbf{r}, \mathbf{r}', \tau)$  can then be expressed in energy-position representation resulting in  $G(\mathbf{r}, \mathbf{r}', \omega)$ . The local density of states (LDOS) at position  $\mathbf{r}$  and energy  $\omega$ ,  $N(\mathbf{r}, \omega)$ , can be calculated using Green's function formalism through the single-particle spectral function:

$$N(\mathbf{r}, \omega) = A(\mathbf{r}, \mathbf{r}, \omega), \quad (2.3.2)$$

where the spectral function  $A(\mathbf{r}, \mathbf{r}', \omega)$  is

$$A(\mathbf{r}, \mathbf{r}', \omega) \equiv -\frac{1}{\pi} \text{Im} G(\mathbf{r}, \mathbf{r}', \omega). \quad (2.3.3)$$

In the following, we only consider uniform systems which are translation invariant. Therefore, the spectral function has the property

$$A(\mathbf{r}, \mathbf{r}', \omega) = A(\mathbf{r} - \mathbf{r}', 0, \omega),$$

which allows us to define the spatial Fourier transformed spectral function or the spectral function in momentum space  $A(\mathbf{k}, \omega)$ :

$$A(\mathbf{k}, \omega) = \int d\mathbf{r} A(\mathbf{r}, 0, \omega) e^{-i\mathbf{k}\cdot\mathbf{r}},$$

which gives for the DOS

$$N(\omega) = \frac{1}{N} \sum_{\mathbf{k}} A(\mathbf{k}, \omega), \quad (2.3.4)$$

where  $N$  is the number of points in  $\mathbf{k}$  space.

The Green's function for an interacting system of fermions in a solid is

$$G(\mathbf{k}, \omega) = \frac{1}{\hbar\omega - \xi_{\mathbf{k}} - \Sigma(\mathbf{k}, \omega)}, \quad (2.3.5)$$

where all the interactions are included in the self energy term  $\Sigma(\mathbf{k}, \omega)$ . Its imaginary part gives the inverse lifetime of the excitations and its real part re-normalizes their energy.

### 2.3.1 BCS

We want to compute the density of states (DOS) using Green's function formalism. In BCS theory, the diagonal term of the single-particle Green's function at  $T = 0$  gives [79]:

$$G(\mathbf{k}, \omega) = \frac{u_{\mathbf{k}}^2}{\hbar\omega - E_{\mathbf{k}} + i\eta} + \frac{v_{\mathbf{k}}^2}{\hbar\omega + E_{\mathbf{k}} + i\eta}, \quad (2.3.6)$$

where  $E_{\mathbf{k}}$  is given by

$$E_{\mathbf{k}} = \sqrt{\xi_{\mathbf{k}}^2 + |\Delta_{\mathbf{k}}|^2}, \quad (2.3.7)$$

and is the energy of the excited quasi-particles with  $\xi_{\mathbf{k}}$  the electron band dispersion and  $\Delta_{\mathbf{k}}$  the superconducting gap,  $\eta$  is a positive infinitesimal value and  $u_{\mathbf{k}}^2$  ( $v_{\mathbf{k}}^2$ ) is the number of available states for an added (removed) electron. Using Eq. 2.3.3, we calculate the spectral function for a superconductor:

$$A(\mathbf{k}, \omega) = u_{\mathbf{k}}^2 \delta(\omega - E_{\mathbf{k}}) + v_{\mathbf{k}}^2 \delta(\omega + E_{\mathbf{k}}), \quad (2.3.8)$$

The first term represents the spectrum of states available for an electron with energy  $E_{\mathbf{k}}$  above the Fermi energy  $\epsilon_F$ . The number of available states for the added electron is given by the pre-factor

$$u_{\mathbf{k}}^2 = \frac{1}{2} \left( 1 + \frac{\xi_{\mathbf{k}}}{E_{\mathbf{k}}} \right),$$

where states above as well as below the Fermi surface contribute to this term. The second term of the spectral function (Eq. 2.3.8) describes the spectrum of states available for a hole. Its energy is  $E_{\mathbf{k}}$  below the Fermi energy and the number of available states is given by the pre-factor

$$v_{\mathbf{k}}^2 = \frac{1}{2} \left( 1 - \frac{\xi_{\mathbf{k}}}{E_{\mathbf{k}}} \right),$$

where an electron can be also removed from all states above and below the Fermi surface.

In Nambu notation, Eq. 2.3.6 becomes

$$\hat{G}(\mathbf{k}, \omega) = \left( \omega - \xi_{\mathbf{k}} - \hat{\Sigma}_{BCS}(\mathbf{k}, \omega) \right)^{-1}, \quad (2.3.9)$$

where  $\hat{\Sigma}_{BCS}(\mathbf{k}, \omega)$  is the BCS self-energy

$$\hat{\Sigma}_{BCS}(\mathbf{k}, \omega) = \begin{pmatrix} 0 & \Delta_{\mathbf{k}} \\ \Delta_{\mathbf{k}}^* & 0 \end{pmatrix}. \quad (2.3.10)$$

The spectral function is therefore calculated by the first element of the Green's function  $2 \times 2$ -matrix  $\hat{G}(\mathbf{k}, \omega)$

$$A(\mathbf{k}, \omega) = -\frac{1}{\pi} \text{Im} \hat{G}_{11}(\mathbf{k}, \omega).$$

We wish to allow for a finite lifetime of the Bogoliubov quasiparticles due, e.g., to impurity scattering, and we introduce an additional scattering rate  $\Gamma$  via a self-energy term  $\Sigma_{\text{imp}}(\omega) = -i\Gamma$ . Including this term into Eq. 2.3.9

$$\hat{G}(\mathbf{k}, \omega) = \left( \omega + i\Gamma - \xi_{\mathbf{k}} - \hat{\Sigma}_{BCS}(\mathbf{k}, \omega) \right)^{-1}, \quad (2.3.11)$$

which replaces the delta functions in the BCS spectral function (Eq. 2.3.8) by Lorentzian functions:

$$\hat{A}(\mathbf{k}, \omega) = \hat{u}_{\mathbf{k}} L_{\Gamma}(\omega - E_{\mathbf{k}}) + \hat{v}_{\mathbf{k}} L_{\Gamma}(\omega + E_{\mathbf{k}}), \quad (2.3.12)$$

where the coherence factors  $\hat{u}_{\mathbf{k}}$  and  $\hat{v}_{\mathbf{k}}$  are expressed in Nambu notation by  $2 \times 2$  matrices

$$\hat{u}_{\mathbf{k}} = \frac{1}{2} \begin{pmatrix} 1 + \frac{\xi_{\mathbf{k}}}{E_{\mathbf{k}}} & \frac{\Delta_{\mathbf{k}}}{E_{\mathbf{k}}} \\ \frac{\Delta_{\mathbf{k}}^*}{E_{\mathbf{k}}} & 1 - \frac{\xi_{\mathbf{k}}}{E_{\mathbf{k}}} \end{pmatrix}, \quad \hat{v}_{\mathbf{k}} = \mathbb{1} - \hat{u}_{\mathbf{k}}. \quad (2.3.13)$$

### 2.3.2 Coupling to a collective mode

Next, we couple the Bogoliubov quasiparticles with a collective mode. In a superconductor the interaction of Bogoliubov quasiparticles with bosonic excitations leads to inelastic scattering processes, in which a quasiparticle of momentum  $\mathbf{k}$  and energy  $\omega$  is scattered to a state with momentum  $\mathbf{k} - \mathbf{q}$  and energy  $\omega - \Omega$  through emission of a bosonic excitation with quantum numbers  $(\mathbf{q}, \Omega)$ . These processes induce a damping of the quasiparticles -reflected mathematically by an increase of the imaginary part of the self-energy  $\Sigma(\mathbf{k}, \omega)$ - and a redistribution of the spectral weight -encoded in the real part of the self-energy. The minimal model to describe the effects of such an interaction is [80,40,38,81]

$$\hat{\Sigma}(\mathbf{k}, i\omega_n) = \frac{g^2}{N\beta} \sum_{\mathbf{q}\Omega_n} \hat{G}_0(\mathbf{k} - \mathbf{q}, i\omega_n - i\Omega_n) \chi_s(\mathbf{q}, \Omega_n), \quad (2.3.14)$$

which is the leading term of the perturbation theory in the coupling of electrons and bosonic excitations. In Eq. 2.3.14,  $\hat{G}_0$  is the BCS Green's function in the absence of coupling where the band dispersion is present as it is shown in Eq. 2.3.11,  $\chi_s$  describes the bosonic excitations susceptibility,  $g$  is the electron-mode coupling constant,  $\beta = (k_B T)^{-1}$  is the inverse temperature,  $i\omega_n$  and  $i\Omega_n$  are the fermionic and bosonic Matsubara frequencies, respectively, and  $N$  is the number of  $\mathbf{q}$  points.

Below, we model the bosonic excitations to reproduce the experimental results of inelastic neutron scattering in high- $T_c$  superconductors. Following Eschrig and Norman [38], we use a phenomenological expression for the energy and  $\mathbf{q}$  dependence of the spin susceptibility  $\chi_s$  in the superconducting state. Guided by the experimental results of inelastic neutron scattering [82, 83] (INS), we assume that below  $\sim 100$  meV, the spin response is dominated by a sharp resonance at energy  $\Omega_s$  near the antiferromagnetic vector  $\mathbf{Q} = (\pi/a, \pi/a)$  of the two-dimensional Brillouin zone. Also we assume that in the region of  $\mathbf{q}$  space where the resonance is present, its dispersion away from  $\mathbf{q} = \mathbf{Q}$  is small enough that it can be neglected. Such assumptions allow one to separate the frequency and momentum dependencies of the spin susceptibility as

$$\chi_s(\mathbf{q}, \omega) = -F(\mathbf{q}) \int d\epsilon \frac{I(\epsilon)}{\omega - \epsilon}. \quad (2.3.15)$$

The function  $F(\mathbf{q})$  is peaked at  $\mathbf{q} = \mathbf{Q}$  and may be written as [38]

$$F(\mathbf{q}) = \frac{\chi_{\mathbf{Q}}}{1 + 4\xi_s^2[\cos^2(aq_x/2) + \cos^2(aq_y/2)]}, \quad (2.3.16)$$

where the correlation length  $\xi_s$  is of the order of the lattice spacing  $a$  and the intensity at  $\mathbf{Q}$  has been determined to be  $\chi_{\mathbf{Q}} \sim 2\mu_B^2$  in Y123 and Bi2212 [83, 84]. We model the energy distribution  $I(\epsilon)$  using Lorentzian functions  $L_{\Gamma}(\epsilon) = (\Gamma/\pi)/(\epsilon^2 + \Gamma^2)$  [85],

$$I(\epsilon) = L_{\Gamma_s}(\epsilon - \Omega_s) - L_{\Gamma_s}(\epsilon + \Omega_s), \quad (2.3.17)$$

which allows to take into account a possible finite lifetime  $\tau_s \sim \Gamma_s^{-1}$  of the spin excitation.

Inserting Eqs 2.3.15 and 2.3.11 into Eq. 2.3.14, one can perform the summation over Matsubara frequencies, and using Eqs. 2.3.17 and 2.3.12 one obtains the self-energy on the real-frequency axis:

$$\hat{\Sigma}(\mathbf{k}, \omega) = \frac{g^2}{N} \sum_{\mathbf{q}} F(\mathbf{q}) [\hat{u}_{\mathbf{k}-\mathbf{q}} B(\omega, E_{\mathbf{k}-\mathbf{q}}) + \hat{v}_{\mathbf{k}-\mathbf{q}} B(\omega, -E_{\mathbf{k}-\mathbf{q}})]. \quad (2.3.18)$$

For definiteness the function  $B(\omega, E_{\mathbf{k}})$  is written down explicitly in the Appendix A. From the self-energy 2.3.18 one can compute the full propagator  $\hat{G}$  using the Dyson equation,  $\hat{G}^{-1} = \hat{G}_0^{-1} - \hat{\Sigma}$ . The first component is given by

$$G_{11}(\mathbf{k}, \omega) = \frac{1}{\omega - \xi_{\mathbf{k}} + i\Gamma - \Sigma_{11}(\mathbf{k}, \omega) - \frac{|\Delta_{\mathbf{k}} + \Sigma_{12}(\mathbf{k}, \omega)|^2}{\omega + \xi_{\mathbf{k}} + i\Gamma - \Sigma_{22}(\mathbf{k}, \omega)}}, \quad (2.3.19)$$

and directly provides the one-particle density of states

$$N(\omega) = \frac{1}{N} \sum_{\mathbf{k}} \left( -\frac{1}{\pi} \right) \text{Im} G_{11}(\mathbf{k}, \omega). \quad (2.3.20)$$

The different roles of the various components of the matrix  $\hat{\Sigma}$  are obvious in Eq. 2.3.19:  $\Sigma_{11}$  and  $\Sigma_{22}$  re-normalize the quasiparticle dispersion on the electron and hole branches, while  $\Sigma_{12}$  re-normalizes the gap  $\Delta_{\mathbf{k}}$ .

## 2.4 Discussion and interpretation

The single-particle density of states  $N(\omega)$  modelled by Eq. 2.3.20 describes Bogoliubov quasiparticles having a gap energy  $\Delta_{\mathbf{k}}$  excited in an electronic band with dispersion  $\xi_{\mathbf{k}}$  and coupled to bosonic excitations through the self-energy term  $\hat{\Sigma}(\mathbf{k}, \omega)$ . This DOS will be used to compute the differential tunnel conductance using Eq. 2.2.18 which will allow us to identify the different features of the tunneling spectra. The final result is convoluted with a Gaussian function  $g_{\sigma}$  of width  $\sigma$ , in order to mimic the finite experimental resolution. We discuss next the trends expected from these three components:  $\Delta_{\mathbf{k}}$ ,  $\xi_{\mathbf{k}}$  and  $\hat{\Sigma}(\mathbf{k}, \omega)$  on the DOS. But first, we describe the electron tunneling process into superconductors.

### 2.4.1 Electron tunneling process in superconductors

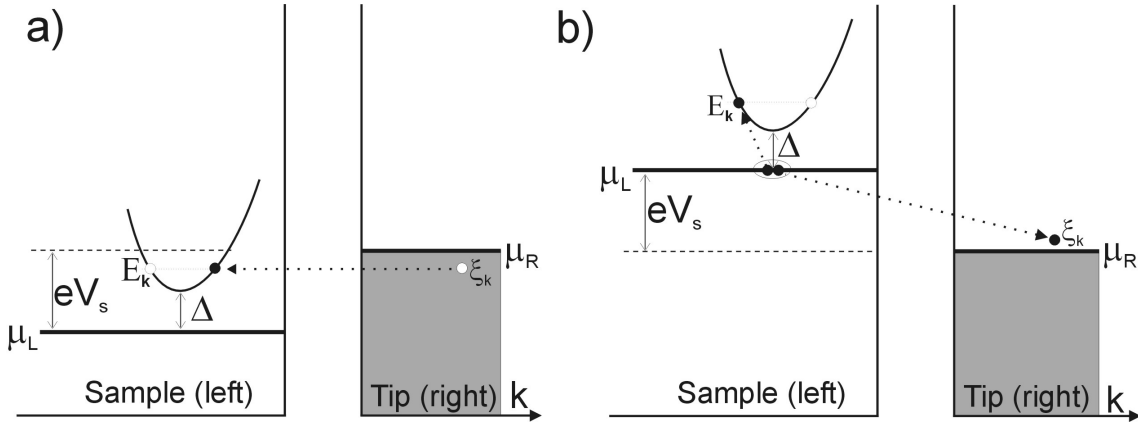


Figure 2.4.1: Energy vs. momentum schematic representation of tunneling into superconductors from a metallic tip. (a) A positive bias potential is applied representing electron tunneling. (b) When a negative bias potential is applied, hole tunneling occurs which involves breaking a Cooper pair.

Since in this work we use the electron tunneling process to determine the local density of states in superconductors, we briefly discuss below the normal-superconductor electron tunneling process. More detailed discussions can be found in literature [79] [86] [87]. In particular it is shown that the physical tunneling process is not the same for positive and negative bias polarities. At positive bias voltage an electron with energy  $eV > \Delta$  can tunnel from the metallic tip into the sample, where it becomes a quasiparticle excitation of energy  $E_{\mathbf{k}} = eV$  (see Fig. 2.4.1a). Later this excitation can decay into the superconducting ground state by forming a pair. At negative bias voltage a hole can be injected into the superconductor. This means that an electron has to tunnel from the superconductor to the tip. However at zero temperature there are no thermal excitations in the superconductor, therefore the tunnel electron has to come from a broken pair state at the Fermi energy

and the partner of the tunnel electron becomes an excitation above the gap energy in the superconductor (see Fig. 2.4.1b). Energy conservation requires that the energy  $\xi_{\mathbf{k}}$  of the tunnel electron in the tip plus the energy of the excited state in the superconductor  $E_{\mathbf{k}}$  is equal to the bias potential  $eV = |E_{\mathbf{k}}| + \xi_{\mathbf{k}}$ . As we can see, the injection of one electron in the tip and another in the excited states of the superconductor is equivalent to the tunnel injection of a hole into the superconductor. However the physical tunneling process for injecting an electron into the superconductor is different from the injection of a hole, because in the latter process a Cooper pair is broken.

## 2.4.2 Gap symmetry in a free electron model

First, we only consider the effect of the gap magnitude on the spectra. Thus, we suppose a constant DOS above  $T_c$  and we do not couple the superconducting quasiparticles with a bosonic mode. The existence of a gap in the single-particle excitations means that there are no excitations below the energy  $\Delta$ , the minimum  $\Delta_{\mathbf{k}}$  value on the Fermi surface. Originally, BCS theory only consider a momentum independent interaction between electrons which gives a  $s$ -wave symmetry for the gap. Later, other symmetries were discovered, like  $d$ -wave symmetry in the high-temperature superconductors [88]. In the case of  $d$ -wave superconductivity in a two-dimensional system the momentum dependence of the gap is given by

$$\Delta_{\mathbf{k}} = \frac{\Delta_0}{2} (\cos(k_x a) - \cos(k_y a)), \quad (2.4.1)$$

for a tetragonal crystal with  $a$  as the interatomic distance. Fig. 2.4.2a shows the momentum dependence of a  $s$ -wave gap (full line) and  $d$ -wave gap (dashed line). A  $d$ -wave gap vanishes along certain directions on the Fermi surface referred to as nodes.

In the case of a  $s$ -wave gap and assuming a constant normal DOS  $N_n(0)$  around the Fermi level, the single-particle excitation density of states (DOS) is

$$N_s(\omega) = N_n(0) \frac{\omega}{\sqrt{\omega^2 - \Delta^2}}, \quad (2.4.2)$$

if  $E > \Delta$  and zero otherwise. The DOS of a  $s$ -wave superconductor at zero temperature diverges at  $\omega = \pm\Delta$ . Below this energy, the DOS is zero since there are no possible excitations; this DOS is shown as a full line in Fig. 2.4.2b. At temperatures above absolute zero, the temperature distribution occupation probability (the Fermi distribution in this case) of the states in the tip smears these divergences into two peaks. The DOS for a  $d$ -wave gap (see dashed line in Fig. 2.4.2b) displays a linear increase of the spectrum from the Fermi energy ( $\epsilon_F = 0$ ) since as the gap is zero in the nodal directions, there are excited states available around the Fermi surface. As the energy moves away from the Fermi level, the number of excited states per unit energy increases and finally diverges at the gap maximum.

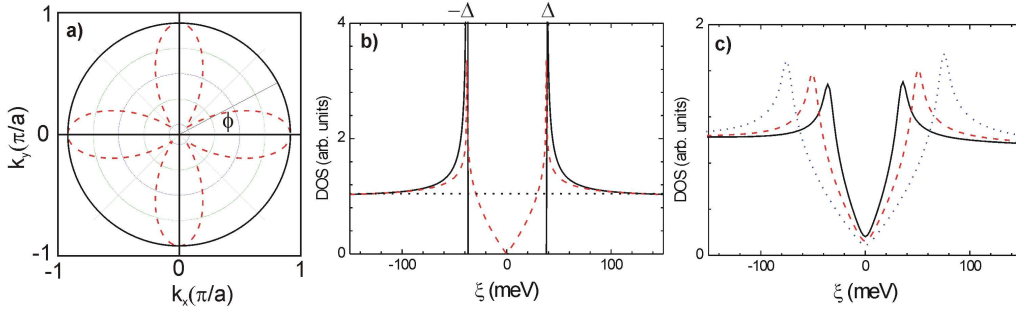


Figure 2.4.2: (a) BCS gap in a  $s$ -wave (full line) and  $d$ -wave (dashed line) symmetry in the Brillouin zone. The angle  $\phi$  is the polar angle between the  $k_x$  and  $k_y$  directions. (b) Spectra showing the corresponding single-particle density of states excitations for a normal metal,  $s$ - and  $d$ -wave superconductors represented by the dotted, dashed and full lines respectively. (c) Spectral variation as the maximum gap value changes. An inverse finite lifetime parameter  $\Gamma = 2$  meV is included and the final curves are convolved with a Gaussian of  $\sigma = 2$  meV.

Since the BCS interaction conserves the number of available states, the integration in energy of the superconducting DOS is conserved. This implies a sum-rule where the states are conserved through the normal metal - superconductor transition. Thus, spectral weight is shifted from below the gap into the coherence peaks (see Fig. 2.4.2b). This sum-rule also implies that as the gap increases, the coherence peaks become wider since more states are removed below the gap. This can be seen in Fig. 2.4.2c where the area missing below the gap is equal to the area above the normal DOS and the superconducting peaks increase in width due to greater spectral weight transfer. In Fig. 2.4.2c, we also observe that the height of the coherence peaks increases also with the gap. However this is due to finite and constant smearing factors used to simulate the BCS DOS. Without these factors, the BCS DOS diverges at the gap value (see Fig. 2.4.2b) and the height of the coherence peaks can not be defined. When the different smearing factors are included, like the finite lifetime of the quasiparticles, the temperature and the finite experimental resolution, the DOS divergences at  $\pm\Delta$  transforms into two peaks. If these smearing factors do not scale with the gap value, the height of the coherence peaks will increase with  $\Delta$ . Therefore, the coherence peak height increase observed in Fig. 2.4.2c is an artifact due to the constant smearing factors used. In chapters 5 and 6, we will compare later these theoretical trends with the experimental spectra of high- $T_c$  superconductors.

### 2.4.3 Effects of band-structure

Now, we discuss the electronic band effects in the DOS. The band dispersion as well as the Fermi surface can be determined by the Angle Resolved Photoemission Spectroscopy

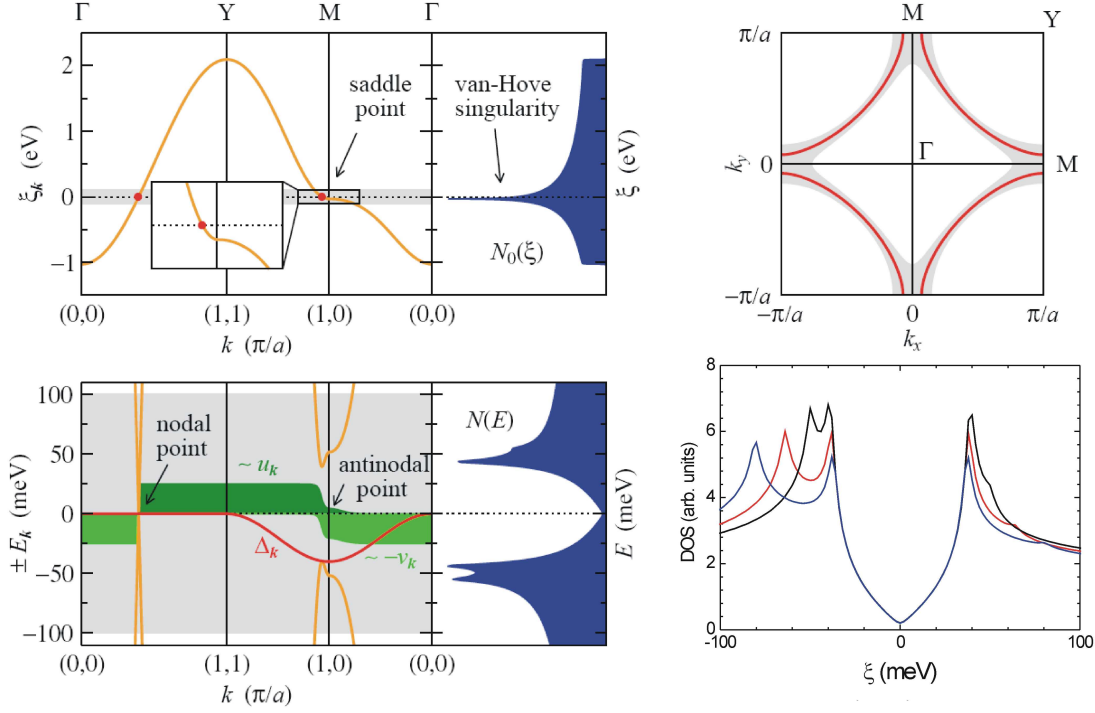


Figure 2.4.3: *d*-wave gap in BCS theory settled in a tight-binding band. [89]

(ARPES) [90]. The ARPES technique measures the spectroscopic characteristics in momentum space and therefore is complementary to STS which measures them in real space. The ARPES experiments have revealed the band structure of the layered high- $T_c$  superconductors (HTS) with great details [90, 91]. It was found that a two dimensional tight-binding model is enough to describe the ARPES results. The tight-binding expression for an effective band up to third nearest-neighbors is

$$\begin{aligned} \xi(\mathbf{k}) = & -2t [\cos(ak_x) + \cos(ak_y)] + 4t' [\cos(ak_x) \cos(ak_y)] \\ & - 2t'' [\cos(2ak_x) + \cos(2ak_y)] - \mu, \end{aligned} \quad (2.4.3)$$

where  $a = 3.8 \text{ \AA}$  is the Cu-Cu distance in the  $\text{CuO}_2$  plane,  $t$ ,  $t'$  and  $t''$  are the first, second and third respective nearest-neighbors hopping parameters, and  $\mu$  is the chemical potential.

These band structures present an extended saddle point near the  $M$  point,  $\mathbf{k} = (\pi, 0)$ , of the two-dimensional Brillouin zone (BZ), consistently with early band calculations [92]. This saddle point leads to a logarithmic peak in the density of states (DOS) known as the van Hove singularity (VHS). The DOS energy position of the VHS is given by the location of the saddle point in the band dispersion. Thus, according to Eq. 2.4.3, the VHS is situated at an energy equal to  $\xi_M = -4(t' - t'') - \mu$ . In the left right panel of Fig. 2.4.3, the saddle point in the band dispersion for optimally-doped  $\text{Bi}_2\text{Sr}_2\text{CaCu}_2\text{O}_{8+\delta}$  [40]

is shown together with the corresponding logarithmic singularity in the DOS. This band dispersion was obtained using Eq. 2.4.3 with the following values for the tight-binding parameters  $t$ ,  $t'$ , and  $t''$ :  $(t, t', t'') = (390, 82, 39)$  meV. The corresponding Fermi surface is shown in the right upper panel of Fig. 2.4.3 corresponding to a hole-like Fermi surface. When a BCS  $d$ -wave gap is settled in this 2D tight-binding band, a maximum gap opens at the antinodal point  $M$  pushing the VHS singularity to higher energies (left lower panel in Fig. 2.4.3). The corresponding BCS spectra displays five singularities, namely the  $V$  at zero energy due to the superconducting gap nodes, the peak divergences at the gap-edge at  $\pm\Delta_p$ , the signature of the VHS below the coherence peak at negative energies, and the weak BCS echo of the VHS above the coherence peak at positive energies. These two signatures of the VHS appear at  $\pm\sqrt{\xi_M^2 + \Delta_0^2}$ . In this model, the energy location of the coherence peaks at  $\pm\Delta_p$  is not strictly equals to the gap magnitude  $\Delta_0$ . If we consider, for simplicity, only a first neighbor hopping term  $t$  in the band dispersion ( $t' = t'' = 0$ ), the coherence peaks are at

$$\Delta_p = \pm\Delta_0\sqrt{\frac{(4t - \mu)^2}{\Delta_0^2 + 16t^2}}, \quad (t' = t'' = 0).$$

In practice the difference between  $\Delta_p$  and  $\Delta_0$  is not large for reasonable values of the parameters. We can find the energy position of the different singularities, in particular of the coherence peaks by looking the zeros of the gradient of the energy dispersion relation  $\nabla\xi_{\mathbf{k}} = 0$ . In this way, the VHS peaks are at  $\xi_M = \pm\sqrt{\Delta_0^2 + \mu^2}$  in a simplified band structure ( $t' = t'' = 0$ ). The right lower panel in Fig. 2.4.3 also shows the trend in the DOS when the number of electrons in the first Brillouin zone increases. The VHS peak at negative bias increases in energy reducing the coherence peak intensity.

#### 2.4.4 Collective mode coupling

Finally, through Eqs 2.3.14 to 2.3.20, we couple the Bogoliubov quasiparticles with a bosonic mode and study its effects on the DOS. The resulting DOS is shown in Fig. 2.4.4a, where we observe four important signatures in the spectrum. These are a coherence peak at energy  $\Delta_p$ , a dip at energy  $E_1$ , a hump at energy  $E_3$ , and the inflection point at energy  $E_2$ , between the dip and the hump, which appears as a minimum in the second-derivative spectrum of Fig. 2.4.4b. This particular energy scale is of interest here, since it was recently taken as a way to measure the frequency of the mediating boson from STM spectra [34]. Indeed, in conventional phonon-mediated superconductors the electron-phonon coupling leads to signatures in the tunneling spectrum, which appear as peaks in the  $d^2I/dV^2$  curve [93]. Furthermore, Abanov and Chubukov [94] reached identical conclusions in a spin-fluctuation mediated superconductor, showing that in a spin-fermion model with isotropic linear dispersion (without a van Hove singularity in the non-interacting DOS), the minimum of the second derivative at energy  $E_2$  is simply related to the spin-excitation energy. This suggests that the relation between the peak in

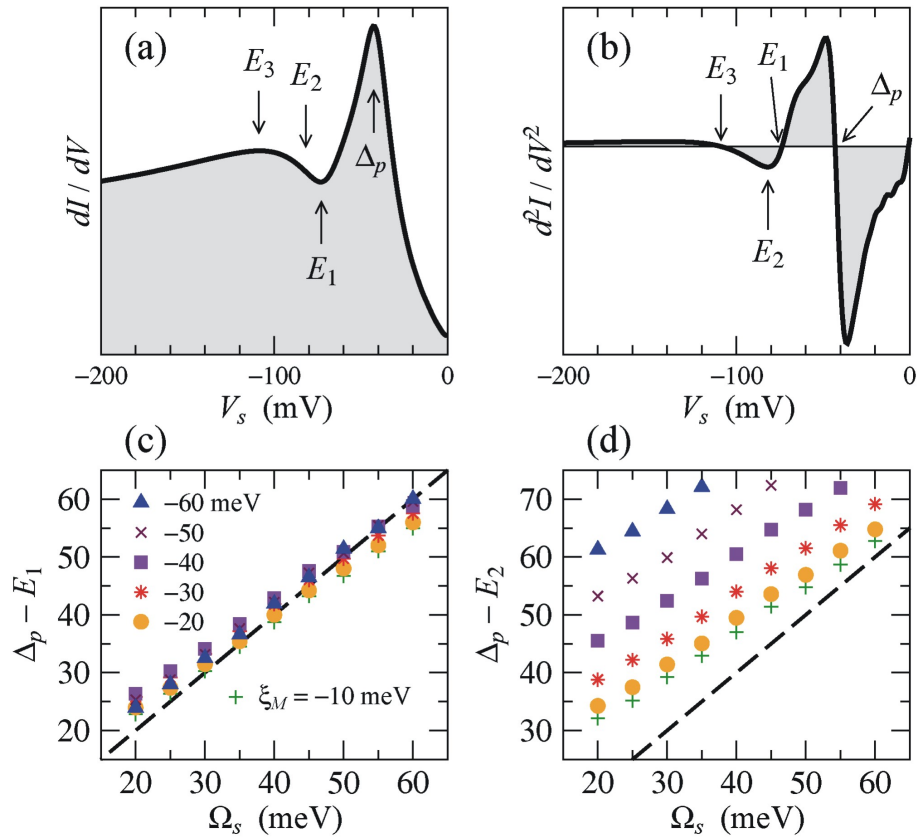


Figure 2.4.4: (a) Model Spectrum including  $d$ -wave BCS quasiparticles settled in a two dimensional tight-binding band and coupled to a bosonic mode. (b) Second derivative of the spectrum. We show the variation of the dip energy  $E_1$  in (c) and of the inflexion point  $E_2$  in (d) to respect to the coherence peak energy  $\Delta_p$  as a function of the bosonic mode energy  $\Omega_s$  for different values of the van Hove singularity. [89]

$d^2I/dV^2$  and the boson energy is generic to all pairing mechanisms. However, in the presence of a van Hove singularity (VHS), the simple relation between  $E_2$  and  $\Omega_s$  is no longer valid, since  $E_2$  is largely controlled by the energy  $\xi_M$ . Previously, it was shown that in presence of the VHS the position of the peak maxima  $\Delta_p$  is not only determined by the gap  $\Delta_0$ , although they are numerically close. In Fig. 2.4.4c, we plot the dip position relative to the coherence peak maximum obtained using Eqs. 2.2.18 and 2.3.20 as a function of the collective mode energy  $\Omega_s$  and the VHS energy position  $\xi_M$ . The dip minimum does not depend substantially on  $\xi_M$ , and provides an accurate measure (within  $\pm 5$  meV) of the resonance energy. In contrast Fig. 2.4.4d shows that the inflection point  $E_2$  does not only correlate with  $\Omega_s$ , but is strongly dependent on the position of the van Hove singularity.

The results in Fig. 2.4.4 receive a natural explanation if one considers the inelastic processes described by the self-energy Eq. 2.3.14. When a particle is injected in the system with momentum  $\mathbf{k}$  and energy  $\omega > 0$ , it can decay by emission of a spin excitation  $(\mathbf{q}, \Omega)$  provided (i) it has enough energy to produce an excitation  $\omega > \Omega$  and (ii) there is a stable quasiparticle state available at momentum  $\mathbf{k} - \mathbf{q}$  and energy  $\omega - \Omega$ . Therefore we expect to have peaks in the imaginary part of the self-energy when  $\omega - \Omega = E_{\mathbf{k}-\mathbf{q}} > 0$ . Similarly, when a hole is injected at energy  $\omega < -\Omega$ , it can relax to a state closer to the Fermi surface if  $\omega + \Omega = E_{\mathbf{k}-\mathbf{q}} < 0$ . Since in a BCS superconductor the quasiparticles have both electron and hole components, these two scattering processes will contribute to the relaxation of an electron. These two processes are immediately apparent in the expression of the self-energy evaluated for simplicity at  $\Gamma = \Gamma_s = 0^+$  and zero temperature since, using Eqs. 2.3.18 and A.0.6,

$$\begin{aligned} \text{Im } \hat{\Sigma}(\mathbf{k}, \omega) = & \frac{g^2}{N} \sum_{\mathbf{q}} F(\mathbf{q}) \left[ \frac{\hat{u}_{\mathbf{k}-\mathbf{q}}}{\omega - \Omega_s - E_{\mathbf{k}-\mathbf{q}} + i0^+} \right. \\ & \left. + \frac{\hat{v}_{\mathbf{k}-\mathbf{q}}}{\omega + \Omega_s - E_{\mathbf{k}-\mathbf{q}} + i0^+} \right] \end{aligned} \quad (2.4.4)$$

As anticipated,  $\text{Im } \hat{\Sigma}(\mathbf{k}, \omega)$  is made of a pair of peaks at  $\omega - \Omega = E_{\mathbf{k}-\mathbf{q}}$  and  $\omega + \Omega = E_{\mathbf{k}-\mathbf{q}}$ , with weights  $\hat{u}_{\mathbf{k}-\mathbf{q}}$  and  $\hat{v}_{\mathbf{k}-\mathbf{q}}$  for the particle and hole components, respectively. The  $(\pi, 0)$  region mostly contributes to the peaks that appear in the DOS without the coupling to a bosonic mode: the coherence peaks at energy  $\Delta_p$  and the VHS at  $\sqrt{\xi_M^2 + \Delta_0^2}$ . The coupling to a collective mode peaked at  $q = (\pi, \pi)$  and centered at energy  $\Omega_s$  strongly couples these regions around the M-point  $(\pi, 0)$ . This coupling produces peaks in the imaginary part of the self-energy when  $|\omega| = E_{\mathbf{k}-\mathbf{q}} + \Omega_s$  ( $E_{\mathbf{k}-\mathbf{q}} > 0$ ), mainly at energy  $|\omega_1| = \Delta_p + \Omega_s$  and  $|\omega_2| = \sqrt{\xi_M^2 + \Delta_0^2} + \Omega_s$ . The peaks in the imaginary part of the self-energy are accompanied by strong band renormalization which produce the dips in the DOS. However, the energy width of the collective mode smears out the two dips at  $\omega_1$  and  $\omega_2$  confounding them into a single dip. Part of the spectral weight removed from the dip

is build up at higher energy producing the hump structure. The rest of the spectral weight is transferred to lower energy increasing the spectral weight of the coherence peaks. The hump energy position is largely determined by the second dip position  $\omega_2$ , thus by the interplay of the VHS, the gap and the collective mode energy.

The model developed in this chapter will be used later in this work to analyze the measured spectra. It allows us to associate the energy position of the peaks in the spectra at  $\pm\Delta_p$  to the superconducting gap  $\Delta_0$ . A coupling of the quasiparticles to a collective mode originates the dip in the spectrum and masks the van Hove singularity. From this results that a good estimation of the collective mode energy is the energy position of the dip. Also, the presence of the van Hove singularity on the density of states can indirectly be seen in the energy position of the hump or on the inflection point. However, the energy position of these two features is also determined by the interplay of the gap and the collective mode.

# Chapter 3

## High-Temperature superconductors

We describe the phase diagram of high  $T_c$  superconductors (HTS) focusing on tunneling spectroscopy results. We present the crystal structure of the Bi-family compounds and discuss the doping and temperature evolution of the HTS physical properties relevant for spectroscopy. Furthermore, different spatial modulations have been reported recently. The characteristics of these spatial modulations are reviewed in this chapter.

### 3.1 Introduction

The high  $T_c$  superconductors (HTS) are complex materials with a layered crystallographic structure. They all share  $\text{CuO}_2$  planes separated by block layers which act as charge reservoirs. It is generally agreed that the low-energy excitations in HTS cuprates are determined by the interactions within the  $\text{CuO}_2$  layers. Usually in the HTS stoichiometric compounds, the copper ions are doubly ionized in an oxidation state  $2+$  giving a  $3d^9$  electronic configuration with a total spin  $S = 1/2$ . In the compounds with only one  $\text{CuO}_2$  layer per the unit cell, each copper ion is surrounded by six oxygen atoms in an octahedral environment. In this octahedral environment, the electronic levels of the  $3d$  orbital are split into  $t_{2g}$  and  $e_g$  orbitals. Furthermore, the degeneracy of the  $e_g$  orbitals is lifted since the out-of-plane oxygens (known as apical oxygens) are displaced from a perfect octahedral structure. The highest partially occupied orbital state of  $\text{Cu}^{2+}$  therefore has  $x^2 - y^2$  symmetry. The  $d_{x^2-y^2}$  orbital states overlap with the  $2p$  orbitals of the oxygen ions forming electronic bands. These materials should be metallic according to band theory since there should be bands that cross the Fermi level according to band calculations [92]. However, they are insulators due to strong correlations between electrons giving charge-transfer insulators. The ions  $\text{Cu}^{2+}$  have spins  $S = 1/2$  which interact via a super-exchange mechanism along the Cu-O-Cu bond. This interaction orders the magnetic moments of the ions antiferromagnetically within the  $\text{CuO}_2$  planes. The transition temperature (the Néel temperature  $T_N$ ) is around 300 – 400 K.

Depending on the number of  $\text{CuO}_2$  planes in the unit cell, the HTS are classified as single-layer, bilayer and trilayer compounds. The superconducting  $T_c$  is affected by these structural characteristics: for the same family of compounds, the  $T_c$  increases with the number of  $\text{CuO}_2$  planes. For example, in the Bi-family the maximum  $T_c$  is 12, 92 and 111 K for single-layer, bilayer and trilayer compounds, respectively.

## 3.2 The Bi-family of high $T_c$ superconductors

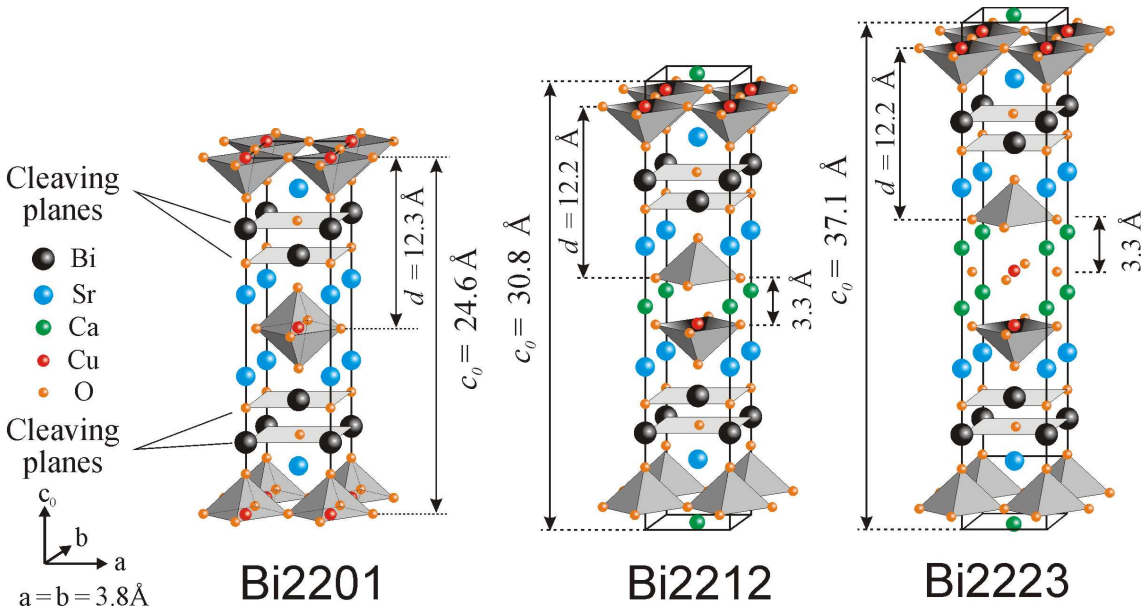


Figure 3.2.1: Unit cell structure for the Bi-based HTS. The unit formula is  $\text{Bi}_2\text{Sr}_2\text{Ca}_{n-1}\text{Cu}_n\text{O}_{4+2n+\delta}$  (abbreviated by  $\text{Bi}22[n-1][n]$ ) with corresponding  $n$   $\text{CuO}_2$  planes.

In this work, we have studied the  $\text{Bi}_2\text{Sr}_2\text{CaCu}_2\text{O}_{8+\delta}$  and  $\text{Bi}_2\text{Sr}_2\text{Ca}_2\text{Cu}_3\text{O}_{10+\delta}$  compounds. Therefore, we present below the crystal structure of these compounds. The Bi-family of HTS compounds have a general chemical formula of  $\text{Bi}_2\text{Sr}_2\text{Ca}_{n-1}\text{Cu}_n\text{O}_{4+2n+\delta}$ . They all have a quasi tetragonal unit cell with lattice parameters  $a_0 \simeq b_0 = 5.4 \text{ \AA}$  in the  $ab$ -plane. Depending on the number of  $\text{CuO}_2$  planes, the  $c$ -lattice parameter is  $24.6 \text{ \AA}$ ,  $30.8 \text{ \AA}$  and  $37.8 \text{ \AA}$  for  $n = 1, 2$  and  $3$  respectively. When there are more than one  $\text{Cu-O}$  layer in the unit cell, the distance between two of these layers is  $3.3 \text{ \AA}$  with an intercalated Ca layer between them. Therefore the number of Ca-layers is  $n - 1$  for  $n$   $\text{Cu-O}$  layers. The  $\text{CuO}_2$  plane projection along the  $a - b$  plane is shown in Fig. 3.2.2 where we show the primitive unit cell according to the symmetry of the whole crystal structure with the lattice parameter  $a_0$ . The Cu interatomic spacing is  $a = 3.8 \text{ \AA}$ .

For each compound, the oxygen composition can be changed from the stoichiometric composition ( $\delta = 0$ ). The extra oxygen fraction ( $\delta$ ) per unit cell is located in the Bi-O planes with an oxidation state of  $-2$ . Hence each extra oxygen localizes two electrons or conversely it contributes with two holes to the electronic structure. These extra holes are transferred to the  $\text{CuO}_2$  planes through the Sr-O layers. Indeed, the apical oxygen situated in the Sr-O layers acts as a chemical bridge for the charge transfer between the Bi-O to the Cu-O planes. In this way, the Cu valence changes between  $+1$  to  $+2$  for each extra hole added. Therefore the compounds in the Bi-family can be doped with holes by adding extra oxygen to the Bi-O layers.

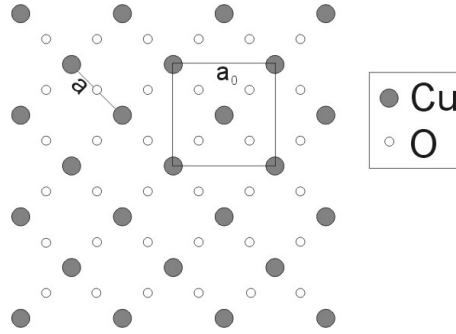


Figure 3.2.2: Schematic atomic positions in the  $\text{CuO}_2$ . We show the primitive unit cell corresponding to the whole crystal structure with a cell parameter  $a_0 \simeq b_0 = 5.4 \text{ \AA}$  and the Cu interatomic spacing  $a \simeq b = 3.8 \text{ \AA}$ .

Along the  $b_0$ -axis, there is an incommensurate supermodulation with a  $\sim 26 \text{ \AA}$  period. This supermodulation affects strongly the Bi-O layer and has almost no effect in the other layers [95]. It was proposed that the excess of oxygen is the major cause of the supermodulation [95]. Thus the period of the supermodulation should decrease when the excess oxygen increases (or equivalently with hole concentration). However, it was observed that the period of the supermodulation does not change with oxygen composition. So the lattice mismatch between the Bi-O planes to the other layers is most probably the origin of the supermodulation.

The  $\text{Bi}_2\text{Sr}_2\text{CaCu}_2\text{O}_{8+\delta}$  system (Bi2212) is the most studied material with STM since high-quality crystals can be obtained together with pristine surfaces. In fact, the compound can be easily cleaved between the Bi-O planes (see Fig. 3.2.1) due to the weak van der Waals forces between them [96]. In this way, clean surfaces can be obtained but due to their oxide composition, its surface rapidly degrades in not controlled atmospheres. Hence, a UHV atmosphere is needed to avoid the surface degradation of cleaved samples. The UHV condition allows to perform reproducible STM measurements for large periods without any observable surface degradation.

### 3.3 Phase diagram and spectroscopy

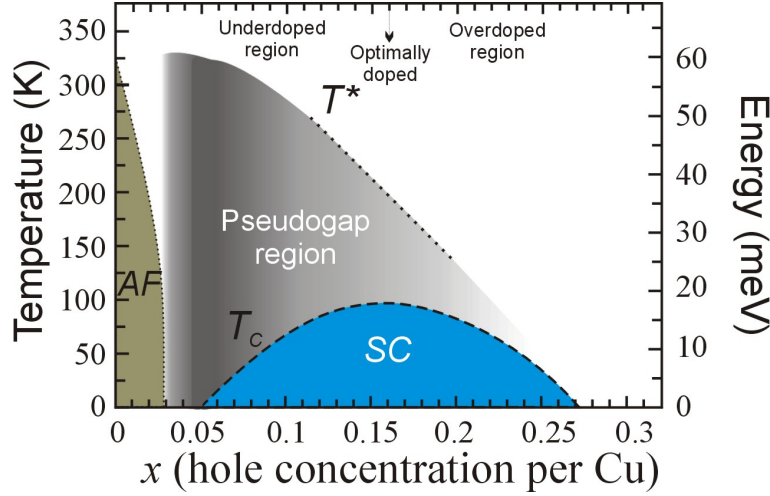


Figure 3.3.1: Schematic phase diagram of HTS.

By changing the chemical composition of the charge reservoir layers in HTS, the valence state of the Cu ions can be varied, which is equivalent to dope the  $\text{CuO}_2$  planes. They can be doped by either injecting electrons (electron doping) or by removing electrons (hole doping). In the following discussion I will only consider the temperature-doping phase diagram for the hole-doped cuprates.

In the charge-transfer insulator parent compound containing one electron per unit cell (half-filling), the incorporation of holes gradually suppresses the initial antiferromagnetic order (AF region in Fig. 3.3.1). At a doping concentration  $x \approx 0.02 - 0.04$  holes per unit cell, this global magnetic order is destroyed. Its destruction by hole doping can be understood by the movement of holes through a lattice of singly occupied sites (due to the strong on-site Coulomb repulsion) which rearranges the spin configuration.

At a doping concentration around  $x \approx 0.05 - 0.06$  holes per unit cell, the compound becomes metallic and even superconducting below a critical temperature  $T_c$  which varies with doping. The  $T_c$  doping variation resembles an inverse parabola forming a dome shaped region where superconductivity exists (SC region in Fig. 3.3.1).  $T_c$  reaches a maximum at a doping concentration  $x^{opt}$  known as optimal doping. This optimal doping allows us to define two regions in the phase diagram: the underdoped region corresponding to  $x < x^{opt}$  and the overdoped region for  $x > x^{opt}$ . The  $T_c$  versus doping relation  $T_c(x)$  was empirically parameterized by Presland *et al.* [6] as

$$T_c(x) = T_c^{max} \left[ 1 - 82.6 (x - x^{opt})^2 \right], \quad (3.3.1)$$

where  $T_c^{max}$  is the critical temperature at optimal doping.

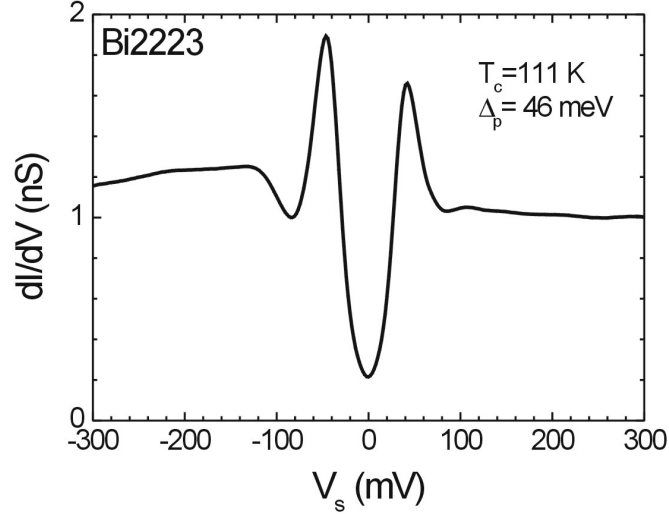


Figure 3.3.2: Tunneling spectra measured on a  $\text{Bi}_2\text{Sr}_2\text{Ca}_2\text{Cu}_3\text{O}_{10+\delta}$  (001) surface at 2K, 0T. The spectra is an average of a 100 nm spectral trace. The sample has a  $T_c = 111$  K corresponding to optimal doping.  $I = 0.6$  nA,  $V_t = 0.6$  V.

Scanning tunneling microscopy (STM) allows to determine the spectroscopic characteristics of HTS in the different regions of their phase diagram. As an example, a STM spectrum on the trilayer compound  $\text{Bi}_2\text{Sr}_2\text{Ca}_2\text{Cu}_3\text{O}_{10+\delta}$  at optimal doping ( $T_c = 111$  K) and 1.8 K is shown in Fig. 3.3.2. Its main spectral characteristics are a V-shape at low bias voltage with strong peaks at  $\pm 46$  mV plus an asymmetric dip-hump structure at  $\sim 80$  mV and a rather flat, also asymmetric, background at high energies ( $E > 150$  mV). The V-shape form of the spectrum at low energy ( $E \sim 0$ ) mV is consistent with *d*-wave superconductivity for this material. The strong peaks are usually interpreted as superconducting coherence peaks and from its position an estimation of the gap is obtained, in this case  $\Delta_p = 46$  mV. The dip-hump feature is usually associated to strong coupling effects of the quasiparticles to a bosonic mode [9]. Finally, variations on the asymmetry of the background conductance for  $|E| > 150$  meV was related to strong correlation effects on these materials [10, 11, 12]. Below, we discuss the different physical properties observed in the underdoped and overdoped regions.

Within the underdoped region, the critical temperature increases with doping, although the superconducting gap amplitude estimated from tunneling  $\Delta \sim \Delta_p$  decreases [70]. The ratio of  $2\Delta_p/k_B T_c$  can be as high as 28 in this region, indicating that the mean field approximation is no longer valid in these materials. Measurements of the penetration depth have shown that the superconducting carrier density  $n_s$  scales linearly with  $T_c$  and the hole doping  $x$  in the underdoped region [97]. This behavior is quite different from a Fermi liquid where  $n_s$  should be determined by the electron density and not the hole

doping. Furthermore, the normal metal above  $T_c$  shows a non-Fermi liquid behavior [98], indicating that BCS theory should not apply since it arises from a Fermi liquid ground state.

In the overdoped region, the estimated superconducting gap  $\Delta_p$  follows the critical temperature and decreases with doping [70]. For strongly overdoped concentrations ( $x > 0.2$ ), the materials behave like a normal metal above  $T_c$ . Its electrical conductivity varies with the square of the temperature and the relation between the electrical and thermal conductivity satisfies the Wiedemann-Franz law [99] indicating a Fermi liquid behavior. Furthermore, there is evidence that the superconductivity in this region can be described by BCS theory: the specific heat shows a clear jump at  $T_c$  and the spectral weight transfer between the normal metal and the superconducting phase agrees with the BCS prediction [100].

Above the superconducting dome, several experiments [101] show a spectral weight suppression at low energies above  $T_c$  and up to a characteristic temperature  $T^*$ . The spectral weight suppression in this region is associated with the opening of a pseudogap which appears in the underdoped region of the phase diagram. It gets weaker as the hole doping is increased and finally merges  $T_c$  in the overdoped region. It is believed to be related to the superconducting gap since the pseudogap evolves smoothly into the superconducting gap when the temperature is decreased from  $T^*$  [98]. Also, the pseudogap has the same  $d$ -wave symmetry as the superconducting gap and its characteristic temperature  $T^*$  follows the same doping behavior as the gap  $\Delta_p$ , the former being proportional to the latter for all doping rates. Indeed, the ratio  $2\Delta_p/k_B T^*$  is 4.3, which is expected for a  $d$ -wave pairing symmetry in the BCS theory for superconductivity [55]. All these observations point to a common origin for the superconducting gap and the pseudogap. Furthermore, it was shown that the spectra present inside the vortex core is similar to the spectra in the pseudogap state [23] suggesting that pseudogap properties can be studied directly inside the vortex core.

In the tunneling spectra (see Fig. 3.3.2), a strong dip appears just next to the coherence peaks which is stronger at negative bias voltage. The dip is followed by a smooth maximum named hump. The dip-hump structure could originate from strong-coupling effects [9] or the superconducting gap opening in a pseudogap background. The fact that the pseudogap smoothly joins the superconducting gap [70] indicates that the two-gap explanation of the dip-hump feature is less probable.

Schrieffer *et al.* [86] showed that strong coupling effects could produce similar structures in the DOS and thus it deviates from BCS prediction for the tunnelling spectrum in superconductors. In particular for lead, the electron-phonon coupling treated by Eliashberg equations produces deviations from the predicted BCS DOS [86] seen in the spectra by a peak-dip structure around the energy gap plus the characteristic energy of the phononic spectrum. Later, Scalapino *et al.* [102] modelled the phonon density of states measured by inelastic neutron scattering (INS) which allowed McMillan and Rowell [30] to invert the tunneling spectrum. A similar approach has been used for the HTS cuprates

to fit a particular symmetric  $\text{Bi}_2\text{Sr}_2\text{CaCu}_2\text{O}_{8+\delta}$  spectrum normalized to an arbitrary state-conserving normal-state background [103, 42]. These authors have included a  $d$ -wave gap into Eliashberg's equations in order to perform a self-consistent fit to the particular spectrum. With a single narrow bosonic mode at 36.5 meV, the fit reproduces the overall shape of the spectra, although a second peak appears near the coherence peaks due to the Lorentzian form of the bosonic mode. Their model does not take account of the band dispersion and in particular of the existence of a van Hove singularity (VHS) near the Fermi level. The inclusion of a VHS singularity can account for different asymmetries in the spectra. Therefore, a model that intends to reproduce the tunnel spectra at low energy should have  $d$ -wave Bogoliubov quasiparticles settled in an effective band structure that includes a VHS and coupled to a bosonic mode. Such model was developed in section 2.3 which will be used in this work to interpret the tunneling spectra on HTS.

## 3.4 Spatial variations of the STM spectra

Recently, different electronic modulations has been observed in the superconducting phase, and when superconductivity is suppressed by either temperature, magnetic field or doping. The spatial resolution of STM allows to observe local variation of the DOS at a nanometer scale due to charge density waves [50] or quantum interference oscillations around impurities [51]. Therefore, STM technique is an ideal tool to study these variations due to its spatial resolution to the atomic level. In the following section, I review the different spatial variations of the LDOS found in literature.

### 3.4.1 Spatial gap distribution

The superconducting gap in HTS usually varies at a nanometer scale. This is revealed by real space spectral maps of the local superconducting gap  $\Delta_p$  known as gap maps. These gap maps show islands between 3 to 5 nm wide with different gap amplitudes [104, 105, 106, 107, 108]. Recently, McElroy *et al.* [109] found that gap magnitude variations are directly correlated with oxygen impurity distributions in real space. They observe an increase on the tunnel conductance at  $-0.96$  V which they associate to an impurity state due to  $\text{O}^{2-}$  dopant atoms. This feature occurs at a distance of  $\sim 1.9$  Å away from the Bi along the Bi-O bond direction. They relate the spatial location of these impurity states to the gap amplitude variations. Mainly, they found that the gap amplitude increases predominantly near each dopant oxygen atom. Also a suppression of the coherence peaks happens primarily around dopant oxygen defect clusters. This implies that a spatially uniform gap magnitude can be produced if the dopant oxygen atoms are uniformly distributed.

Following this idea, Hoogenboom *et al.* [40, 110] showed that a spatial uniform distribution of the gap can be obtained by an adequate annealing treatment of the sample, at

least in the overdoped region of the phase diagram. Furthermore, they demonstrated that the gap inhomogeneities were intimately associated with broad superconducting transitions measured by *ac*-susceptibility. In particular, narrow superconducting transitions lower than 0.5 K yield very uniform gap distributions. Generally, as-grown samples tend to be inhomogeneous if special post-synthesis treatments are not performed to produce an uniform distribution of dopant oxygens.

Finally, it is important to remark that lead impurities on Bi-O layers or disorder in the Sr and Ca layers have no effect on the gap inhomogeneity [108]. However, the oxygen concentration and distribution are probably not the only differences between samples from different sources and batches.

### 3.4.2 Quasiparticle interference

Hoffman *et al.* [17] observed that in the superconducting phase and in absence of magnetic field, the Fourier transform spectral maps of  $\text{Bi}_2\text{Sr}_2\text{CaCu}_2\text{O}_{8+\delta}$  displays characteristic spots besides the structural points of the atomic lattice. These spots were observed at energies smaller than the coherence peaks, namely in the sub-gap region. The energy of the spectral maps is determined by the bias potential  $V_s$ . Generally, if there are periodic spatial modulations in the spectral maps, its Fourier transformed images will present spots centered at the characteristic wave-vectors of this modulations and with a decay length inversely proportional to their spatial coherence. Hoffman *et al.* [17] reported eight spots inside the Brillouin zone with a wavelength between 1.6 to 2 nm. Four of them are along the Cu-O bond and the other four along the diagonal of the bond (at  $45^\circ$ ). These two kind of spots (along the Cu-O bond and at  $45^\circ$ ) present different dispersion behavior with energy: The wave-vector of the former decreases with increasing energy when the wave-vector of the latter increases.

This behavior was understood in the framework of quasiparticle interference in *d*-wave superconductivity. States at the same energy  $E_k = \sqrt{\xi_k^2 + \Delta_k^2}$  will interfere when they are scattered by a potential. The resulting scattering pattern will depend of the Fermi surface structure and of the symmetry of the gap. In the case of HTS, the iso-energetic states that interfere can have a wave-vector difference either parallel to the Cu-O bond or at  $45^\circ$ . Therefore, in this model, the wave-vector energy dispersion for the different interference patterns is a consequence of *d*-wave superconductivity plus the Fermi surface structure. Furthermore, a detail analysis of this energy dispersion allowed McElroy *et al.* [111] to reproduce the Fermi surface of this material and the *d*-wave behavior of the gap, which are in excellent agreement with ARPES measurements. This interpretation of the pattern found in the Fourier transformed spectral maps presumes the existence of defined quasiparticles with an inverse lifetime smaller than the scattering potential. Up to now, a clear identification of the scattering centers which produce these periodic modulations is missing. Resuming, there are spatial periodic modulations in the superconducting phase that disperse with energy due to quasiparticle interference scattering.

### 3.4.3 Non-dispersive electronic modulations

Above the critical temperature, in the pseudogap state, Vershinin *et al.* [20] observed a square superstructure at low energies characterized by four spots in the Fourier transformed spectral maps. These spots were located along the  $(\pm\pi, 0)$  and  $(0, \pm\pi)$  directions with  $q$ -values equal to  $2\pi/4.7a$  where  $a = 3.8 \text{ \AA}$  is the interatomic distance. They do not change their position in  $q$ -space as a function of energy which is contrary to the dispersive modulations behavior found in the superconducting state discussed previously. Furthermore, Misra *et al.* [112] showed that the non-dispersive modulations in the pseudogap state can not be understood by a quasiparticle interference scattering model. However, the intensity of the non-dispersive modulations depends on the energy, being more pronounced at low energies  $\leq 20 \text{ meV}$ . This energy should be compared with the pseudogap magnitude found around  $40 \text{ meV}$ .

A four-fold symmetric modulation that does not disperse with energy was also observed in underdoped samples [18, 22, 113]. These modulations are more intense in regions showing pseudogap spectra. It is important to note that the pseudogap spectra is characterized by a suppression of the coherence peak at negative bias together with no dip-hump features.



# Chapter 4

## Vortex core Spectroscopy in $\text{Bi}_2\text{Sr}_2\text{CaCu}_2\text{O}_{8+\delta}$

We present here a detailed study of vortex-core spectroscopy in a slightly overdoped  $\text{Bi}_2\text{Sr}_2\text{CaCu}_2\text{O}_{8+\delta}$  sample. Inside the vortex core we observe a four-fold symmetric modulation of the local density of states with an energy-independent period of  $(4.3 \pm 0.3)a$ . Furthermore, we demonstrate that this square modulation is related to the vortex core states which are located at  $\pm 6$  meV. Since the core-state energy is proportional to the superconducting gap magnitude  $\Delta_p$ , our results strongly suggest the existence of a direct relation between the superconducting state and the local electronic modulations in the vortex core.

### 4.1 Introduction

In type II superconductors, when the applied magnetic field is bigger than  $H_{c1}$ , the magnetic field penetrates into the sample as lines with quantized flux that locally suppress superconductivity. These regions are known as vortices and their study provide a direct access to the fundamental properties of superconductors. STM can directly detect individual flux lines allowing to visualize the spatial vortex distribution as well as the structure of the cores. Thus, a promising approach to investigate the superconducting state in HTS is to study the electronic properties of vortices, in particular the quasiparticle excitation spectra of the vortex cores.

Scanning tunneling microscopy (STM) observations of vortex cores were first carried out on  $\text{NbSe}_2$  [47]. The behavior of the tunneling conductance, which measures the local density of states (LDOS), was found to agree with the prediction by Caroli *et al.* [48], that a band of localized states develops in the cores. The subsequent observation of vortices in  $\text{YBa}_2\text{Cu}_3\text{O}_{7-\delta}$  (YBCO) [114] gave a surprising result: contrary to the observations in  $\text{NbSe}_2$ , the vortex-core spectra showed two peaks staying at a constant energy irrespective

of the distance to the vortex center, as if the vortex would contain only two localized states instead of a whole band. Following this, several groups investigated theoretically the vortex core in a  $d$ -wave superconductor, leading to the conclusion that the spectra observed in YBCO cannot be explained in the framework of the BCS theory [115] and that an extension of this theory is necessary at the very least [116, 117, 118]. The STM study of  $\text{Bi}_2\text{Sr}_2\text{CaCu}_2\text{O}_{8+\delta}$  (Bi2212) uncovered another property of the vortex-core spectra: they display the low temperature pseudogap [23]. Subsequently it was found that the two localized states are also present in this compound [13, 14, 15], and that the states seen in YBCO and in Bi2212 have a common characteristic, appearing at an energy of about  $0.3\Delta_p$ , where  $\Delta_p$  is the position of the coherence peaks in the superconducting state [119].

Hoffman *et al.* observed a spatial modulation of the low energy tunneling conductance in the vortex cores having a period of about  $4a$  [16]. Later, it was found that similar modulations also appear in the absence of magnetic field [17, 18]. Hoffman *et al.* noticed that the wavelength of these modulations disperse with energy and it was proposed that the effect can be understood in terms of quasiparticle interference due to scattering on impurities and other inhomogeneities [17, 19]. However, some of the periodic modulations reported by Howald *et al.* [18] did not disperse in energy, and an explanation in terms of static stripes was put forward. More recently, Vershinin *et al.* [20] studied the spatial dependence of the tunneling conductance in the pseudogap phase. They observed an incommensurate square lattice with period  $(4.7 \pm 0.2)a$ . The modulations observed above  $T_c$  do not disperse and it was thus concluded that they are different from the interference modulations seen in the superconducting state. A non-dispersing square pattern was also reported at low temperatures in strongly underdoped Bi2212 [21] and  $\text{Ca}_{2-x}\text{Na}_x\text{CuO}_2\text{Cl}_2$  (NCCOC) [22], which are characterized by pseudogap-like spectra. Thus there is considerable evidence that a square pattern with a non-dispersing wavelength is associated with the pseudogap, whereas in the superconducting state one observes predominantly dispersing modulations, presumably due to quasiparticle interference.

Here, we report a detailed study of the LDOS modulation inside the vortex core. We confirm the early observations by Hoffman *et al.* [16], but our measurements show in addition that this modulation does not disperse with energy, like the ones observed in the pseudogap phase [20]. We further demonstrate that this square modulation is linked to the localized vortex-core state [114, 13, 14, 15], and we thereby establish a direct relation between the vortex core electronic modulations and the superconducting state.

## 4.2 Zero Field Characterization

Our STM measurements were performed on a Bi2212 single crystal grown by the travelling solvent flux zone method [120] and annealed in  $500^\circ\text{C}$  under 15 bar oxygen pressure. After annealing we measured  $T_c^{\text{onset}} = 88 \text{ K}$  ( $\Delta T_c = 4 \text{ K}$ ) by  $ac$ -susceptibility. The relatively flat background slope of the conductance spectra, as well as the magnitude

of the superconducting gap  $\Delta_p$  indicate that the sample is slightly overdoped. In the region studied, we observe an average gap  $\bar{\Delta}_p = 25.2$  meV with a standard deviation  $\sigma = 4$  meV. This gap distribution is consistent with the observed superconducting transition width [121].

We performed the measurements with a home-built STM [122] under ultrahigh vacuum. The sample was cleaved *in situ* at room temperature before cooling and applying the magnetic field and the tunnel junction was made between the (001) sample surface and an electrochemically etched Iridium tip. All data presented here was acquired at 2 K, first at zero field and then at 6 T.

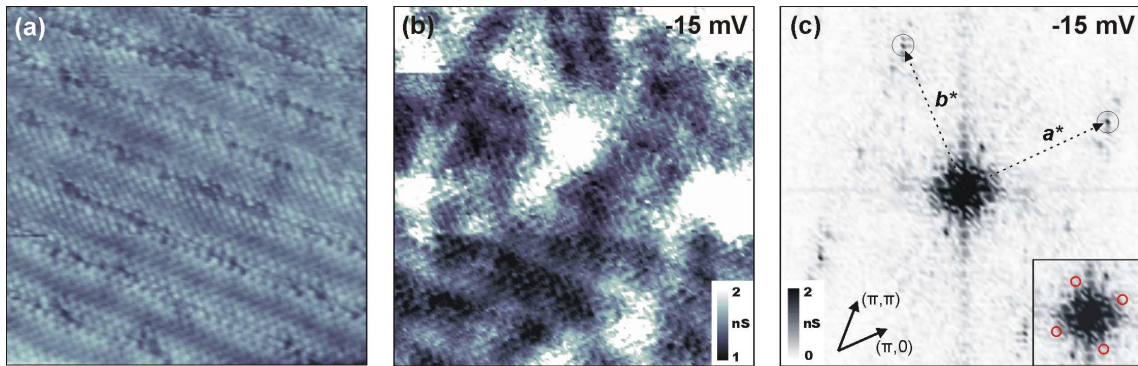


Figure 4.2.1: (a)  $16 \times 16$  nm<sup>2</sup> topographic image of Bi2212 showing the atomic lattice on the BiO plane. The atomic corrugation is 2 Å. The image was acquired at a bias voltage  $V_t = 0.6$  V and a tunnel current  $I = 0.8$  nA. (b)  $dI/dV$  conductance map in the same area at  $V_s = -15$  mV, zero field and  $T = 2$  K. (c) Absolute value of the Fourier transform of (b).  $a^*$  and  $b^*$  are the reciprocal vectors of the atomic lattice with modulus  $2\pi/a$  and  $2\pi/b$ , respectively ( $a \simeq b = 3.8$  Å). The position where peaks corresponding to a  $4a \times 4a$  period would be expected are indicated in red in the inset.

In Fig. 4.2.1a we show a topographic scan at zero field which clearly resolves the atomic lattice of the BiO top layer, as well as the characteristic supermodulation running along the (1,1) direction (the  $b_0$  axis). Figure 4.2.1b is a conductance map at  $V_s = -15$  mV, which was acquired in the same area simultaneously with the topographic image. The Fourier transform (FT) shown in Fig. 4.2.1c reveals four peaks corresponding to the Bi lattice and several peaks due to the supermodulation and its harmonics running along the  $(\pi, \pi)$  direction. In contrast to earlier reports [17, 18, 20] we do not observe quasiparticle interference peaks in zero field, presumably because of the absence of sufficiently strong scattering centers. The red circles in the inset of Fig. 4.2.1c indicate the positions where the peaks of a  $4a \times 4a$  modulation would have been located.

### 4.3 Vortex core spectroscopy

The electronic properties of vortex cores is studied with an applied magnetic field of 6 T perpendicular to the a-b plane. Here, I focus on the properties of a single vortex core. Its spatial distribution is shown in Fig. 4.3.1a. In this region and outside the core, we observe an average gap of  $\bar{\Delta}_p = 25$  meV. The vortex core imaging is possible because it affects the quasiparticle excitation spectra. In particular for HTS, the superconducting coherence peak at negative bias is suppressed. This allows a direct imaging of the vortex core by mapping the intensity of the tunnel conductance signal at  $-25$  mV. Thus the vortex core appears as a black area since the coherence peak at negative bias is reduced.

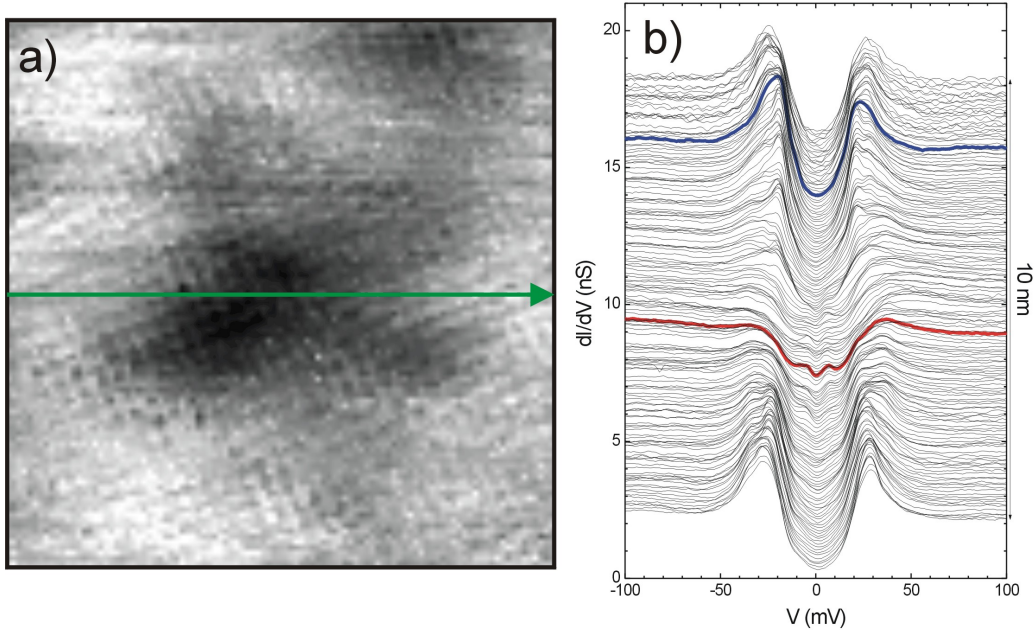


Figure 4.3.1: (a)  $10 \times 10$  nm<sup>2</sup> spectral image acquired at  $V_s = 25$  mV. The intensity contrast shows where the vortex core is situated. The line indicates a 10 nm spectral trace along the vortex core shown in (b).

The detection of single vortices in HTS is difficult due to the nanoscale variations of the spectra. Inhomogeneities like structural defects, chemical adsorbates, impurities or electronic inhomogeneities will generally perturb its detection [70]. Thus, an efficient detection of vortex cores relies on the observation of several characteristics in the spectra. In the vortex core the spectra presents a higher zero bias conductance, the appearance of localized quasiparticles excitations at  $\sim 0.3\Delta_p$ , the suppression of the coherence peak at negative bias together with a reduction of the coherence peak at positive bias which appears at a slight higher energy, and the appearance of a spatial modulation inside the vortex core with a period of  $\sim 4$  times the Cu-Cu distance along the Cu-O bond direction.

All these properties has been observed in the single vortex core studied here and are shown in figures 4.3.1 and 4.4.1. The highlighted spectra in the center of the trace shown in Fig. 4.3.1b present a vortex core spectra characterized by a gap-like structure similar to the pseudogap measured above  $T_c$  [23] and weak low-energy structures attributed to localized quasiparticle excitations [13, 14, 15]. Furthermore, in Fig. 4.3.1a, we observe that the vortex core extends over an area of about  $25 \text{ nm}^2$  having an irregular shape. A quantitative fit of the zero bias conductance profile across the vortex core allowed Martin Kugler [55] to determine the coherence length  $\xi$  of the order of 1 nm. This small coherence length implies that the vortices get easily pinned by defects and can explain in general the irregular shape of the core since it follows the pinning potential. Fig. 4.3.1b shows the evolution of the spectra across the vortex core. When entering the core, the spectra evolve in the same way as when the temperature is raised above  $T_c$ : the coherence peak at negative energy vanishes over a very small distance, the coherence peak at positive energy is reduced and shifts to slightly higher energies, and the dip-hump structure disappear. At the same time that the pseudogap-like spectra emerges, small peaks appears at  $\pm 6 \text{ mV}$  inside the core. These core states appears smoothly inside the core and do not disperse in energy as a function of position. It was found that they are magnetic field independent and scales linearly with the gap magnitude  $\Delta_p$  [110].

Now, we address the question that if vortices get easily pinned by defects, why these inhomogeneities do not also produce quasiparticle interference patterns. The vortex core shape predicted by theory is expected to show a four-fold symmetry [123]. Up until now, no regular shape of any kind has ever been observed in Bi2212 vortex cores. This is because inhomogeneities will dominate the core shape. A vortex core as seen in Bi2212 is typically 4-5 nm in size, thus several times the coherence length. It is therefore the spatially slowly varying part of the potential which modify the shape of the vortices. The quasiparticle oscillations on the other hand, appear strongly if the potential shows abrupt variations on the atomic scale. A given potential will thus not affect the two phenomena in the same manner: a potential modifying the vortex shape may very well not produce any quasiparticle oscillations and vice versa. As an example we may consider an analysis of Fig. 4.2.1. Looking at the topography in Fig. 4.2.1a, inhomogeneities (missing atoms) are clearly visible. From Fig. 4.2.1b it is also apparent that the surface is not perfectly homogeneous. These kinds of inhomogeneities obviously do not lead to any regular interference pattern with a strength comparable to what we see in the vortex core, as we demonstrate in Fig. 4.2.1c. However, these inhomogeneities might very well provide a slowly varying potential resulting in irregular vortex core shapes. In conclusion, the irregular shape of vortex-cores is affected by smoothly varying potentials, with longer characteristic length scales than the potentials causing the quasi-particle interference pattern.

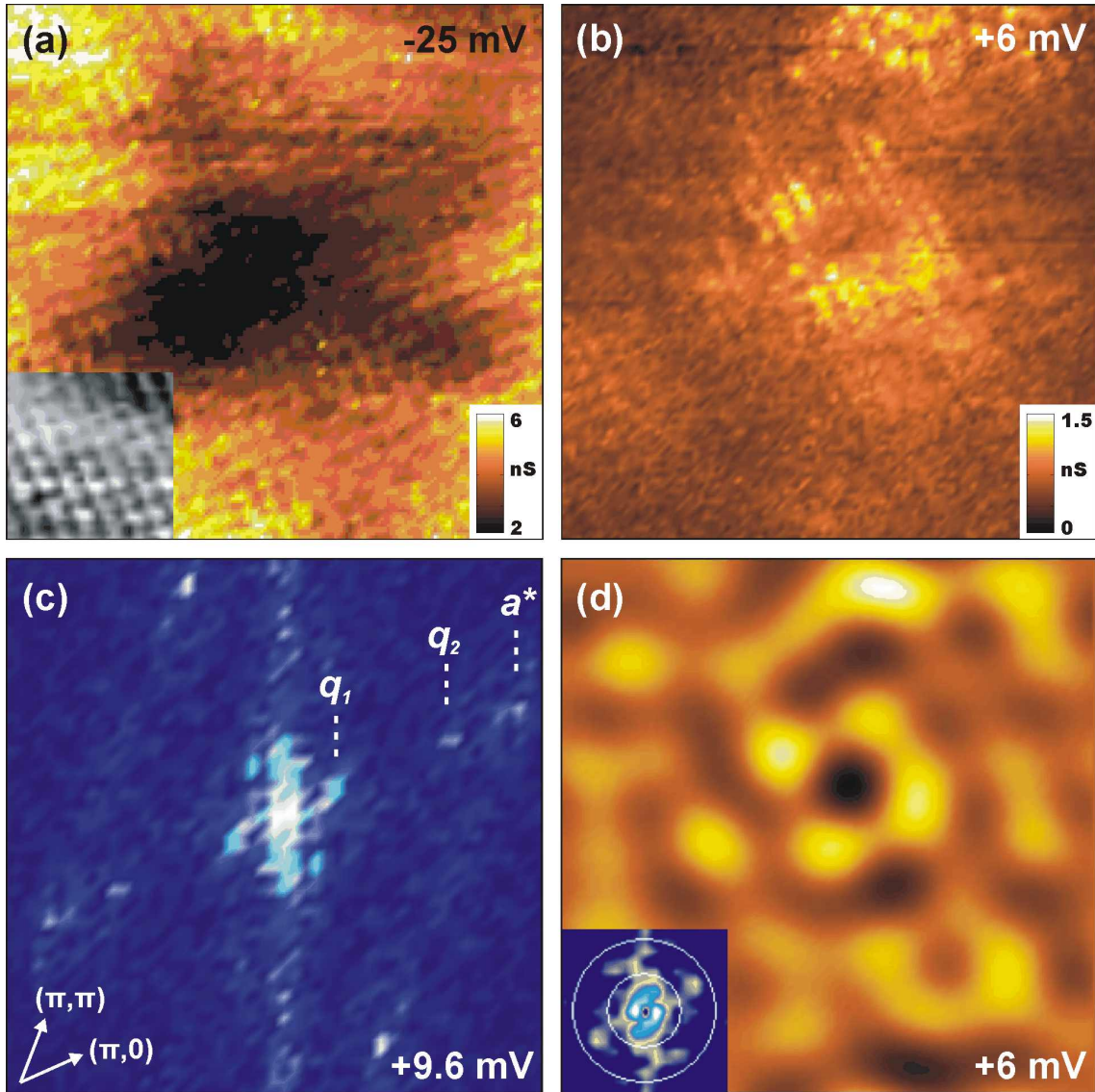


Figure 4.4.1: (a)  $8.7 \times 8.7$  nm<sup>2</sup> conductance map at  $V_s = -25$  mV. The inset shows the simultaneously acquired topography at the same scale as the underlying conductance map. (b) Conductance map in the same area as (a) at  $V_s = +6$  mV. (c) FT image at  $V_s = +9.6$  mV. (d) Filtered inverse FT image. The inset shows the filter applied to the image acquired at  $V_s = +6$  mV and which selects the region between the two circles with radii  $q[2\pi/a] \sim 0.17$  and  $\sim 0.32$ .

## 4.4 Square modulation

In Fig. 4.4.1a we show a conductance map at  $V_s = -25$  mV which clearly displays the location of the vortex core. Its size and irregular shape are consistent with previous studies [23, 24]. In Fig. 4.4.1b we present a conductance map at  $V_s = +6$  mV which corresponds to the energy of the core state. Inside the core one can observe a striking square pattern formed by four bright regions, similar to the observations by Hoffman *et al.* [16]. In order to quantitatively analyze these structures we performed the Fourier transform (FT) of conductance maps at several energies. In Fig. 4.4.1c we show the FT obtained at  $V_s = +9.6$  mV. In addition to the peaks corresponding to the atomic lattice, we observe two clear structures. First we see four peaks at  $q_1 \simeq 0.25\pi/a$  corresponding to an incommensurate period of  $(4.3 \pm 0.3)a$  oriented parallel to the CuO bond direction. These maxima are clearly visible in all LDOS-FT taken between 4 and 12 mV, and between  $-8$  and  $-12$  mV. We note that their intensity at negative bias (occupied states) is  $\sim 2/3$  smaller than at positive bias (empty states). Second we see two maxima at  $q_2 \simeq 0.75\pi/a$  which only appear along the  $(\pm\pi, 0)$  direction. Looking closer, one can observe that the quartet of  $q_1$  peaks is slightly rotated with respect to the atomic lattice, while the two  $q_2$  peaks are not.

To clearly identify which signal in the real-space conductance map of Fig. 4.4.1b originates from the  $q_1$  peaks, we show in Fig. 4.4.1d the filtered inverse FT. We selected a region in  $q$ -space containing the four  $q_1$  peaks (see inset). The inverse FT exhibits four bright regions at the corners of a square which clearly correspond to the pattern observed in the raw data. We thus demonstrate that the low energy structure in the vortex core shown in Fig. 4.4.1b is indeed at the origin of the four  $q_1$  peaks.

## 4.5 Spatial variation of core states

We now address the spatial variation of the LDOS inside the vortex core. In Fig. 4.4.2a we indicate 27 circular areas, each of containing 21 pixels of our spectroscopic image. For clarity we used the filtered image (Fig. 4.4.1d) to identify the positions. In Fig. 4.4.2b we display three spectra: A' and C' were taken at the center of area A and C, respectively and G' was taken at point G, at a distance of 3.4 nm from the center of the square pattern. Whereas G' is similar to the zero field spectrum, A' and C' differ in a remarkable manner. The core states appear very distinctly in spectrum C', which is at one maximum of the fourfold pattern, but in A' there is hardly any signature of the core states. Thus it appears that the square pattern reflects the spatial variation of the localized states. In order to investigate this further and extract the most robust features we have averaged spectra inside each circle of Fig. 4.4.2a. Figure 4.4.2c shows the average spectra of each circle along the trace indicated by the arrow in Fig. 4.4.2a. The core states appear clearly in the two circles located on the maxima of the square pattern (red). At the center A, only a

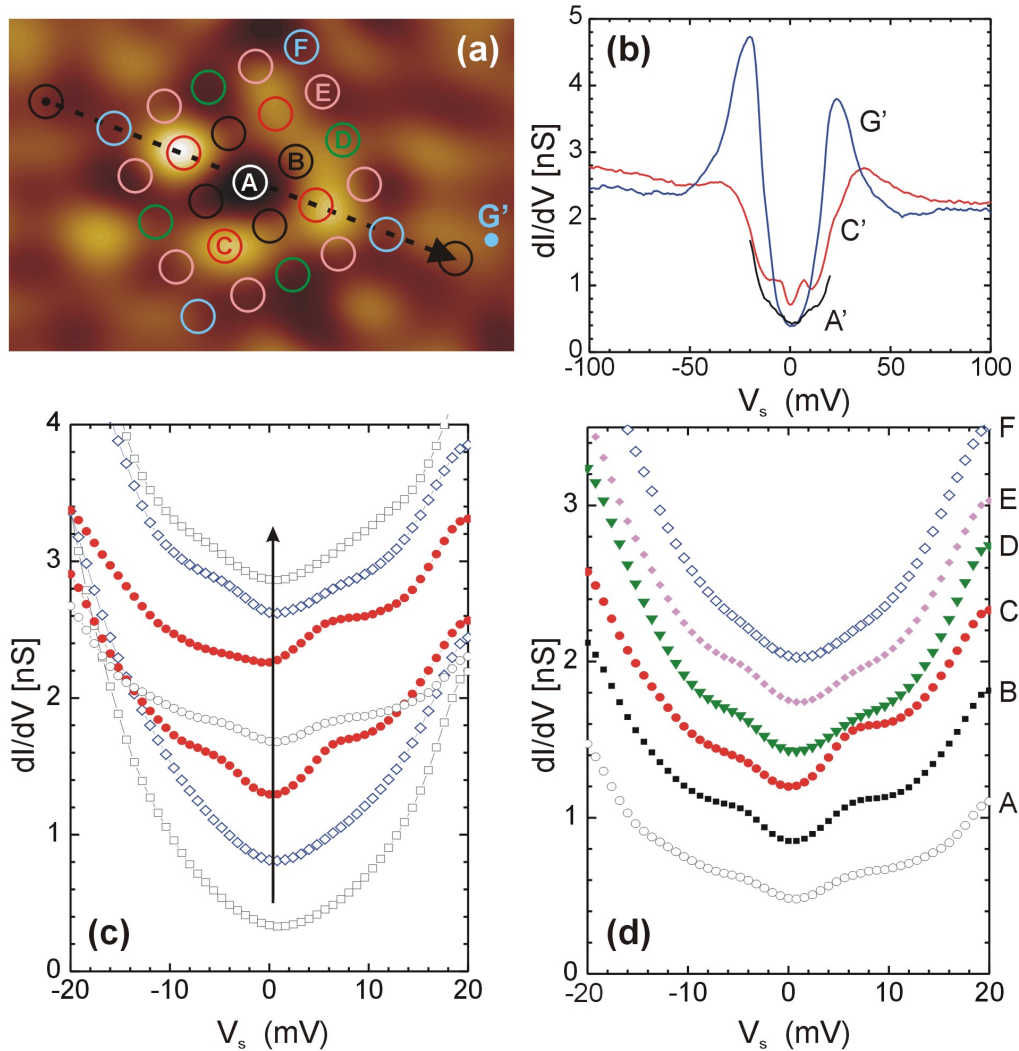


Figure 4.4.2: (a) Central region of Fig. 4.4.1d. Each circle contains 21 pixels. (b) Spectra taken at the core center (A'), on a maximum of the square pattern (C') and outside the core (G'). (c) Spectra averaged in the 7 circles along the arrow in (a); For clarity, the spectra were shifted vertically by 0.4 nS. (d) Spectra averaged over the four-fold symmetry equivalent circles, drawn with identical color in (a); The spectra are offset vertically by 0.3 nS.

weak signature of the localized states is seen, and this signature disappears when moving outside the four-fold pattern. In Fig. 4.4.2d we show a different representation of this data. Whereas A again shows the average spectrum of the central circle, the curves B–F correspond to an average of spectra taken in circles which are equivalent by the four-fold

symmetry (same color in Fig. 4.4.2a) and at increasing distance from the center. The strongest signature of core states is again seen in curve C taken on the maxima of the square pattern.

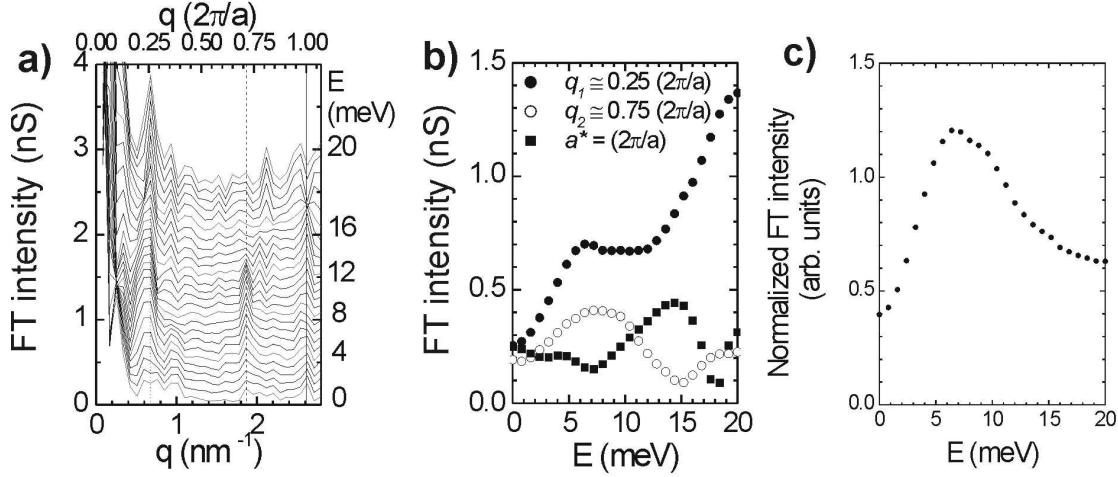


Figure 4.5.1: (a) Tunneling conductance at energies between 0 and +16 meV measured along  $(\pi, 0)$ . (b) FT intensity of  $q_0 = 2\pi/a$ , corresponding to the atomic lattice,  $q_1 \simeq 0.25(2\pi/a)$  corresponding to the square pattern in the vortex core, and  $q_2 \simeq 0.75(2\pi/a)$  which only appears along the  $(\pm\pi, 0)$  directions. The intensities were measured on the peaks indicated in Fig. 4.4.1c. (c) Normalized Fourier transform intensity corresponding to  $q_1 \simeq 0.25(2\pi/a)$ . The FT was normalized by the average value of the whole Fourier transform map at each energy.

We therefore conclude that the vortex-core states are closely related to the square pattern. In Fig. 4.5.1a we plot a cut in the Fourier transform along the  $(\pi, 0)$  direction at several energies. The peak at  $q_1$  corresponding to the  $4a$ -period does not disperse with energy within the error margins of our measurement. While a weak dispersion towards longer wavelengths cannot be excluded given our present resolution, this possible dispersion would be in the opposite sense than the one observed along  $(\pi, 0)$  in the superconducting state and attributed to quasiparticle interference [17]. We also remind that the peak at  $q_2$  corresponding to a wavelength of  $(4/3)a$  is present in the  $(\pi, 0)$  direction, but not in the  $(0, \pi)$  direction.

Figure 4.5.1b shows the intensities of the three dominant peaks as a function of energy. The intensity of the  $q_1$  peak has a clear maximum at the energy of the localized state and increases again when approaching 20 meV. This increase is fortuitous because there is a general increase in intensity at high energy. Also, the direct images as well as the Fourier transform images do not show an obvious four-fold pattern at higher energies. Thus the increase does not mean that the pattern is present also at these energies. If we normalize the Fourier transform by the average value of the whole Fourier transform map at each

energy the maximum at 6 meV remains but the increase at higher energies disappears (see Fig. 4.4.1c). The applied Fourier Transform expressions are defined in Appendix C, there we also give expressions for the normalization to the average value of the FT.

## 4.6 Discussion and Conclusion

Comparing our results with the observations of Vershinin *et al.* [20] in the pseudogap state above  $T_c$ , we find that the ordering in the vortex core is very similar to the ordering in the pseudogap state. The basic structure is a non-dispersing square modulation in the Cu-O bond direction. The period  $(4.3 \pm 0.3)a$  in the vortex core at 2 K is slightly smaller than the period  $(4.7 \pm 0.2)a$  in the pseudogap state at 100 K. In the pseudogap state, the intensity of the peak in the FT was found to be largest and energy independent below 20 meV, whereas we find an energy dependence resembling the tunnel conductance. This discrepancy may be due to temperature broadening at 100 K. Another difference is that we find a  $(4/3)a$  modulation in one direction. Such ordering was also seen by Hanaguri *et al.* [22] at low temperature in  $\text{Ca}_{2-x}\text{Na}_x\text{CuO}_2\text{Cl}_2$  with a main period of  $4a$ .

The pattern inside the vortex core shown in Fig. 4.4.1 is consistent either with a decaying square modulation or with a square pattern. A decaying square modulation is a four-fold symmetric modulation whose intensity decays in space. A square pattern is formed by four spots situated in a square arrangement. In Fig. 4.6.1, we show the different signatures of these two patterns. Fig. 4.6.1 shows a real space image where we have simulated the atomic lattice plus a square-modulation enveloped by a Gaussian. In order to reproduce more accurately the experimental data, we also include a  $(4/3)a$  modulation only along one direction. The corresponding FT image shown in Fig. 4.6.1b is in perfect agreement with the data shown in Fig. 4.4.1c. The square pattern characteristics are simulated in Fig. 4.6.1c, where the atomic lattice plus four spots in a square have been simulated. Each spot is simulated by magnifying the signal with a Gaussian function. Its FT image shown in Fig. 4.6.1d displays satellite peaks around the reciprocal atomic peaks at  $a^*$  and  $b^*$ . These simulations seem to indicate that the vortex core pattern is most possibly due to a four-fold symmetric modulation inside the vortex core. However more detailed studies should be carried out to clarify this question.

In this section we evidence that the amplitude of the vortex core states has a four-fold structure directly reflecting the modulation observed in the vortex core. Since these states appear at an energy proportional to the gap  $\Delta_p$ , our results connect the superconducting state to the electronic modulation. We further find that the four-fold modulation has the same behavior as in the pseudogap phase [20], what could be expected since the vortex cores display the pseudogap [23]. However, the role played by the vortex core on the core states and therefore on the square modulation is not clear yet. This question should be investigated in further studies. Above the critical temperature, vortex-like excitations were reported [124] evidenced by an anomalously enhancement of the Nernst signal.

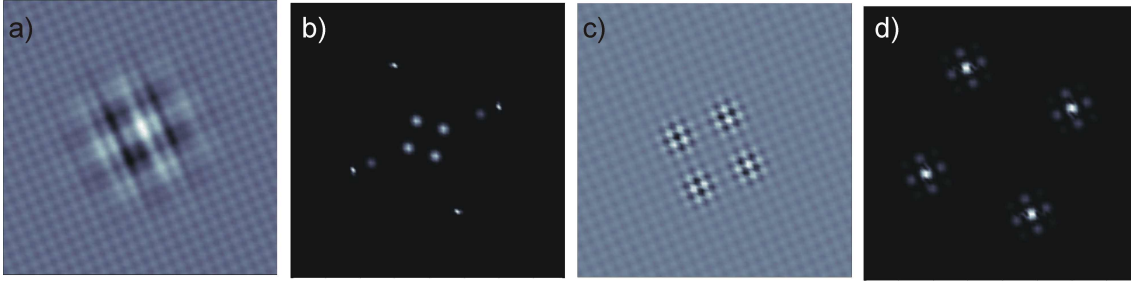


Figure 4.6.1: Real space simulated images of (a) a square modulation and its FT image in reciprocal space shown in (b) and (c) of a square pattern with its FT shown in (d). The square modulation and the spot forming the square pattern are convolved by Gaussian functions.

This observation is directly relevant to the central issue of the pseudogap state in the cuprates. The relation between the pseudogap and the superconducting state has been the topic of many theoretical studies possibly leading to spatially modulated structures [125, 126, 127, 128, 129, 130]. In particular, several authors have proposed that a pair density wave (PDW) is at the origin of the observed structures [131, 132, 133, 134]. In the context of our study this model is attractive, since we establish a clear link between the superconducting state, the pseudogap and the square modulation in the vortex core. Within the PDW picture, this suggests that the localized states at  $E \approx 0.3\Delta_p$  correspond to the lowest pair breaking excitations of the PDW. The relation between the localized states and the square modulation thus sets a critical test for these theories.



# Chapter 5

## Low Temperature Spectroscopy in $\text{Bi}_2\text{Sr}_2\text{CaCu}_2\text{O}_{8+\delta}$

We present a detailed study of tunneling spectroscopy in slightly overdoped Bi2212 ( $T_c = 88$  K) using a low temperature scanning tunneling microscope. In the superconducting state, a peak-to-peak mean gap  $\Delta_p = 36$  meV has been measured consistent with previous measurements. We focus on the nanoscale variations of the spectra present in a particular inhomogeneous sample. Nanoscale spectral variations has been interpreted due to an inhomogeneous distribution of oxygen dopant atoms. This nanoscale variation of the gap is consistent with a 4 K transition width measured by *ac*-susceptibility. A double-peak structure of the coherence peaks is usually observed in the tunneling spectra. We have observed that the two peaks are separated by  $\sim 12$  meV and their intensity varies at an atomic level. Finally, we discuss the possible origins of the double-peak feature.

### 5.1 Introduction

The  $\text{Bi}_2\text{Sr}_2\text{CaCu}_2\text{O}_{8+\delta}$  (Bi2212) material has been extensively study with spectroscopic techniques since pristine surfaces can be obtained. Measurements performed with scanning tunneling microscope (STM) in this material have unveiled remarkable properties above and below the superconducting critical temperature such as microscopic variations of the local density of states (LDOS), electronic modulations in the superconducting and pseudogap states. Recently, it was shown that these properties are not exclusive to the Bi2212 compound demonstrating that a theory for high  $T_c$  superconductors (HTS) should explain these observations. Usually, STM measurements in the Bi2212 compound display inhomogeneous spectra and an important aspect of these studies have focused on the role of these inhomogeneities on its superconducting properties. Here, we will present STM measurements performed in the superconducting state of a Bi2212 sample focusing on the nanoscale and atomic spectral variation. We start by discussing the sample's preparation

and the tunnel vacuum junction characterization.

## 5.2 Characterization

Our STM measurements were performed on a Bi2212 single crystal grown by the travelling solvent flux zone method [120] and annealed in 500°C under 15 bar oxygen pressure. After annealing we measured  $T_c^{onset} = 88$  K ( $\Delta T_c = 4$  K) by *ac*-susceptibility.

We performed the measurements with a home-built STM [122] under ultrahigh vacuum. The sample was cleaved *in situ* at room temperature before cooling without an applied magnetic field. The tunnel junction was made between the (001) sample surface and an electrochemically etched Iridium tip. All data presented here was acquired at 2 K, first at zero field and then at 6 T.

First, I characterize the tunnel barrier quality in zero field. A typical  $I(V)$ -spectrum is shown in Fig. 5.2.1a. The tunnel condition used to regulate the tip-sample distance is shown by a dot corresponding to a tunnel resistance  $R_t = 0.5$  G $\Omega$ . The characteristics of the tunneling current are best seen in the numerical derivative of the  $I(V)$  curve. The characteristics of the tunneling current are seen in the curve shown in Fig. 5.2.1b as a full line. The superconducting gap estimated from the coherence peak distance is  $\Delta_p = 34$  meV. In order to improve the signal to noise ratio, we use a lock-in technique to measure directly the differential conductance  $dI/dV(V)$  (see Section 1.3). The resulting spectra is shown as a dashed line in Fig. 5.2.1b and can be directly compared with the numerical derivative. As observed the signal to noise ratio is improved especially outside the gap and all the spectral signatures are located at the same energy. We note that the lock-in method tends to reduce the height of the coherence peaks.

According to Renner *et al.* [135], in a true vacuum tunnel junction the spectra should be independent of the tip-sample distance, apart from a constant factor. As it is discussed in Section 2.2, the tip-sample distance is controlled by the tunnel condition. To verify this, we measure a series of spectra at different tunneling resistances. The tunneling resistance is varied by keeping fix  $V_t$  and by varying  $I$ . The spectra measured at different tunneling resistance  $R_t$  are shown in Fig. 5.2.1c and when these spectra are normalized by  $R_t$  all spectra fall into a single curve, indicating a true vacuum tunnel junction. We attribute the slight difference between the curves at negative bias to a shift of the tip toward the sample induced by an electrostatic change during the bias voltage  $V_s$  scan. Such differences appear at positive bias if the tip is stabilized at negative bias. The apparent barrier height between an iridium tip and the Bi2212 surface was estimated to be around 1.27 eV by Bart Hoogenboom [110] for a junction similar to ours. The bias voltage applied is lower or equal to 0.6 V which assures that the measurements were performed in the tunneling regime condition.

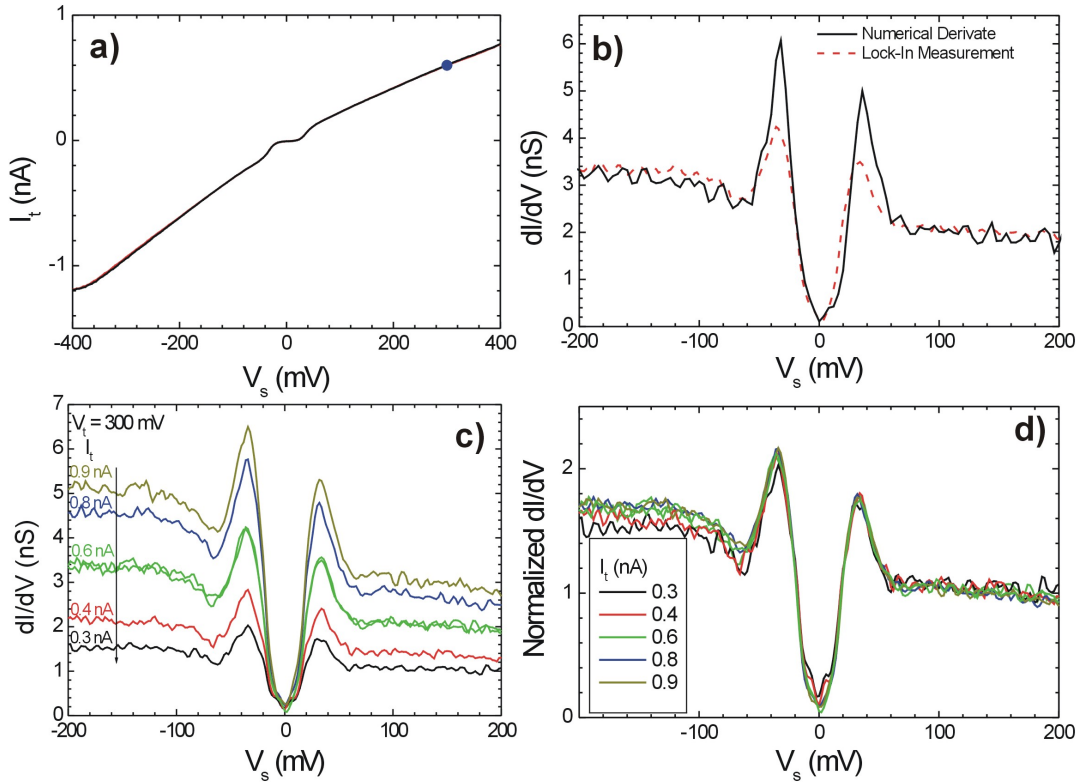


Figure 5.2.1: Zero-field spectroscopy in an overdoped Bi2212 sample with  $T_c = 88$  K. (a)  $I(V)$ -spectrum acquired at 2.1 K with a bias potential of  $V_t = 0.3$  V and a tunnel current of  $I = 0.6$  nA. (b) The corresponding numerical derivative (full line) and the  $dI/dV$  spectrum measured with the lock-in technique (dashed line). The lock-in excitation has a mean amplitude  $V_{rms} = 1$  mV and a frequency  $f = 321$  Hz. (c) Tip-sample dependence of the spectra by varying the tunnel current between 0.3 – 0.9 nA at  $V_t = 0.300$  V. (d) Spectra normalized by the tunnel resistance  $R_t$  showing their independence on the tip-sample separation.

From to the generic formula of Presland *et al.* [6]

$$p = 0.16 \pm \sqrt{(1 - T_c/T_c^{max})/82.6}$$

where  $T_c^{max} = 92$  K, we estimate from the critical temperature a nominal doping  $p \sim 0.18$  for the sample. At this doping, the sample is slightly overdoped which is consistent with the background slope of the conductance spectra, as well as the magnitude of the superconducting gap  $\Delta_p$  consistent with literature [70].

### 5.3 Nanoscale spectral variations

In this section, we concentrate on the spectral signatures that cause the spatial variations of the conductance signal. We will see that the superconducting gap  $\Delta_p$  varies strongly in regions of  $\sim 1$  nm explaining the conductance variations at energies below the gap. Since the gap variations have been correlated with the oxygen distribution in the Bi-O planes [109], a non-uniform distribution of the extra oxygen atoms in the Bi-O layers is the most likely origin of the nanoscale variations of the spectra. This interpretation is also consistent with the fact that more uniform spectra can be obtained after adequate annealing treatments [121].

In Fig. 5.3.1a we show a topographic scan at zero field which clearly resolves the atomic lattice of the BiO top layer, as well as the characteristic supermodulation running along the  $b_0$ -axis. The atomic lattice observed is believed correspond to the Bi atoms which are  $3.8 \text{ \AA}$  away from each other. The period of the supermodulation is  $26 \pm 1 \text{ \AA}$ . On top of the intensity variations due to atomic corrugations, the topography presents smaller variations at longer length scales. Since the tip-sample distance measured by a topography image is related to the integrated local density of states (ILDOS, see Section 2.2), these variations suggest non-uniform spectral properties. This was illustrated in the spectral map taken at  $V_s = -15$  mV shown in Fig. 4.2.1b. The tunneling conductance at this energy varies on a typical distance of  $\sim 20 \text{ \AA}$ . Similar spatial variations have been reported earlier [106, 109].

The spatial gap distribution is plotted in Fig. 5.3.1b showing that the gap varies strongly from 22 to 54 meV. The regions with the same gap magnitude have a characteristic size of  $\sim 15 \text{ \AA}$ . The strong variation of the gap is also seen in the spectral trace shown in Fig. 5.3.1c along 50 nm. In the spectral trace we observe a stable and reproducible background conductance ( $V_s > \Delta_p$ ) which is another criterion indicating vacuum tunneling [135]. We show in Fig. 5.3.1d five spectra with different gap values corresponding to the numbered dots in Fig. 5.3.1b. The coherence peaks intensity at  $\pm\Delta_p$  decreases as the gap increases. For the spectrum with  $\Delta_p \simeq 50$  meV, the conductance below the gap energy presents a kink at  $\sim 22$  mV. The spectra with lowest gap magnitude in Fig. 5.3.1d display shoulders above the coherence peaks at an energy  $\sim \Delta_p + 12$  mV. We will discuss this feature in the following section. Finally, the spatial variation of the gap

magnitude implies that the conductance map made at  $-15$  mV will show high intensity regions where the superconducting gap is smaller which explains the intensity variations observed in Fig. 4.2.1b.

The statistical distribution of the gap is shown in Fig. 5.3.1e. The gap magnitude plotted is the average of the negative and positive coherence peak position  $\Delta_p = (\Delta_p^+ - \Delta_p^-)/2$ . In the inset, the gap distribution of the corresponding coherence peaks present an increase count of spectra having superconducting gaps at  $\Delta_p = \pm 30$  mV and  $\pm 38$  mV. However such a bimodal distribution is not always observed. The average spectra distribution has been fitted with a Gaussian function (full line in Fig. 5.3.1e) giving a mean gap  $\bar{\Delta}_p = (36 \pm 2)$  mV and a standard deviation  $\sigma = 7$  mV. The mean superconducting gap is consistent with the doping concentration  $p = 0.18$  estimated from  $T_c$  [70]. The gap standard deviation observed implies that about 95% of the gap values are within 22 and 50 meV. Since superconducting transition widths larger than 1% of  $T_c$  indicates large degree of inhomogeneity [121], the 4 K transition width measured when  $T_c$  is 88 K, already indicates a large standard deviation of the gap.

In order to quantify the characteristic length of the gap amplitude variation, we have calculated the angular-averaged auto-correlation of the gap map image shown in Fig. 5.3.1b. The auto-correlation  $A_f(\mathbf{R})$  of a signal  $f(\mathbf{r})$  and the cross-correlation  $C_{fg}(\mathbf{R})$  of two signals  $f(\mathbf{r})$  and  $g(\mathbf{r})$  are defined in Appendix B. The auto-correlation of the gap map is plotted in Fig. 5.3.1f, together with the cross-correlation of the gap map with the simultaneously acquired topography. The auto-correlation of any signal is equal to 1 at  $r = 0$ . A fit to an exponential function of the gap map auto-correlation yields a characteristic length  $\xi = 1.77$  nm. This shows that the gap varies in a typical distance  $\sim 1.8$  nm which is consistent with the  $\sim 1.5$  nm size of the regions having the same gap magnitude as it was directly deduced from Fig. 5.3.1b. It is important to remark that the spatial auto-correlation of the gap map does not present any characteristic pattern.

The cross-correlation of the topography and the gap map images shows that they are anti-correlated meaning that the topography signal is lower in the regions where the gap is bigger. A closer look to Figs 5.3.1a and (b) shows this; we observe that dark region in the topography (related to small  $z$ -values) usually corresponds to the regions where big gaps appear. In Fig. 5.3.1a, the small intensity variations of the topography signal at a larger spatial scale  $\sim 2 - 3$  nm can be associated to the integrated local density of states (ILDOS) variation, as it has been previously discussed in section 2.2. The ILDOS variation is proportional to the changes in the total number of states measured up to the bias potential  $V_t$ . Therefore, the anti-correlation between the topography and the gap map shows that there is a low number of total states when the gap is big. This can be understood if we tentatively assign the ILDOS magnitude to the local doping concentration [106]. In regions where the doping concentration is small, the gap magnitude is big (see Section 3.3). In this interpretation, the anti-correlation of the topography and the gap map shown in Fig. 5.3.1f could indicate that the local doping concentration affects the gap at distances smaller than 2 nm.

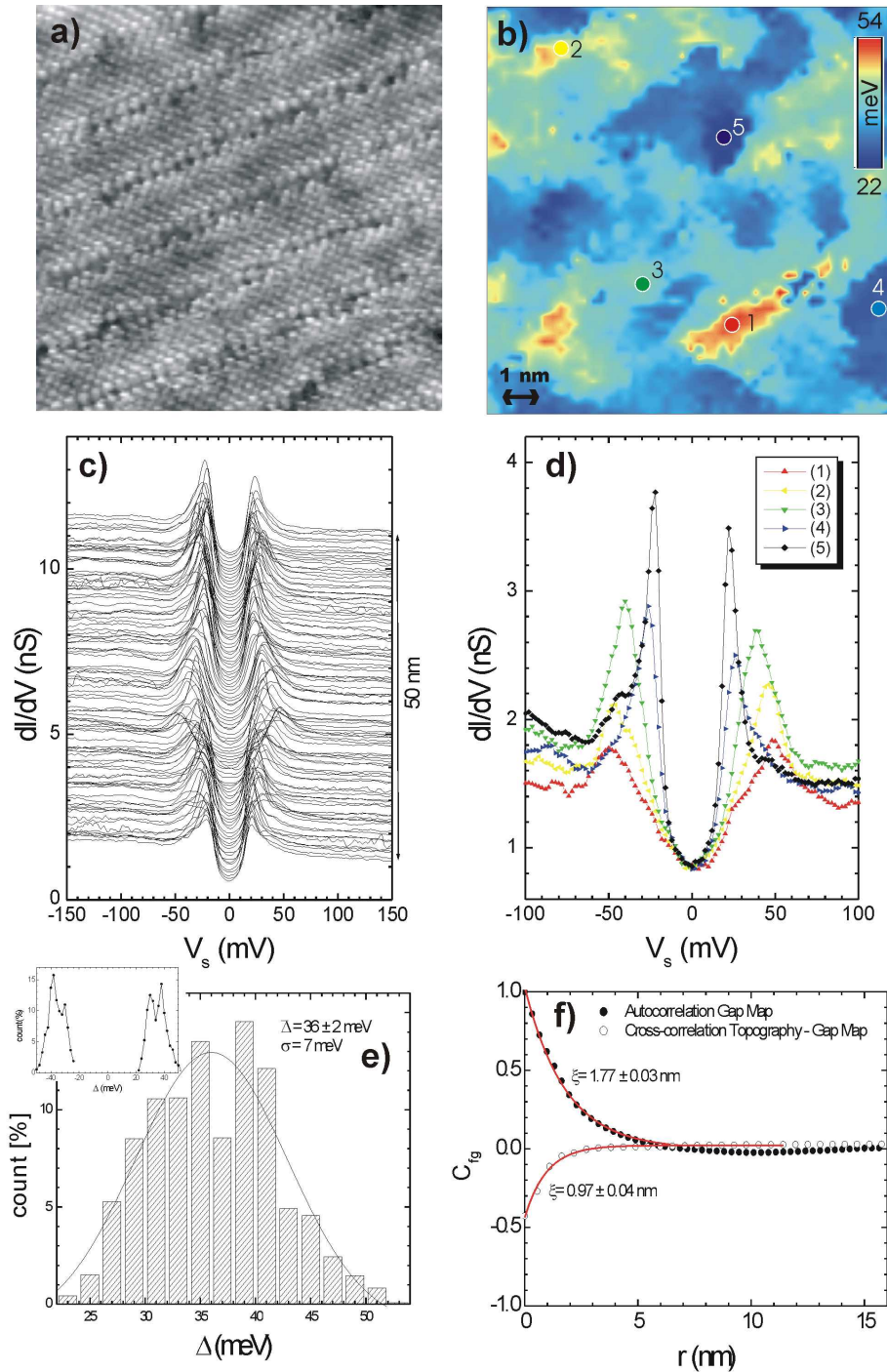


Figure 5.3.1: (a)  $16 \times 16 \text{ nm}^2$  topography image on Bi2212 showing atomic resolution. (b) Color coded image of the superconducting gap variation  $\Delta_p$  in the same region. (c) Trace showing 101 spectra along 50 nm. (d) Selected spectra from the regions marked by dots in the gap map (Fig. 5.3.1b). (e) Gap distribution of Fig. 5.3.1a. A Gaussian fit gives an average gap  $\bar{\Delta}_p = 36 \pm 2 \text{ meV}$ . The inset shows the statistical distribution of the negative and positive bias coherence peaks position. (f) Auto-correlation (full dots) of the gap map in Fig. 5.3.1b and its cross-correlation with topography shown in Fig. 5.3.1a. Tunnel conditions:  $V_t = 0.6 \text{ V}$ ,  $I = .8 \text{ nA}$ . Lock-in amplitude 2 mV rms with a frequency of 827 Hz.

The local doping concentration can vary due to a non-uniform distribution of extra oxygen atoms. The previous observations indicate that homogeneous spectral properties could be obtained if a more uniform distribution of the extra oxygen atoms is produced. Indeed, Hoogenboom *et al.* [121] have shown that homogeneous spectral properties can be obtained by adequate annealing treatments that presumably produce more uniform oxygen distributions. Further studies should quantify the interplay of the standard deviation of the gap and the superconducting transition width. In particular a careful determination of the relation between the spectral variations and the oxygen distribution will allow to establish the spatial influence of the dopant oxygens on the spectral properties of HTS compounds.

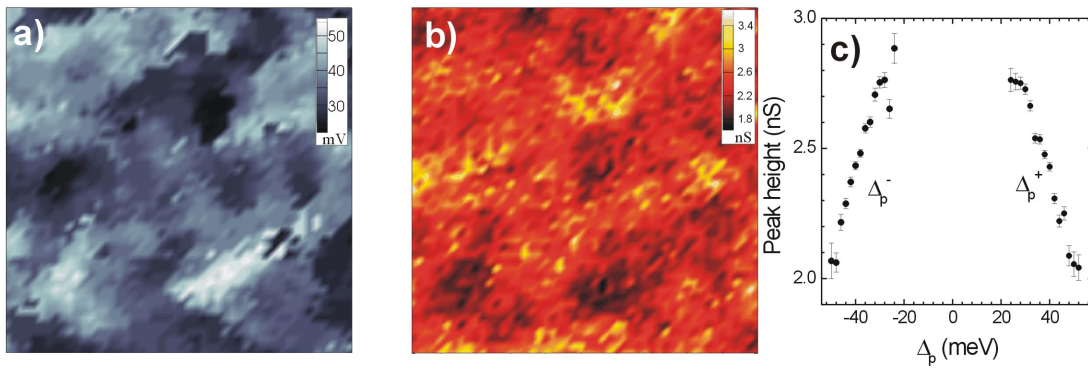


Figure 5.3.2:  $16 \times 16 \text{ nm}^2$  maps of the energy of the coherence peak at positive bias  $\Delta_p^+$  (a) and of the peak height  $dI/dV(\Delta_p^+)$  (b). (c) Variation of the mean coherence peak height with the gap magnitude. The mean peak height was obtained by averaging several spectra with identical values of  $\Delta_p^+$  and  $\Delta_p^-$ .

Another property of the superconducting spectra is the relation between the coherence peak height and the gap magnitude. The trend observed in the spectra of Bi2212 and showed in Fig. 5.3.1d indicates that the coherence peak height decreases with increasing gap. This anti-correlation between the gap magnitude and the coherence peak height is shown in more detail in Fig. 5.3.2 where we compare the spatial variations coherence of the positive-energy peak ( $\Delta_p^+$ ) plotted and of the peak height  $dI/dV(\Delta_p^+)$  in the same area. Comparing these images we observe that the regions which present higher gap magnitude also present lower peak heights. In order to follow the intensity decrease as a function of the gap magnitude, we average the peak height of all spectra with identical peak energy position, the result is plotted in Fig. 5.3.2c. There is almost a linear decrease of the peak height as the gap magnitude decreases. BCS theory predicts that the width of the coherence peaks should increase proportionally to the gap. Fig. 5.3.1d shows that there is a small increase of width of the peaks with  $\Delta_p$ , however it does not seem to be proportional to the gap. We will come back to this question later when we discuss the overall form of the spectra in chapter 7.

Several explanations have been proposed to explain this anti-correlation between the

peak height in the superconducting gap. A modulation of the pair-potential interaction was reported to reproduce such a trend. Nunner *et al.* [136] proposed that the oxygen dopants can modulate the pair-potential in such a way. Another possibility would involve band structure effects: when the compound is hole doped, the van Hove singularity (VHS) appears below the Fermi level (see Section 2.4.3). In the DOS, its proximity to the Fermi level produces an increase of the coherence peaks spectral weight. With underdoping, the gap magnitude and the Fermi level increases. The latter increase moves away the VHS to lower negative energy which reduces the spectral weight around the coherence peaks, thus reducing the coherence peaks height. The effect of the VHS in the tunneling spectra is discussed in detail in chapter 8.

## 5.4 Atomic variations of the spectra

Previously, we have seen that the sample displays spectral variations at a nanometer scale. Since Bi2212 has a coherence length  $\xi \simeq 5 \text{ \AA}$  of the order of the lattice parameter  $a = 3.8 \text{ \AA}$ , we may expect changes in the spectra at an even shorter scale. Here, I will focus on spectral changes which indeed occur at smaller distances than the Cu atomic separation.

When looking at spectral variations at a subatomic scale, it is important to consider one peculiarity of the constant-current STM mode. Within the Tersoff-Hamman [7] theory, the tunneling conductance is given (at  $T = 0$ ) by  $\sigma(x, y, V) \propto e^{-2\kappa d} N_{\parallel}(x, y, eV)$  if we assume an energy-independent decay of the LDOS outside the sample (see Section 2.2). In constant-current mode the tip-sample distance  $d$  is adjusted so as to keep the total current  $I \propto \int_0^{eV} \sigma(x, y, \omega) d\omega$  fixed to a value  $I_{reg} \propto e^{-2\kappa d} \int_0^{eV_{reg}} N_{\parallel}(x, y, \omega) d\omega$ . Solving for  $e^{-2\kappa d}$  and inserting in the expression of  $\sigma(x, y, V)$  we see that

$$\sigma(x, y, V) \propto B(x, y, V_{reg}) N_{\parallel}(x, y, eV), \quad (5.4.1)$$

where  $B(x, y, V_{reg}) = I_{reg} / \int_0^{V_{reg}} N_{\parallel}(x, y, \omega) d\omega$ . Hence, we expect to observe two differential kinds of spectral variations. The first, encoded in  $B(x, y, V_{reg})$ , are independent of bias voltage  $V$  and integrate over states up to the regulating voltage  $V_{reg}$ . The second are due to local variations of the LDOS  $N_{\parallel}(x, y, eV)$ . All the measurements presented in this section were performed with the same regulation voltage  $V_{reg} = 0.3 \text{ V}$ , thus the factor  $B(x, y, V_{reg})$  should only depend on the spatial position of the tip. We may therefore divide out this factor in order to extract the variation of the local density of states  $N_{\parallel}(x, y, \omega = eV)$ .

Here we present measurements performed in zero field and at  $H = 6 \text{ T}$ . The last were carried out in-between vortices; the spectral changes inside magnetic vortices were discussed in 4. It was reported previously [55] that the spectra are essentially field independent at least up to 6 T. Thus we have assumed that the magnetic field does not affect

the superconducting spectra outside vortices. Furthermore, the observations which we discuss in this section are present in zero field and also a 6 T magnetic field.

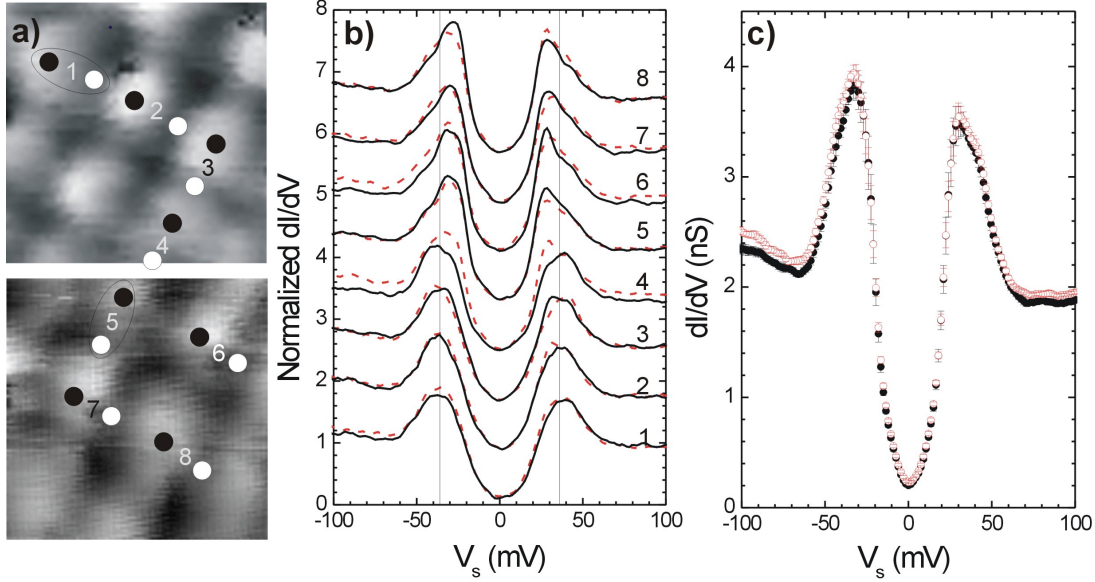


Figure 5.4.1: (a) Topographic images of  $1 \times 1 \text{ nm}^2$  regions showing where the spectra were measured. Each number corresponds to a pair of spectra shown in (b) and measured on top of an atom (full line) and between atoms (dashed line). (c) Averaged spectra measured above an atom (full dots) and between them (open circles). The tunnel conditions are  $I_t = 0.6 \text{ nA}$  and  $V_t = 0.3 \text{ V}$ ,  $T = 2.1 \text{ K}$  and  $H = 0 \text{ T}$ .

In Fig. 5.4.1, we show how the differential conductance varies at the atomic scale in two different regions. Four pairs of positions are indicated in the the topography of these regions showed in Fig. 5.4.1a. Each pair is formed by two measurements performed one above an atom (black dot) and another next to it (white dot) and the corresponding spectra are shown in Fig. 5.4.1b. The full lines correspond to spectra measured above an atom, while the dashed lines are the spectra measured between two atoms. When the spectra at these two positions are compared, we observe (a) a small difference on their intensity which is almost voltage independent, and (b) small changes in the form of the coherence peaks. We consider first the voltage independent changes of the spectra. In order to extract the most robust features, we average the spectra at the two characteristic positions (Fig. 5.4.1c). We observe a net difference between the mean spectra with a very weak energy dependence. The energy-independent difference is certainly due to variations of the factor  $B(x, y, V_{reg})$  and their very weak energy dependence can be attributed to LDOS  $N_{||}(x, y, \omega)$  variations. In particular, Fig. 5.4.1c indicates that the conductance is slightly higher between atoms.

In order first to verify that the conductance measured in constant-current mode is

higher between the atomic positions determined by topography, a trace of spectra between two atoms has been measured (Fig. 5.4.2a). The atoms are identified in the  $z$ -variation of the tip shown next to the trace. In Fig. 5.4.2b, the differential conductance evolution along the trace is followed at two bias potentials:  $\pm 30$  mV and  $\pm 80$  mV and compared with the topography. An anti-correlation is directly observed between the atomic positions and the corresponding conductance at these energies, showing a systematically higher conductance between the atoms. This anti-correlation is seen both at 30 mV and at 80 mV. Therefore, this energy-independent variations of the tunneling conductance can be related to the spatial variations of the factor  $B(x, y, V_{reg})$  which changes the overall intensity of the spectra. This indicates a procedure to compare spectra taken at different positions: We can normalize these spectra by their respective intensities measured at a given voltage. This should eliminate the spectral variations due to the energy-independent factor  $B(x, y, V_{reg})$ .

Next, we focus on the energy-dependent variations of the spectra. Fig. 5.4.2b shows a marked difference between the traces at positive and negative bias. While the energy-independent variations of the differential conductance along the trace were related to the spatial variations of the factor  $B(x, y)$ , the energy-dependent contributions must be attributed to variations in the LDOS  $N_{||}(x, y, \omega)$ . Energy-dependent variations can be distinguished directly on the trace shown in Fig. 5.4.2a, where two peaks are often seen around the coherence peak energy. The relative intensity of these two peaks changes over atomic distances and it seems unrelated to the atomic positions. Their energy position also changes smoothly along the trace, but their energy difference seems to stay constant around  $\simeq 12$  meV. Also the total width of these two peaks structure does not appear to change in space.

The two-peaks structure can vary microscopically over lengths smaller than atomic distances and it is not always present. In Fig. 5.4.3a, we show an example of the atomic variation of this feature. The differential conductance above the atom presents clearly peaks at  $\pm 22$  mV and  $\pm 34$  mV, the former being higher than the latter. The spectrum only 1.8 Å away from the atom has peaks at  $\pm 34$  mV with small kinks at  $\pm 22$  mV. Besides the suppression of the peaks at  $\pm 22$  mV, there is no other spectral difference. Indeed both spectra have the same behavior above 34 mV and around zero bias. The total width of the two-peaks structure is also identical in the two spectra.

In Fig. 5.4.3b, we show a case where the spectra do not change microscopically and do not have a double-peak structure. The total spectral weight of the peaks is similar to the spectral weight in the double-peak structure in Fig. 5.4.3a. At energies above  $\sim 40$  mV, the spectra in Fig. 5.4.3a and (b) have similar absolute values for the differential conductances. One striking difference between the spectra in Fig. 5.4.3a and (b) is the shape they have around the zero bias. While in Fig. 5.4.3a and 5.4.2a the spectra display a rather flat shape around the Fermi level, the spectra in Fig. 5.4.3b have a clear  $V$ -shape behavior.

Frequently, in Bi2212 spectra with a double-peak structure are seen [137, 138] with

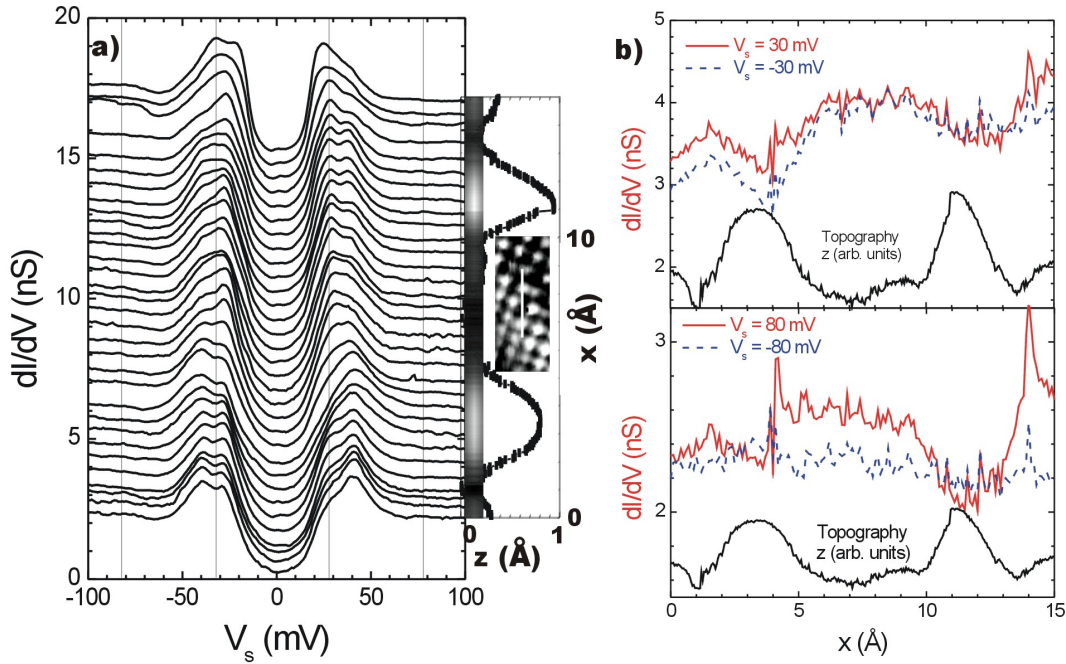


Figure 5.4.2: (a) Trace of spectra between two atoms. The position of the atoms as well as the  $z$ -variation of the tip along the trace are plotted next to the trace in a color coded representation (topographic image, the atoms are identified with the brightest areas) and as a  $z$  vs.  $x$  plot. The inset shows the trace position with respect to the atomic lattice. (b) Variation of the differential conductance along the trace at  $V_s = \pm 30$  mV (upper panel) and  $V_s = \pm 80$  mV. The conductance at positive bias potential is represented by a full line, and a dashed line shows the corresponding at negative bias. The  $z$ -variations of the tip obtained from the topography images are also plotted (lowest curve). The applied magnetic field is 6 T and the temperature 2.1 K. The tunnel conditions are  $I_t = 0.6$  nA and  $V_t = 0.3$  V.

a separation between the two peaks around 12 mV. Previously, we have shown that the gap magnitude is not uniform on the surface. Thus, we are tempted to interpret the two peaks as a double gap structure measured in the boundary region delimiting two areas with different gaps. Following this idea, the double-peak spectra would come from a simultaneous contribution to the tunneling conductance of regions with different gaps due to local variations of the doping concentration. However, this interpretation is not consistent with the fact that the variations occur over distances  $\sim 1.8 \text{ \AA}$ , much smaller than the coherence length  $\xi \simeq 5 \text{ \AA}$ .

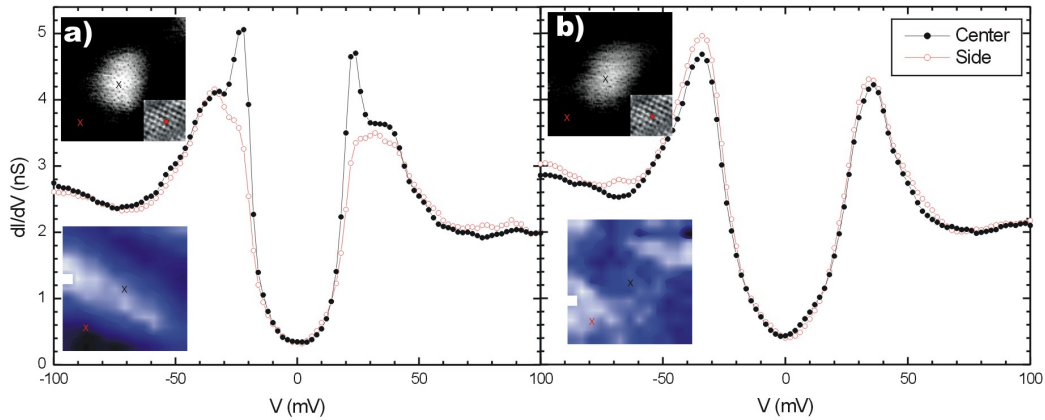


Figure 5.4.3: (a) Spectra measured above an atom (full dots) and at  $1.8 \text{ \AA}$  away from it (open circles). Upper left inset:  $4.35 \times 4.35 \text{ \AA}^2$  topography showing the atom as a bright signal. In the sub-inset the position of the atom in the atomic lattice is shown. Lower left inset: spectroscopic image at  $V_s = -22 \text{ mV}$  acquired at the same time as the topography. It determines the spatial distribution of the  $-22 \text{ mV}$  peak. (b) The same as (a) but in a different region where the spectra does not present large atomic variations and has only one peak.  $H = 6 \text{ T}$ ,  $T = 2 \text{ K}$ .

Another possible explanation for the double-peak structure could be that it has a magnetic origin. However, this possibility can be ruled out since it has been also seen in zero magnetic field.

In another line of thought, the double-peak structure could be tentatively attributed to inelastic scattering on a local impurity: In its tunneling path from the  $\text{CuO}_2$  plane to the tip, the quasiparticle would interact with an impurity exciting an impurity state. Through this interaction, an energy  $\Lambda$  is exchanged between the tunneling quasiparticle and the impurity producing a second peak at  $\sim \Delta_p + \Lambda$  [35]. However, in the calculations this second peak has systematically lower intensity than the superconducting coherence peak, which is not consistent with our observations (see Fig. 5.4.2a).

A similar interpretation which we consider unlikely for the same reason would invoke

strong coupling of quasiparticles to a collective mode. Such coupling can produce shoulders in the spectra corresponding to the onset of inelastic scattering (see Ref. [103] and Section 2.3.2), but like for the inelastic scattering on impurities the additional peaks are always weaker than the coherence peaks. Furthermore, while scattering on impurities would naturally imply local variations at the atomic scale, collective modes are not localized in space and their effects should be visible everywhere on the surfaces. A similar argument allows one to rule out a two-peak structure as a band structure effect. The presence of a van Hove singularity in the quasi-two dimensional electronic bands of Bi2212 would originate an asymmetric double-peak structure in the tunneling spectra. However, in this interpretation, the outer peak should be systematically higher at negative energy, which is not observed.

Finally, the two-peak structure could be tentatively interpreted as two superconducting gaps. Since the Bi2212 has two  $\text{CuO}_2$  planes, it has two bands associated with these planes which has been resolved individually by ARPES [139]. Locally, an impurity could affect differently these two bands producing a double-gap structure in the superconducting tunneling spectra. A double-gap structure has been observed in  $\text{MgB}_2$  [140]. This material has two different electronic bands and the tunnel spectra present two peaks at  $\pm 2.9$  and  $\pm 6$  mV corresponding to two superconducting gaps, one for each band.

Concluding, a procedure to compare spectra at different positions has been given in order to normalize out their overall intensity variations. It has been shown that a two-peak structure is usually seen in the tunneling spectra of Bi2212. We have observed that the two peaks present a  $\sim 12$  meV separation and their intensity varies at an atomic scale. We have ruled out different possible explanations for this two-peaks structure in the tunneling spectra. Further detailed studies should be performed to clarify the conditions for the double-peak structure apparition and to reveal their nature. This shows an example of inter-atomic LDOS variations in HTS.



# Chapter 6

## Low Temperature Spectroscopy in $\text{Bi}_2\text{Sr}_2\text{Ca}_2\text{Cu}_3\text{O}_{10+\delta}$

We report the first low temperature scanning tunnelling microscopy and spectroscopy study of high quality  $\text{Bi}_2\text{Sr}_2\text{Ca}_2\text{Cu}_3\text{O}_{10+\delta}$  single crystals. We present atomic resolution and show spectroscopic data acquired on different samples. The samples have been annealed yielding various doping concentrations from optimum to strongly under-doped samples. In one case, for  $T_c = 109$  K and a transition width of only 1 K, we obtained an extremely homogeneous sample with  $\overline{\Delta}_p = 60$  meV over at least 50 nm. We evidence strong similarities with  $\text{Bi}_2\text{Sr}_2\text{CaCu}_2\text{O}_{8+\delta}$  and discuss the doping level of our samples.

### 6.1 Introduction

The trilayer cuprate  $\text{Bi}_2\text{Sr}_2\text{Ca}_2\text{Cu}_3\text{O}_{10+\delta}$  (Bi2223) attracted a strong interest due to its high critical temperature  $T_c^{max} = 111$  K and its potential for applications. However, the difficulty in synthesizing large sized single-phase crystals significantly impeded the study of fundamental properties. Very recently the effort in developing new crystal growth processes was rewarded by a successful production of homogeneous high quality Bi2223 single crystals [141], thus opening the door to scanning tunnelling spectroscopy (STS) investigations. The determination of the intrinsic superconducting properties of this trilayer compound is of crucial importance for the determination of the generic features and behaviors of Bismuth based cuprates and more generally in the quest of the understanding of high- $T_c$  superconductivity.

In this chapter, we present the first low temperature STS study of high quality Bi2223 single crystals. We investigate the spatial dependence of the local density of states (LDOS) in three different samples and discuss parallels with the parent double layer compound  $\text{Bi}_2\text{Sr}_2\text{CaCu}_2\text{O}_{8+\delta}$  (Bi2212).

## 6.2 General Sample Characteristics

We studied three Bi2223 single crystals grown by the travelling solvent floating zone method [142], which were post-annealed under different conditions. All the samples used in this chapter were grown by Alexandre Piriou and Enrico Giannini, the post-annealing treatments and sample characterization were performed by Alexandre Piriou. They were annealed at 500°C at different partial oxygen pressures. The critical temperatures obtained varied between 104 and 111 K, measured by *ac*-susceptibility. The magnitude of the superconducting transition widths, also measured by this method, was used as a selective criterion for the samples to be studied in the STM. The samples chosen to be measured with STM had the smallest transition widths which should indicate their degree of homogeneity. We present measurements on three samples *A*, *B* and *C* with  $T_c = 109$ , 111 and 104 K, respectively. The measurements were obtained using a home-built scanning tunnelling microscope which operates under ultrahigh vacuum and low temperatures [122]. They were performed in collaboration with Martin Kugler. The vacuum tunnel junctions were made between the in-situ cleaved Bi2223 (001) surface and an electrochemically etched iridium tip mounted perpendicular to the sample surface. All spectra were obtained at 1.8 K and zero magnetic field with tunnelling resistances ranging between 0.5 and 1 GΩ.

## 6.3 Zero-Field Spectroscopy

### 6.3.1 Tunnel junction characterization

In Fig. 6.3.1a we present a topographic scan showing atomic resolution. We further observe a 26 Å supermodulation along the *b*-axis which is also seen in Bi2201 [143] and Bi2212 [135] where it is attributed to extra oxygen in the BiO planes [144]. In Fig. 6.3.1b we show a typical *IV*-curve and its corresponding differential conductance. The *IV*-characteristic clearly shows a metallic-like background over a large energy range and the existence of a clear *d*-wave gap at the Fermi level. The differential tunnelling conductance presents well-developed coherence peaks at  $\pm\Delta_p \simeq 56$  meV and clear dip-hump structures which appear asymmetrically on both sides of the Fermi level. These features are consistent with Bi2212 [135, 9], where the broad hump observed at negative bias has been related to a van Hove singularity [40].

A true vacuum tunneling junction is indicated by a scaling of the spectra with the tunneling resistance. In constant-current mode, the tunneling resistance  $R_t$  is determined by the tunneling current  $I$  and the bias voltage regulation  $V_t$ ,  $R_t = V_t/I$ . In Fig. 6.3.2a, we show a set of spectra measured at different tunneling resistances, when the spectra are normalized to the corresponding  $R_t$  values (Fig. 6.3.2b), they lie on top of one another which indicates a vacuum tunneling junction. Deviations at negative bias are possibly due

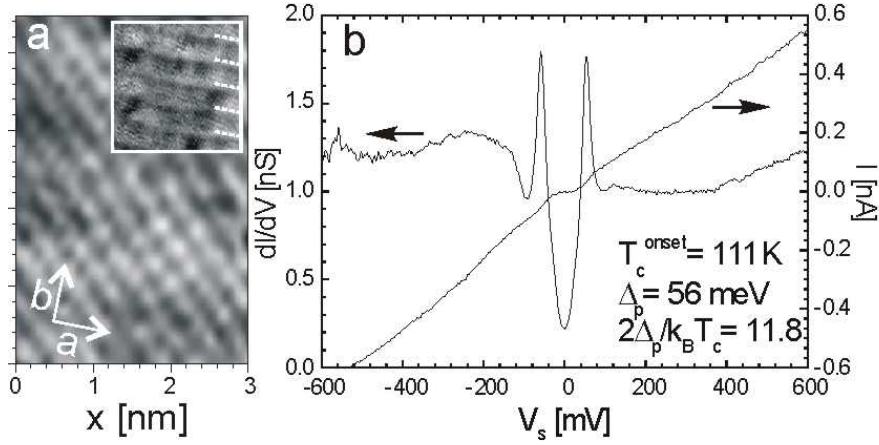


Figure 6.3.1: (a) Topographic image of in-situ cleaved Bi2223 obtained under UHV at 1.8K ( $I=0.8\text{nA}$ ,  $V_s=0.6\text{V}$ ). The  $13 \times 13 \text{ nm}^2$  inset shows the  $26 \text{ \AA}$  supermodulation. (b) Typical  $IV$ -curve and corresponding  $dI/dV$  spectrum acquired on sample  $B$  at 1.8K ( $R_t=1\text{G}\Omega$ ).

to electrostatic effects on the junction which destabilizes it.

In tunneling regime, an exponential dependence of the tunneling current on the tip-sample distance is usually assumed. This assumption allowed us to obtain a simple expression for the tunneling current  $I \propto e^{-2C\sqrt{\Phi_A}z}$ . In this way, the apparent barrier height  $\Phi_A$  can be directly determined from the tunnel current dependence on the vertical tip position. More precisely, the apparent barrier height  $\Phi_A$  is [69]

$$\Phi_A(\text{eV}) = 0.952 \left[ \frac{d \ln I}{dz(\text{\AA})} \right]^2. \quad (6.3.1)$$

where  $\Phi_A$  is obtained in eV when the  $z$  displacement is measured in  $\text{\AA}$ . In Fig. 6.3.3, we show the tunneling current variation (full lines) with the tip-sample distance measured in constant-current mode. By performing an exponential fit, we obtain an apparent barrier height  $\Phi_A = 4.44 \text{ eV}$ . However, we observe that this value changes with the tunnel current resistance and thereby with the initial tip position. By changing the tunnel resistance from 0.66 to 2  $\text{G}\Omega$  we determine a mean barrier height  $\bar{\Phi}_A = 4.00 \pm 0.5 \text{ eV}$ . This allows us to safely conclude that in the typical regulation voltage used  $V_t \leq 0.6 \text{ V}$ , we are in the tunneling regime since  $V_t \ll \Phi_A$ .

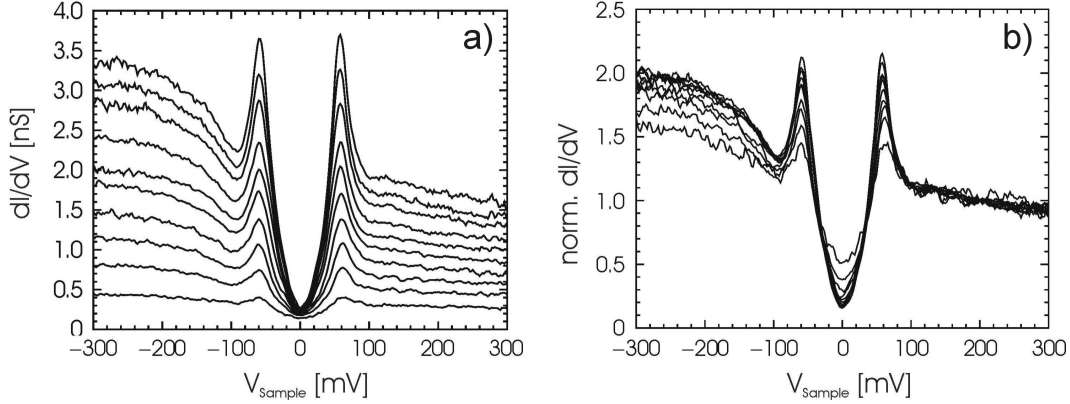


Figure 6.3.2: (a) 10 spectra measured in constant current mode at different tunnel resistances  $R_t$ , taken by varying the regulation tunnel current  $I$  between 0.1 and 1 nA,  $V_t=0.6$ V. (b) Same spectra as (a) but normalized to  $R_t$ . The spectra were acquired in sample B.

### 6.3.2 Correlation between transition widths and inhomogeneity

The power of STS lies in the ability to investigate the spatial dependence of the LDOS. Recently, much attention has been paid to the question of whether the electronic structure of high- $T_c$  cuprates is intrinsically inhomogeneous at the nanometer scale [107] or if long range homogeneity of the spectral signature can be obtained. In fact, for overdoped Bi2212 it has been demonstrated that an appropriate crystal preparation yields homogeneous samples [121]. A necessary, however not exclusive, criterium for sample homogeneity is a sharp superconducting transition width  $\Delta T/T_c < 1\%$  in susceptibility measurements. Narrower transition widths are obtained by annealing the as-grown samples. In the annealing process the temperature is usually set to  $500^\circ\text{C}$  and the oxygen partial pressure is varied. Indeed, the critical temperature in Bi2223 system can be tuned by controlling the oxygen pressure in the annealing atmosphere. In this way, the critical temperature in Bi2223 can be easily varied between 104 and 111 K which represents small changes. Indeed, under the same annealing conditions the parent compound Bi2212 presents  $T_c$  variations of several tenths of degrees.

In this section, we present STS measurements performed in samples *A*, *B* and *C* annealed at  $500^\circ\text{C}$  and at 100, 20 and 0.001 bar of oxygen pressure respectively [145]. In Fig. 6.3.4 we compare traces of equidistant spectra acquired along a line on the surfaces of sample *A*, *B* and *C* respectively. As anticipated by the sharp transition width  $\Delta T/T_c = 0.9\%$ , sample *A* shows an extremely high homogeneity, as demonstrated by the gap distribution in Fig. 6.3.5a: the standard deviation  $\sigma$  is of only 3 meV for a mean gap  $\bar{\Delta}_p = 60$  meV. In contrast, sample *B*, with  $\Delta T/T_c = 1.5\%$ , shows a much broader distribution  $\sigma = 7$  meV and  $\bar{\Delta}_p = 45$  meV. Finally, sample *C* with  $\Delta T/T_c = 2.4\%$ , shows a gap distribution  $\sigma = 13$  for a mean gap  $\bar{\Delta}_p = 76$ . This behavior is consistent with the empirical criterium mentioned above and demonstrates that homogeneity can be

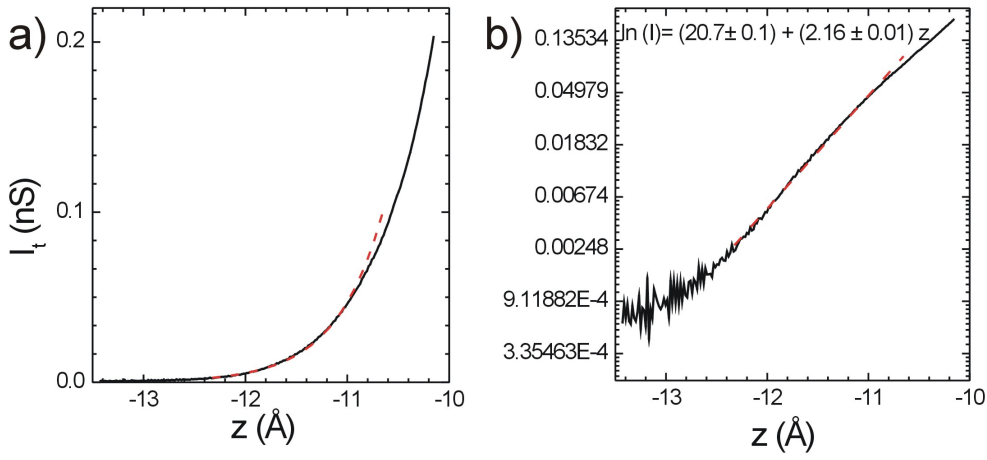


Figure 6.3.3: (a) Tunnel current  $I$  dependence on the vertical tip position  $z$ . (b) Natural logarithmic scale of the tunnel current vs. the  $z$  displacement of the tip showing the exponential behavior. The dashed line corresponds to a linear fit  $\ln(I_t) = I_0 + \kappa z$  giving an apparent barrier height  $\Phi_A = 4.4$  eV. ( $V_t = 0.6$  V,  $I = 0.3$  nA)

obtained on Bi2223 over a range of at least 50 nm. Note the spatial reproducibility of the background conductance outside the peak-dip-hump structure for both traces, which is characteristic for a stable vacuum tunnelling junction.

Fig. 6.3.5 indicates that a correlation exists between the gap dispersion and the superconducting transition width which indicates that the transition width could be a good parameter to identify more homogeneous samples. Although, the observed increasing of the gap dispersion for the three samples could not only be due to the increase of the transition widths, but also due to a different doping concentration, where its effect could be ruled out by studying the correlation between the gap distribution and the transition widths keeping constant the doping concentration. This indicates that in future work, a systematic study of the interplay between the doping, the oxygen distribution and the local variations of the spectra would allow to determine if a non-uniform spatial distribution of the oxygen is the principal cause for the spectral inhomogeneities.

### 6.3.3 Doping evolution of the spectra

The doping relation  $T_c(p)$  of Bi2223 has not been established yet. However, various observations point out that  $T_c(p)$  could deviate from the generic dome shaped relation by Presland *et al.* [6]. Indeed, the doping dependence has been studied by other methods suggesting a large plateau with  $T_c = T_{c,max}$  in the overdoped phase [146, 147]. Furthermore, it has been found that the  $T_c$  of Bi2223 is far less sensitive to oxygen doping than

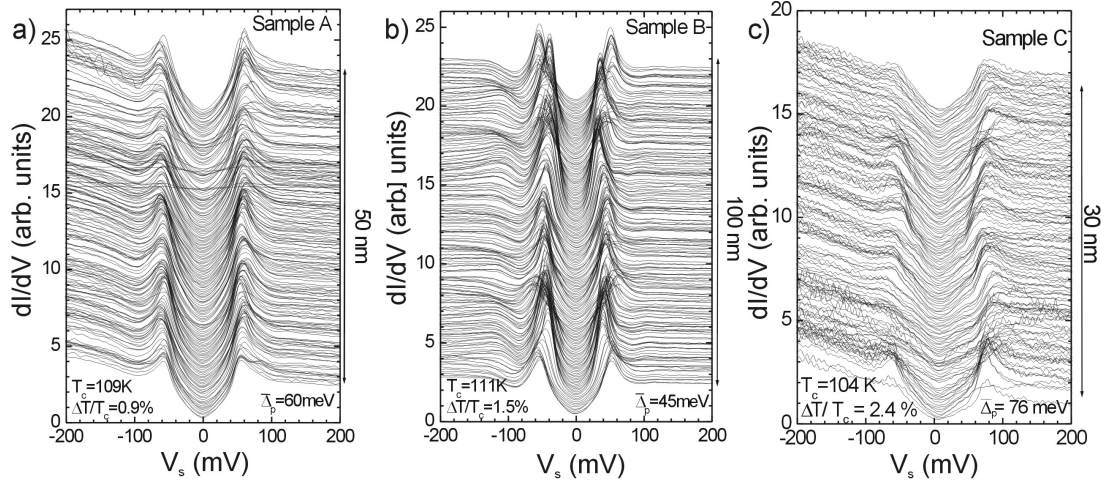


Figure 6.3.4: (a) Trace of 201 spectra along 50nm line on sample *A* at 1.8K ( $I=0.6$ nA,  $V_t=0.3$ V). (b) Trace of 201 spectra along 100nm line on sample *B* at 1.8K ( $I=0.6$ nA,  $V_t=0.6$ V). (c) Trace of 151 spectra along 30nm line on sample *C* at 1.8K ( $I=0.6$ nA,  $V_t=0.6$ V).

the corresponding one for Bi2212 since upon post-annealing only small variations of  $T_c$  are achieved, even with high oxygen pressure treatments [146]. In that respect it is striking that for a variation of only 2% of  $T_c$  we observe a gap variation of about 28% between sample *A* and *B*.

Two observations allow us to tentatively assign sample *A*, *B* and *C* as being underdoped, optimally doped and strongly underdoped, respectively. First, the gap magnitude is larger in sample *A* than in *B*. Assuming that the gap falls monotonically with increasing doping, as established for Bi2212 [98, 148] and suggested for Bi2223 by *c*-axis conductance experiments [147], this indicates that sample *A* has a lower hole content than *B*. Second, for sample *B* we have  $T_c = T_{c,max}$ , which is characteristic for optimally or possibly overdoped samples [146].

This conclusion is corroborated by a careful comparison of the background conductance in Bi2212 and Bi2223 spectra. Various tunneling experiments on Bi2212 revealed that the background conductance outside the gap is asymmetric and varies with doping [98, 9], the strongest effect occurring below the Fermi level. The background slope  $\alpha$ , taken reasonably far from the Fermi level and the dip-hump structure ( $V_s \simeq -200$  meV), is positive for overdoped samples, about zero for optimal doping and negative for the underdoped case as illustrated in the top panel of Fig. 6.3.6. In Bi2212, this observation could be due to a broad van Hove singularity at negative bias that shifts away from the Fermi level as *p* decreases [40] or possibly the increase of strong correlation effects with underdoping [12, 11, 10]. In the lower panel of Fig. 6.3.6 we show the average spec-

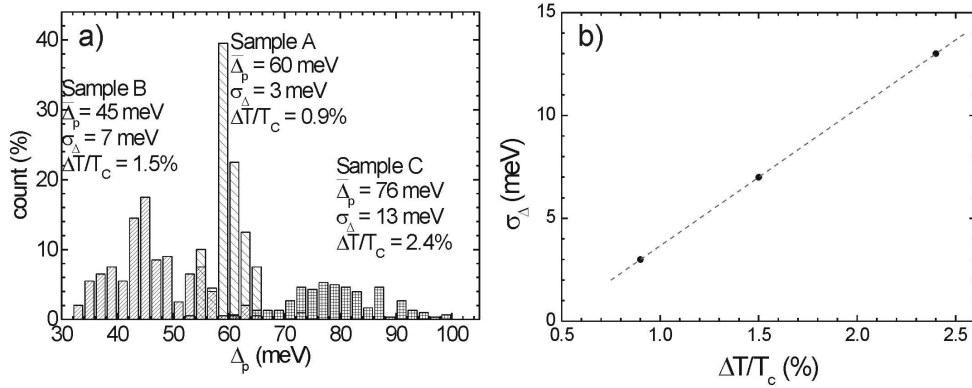


Figure 6.3.5: a) Gap distributions in samples *A*, *B* and *C*. b) Correlation between the gap dispersion  $\sigma_{\Delta}$  and transition width  $\Delta T/T_c$ .

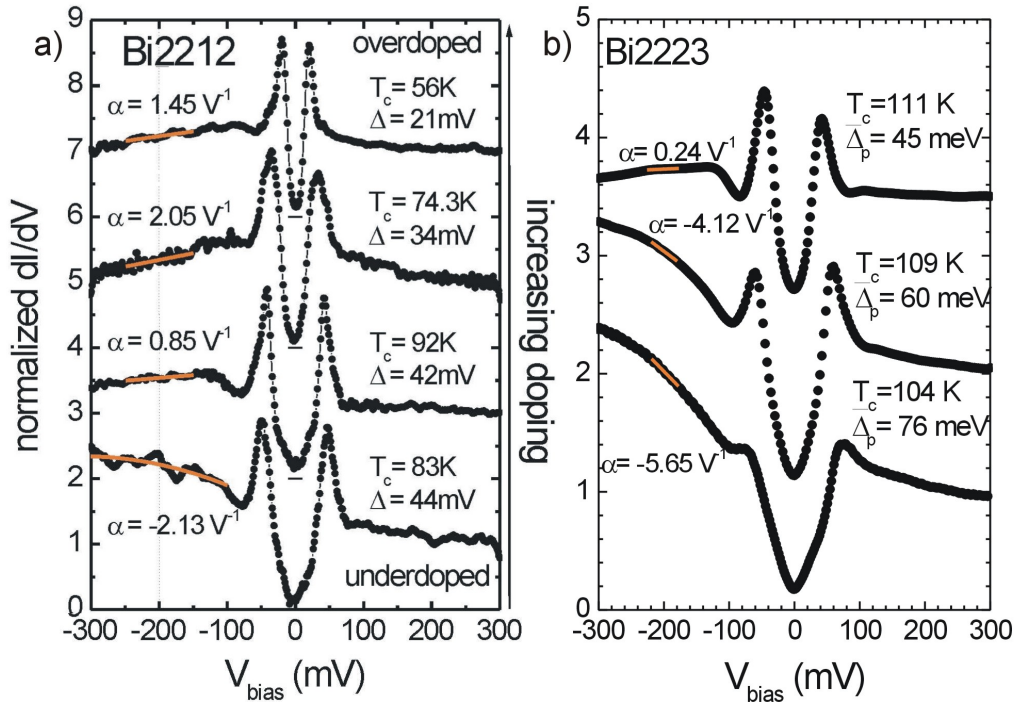


Figure 6.3.6: Comparison of the LDOS doping dependence in Bi2212 (Ref. [98]) and Bi2223. All spectra have been normalized to the background conductance at  $V_s=300\text{meV}$  and shifted vertically for clarity.  $\alpha$  is the slope of the background fit at  $V_s=-200\text{meV}$ . The Bi2223 panel shows the average spectra from Fig. 6.3.4.

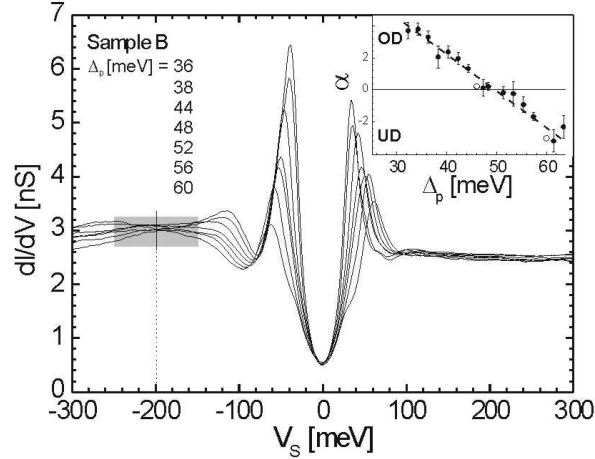


Figure 6.3.7: Average spectra corresponding to energy intervals of the gap distribution of sample *B* (see Fig. 6.3.5). The shaded energy interval indicates where the background has been linearly fitted to determine the slope  $\alpha$ . The inset shows the relation between the background slope at  $V_s = -200$  meV and  $\Delta_p$ . Open symbols correspond to the average spectra shown in the bottom of Fig. 6.3.6. Not all the average spectra obtained are shown for figure clarity.

tra of the traces on sample *A*, *B* and *C*. Focusing on the background slope at negative bias shows a striking similarity between underdoped Bi2212 and samples *A* and *C*, and respectively between optimally doped Bi2212 and sample *B*.

We now turn to the analysis of the LDOS variations observed along the trace of sample *B*. Fig. 6.3.7 displays the average spectra corresponding to the energy intervals of the gap distribution shown in Fig. 6.3.5. The systematic decrease of the coherence peak intensity with increasing gap magnitude and the corresponding dip-hump shift, are strikingly similar to what is observed in Bi2212 when reducing the doping [149, 21]. Furthermore, for each spectrum we again determined the slope  $\alpha$  at -200 meV which appears to depend linearly on the gap magnitude (see Fig. 6.3.7 inset). In addition the sign change of the slope occurs at what is believed to be optimal doping. With the tentative background versus doping relation discussed above, it is therefore possible to interpret the spatially varying LDOS in less homogeneous samples as being related to a local variation of doping, as reported in Bi2212 [106].

In summary, we have shown the first STS study on Bi2223 single crystals. Atomic resolution as well as the characteristic supermodulation have been observed. One sample with a transition width of only  $\Delta T/T_c = 0.9\%$  exhibits an extremely homogeneous LDOS. The LDOS features, i.e. the *d*-wave spectral shape, strong coherence peaks and the existence of a dip-hump structure, as well as the various LDOS on the surface of a less ho-

homogeneous sample, show striking similarity with Bi2212. Using the doping dependence of the gap and background conductance in Bi2212 as a template, we made a qualitative estimate of the doping level in our samples. We further observed a linear dependence and sign change of the slope of the background as a function of the gap magnitude.

## 6.4 Nanoscale variations of the spectra

Usually, microscopic spectral variations are observed in the parent compound Bi2212. The existence of such variations in Bi2223 can already be observed in the spectral traces shown in Fig. 6.3.5. In this section we discuss the spectral variations observed in a very inhomogeneous sample of Bi2223.

The sample was grown by the travelling solvent flux zone method by Alexandre Piriou and Enrico Giannini [150]. The as-grown sample was annealed at 500°C in vacuum  $P = 10^{-6}$  bar, resulting in a non-superconducting sample. The same sample is then annealed again at 500°C and 400 bar of oxygen partial pressure, giving a superconducting transition  $T_c = 108$  K [145]. It was initially believed that this procedure should yield more homogeneous samples, however this is not always the case. Furthermore, this sample yields a non-uniform gap distribution with a standard deviation  $\sigma \sim 10$  meV.

In Fig. 6.4.1a, we show the spatial variations of the gap in a  $16 \times 16$  nm<sup>2</sup> region. The gap magnitude  $\Delta_p$  at each position was determined from the maximum value of the tunnel conductance at negative bias  $\Delta_p^-$  and positive bias  $\Delta_p^+$  between  $\pm 120$  mV:  $\Delta_p = (\Delta_p^+ - \Delta_p^-)/2$ . The lowest gap value observed is 50 meV. For gap values bigger than  $\sim 80$  meV the spectra do not present well-developed peaks at both bias polarizations, which makes it difficult to determine the gap. The spectra with gap values larger than 100 meV are shown as black regions in Fig. 6.4.1a. We have selected five typical spectra from Fig. 6.4.1a, numbered from 1 to 5, in order to display a characteristic spectrum from different regions with similar gap amplitude. The corresponding spectra are shown in Fig. 6.4.1b. This figure shows that as the gap increases, the height of the coherence peaks decreases being their width almost constant. For the spectra with gap values bigger than  $\sim 80$  meV, no clear coherence peaks can be determined at both bias polarities. Such spectra are measured near dark regions. As an example, the spectrum measured near the position numbered by 1 in Fig. 6.4.1a is shown in Fig. 6.4.1b. We observe that it only presents a positive coherence peak at 90 mV, with the negative coherence peak suppressed. Similar spectra have been observed in Bi2212 where they were attributed to the existence of pseudogap regions below  $T_c$ , associated with a low doping concentration in these areas. Thus, we tentatively associate the dark regions of Fig. 6.4.1a with the pseudogap, although pseudogap spectra above  $T_c$  have not yet been measured in this material.

The spectrum associated to the pseudogap regions present a kink only at positive bias voltage. The kink is found at  $\sim 30$  meV for the spectra with a peak at  $\sim 90$  meV. In

Bi2212, a kink has been also seen at  $\sim 22$  meV in a spectrum with coherence peaks at  $\pm 50$  meV. Up to now, it is not clear which is the origin of the kink. It could be related to the localized states in the vortex cores, however further studies are needed to clarify this.

In Bi2212, a spatial anti-correlation between the gap amplitude and the height of the coherence peaks has been observed. In the case of Bi2223, Fig. 6.4.1b already indicates that a similar behavior exists. In order to better study this, we compare the spatial variation of the gap magnitude with the corresponding peak height. Fig. 6.4.1c shows the energy position of the coherence peak at positive bias  $\Delta_p^+$  and Fig. 6.4.1d displays the spatial variation of the conductance intensity at this energy  $dI/dV(\Delta_p^+)$ . By comparing Figs 6.4.1b and c, we conclude that an anti-correlation between these two magnitudes also exists in Bi2223. Regions with small gap values correspond to regions with high coherence peaks and viceversa.

The existence of regions where the negative coherence peak is suppressed can affect the statistical analysis of the gap distribution. The statistical distribution of the gap at positive  $\Delta_p^+$  and negative bias  $\Delta_p^-$  is shown in Fig. 6.4.1e. The distribution at negative bias presents a large number of counts at 100 meV due to the absence of negative coherence peaks in the spectra for gap values around this energy. When negative coherence peaks do not exist, the maximum of the tunnel conductance at negative energy  $\Delta_p^-$  was set to  $-95$  meV giving an increase in the statistical count. The spectra with no negative coherence peaks have been associated with pseudogap-like spectra and we thus attribute this peak to the existence of pseudogap regions. Each distribution was fitted using a Gaussian function. At positive bias the Gaussian is centered at  $\bar{\Delta}_p^+ = 82$  meV with standard deviation  $\sigma_{\Delta}^+ = 12$  meV; at negative bias it yields a mean gap  $\bar{\Delta}_p^- = -74$  meV with standard deviation  $\sigma_{\Delta}^- = 12$  meV. This gives a mean gap  $\bar{\Delta}_p = 78$  meV.

In order to observe how the gap varies along a spectral trace, we present in 6.4.1f, a spectral trace along 100 nm represented as a color-coded image. Well developed coherence peaks are displayed as bright areas around  $\pm 50$  mV. We observe that their energy position varies along the trace being this energy variation consistent with the dispersion of the gap observed in the gap map. Finally, we observe that the tunnel conductance is uniform around  $\pm 200$  mV, which is characteristic of a vacuum tunnel junction.

In this section, we have measured a particular inhomogeneous Bi2223 sample in order to study the trends in the Bi2223 spectra. In the studied area, superconducting spectra with well developed peaks have been observed together with spectra presenting only a peak at positive bias. The regions presenting the last kind of spectra have been tentatively assigned to pseudogap regions. These spectra also shows a kink only at positive bias voltages. Finally, a statistical analysis allows us to assign a mean gap  $\bar{\Delta}_p = 78$  meV to this area.

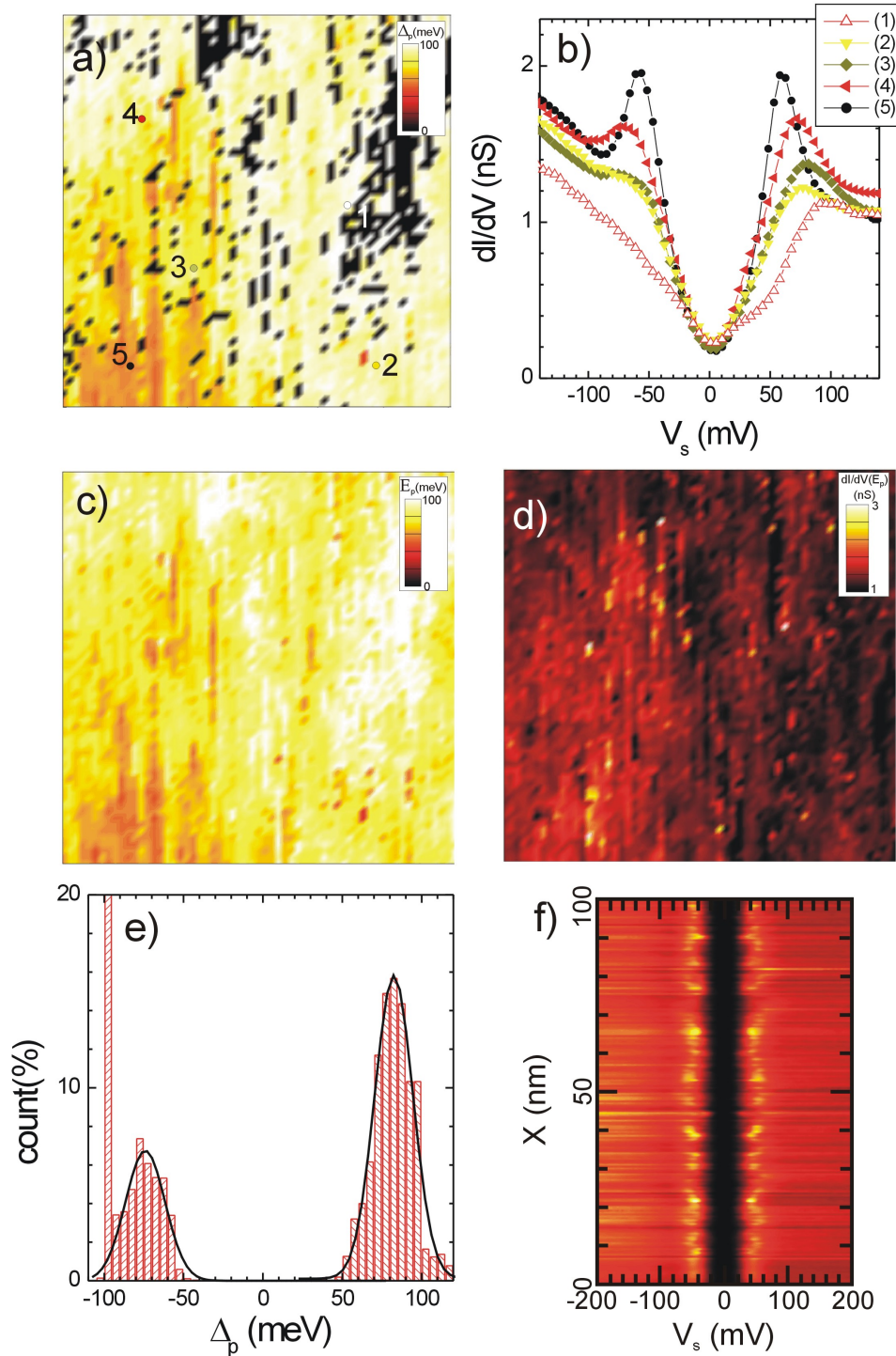


Figure 6.4.1: (a)  $16 \times 16 \text{ nm}^2$  gap map in Bi2223, the gap magnitudes bigger than 100 meV has been set to 0 meV giving the dark areas. (b) Different spectra taken in the numbered regions of a). (c) Positive peak position  $\Delta_p^+$  spatial distribution. (d) Spatial variation of the tunnel conductance at the positive peak position  $dI/dV(\Delta_p^+)$ . (e) Gap statistics of the region shown in a). (f) Spectral trace along 100 nm of 201 spectra. The tunnel conditions are  $V_t = 0.6 \text{ V}$ ,  $I = 0.6 \text{ nA}$ .

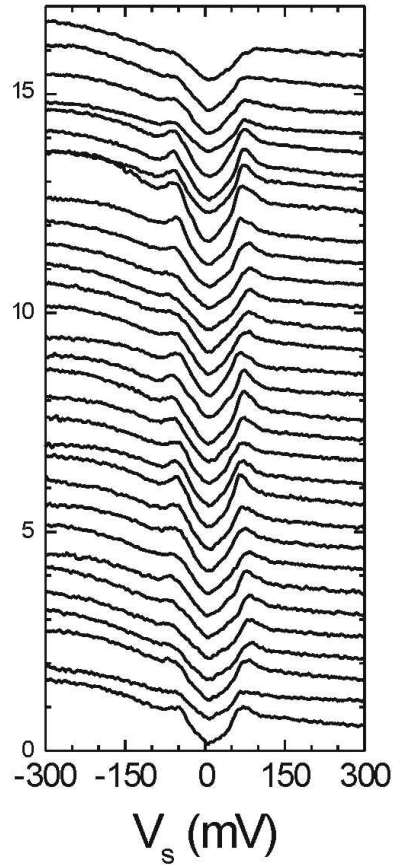


Figure 6.5.1: Tunneling spectra measured every 2 nm along a 60 nm path at 2 K, 6T and  $R_t = 1 \text{ G}\Omega$ . The spectra are displaced vertically as a function of scan distance for clarity.

## 6.5 Tunneling spectra in a magnetic field

We have not imaged the vortex lattice by spatially resolved tunneling spectroscopy on  $\text{Bi}_2\text{Sr}_2\text{Ca}_2\text{Cu}_3\text{O}_{10+\delta}$  in the mixed state. Consequently, we could not probe the core states and the associated spatial modulations. The large spatial variations of the spectra and the small vortex core size ( $\xi \sim 1 \text{ nm}$ ) are among the reasons for this failure. More homogeneous samples of this material suitable for vortex core spectroscopy are needed in this material and current efforts are concentrated on improving sample homogeneity.

The spectra measured in a magnetic field exhibit the same features as those measured in the Meissner state. A spectral trace measured under a field  $H = 6T$  is shown in 6.5.1. It presents a constant conductance background beyond  $\pm 150 \text{ mV}$  consistent with a vacuum tunneling junction. The spectra have a  $V$ -shape near zero bias with coherence peaks at  $\Delta_p \simeq \pm 60 \text{ meV}$ .

To conclude, microscopic variations of the spectra have been observed. In particular regions with "pseudogap"-like spectra have been identified. Similar phenomena have been previously observed in underdoped Bi2212 samples. The vortex core lattice has not been successfully imaged possibly due to LDOS inhomogeneities in the samples. No difference was observed between the tunneling spectra measured in zero magnetic field and at 6T. In the future, tunneling spectroscopy studies under magnetic field in Bi2223 will be important since in Bi2212 the vortex core states are linked to a fourfold modulation.



# Chapter 7

## Spectral Form

A statistical analysis of the spectra measured in  $\text{Bi}_2\text{Sr}_2\text{CaCu}_2\text{O}_{8+\delta}$  (Bi2212) and  $\text{Bi}_2\text{Sr}_2\text{Ca}_2\text{Cu}_3\text{O}_{10+\delta}$  (Bi2223) allows us to discuss their similarities and differences. Based on this analysis, reproducible spectral characteristics of spectra with same gap values are obtained. We also discuss the evolution in the form of the spectra when the gap increases. In particular, we find out a linear decrease of the background slope  $\alpha$  and the energy position of the dip relative to the gap  $E_{dip} - \Delta_p$  with  $\Delta_p$ . Finally, a spectrum of Bi2223 with  $\Delta_p = 45$  meV present similar spectral characteristics to a spectrum of Bi2212 with  $\Delta_p = 36$  meV.

### 7.1 Form of the spectra in $\text{Bi}_2\text{Sr}_2\text{CaCu}_2\text{O}_{8+\delta}$

We present tunneling spectroscopy measurements performed in  $\text{Bi}_2\text{Sr}_2\text{CaCu}_2\text{O}_{8+\delta}$  (Bi2212) single crystals from two different sources. A sample coded "MPB0" was grown by melting zone method [151]. The as-grown sample was annealed at  $500^\circ$  in a 15 bar oxygen overpressure atmosphere yielding a superconducting transition  $T_c = 85$  K. The coded samples "PP" were grown by travelling solvent flux zone method [152]. The as-grown samples were annealed at  $500^\circ\text{C}$  at 15 bar oxygen atmosphere. The two samples "PP1C" and "PP3B" have similar critical temperatures  $T_c = 79$  and  $78$  K, respectively. Therefore, samples from the same source when they are annealed under the same conditions yield similar critical temperatures.

These samples were cleaved at room temperature in ultra-high vacuum conditions. The low temperature STM measurements (2 K) were performed between the (001) surface and an Ir tip. These measurements were performed in collaboration with Yanina Fasano.

Fig. 7.1.1 shows spectral traces measured in these three samples: MPB0, PP1C and PP3B. A reproducible background conductance beyond  $\pm 150$  mV indicates a vacuum tunneling junction between the (001) surface and the Ir tip. This is confirmed by the

scaling of the tunneling spectra with the tunnel resistance  $R_t$ . The traces were taken along distances that varied between 10 and 50 nm. A statistical analysis of the traces yields the following mean gap values:  $\overline{\Delta}_p = 52, 36$  and  $46$  meV with respective standard deviations  $\sigma = 9, 7$  and  $11$  meV for the samples with  $T_c = 85, 79$  and  $78$  K, respectively. We first observed there is not a direct correspondence between the mean gap  $\overline{\Delta}_p$  and the critical temperature  $T_c$ . Furthermore, the standard deviation of the gap  $\sigma$  is not related to the transition width  $\Delta T_c$  as it was previously reported in Bi2223. A local doping concentration different from the rest of the sample could explain these discrepancies, may be due to their different quality.

Each spectral trace presents a distribution of superconducting gaps. In order to average out small variations of the local tunnel conductance, a mean tunnel conductance was obtained by averaging the spectra presenting similar gap amplitudes:

$$\left(\frac{dI}{dV}\right)_{\Delta_p} = \frac{1}{N} \sum_{\Delta=\Delta_p-\epsilon}^{\Delta_p+\epsilon} \left(\frac{dI}{dV}\right)_{\Delta},$$

where  $N$  is the number of spectra averaged between the interval  $\Delta_p - \epsilon$  and  $\Delta_p + \epsilon$ . Since we are interested in the most robust features of the averaged tunneling spectra, we only consider mean spectra with  $N \geq 10$ . The resulting averaged spectra are plotted in Figs 7.1.1 ((d), (e) and (f) with respective energy intervals  $\epsilon = 4, 2$  and  $4$  mV, corresponding to samples MPB0, PP1C and PP3B, respectively.

All averaged spectra present an asymmetric background conductance at  $|V_s| > 150$  mV which increases with the gap ( $\Delta_p$ ). They present a dip between 80 and 100 mV which is much more pronounce at negative bias voltage. At positive bias, the dip fades away with  $\Delta_p$ . Also, the coherence peak height decreases with  $\Delta_p$ . The spectra with gap values lower than 40 meV have coherence peaks at positive energy lower than the corresponding one at negative energy. Their asymmetry decreases as the gap increases, being rather symmetric around 45 meV. As the gap increases above  $\sim 55$  meV, the coherence peak at negative energy becomes lower than at positive energy. This trend is opposite to the increase of the background conductance with  $\Delta_p$ . Around the zero bias, the spectra present a  $V$ -shape with very little spectral variations.

By averaging the spectra that present similar gap values, we presume that the physical parameter which determines the gap, also determines the overall form of the spectra. In order to verify this, we show in Fig. 7.1.2 all the selected spectra which were averaged to obtain the mean spectra with  $\Delta_p = 36$  meV. In the case of the spectral trace measured in the MPB0 sample, the selected spectra have the same tunneling conductance at energies  $|E| > 100$  meV and  $|E| < 20$  meV. They present a dip feature located around 76 mV with similar asymmetries of the coherence peaks, albeit their peak height varies from one to another spectra. Regarding samples PP1C and PP3B, bigger spectral variations are observed on the spectral traces (Figs. 7.1.2a and (b), respetively). In particular, the background conductance varies significantly in some spectra and the coherence peaks usually present several peaks. However, they also present similarities; the dip feature is

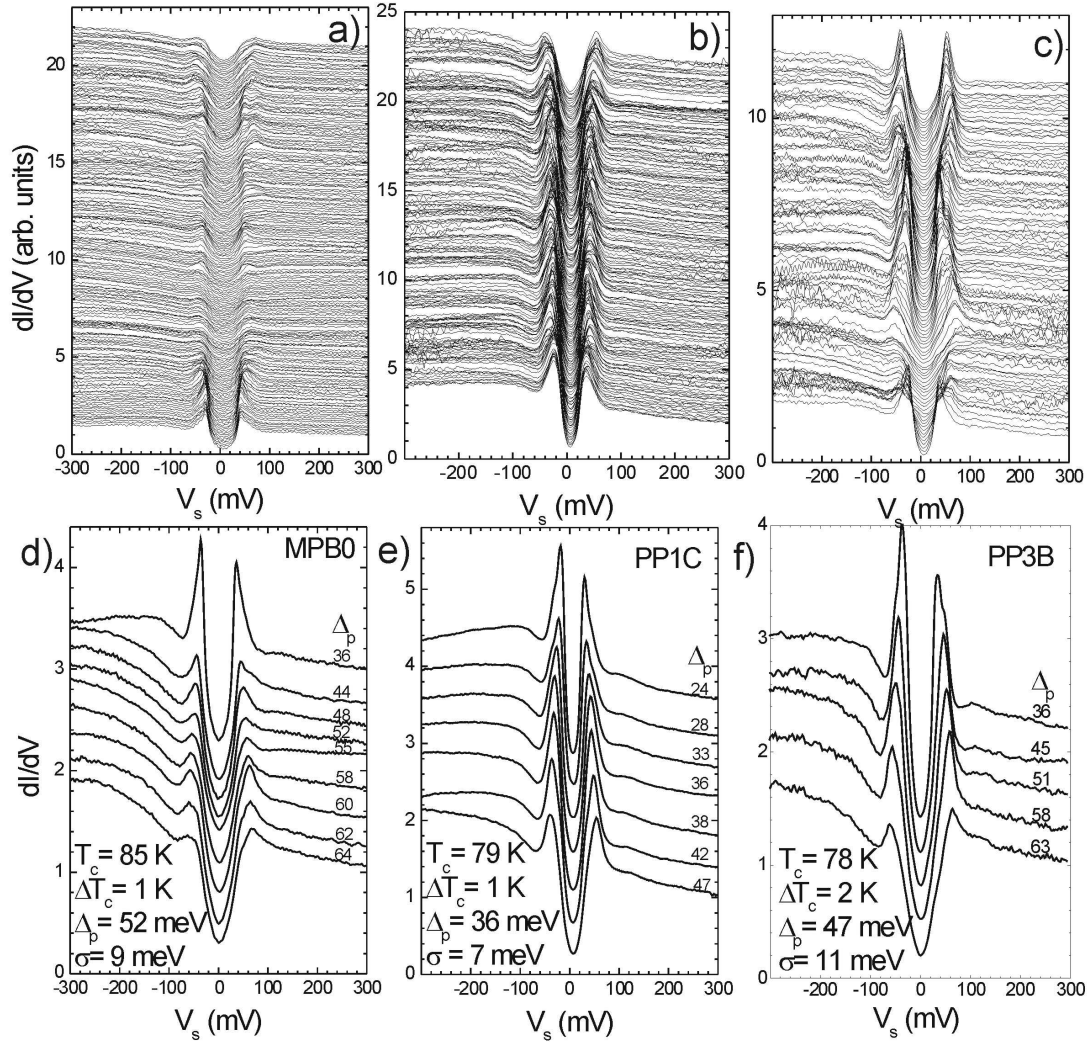


Figure 7.1.1: (a) 201 spectra taken along 20 nm on MPB0 sample.  $I = 0.6$  nA,  $V_t = 0.6$  V. (b) 201 spectra taken along 50 nm on PP1C sample.  $I = 0.6$  nA,  $V_t = 0.6$  V. (c) 101 spectra taken along 10 nm on PP3B sample.  $I = 0.6$  nA,  $V_t = 0.6$  V. (d), (e) and (f) Averaged spectra with different gap values from the spectral traces shown in (a), (b) and (c), respectively. The spectra are vertically displaced for clarity.

located at a similar energy in all spectra obtained from the same spectral trace, being at 68 and 76 mV for the corresponding traces taken on PP1C and PP3B samples.

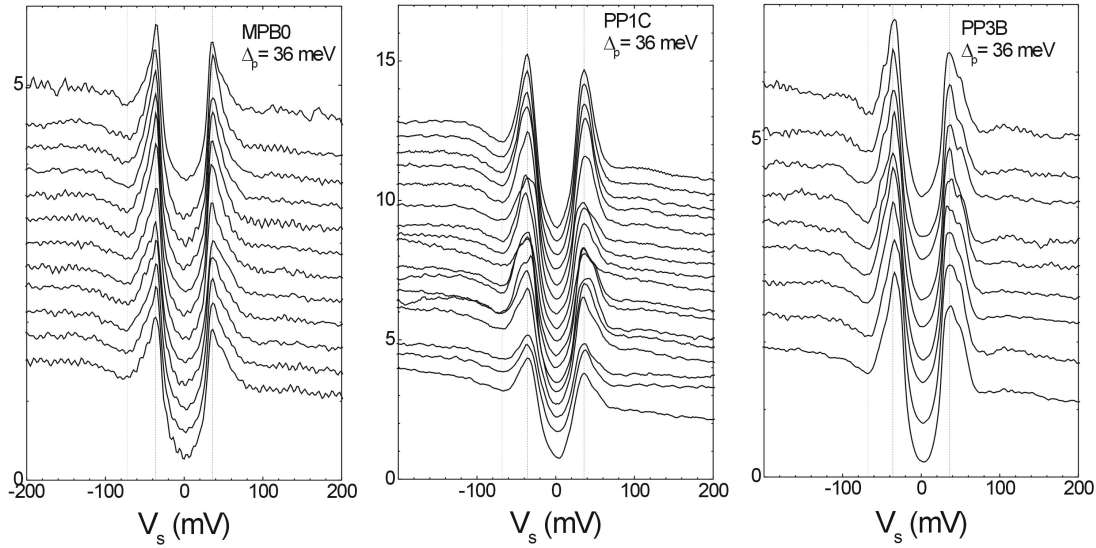


Figure 7.1.2: (a), (b) and (c) present selected spectra obtain from the traces shown in Fig. 7.1.1a, b and c, respectively. The selected spectra have a gap magnitude  $\Delta_p \simeq 36$  meV and they are vertically displaced for clarity.

The mean spectra with  $\Delta_p = 36$  meV are shown in Fig. 7.1.3. In order to compare them, the spectra were normalized to give a tunneling conductance around 1 at  $V_s = 300$  mV. We observe that they do not fall into one universal spectrum, however they present similar spectral characteristics. They all have a  $V$ -shape behavior near zero bias with asymmetric coherence peaks being the positive energy peak lower than the corresponding one at negative energy. The dips are clearly seen at negative bias and they have similar energy positions and depths. The slope  $\alpha$  of the conductance at  $V_s = -200$  mV is  $\sim 0$ . The differences in these spectra could be attributed to different background conductances which clearly affects more the occupied states than the empty states. This could be possibly due to strong correlation effects [12, 11, 10] which are different for different samples and it shows that the background is not only determined by the same parameter that controls the gap.

It was reported that the gap magnitude decreases linearly with doping (see section 5.3). Thus, the physical parameter that produces the local variations of the gap is most probably the local doping concentration. Therefore, by selecting all spectra with a similar gap, we are choosing the spectra with similar doping concentrations. Besides the gap variations, the background also changes with doping. In particular, the background slope  $\alpha$  changes sign at optimal doping. Thus, a linear dependence of  $\alpha$  with the gap  $\Delta_p$  is expected if we assume that both parameters are determined by the doping concentration. Fig. 7.1.4a

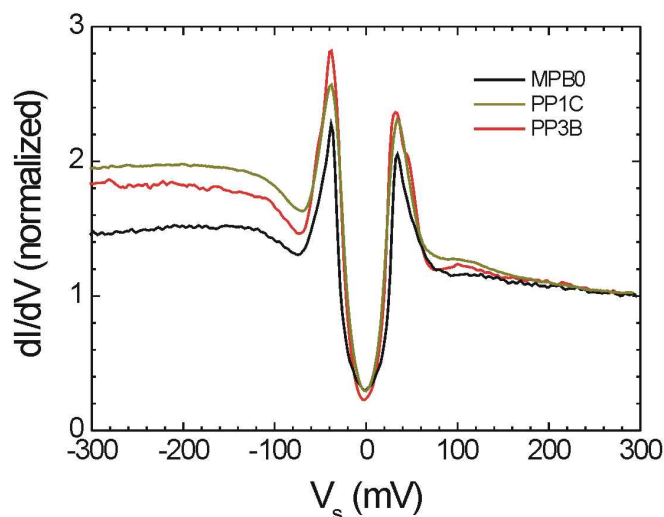


Figure 7.1.3: Averaged spectra with  $\Delta_p = 36$  meV for the different traces MPB0, PP1C and PP3B. The spectra were normalized to give  $dI/dV \sim 1$  at  $V_s = 300$  mV.

plots the background slope as function of  $\Delta_p$ . The background slope was taken at a bias voltage  $V_s \simeq -200$  mV which is reasonably far from the Fermi level and the dip-hump structure. A rather linear relation is obtained between  $\alpha$  and  $\Delta_p$  giving  $\alpha \simeq 0$  for  $\Delta_p \simeq 36$  meV.

In section 2.3.2, we associated the dip feature to a coupling of Bogoliubov quasiparticles with a collective mode. The dip position relative to the gap  $E_{dip} - \Delta_p$  gives an estimate of the collective mode energy which is plotted in Fig. 7.1.4b as a function of the gap. Possible candidates of the collective mode are the 41-meV resonance mode and the  $B_{1g}$  symmetry phonon [80]. The 41-meV resonance mode has been extensively studied with the inelastic neutrons scattering technique (INS). It was deduced that this mode follows  $E_r \sim 5.4k_B T_c$  from INS data: when the gap increases, its energy decreases in the underdoped region and increases in the overdoped region. Fig. 7.1.4b shows that our data are consistent with INS experiments in the underdoped region [37].

Concluding, in this section we have discussed the overall form of the tunneling spectra in the Bi2212 material. We have shown that reproducible spectral information can be extracted from averaged spectra on different samples. In particular, a linear decrease of the background slope and the collective mode with  $\Delta_p$  was observed.

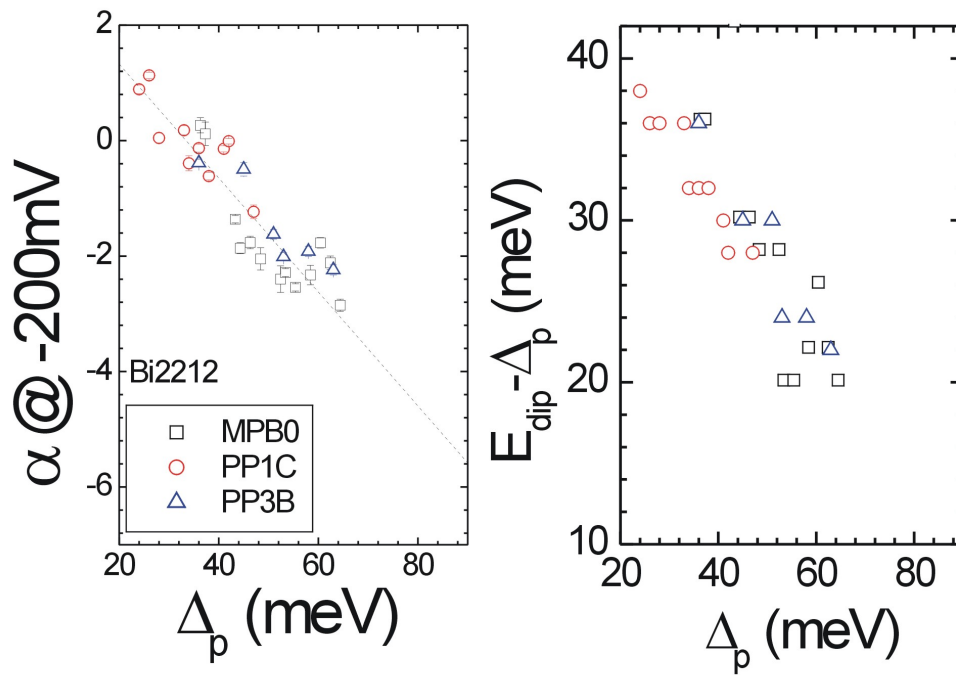


Figure 7.1.4: (a) Background slope  $\alpha$  taken at  $V_s = -200$  mV versus the gap magnitude  $\Delta_p$ . (b) Absolute energy position of the dip feature relative to the gap  $E_{dip} - \Delta_p$  versus the gap  $\Delta_p$ . The values were extracted from all mean spectra shown in Figs 7.1.1 d, e and f. The spectra were normalized to the corresponding tunneling resistance.

## 7.2 Form of the spectra in $\text{Bi}_2\text{Sr}_2\text{Ca}_2\text{Cu}_3\text{O}_{10+\delta}$

In the previous section we have obtained average spectra from different samples in Bi2212. We have shown that reproducible spectral information can be obtained in this way. An analysis of the evolution of the spectral features has given a systematic decrease of the background slope  $\alpha$  and of the estimated collective mode energy  $\Omega_{dip} = E_{dip} - \Delta_p$  with the gap. In order to compare these findings in Bi2212 with possible systematics in Bi2223, we proceed to a similar analysis of the spectral traces taken in the last material. In Fig. 6.3.4, we have shown three spectral traces taken in different samples of the Bi2223 compound. As it was discussed in Section 6.3.3, a different doping concentration was assigned to each sample.

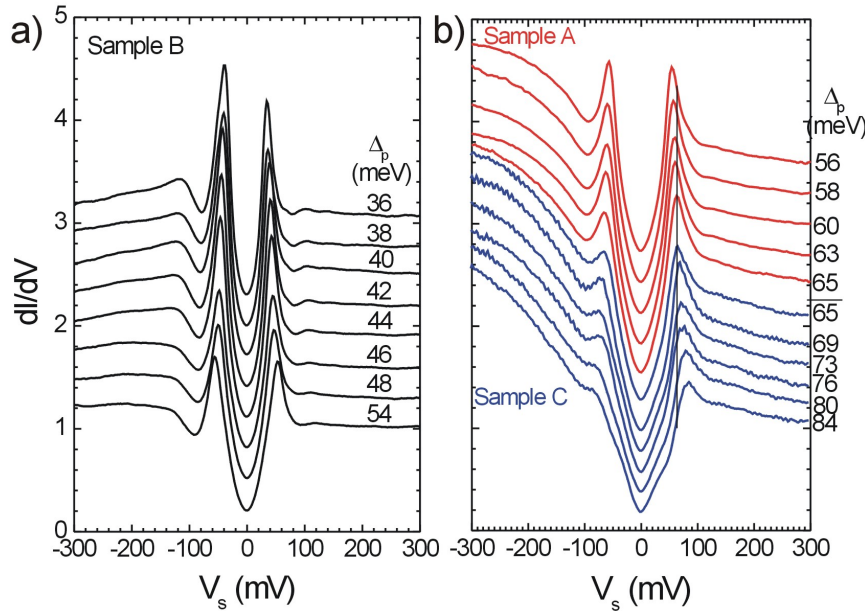


Figure 7.2.1: Mean spectra obtained from the spectral traces in (a) samples B and (b) in samples A and C. The corresponding spectral traces are shown in Fig. 6.3.4. The spectra have been displaced vertically for clarity.

In order to obtain the most robust features, we only consider average spectra where more than 10 conductance curves have been averaged. In Fig. 7.2.1a, we show the so obtained spectra corresponding to sample B (see Fig. 6.3.4b). The same analysis was performed on the spectral traces measured on samples A and C (see Fig. 6.3.4). The resulting averaged spectra are shown in Fig. 7.2.1b. The gap magnitude varies between 36 and 84 meV where a clear  $V$ -shape form of the conductance is observed around zero bias for the spectra with  $\Delta_p \leq 73$  meV. The spectra with gap values bigger than 76 meV present a kink around  $\sim 50$  mV. In Bi2212, the highest gap value reported in literature is

62 meV [21, 70, 153].

In Fig. 7.2.1, we observe a systematic evolution of different spectral features as the gap increases:

- The height of the coherence peaks decreases.
- The width of the coherence peaks seems to be almost constant.
- The asymmetry of the coherence peak height changes. The peak at positive bias is lower than at negative bias for  $\Delta_p < 44$  meV. When the gap is between 44 and 58 meV, both coherence have similar height. Finally, for  $\Delta_p > 58$  meV, the peak at negative bias is lower than the corresponding one at positive bias.
- The depth of the dip at negative bias decreases following apparently the decrease of the coherence peaks height.
- The hump only observed on Fig. 7.2.1a smears out.

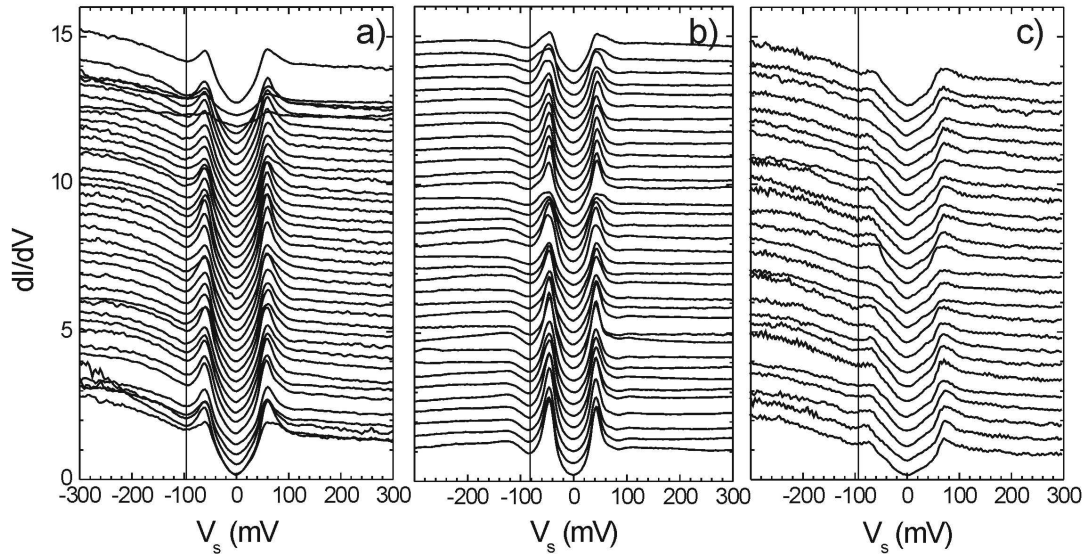


Figure 7.2.2: Spectra used to obtain averaged spectra with  $\Delta_p$  equals to (a) 60 meV, (b) 45 meV and (c) 76 meV corresponding to the respective spectral traces taken on samples A, B and C which are shown in Fig. 6.3.4. The spectra have been displaced vertically for clarity. The line signals the energy position of the dip.

There is an important difference between the spectra on sample B and of samples A and C. The spectra on sample B (see Fig. 7.2.1a) present a different background conductance than the corresponding one for samples A and C (see Fig. 7.2.1b). The background of the

latter is asymmetric with respect to the bias potential, however the former is rather flat. A possible origin for this difference could be different strong-correlations effects [12,11,10]. The asymmetric background conductance shown in Fig. 7.2.1b could hidden the details of the dip-hump structure.

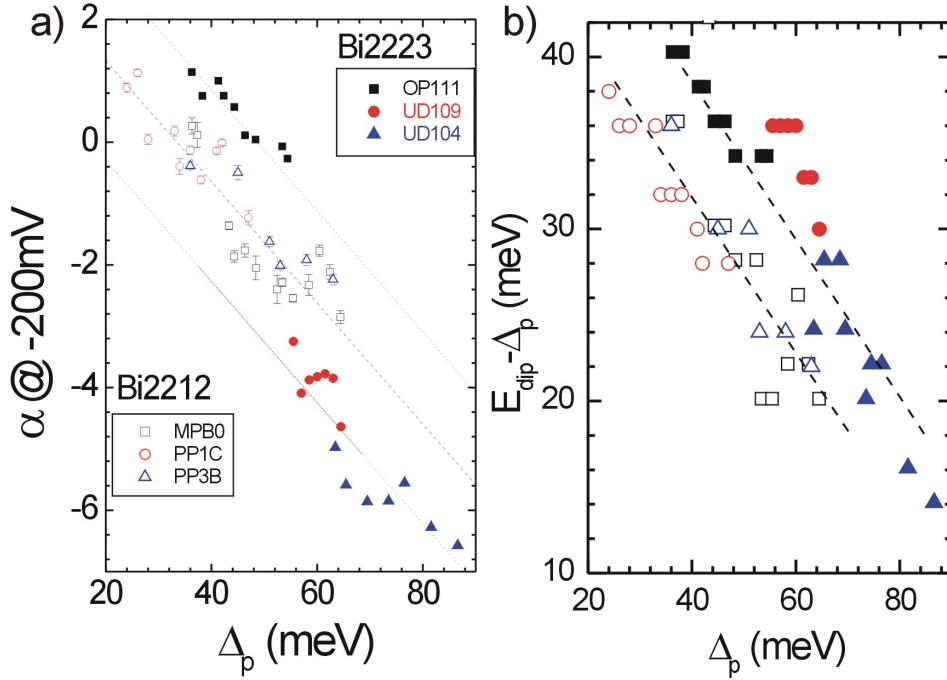


Figure 7.2.3: (a) Background slope  $\alpha$  taken at  $V_s = -200$  mV versus the gap magnitude  $\Delta_p$ . (b) Absolute energy position of the dip feature relative to the gap  $E_{dip} - \Delta_p$  versus the gap  $\Delta_p$ . Closed (open) symbols correspond to the values extracted from all average spectra for Bi2223 (Bi2212) system which are shown in Fig. 7.2.1 (7.1.1). The data coded OP111, UD109 and UD104 were obtained from the spectra measured on samples B, A and C, respectively. Each spectral trace was normalized to give  $dI/dV \simeq 1$  at  $V_s = 300$  mV.

We have described the variations of the form of averaged spectra with different gap magnitudes. We concentrate next on which are the spectral variations of the curves with same gap. In Fig. 7.2.2, we show spectra with same gap values extracted from the respective spectral traces, previously shown in Fig. 6.3.4. These spectra were used to obtain the averaged spectra with  $\Delta_p$  equals to 60, 45 and 76 meV, respectively. We observe that the spectral form is fairly reproducible: the dip position, the peaks asymmetry and the background conductance are almost the same. Big variations are observed in the peak height and on the depth of the dip which should indicate a relation between this two magnitudes. Indeed, the spectra with higher peaks present stronger dip-hump features. Finally, it is

important to remark that all spectra with  $\Delta_p = 76$  meV (see Fig. 7.2.2c) present a kink around 60 mV.

We concentrate next on the evolution with  $\Delta_p$  of a) the background slope  $\alpha$  and b) the energy position of the dip. In Bi2212, the former was related to the doping concentration and the latter to the collective mode energy. These two magnitudes are extracted from the average spectra and are plotted in Fig. 7.2.3. For sample B, we have verified that the values obtained from the average spectra equals the average of the values extracted from each single spectra within the errors. The error of the slope  $\alpha$  was determined to be about  $\pm 0.4$  in general. The energy position of the dip is determined with an error of  $\pm 2$  meV. For comparison purposes, we also plot the corresponding values for Bi2212 system in Fig. 7.2.3.

The fact that samples A and C have a different form of the background than sample B is reflected in Fig. 7.2.3a. In both cases the increase of the asymmetry of the background with the gap gives an approximative linear decrease of the slope  $\alpha$ . However the extrapolated gap value where  $\alpha = 0$  is different for samples A and C than for sample B, being approximatively 18 meV for the former and equal to 44 meV for sample B. A possible explanation for this difference could be that they have a different effective doping concentration.

The energy position of the dip with respect to the gap  $E_{dip} - \Delta_p$  decreases with  $\Delta_p$  giving an estimated value for the collective mode energy about 36 meV when  $\Delta_p \simeq 45$  meV. A similar decrease is observed for the Bi2212 samples where it gives  $E_{dip} - \Delta_p \simeq 36$  meV when  $\Delta_p \simeq 36$  meV. Furthermore, we find that sample B present a similar evolution of these spectral parameters than Bi2212 samples, at least near optimal doping. Indeed, Fig. 7.2.4 shows an averaged spectrum with  $\Delta_p = 36$  meV corresponding to the MPB0 sample and another one with  $\Delta_p = 45$  meV corresponding to the sample B. When the spectra are normalized to give a conductance  $dI/dV \simeq 1$  at  $V_s = 150$  mV, both spectra present similar coherence peaks height with equal peaks asymmetry. Also, the energy position of the dip relative to the coherence peak at negative bias is the same for both spectra, being the dip more profound in Bi2223 than in Bi2212 spectrum.

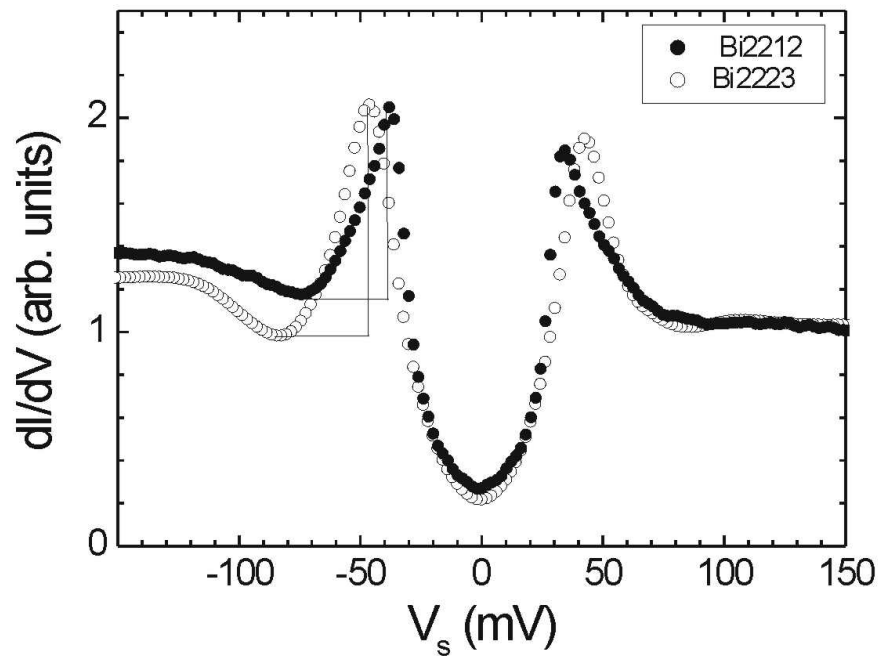


Figure 7.2.4: Averaged spectrum with  $\Delta_p = 36$  meV ( $\Delta_p = 45$  meV) corresponding to sample MPB0 (B) measured on the Bi2212 (Bi2223) system.



# Chapter 8

## Scanning Tunneling Spectra on HTS: The interplay of the gap, the bosonic mode and the van Hove singularity

In two dimensions the non-interacting density of states displays a van Hove singularity (VHS) which introduces an intrinsic electron-hole asymmetry, absent in three dimensions. We show that due to this VHS the strong-coupling analysis of tunneling spectra in high- $T_c$  superconductors must be reconsidered. Based on a microscopic model which reproduces the experimental data with great accuracy, we elucidate the peculiar role played by the VHS in shaping the tunneling spectra, and show that more conventional analysis of strong-coupling effects can lead to severe errors.

### 8.1 Introduction

Scanning tunneling spectroscopy of Bi-based cuprate high- $T_c$  superconductors (HTS) shows a  $d$ -wave gap and a strong dip-hump feature which is nearly always stronger for occupied than for empty states [135]. It has been proposed that the dip-hump structure results from the interaction of electrons with a collective mode [37], but the dip asymmetry has not received an explanation so far. Indeed such a coupling leads to electron-hole symmetric spectra in classical superconductors [28, 29, 30]. The dip-hump was also observed by photoemission, but in those experiments it is not possible to probe the electron-hole asymmetry. Sometimes photoemission spectra are even symmetrized [154], thus ignoring the relevance of the asymmetry seen in tunneling. The fact that in two dimensions the density of states (DOS) has a prominent van Hove singularity (VHS), unlike in 3D, introduces naturally an asymmetry and thereby modifies the strong-coupling analysis and the corresponding determination of the collective mode frequency in an essential way.

Photoemission experiments have provided a detailed account of the band structure in

cuprates [90, 27, 155]. In agreement with early calculations [92], the band crossing the Fermi level presents a saddle point leading to a logarithmic VHS in the DOS. The scanning tunneling microscope (STM) is the ideal tool to look for such singularities, since under suitable conditions it probes directly the DOS with meV resolution [7, 8, 70]. Up to now, however, there has been no report of a direct STM observation of the VHS in HTS materials, neither in the normal nor in the superconducting state. Previous interpretations of the missing VHS invoked the tunneling matrix element: [156, 157] in planar junctions, it is indeed believed that the DOS features in the direction normal to the junction are hidden due to a cancellation with the electron velocity, and that the DOS in the plane of the junction does not show up due to focalization effects [158]. These two mechanisms cannot explain the absence of VHS in *c*-axis STM/HTS tunnel junctions: the HTS materials with a quasi two-dimensional electronic structure have virtually no dispersion in the tunneling direction, and the STM junction, owing to its microscopic size, is qualitatively different from a planar junction and is characterized by a specific matrix element which may not lead to focalization effects [7, 8]. Besides, the ability of the STM to probe DOS singularities was recently demonstrated in carbon nanotubes [159].

The solution to this puzzle lies in the coupling to collective modes. Apart from inducing the dip feature [38, 9], this coupling was also shown to effectively suppress the VHS peak in STM spectra [40]. Here we demonstrate that the interplay of the VHS and the collective mode concludes the picture, providing a complete explanation of both the missing VHS and the pronounced electron-hole asymmetries. Our conclusions are based on a brute force fit of the STM spectra and a careful analysis of the model. The advantage of this method is to allow for unambiguous determinations of relevant physical parameters from the raw tunneling data, and to provide intuition about the relationship between trends in the spectral features and parameter variations.

## 8.2 Accurate fit to an experimental spectrum

As a template material we studied the three-layer compound  $\text{Bi}_2\text{Sr}_2\text{Ca}_2\text{Cu}_3\text{O}_{8+\delta}$  (Bi2223), which has the highest  $T_c$  in the Bi-based family. Reproducible spectroscopy was recently reported in single crystals of Bi2223 cleaved *in situ* at room temperature [160] (see the spectra measured on sample B presented in Chapter 6). The tunneling conductance measured in UHV on an optimally-doped sample is shown in Fig. 8.2.1. The spectrum presents the characteristic *V* shape of *d*-wave superconductors, strong and asymmetric coherence peaks, and an asymmetric dip-hump structure. We have deliberately selected an optimally-doped sample displaying a flat background conductance up to high energies (inset in Fig. 8.2.1). For underdoped samples the spectra acquire an asymmetric background, attributed to strong correlation effects [10, 11, 12], which can conceal other intrinsic asymmetries. By moving to optimal doping where this background is absent, we can thus exclude that the observed asymmetries result from this type of correlations.

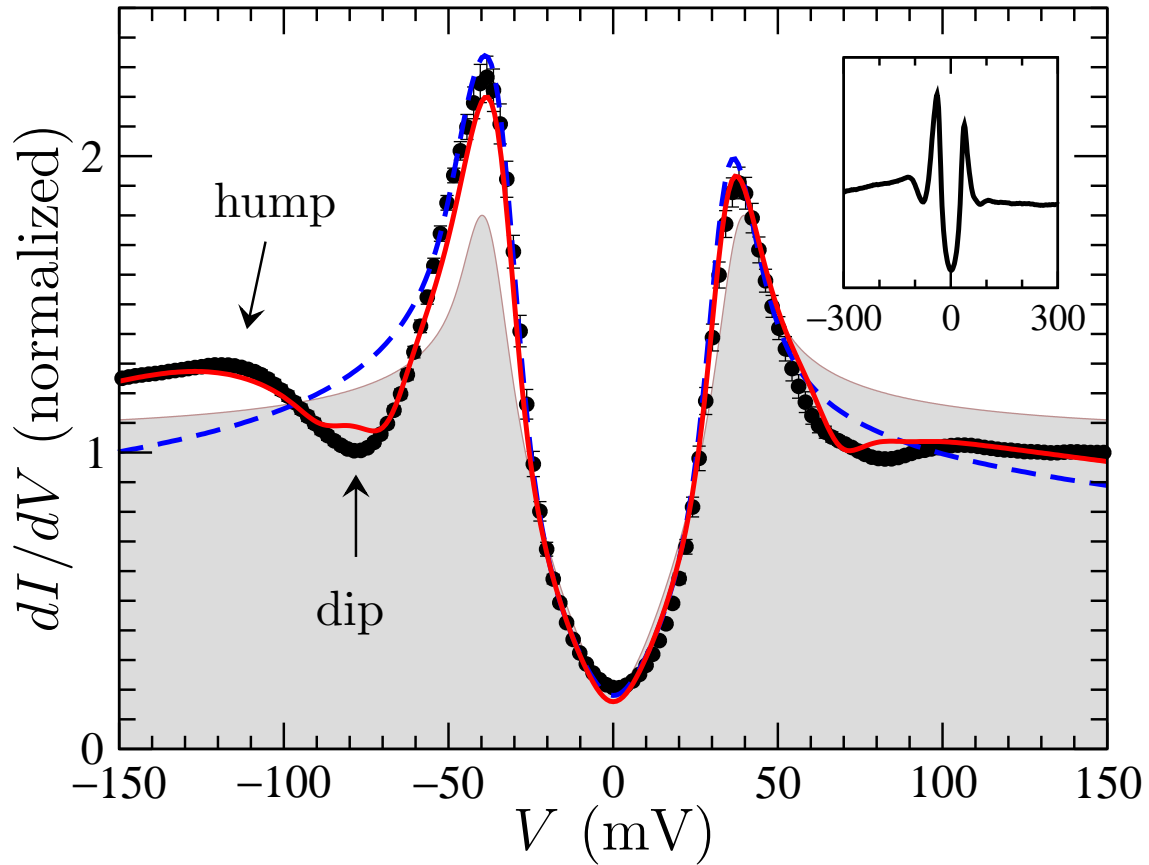


Figure 8.2.1: Typical STM conductance of Bi2223 ( $T_c = 111$  K) at  $T = 2$  K (dots). The data is an average of several spectra taken at different positions on the same sample, and having the same peak-to-peak gap  $\Delta_p = 38$  meV. Error bars give the standard deviation of this average. The inset shows the spectrum on a larger energy scale. Also shown are three model predictions (see text): free-electrons  $d$ -wave BCS (shaded),  $d$ -wave BCS with realistic dispersion including VHS (dashed line), and  $d$ -wave BCS including VHS and coupling to the magnetic resonance (full line). The total spectral weight in the energy range of the figure is the same for all curves.

For illustrative purposes, we plot in Fig. 8.2.1 the prediction of a conventional free-electrons BCS  $d$ -wave model (curve defined by the shaded area) [25, 26]. This model fits the experimental data well at low energy ( $\lesssim \Delta_p/2$ ), but fails to account for the various features present at higher energy, in particular the asymmetry of the coherence peak height. A much better description of the coherence peak height, width, and asymmetry can be achieved by taking into account the actual band structure. At energies below  $\sim 200$  meV a one-band model turns out to be sufficient. We consider the two-dimensional lattice model  $\xi_{\mathbf{k}} = 2t_1(\cos k_x + \cos k_y) + 4t_2 \cos k_x \cos k_y + 2t_3(\cos 2k_x + \cos 2k_y) - \mu$  where  $t_i$  is the  $i$ -th neighbor hopping energy. For this dispersion the VHS lies at energy  $\xi_M = -4(t_2 - t_3) - \mu$  corresponding to the saddle point  $\mathbf{k} = (\pi, 0) \equiv M$ . We determined the parameters of the band through an unconstrained least-squares fit of the whole spectrum in the inset of Fig. 8.2.1, leading to  $t_1 = -882$ ,  $t_2 = 239$ ,  $t_3 = -14$ , and  $\xi_M = -26$  meV, as well as a  $d$ -wave gap  $\Delta_0 = 34.1$  meV. It is very encouraging that these numbers determined from nothing else than the STM tunneling conductance lead to a Fermi surface in semi-quantitative agreement with the one measured by photoemission [27]. In particular, the VHS lies below the Fermi energy as expected for a hole-doped material. The resulting theoretical curve (Fig. 8.2.1, dashed line) is very similar to the free-electron model at subgap energies, but performs much better up to an energy slightly above the coherence peaks. The main effect of the VHS is to provide additional spectral weight below the Fermi level and thus increase the height of the coherence peaks at negative bias. Note that in the absence of broadening factors [26] the VHS would be visible as a secondary peak flanking the main coherence peak (see Fig. 8.3.1 below).

The “BCS plus VHS” model is nevertheless not satisfactory above  $eV \sim 2\Delta_p$ , where it fails to reproduce the significant transfer of spectral weight from the dip to the hump, which is strongest at negative bias in the experimental spectrum. Generically, such transfers signal a strong coupling of the quasiparticles with a collective excitation, which leads to enhanced damping of the former in a limited energy range, and to a simultaneous renormalization of the dispersion. In conventional superconductors, the electron-phonon coupling is known to induce similar features, albeit much less pronounced, at biases related to the phonon frequencies [28, 29, 30]. A phonon-based interpretation of the dip-hump in HTS has been revived recently [31, 32, 33, 34, 35, 36]. Another candidate is the famous  $(\pi, \pi)$  magnetic excitation [37, 38, 9] commonly known as the “41 meV resonance”—although its energy changes from one material to the other and also with varying doping [39]. Coupling the quasiparticles to this collective mode yields a change of the electron self-energy which can be expressed to leading order in terms of the spin susceptibility  $\chi_s(\mathbf{q}, \omega)$  [38]. Using a parametrization of  $\chi_s$  as measured by inelastic neutron scattering, Hoogenboom *et al.* showed that this model provides a very good description of the STM spectra of Bi2212 at several dopings [40]. Apart from the band-structure parameters  $t_i$ ,  $\mu$  and the  $d$ -wave gap  $\Delta_0$ , this model has 3 more parameters, namely the resonance energy  $\Omega_s$ , a characteristic length  $\xi_s \sim 2a$  which describes the spread of the collective mode around  $\mathbf{q} = (\pi, \pi)$  [38], and a coupling constant  $g$ .

In order to estimate these parameters we again performed a least-squares fit of the

whole spectrum in the inset of Fig. 8.2.1, however keeping the  $t_i$ 's fixed to their values determined previously. This procedure yields  $\Delta_0 = 33.9$  meV and  $\xi_M = -42.4$  meV, as well as  $\Omega_s = 34.4$  meV, in reasonable agreement with the properties of the magnetic resonance measured in Bi2223 [41]. The resulting theoretical spectrum matches our experimental data with amazing accuracy (Fig. 8.2.1, full line). In particular, the model reproduces all of the asymmetries found experimentally between positive and negative biases. We would like to stress that these asymmetries cannot be understood in models which neglect the band structure, as, e.g., in Refs [35] and [42]. The shape of the dip minimum in the theory differs somewhat from experiment: we shall come back to this below. Fits of similar quality have been obtained for many different spectra with gaps varying from  $\Delta_p = 36$  to 54 meV.

### 8.3 Effects of the different parameters

The precise interpretation of the theoretical curve in Fig. 8.2.1 seems complicated due to the interplay of three similar energy scales: the  $d$ -wave gap  $\Delta_0$ , the VHS energy  $\xi_M$ , and the collective mode energy  $\Omega_s$ , all in the 30–40 meV range. Still, based on a careful study of the model we can identify the origin of each structure in the spectrum, as illustrated in Fig. 8.3.1. The bare BCS DOS  $N_0(\omega)$  exhibits 5 singularities, namely (a) the V at zero energy resulting from the  $d$ -wave gap; (b) and (b') the coherence peaks at negative and positive energies ( $-\omega_b$  and  $\omega_{b'}$  respectively); (c) the VHS at energy  $-\omega_c$  below the coherence peak, and (c') the weak echo of the VHS at energy  $\omega_{c'}$  due to the BCS electron-hole mixing. The interaction with a collective mode leads to inelastic processes in which a quasiparticle of momentum  $\mathbf{k}$  and energy  $\omega$  is scattered to a state with momentum  $\mathbf{k} - \mathbf{q}$  and energy  $\omega - \Omega$  through emission of a collective excitation with quantum numbers  $(\mathbf{q}, \Omega)$ . The corresponding self-energy diagram is sketched in Fig. 8.3.1. If the only excitation available is a sharp-in-energy mode, all singularities of  $N_0(\omega)$  are mirrored in the self-energy, and exactly shifted by the mode energy  $\Omega_s$ . Hence the DOS  $N(\omega)$  including the interaction with the mode displays 3 pairs of singularities indicated by arrows in Fig. 8.3.1: the onsets at  $\omega = \pm\Omega_s$ , below which the quasiparticles do not have enough energy to excite a collective mode, a first minimum in the dip at  $-\omega_b - \Omega_s$  (resp.  $\omega_{b'} + \Omega_s$ ) corresponding to the negative-energy (positive-energy) coherence peak, and a second minimum in the dip—echoing the VHS peak in  $N_0(\omega)$ —which is more pronounced for occupied states at  $-\omega_c - \Omega_s$ , but also visible at  $\omega_{c'} + \Omega_s$ . Therefore the asymmetry of the dip structure between positive and negative biases receives a natural explanation in terms of the asymmetry of the underlying BCS DOS, which in turn is due to the VHS. The appearance of a double minimum in the dip is a direct consequence of the BCS DOS having both a coherence peak at  $-\omega_b$  and a VHS peak at  $-\omega_c$ . Such a double minimum is not observed in the experimental spectrum of Fig. 8.2.1. At positive bias, the various broadening effects [26] are sufficient to smear out the two minima into one. On the other hand, we have found that if the collective mode has a finite inverse lifetime of

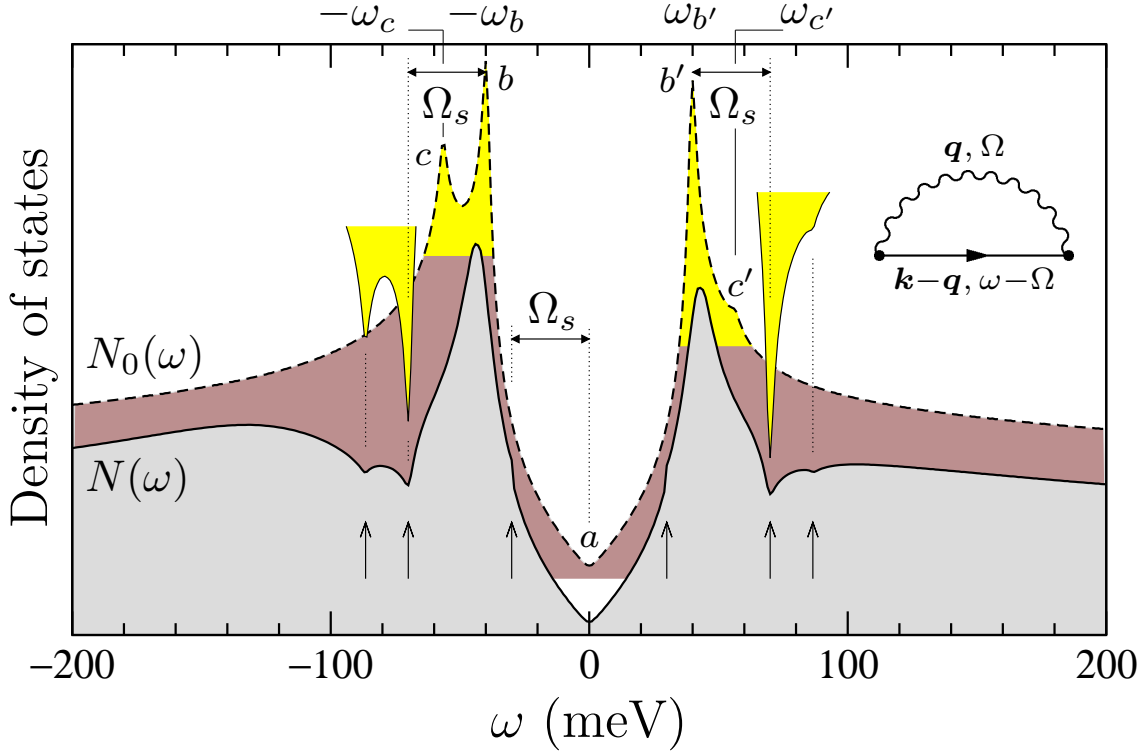


Figure 8.3.1: High-resolution calculation of the DOS in the absence [ $N_0(\omega)$ , dashed line, shifted vertically] and in the presence [ $N(\omega)$ , full line] of the coupling to the spin resonance. The energy and shape of the structures induced by the electron-spin coupling (arrows) is an “inverted image” of the singularities present in the BCS DOS ( $a$ ,  $b$ ,  $b'$ ,  $c$ ,  $c'$ ), shifted by the mode energy  $\Omega_s$ . The parameters are as in Fig. 8.2.1, except for  $\Delta_0 = 40$ ,  $\xi_M = -40$ , and  $\Omega_s = 30$  meV. The inset shows the self-energy diagram with the full line representing the BCS Green’s function and the wavy line the spin susceptibility.

only  $\sim 6$  meV [41], then the two minima in the dip fade away resulting in a smooth dip also at negative bias as observed experimentally.

The exact relationship between the position of the various structures in  $N(\omega)$  and the parameters of the model is not straightforward. The peak maximum, which we have denoted by  $\Delta_p$ , is not related in any simple way to the structures in  $N_0(\omega)$ , although it is numerically close to  $\omega_b$ . Furthermore  $\omega_b$  is not given by  $\Delta_0$ , but by the value of the gap function  $\Delta(\mathbf{k}) = \frac{\Delta_0}{2}(\cos k_x - \cos k_y)$  at the Fermi crossing near the M point. Hence  $\omega_b$  is slightly smaller than  $\Delta_0$ . The case of  $\omega_c$  is simpler, and it can be shown that  $\omega_c = \sqrt{\xi_M^2 + \Delta_0^2}$ . It follows that the first minimum in the dip at negative energy lies to a good approximation at  $-\Delta_p - \Omega_s$ , and the second at  $-\sqrt{\xi_M^2 + \Delta_p^2} - \Omega_s$ . In Fig. 8.3.2 we illustrate these two dependencies by varying  $\Omega_s$  and  $\xi_M$  independently in the model. Our starting point is the spectrum of Fig. 8.2.1 reproduced in bold in Fig. 8.3.2. In order to facilitate the comparison we have positioned the spectra relative to the negative-energy

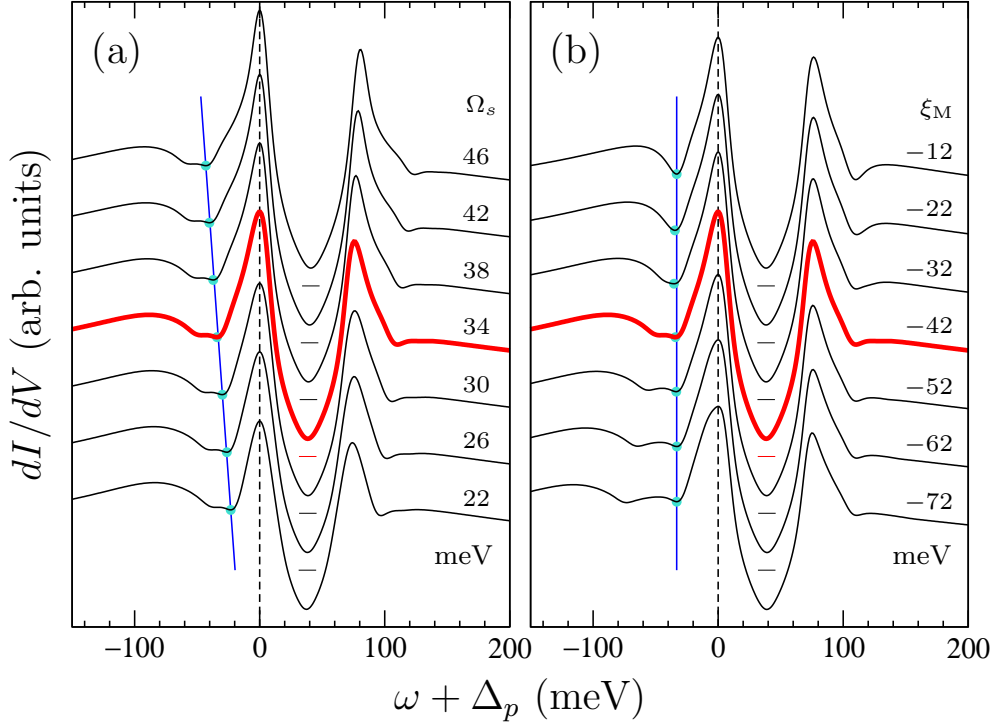


Figure 8.3.2: Evolution of the theoretical tunneling conductance upon varying (a)  $\Omega_s$  or (b)  $\xi_M$ . The remaining parameters are the same as in Fig. 8.2.1. Energies are measured relative to the peak maximum at  $-\Delta_p$ .

coherence peak. Varying  $\Omega_s$  while keeping  $\xi_M$  fixed we clearly see that the main change in the spectrum is a displacement of the dip and hump relative to the peak, consistently with the interpretation given in Fig. 8.3.1. In particular, the width of the dip at negative bias does not depend on  $\Omega_s$ . As  $\Omega_s$  increases, we also observe that the coherence peaks become taller and thinner, while developing a shoulder. This shoulder carries part of the spectral weight expelled from the dip, and progressively exits the coherence peak as the difference in the energy scales  $\Omega_s$  and  $\Delta_0$  increases. Fig. 8.3.2(a) further shows that  $\Omega_s$  has not much influence on the electron-hole asymmetry of the spectra. In contrast, changing the position of the VHS by varying  $\xi_M$  dramatically affects this asymmetry. At the lowest  $\xi_M$  considered the spectrum is almost symmetric. As the VHS moves toward negative energy, the dip at  $\omega < 0$  gets wider (the first minimum in the dip does not move, as expected) and the dip at  $\omega > 0$  dies out. Inspection of Fig. 8.3.2 also shows that the maximum of the hump feature tracks the second minimum in the dip, and thus depends on both  $\Omega_s$  and  $\xi_M$ . Furthermore the hump gets flattened as  $|\xi_M|$  increases.

Having clarified the different roles of  $\Omega_s$  and  $\xi_M$  in the shape of the model DOS, we now come back to experiment. In Fig. 8.3.3 we plot a series of tunneling conductance spectra with peak-to-peak gaps ranging from  $\Delta_p = 36$  to 54 meV. As a function of increasing  $\Delta_p$ , we first observe that (i) the dip for occupied states gets wider, (ii) the dip for empty states

gets weaker, and (iii) the hump at negative energy flattens out. These three trends are all observed in Fig. 8.3.2(b), and therefore strongly suggest that the increase of  $\Delta_p$  goes together with a displacement of the VHS towards negative energies. This is also fully consistent with the idea that local increases of  $\Delta_p$  in inhomogeneous samples reflect local decreases in the hole concentration. Another obvious trend of the data in Fig. 8.3.3 is that the coherence peaks are reduced with increasing gap. As seen in Fig. 8.3.2(b), this is also consistent with a shift of the VHS to lower energy. However, a look at Fig. 8.3.2(a) shows that this trend can also be ascribed to a decrease in the value of  $\Omega_s$ . Our calculations indeed confirm that  $\Omega_s$ , as determined by fits to the spectra in Fig. 8.3.3, decreases from 34 to 24 meV with increasing  $\Delta_p$ . The energy difference between the coherence peak and the dip minimum in the experimental spectra,  $\Omega_{\text{dip}}$ , also decreases with increasing  $\Delta_p$ , but less than  $\Omega_s$  (from 39 to 35 meV), as can be seen in Fig. 8.3.3. From these numbers it appears clearly that  $\Omega_{\text{dip}}$  overestimates  $\Omega_s$  by 5 to 10 meV. Recently the energy difference between  $\Delta_p$  and the inflection point between the dip and the hump (extremum in the  $d^2I/dV^2$  spectrum) was used as an estimate of  $\Omega_s$  in Bi2212 [34], resulting in an average value of 52 meV. This same estimate would give a  $\Delta_p$ -independent result of  $\sim 57$  meV for the data in Fig. 8.3.3, almost a factor of two larger than  $\Omega_s$ .

## 8.4 Fitting program

We have developed a computer program in order to perform the fits of the tunneling conductance spectra. In this section, we briefly describe this program. As an input information, it needs the spectral data  $dI/dV(V_s)$  and the starting values of the parameters to fit. It computes the DOS for the different data energies using the Green's function formalism. A two-dimensional array of typically  $512 \times 512$  points is defined in order to compute the modelled Green's function in momentum space. Therefore, each element of the array represents a given  $\mathbf{k}$ -value which is defined in the first Brillouin zone. A schematic flow chart of the program is shown below in this section. The equations referenced in the flow chart were defined in chapter 2. The most time-consuming part of the DOS computation is the self-energy determination  $\Sigma(\mathbf{k}, \omega)$  which involves basically a convolution of the BCS Green's function and the collective mode. This convolution is performed by applying Fourier transformations. Once the self-energy has been computed, the corresponding DOS is determined to be later compared to the data.

During the fitting process, the parameters are varied using the Levenberg-Marquardt algorithm. This algorithm minimizes  $S_{iter}$  which is the square difference between the computed DOS  $N(\omega)$  and the experimental data  $dI/dV(\omega)$ :

$$S_{iter} = \sum_i \left[ \frac{dI}{dV}(\omega_i) - N(\omega_i) \right]^2, \quad (8.4.1)$$

where  $iter$  is the iteration number of the fitting process and  $i$  runs over all the energies of the data. The fit is stopped either when 100 iterations are performed or convergence has

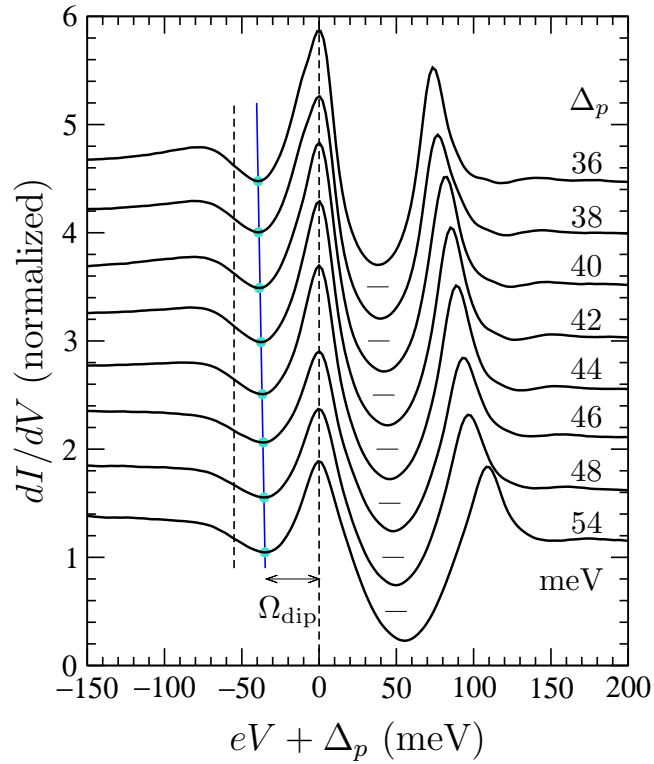


Figure 8.3.3: Various STM conductance spectra of Bi2223 ( $T_c = 111$  K) at  $T = 2$  K. Each curve is an average of several spectra taken at different locations on the same sample, all having the indicated peak-to-peak gap  $\Delta_p$ .  $\Omega_{\text{dip}}$  is the energy difference between the dip minimum (dot) and the peak maximum at negative bias, relative to which voltages are measured.

been reached. This condition is

$$\text{iter} > 100 \quad \text{or} \quad S_{\text{iter}} - S_{\text{iter}-1} < 10^{-6}. \quad (8.4.2)$$

As an output, the program gives the DOS that best fit the data and the resulting parameters. A successful fitting is typically obtained after 16 hours since each iteration takes around 15 minutes.

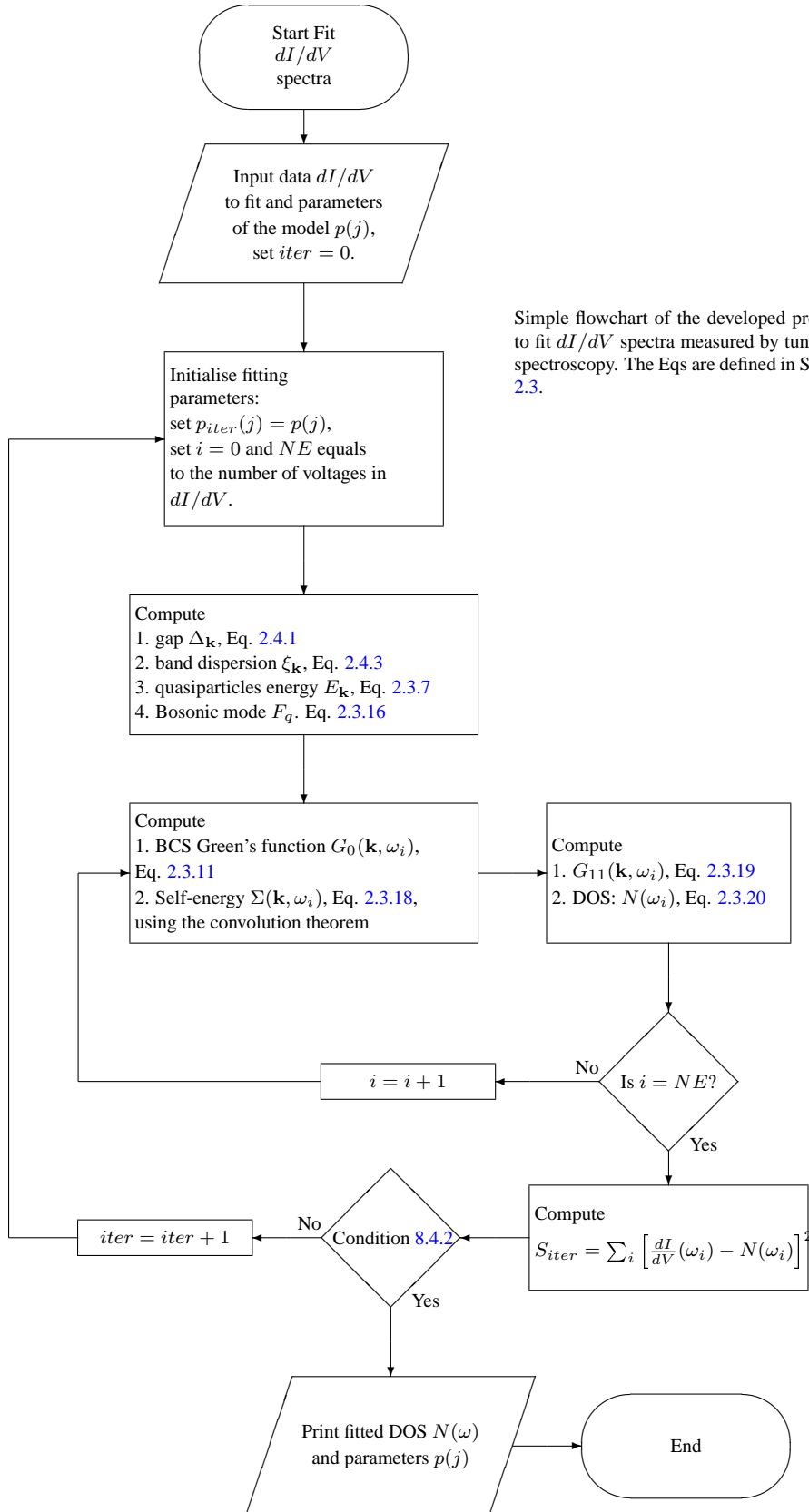


Table 8.5.1: Fitting parameters obtained, see Fig. 8.5.1.

$\Delta_p$ (meV)	$\Omega_{dip}$	$\Delta_0$ (meV)	$ \xi_M $ (meV)	$\Omega_s$ (meV)	$g$ (meV)	$\chi^2$
36	40	32	39	34	1020	0.92
38	40	34	42	34	920	0.31
40	38	36	38	33	1105	0.92
42	38	38	39	33	1230	0.43
44	36	41	40	31	1270	0.80
46	36	45.5	41	27	1230	0.32
48	36	48	44	27	1330	0.39
54	34	56	54	24	1470	0.39

## 8.5 Fits to the spectra

Using the program described in the previous section, we have fitted all the spectra shown in Fig. 8.3.3. The results are shown in Fig. 8.5.1 and they reproduce the overall features of the spectra. The fitting parameters are the gap  $\Delta_0$ , the position of the Van-Hove singularity  $\xi_M$ , the collective mode energy  $\Omega_s$  and the coupling parameter  $g$ . It is important to remark that the coupling parameter  $g$  has dimensions of energy. We observe that the fits describes all the asymmetries present in the spectra: they reproduce with great accuracy the  $V$ -shape form at energies below the gap, the variation of the height of the coherence peaks as well as their asymmetry, and the dip-hump structure at negative bias. As it was previously discussed, the collective mode determined from the energy position of the dip  $\Omega_{dip} = E_{dip} - \Delta_p$  usually overestimates the collective mode energy  $\Omega_s$ . The fits does not reproduce accurately the dip depth at negative bias. This could be improved if we consider a better description of the VHS shape.

The values of the fitted parameters are shown in Table 8.5.1. In this table, we also show the values of the gap extracted from the peak-to-peak gap  $\Delta_p$ , the estimation of the collective mode energy  $\Omega_{dip} \equiv E_{dip} - \Delta_p$ , and the final value of  $\chi^2 \equiv S_{iter}$  as it was defined in Eq. 8.4.1. The difference between the experimental gap  $\Delta_p$  and the gap value extracted from the fit  $\Delta_0$  is as big as 5 meV. Comparing also the collective mode estimation from the dip position  $\Omega_{dip}$  and the result obtained from the fit, their maximum difference is 10 meV.

The evolution of the fitted parameters shown in Table 8.5.1:  $\Delta_0$ ,  $\xi_M$  and  $\Omega_s$  with the peak-to-peak gap  $\Delta_p$  is plotted in Fig. 8.5.2. An almost linear increase of  $\Delta_0$  is observed as expected showing that a good estimation of the gap is the coherence peaks distance. The energy position of the van Hove singularity moves away from the Fermi level which is consistent with a decrease of the doping concentration with  $\Delta_p$ . Finally, the collective mode energy decreases with  $\Delta_p$ .

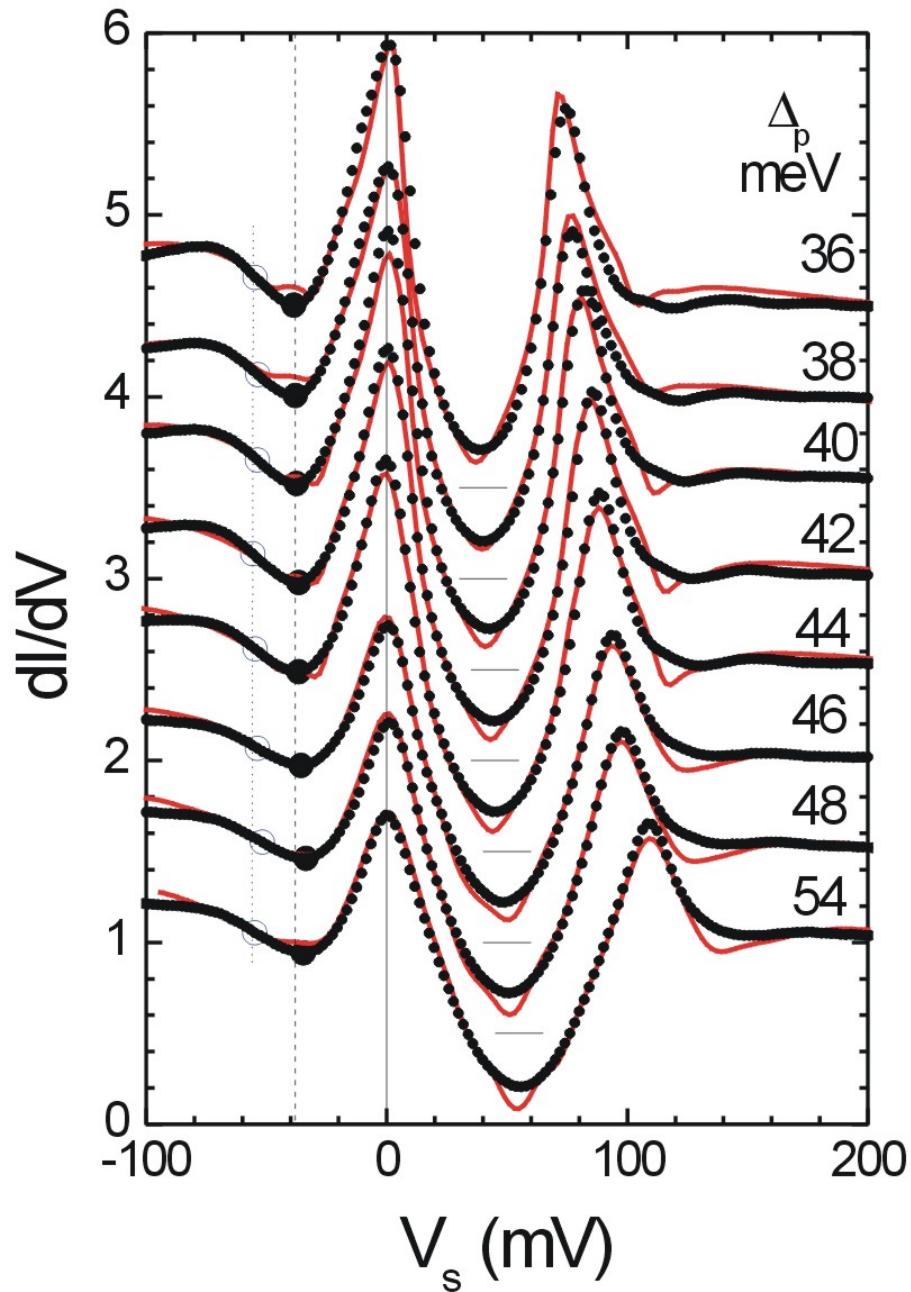


Figure 8.5.1: Averaged spectra for an optimal doped sample of Bi2223 compound (full dots) and the corresponding fitted DOS (lines). The spectra have been shifted vertically for clarity.

In summary, we have shown that the van Hove singularity plays a crucial role in shaping the spectral features induced in the STM spectra by the interaction of quasiparticles with bosonic modes. As a result, the determination of the bosonic mode energy from STM data is not straightforward. The model described in Chapter 2 allowed us to develop a computer program in order to fit the measured tunneling conductance. Our preliminaries fit shows a systematic behavior of the bosonic mode energy and the energy position of the van Hove singularity with  $\Delta_p$ . This model shows that the bosonic mode energy cannot be deduced directly from structures in the  $dI/dV$  or  $d^2I/dV^2$  spectra, due to the presence of the van Hove singularity. These results, valid for a coupling to the  $(\pi, \pi)$  magnetic resonance, might well also apply to phonon models.

In future work, more realistic band structures should be included in the model. Also a more detailed study of the doping dependence of the dip in Bi2223 should be carried out.

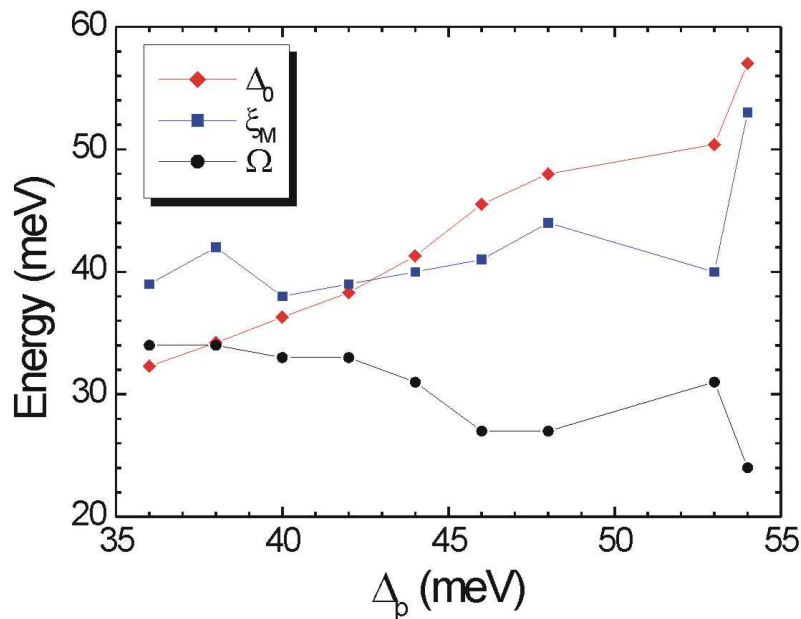


Figure 8.5.2: Evolution of the gap  $\Delta_0$ , the energy position of Van-Hove singularity  $|\xi_m|$  and the collective mode energy  $\Omega_s$  with the peak-to-peak gap  $\Delta_p$  obtained from the fits shown in Fig. 8.5.1.



# Chapter 9

## Conclusion and Perspectives

In this work we have measured the spectroscopic properties of  $\text{Bi}_2\text{Sr}_2\text{CaCu}_2\text{O}_{8+\delta}$  (Bi2212) and  $\text{Bi}_2\text{Sr}_2\text{Ca}_2\text{Cu}_3\text{O}_{10+\delta}$  (Bi2223) systems. In both systems, we observe nanometric spatial variations of the spectra which were interpreted as a manifestation of a non-uniform distribution of local doping concentration. We have related the superconducting transition width obtained from  $ac$ -susceptibility measurements to the standard deviation of the superconducting gap and found that homogeneous samples generally have small transition widths. This macroscopic criterion can be used for selecting the most homogeneous samples at a nanometric scale. In previous work [110], it has been shown that homogeneous spectral properties can also be obtained in Bi2212, at least in the overdoped region. These studies indicate that an inhomogeneous distribution of spectral properties is not crucial for superconductivity. This question is still under debate and further work should test this hypothesis.

A detailed study of a single vortex core in Bi2212 has been performed. We were able to relate the spatial distribution of the vortex core states to a four-fold symmetric modulation present inside the vortex. It has been observed that the intensity of the core states is maximal at the maximum of the four-fold pattern. This pattern had an energy-independent period of  $(4.3 \pm 0.3)a$  oriented along the Cu-O bonds. We found that the intensity of the four-fold modulation was maximal at 6 meV. It was at this same energy where the core states were observed. These observations allowed us to conclude that the vortex-core states are closely related to the four-fold modulation. Comparing our results with the observations of Vershinin *et al.* [20] in the pseudogap state above  $T_c$ , we find that the vortex cores and the pseudogap present similar spectra with the existence of a non-dispersive four-fold modulation. Our results establish a connection between the four-fold modulation, the vortex-core states and the pseudogap. However, the effect of the vortex core on the core states and hence the square modulation is not yet clear. In a previous work [110], it was shown that the core state energy scales with the local gap magnitude. All these observations indicate that there is a link between the superconducting state, the pseudogap and the vortex cores. In the future, further studies should concentrate on the

relations between the core states, the four-fold modulation, the superconducting gap and the pseudogap.

A double-peak structure was usually observed in the Bi2212 spectra. We observed that the two peaks are separated by  $\sim 12$  meV and their intensity varies strongly at a  $1.8 \text{ \AA}$  distance, with  $3.8 \text{ \AA}$  being the interatomic separation of the copper atoms. Based on the observed double-peak phenomenology, certain possible interpretations have been discarded. However, it was not possible to give a clear explanation of its origin which should be revealed in more detailed studies.

We have discussed in detail the spectral form of Bi2212 and Bi2223. By comparing them, we observed similar trends in the spectra as the gap increases: the energy position of the dip relative to the gap decreases and the slope of the spectra taken at  $-200$  mV also decreases. In particular, the Bi2223 spectra with a gap of  $45$  meV present the same spectral characteristics than the Bi2212 spectra with  $\Delta_p = 36$  meV.

We describe a model including Bogoliubov quasiparticles settled in a two dimensional tight-binding model and coupled to a collective mode. We have carried out “brute force” fits of the STM spectra which allowed us to determine the doping evolution of the model parameters. These fits together with a detailed analysis of the model have given us great insight into the relationship between trends in the spectral features and parameters variation. Focusing on the effects of the van Hove singularity (VHS) and the collective mode, we have found that the VHS determines the energy asymmetry of the spectra. In this model, the energy position of the dip is approximatively determined by the collective mode energy plus the gap value. However, the energy position of the hump structure, situated beyond the dip, depends on the interplay of the VHS, the collective mode and the gap. As a result, determining the frequency of the mode from STM data is complicated, and cannot be done directly from simple structures in the  $dI/dV$  or  $d^2I/dV^2$  spectra. This conclusion, obtained for a coupling to the  $(\pi, \pi)$  spin resonance, also applies to phonon models. Finally, we have shown that this relatively simple model includes the most important physical parameters necessary to accurately reproduce the STM spectra. In future work, extensions to this model will be considered in order to fit other features of the tunneling spectra.

# Appendix A

## Evaluation of the Function $B(\omega, E)$

From Eqs. 2.3.14 to 2.3.20 it results that the function  $B(\omega, E)$  entering in Eq. 2.3.18 is

$$B(\omega, E) = \int d\epsilon_1 d\epsilon_2 \frac{L_\Gamma(\epsilon_1 - E)[L_{\Gamma_s}(\epsilon_2 - \Omega_s) - L_{\Gamma_s}(\epsilon_2 + \Omega_s)][1 - f(\epsilon_1) + b(\epsilon_2)]}{\omega - \epsilon_1 - \epsilon_2 + i0^+}, \quad (\text{A.0.1})$$

where  $f$  and  $b$  are the Fermi and Bose functions, respectively. Changing variables this can be rewritten as

$$\begin{aligned} B(\omega, E) &= \int dx L_\Gamma(x) \int dy \frac{L_{\Gamma_s}(y)}{\omega - E - \Omega_s - x + i0^+ - y} \\ &\quad - \int d\epsilon_1 L_\Gamma(\epsilon_1 - E) f(\epsilon_1) \int dy \frac{L_{\Gamma_s}(y)}{\omega - \Omega_s - \epsilon_1 + i0^+ - y} \\ &\quad + \int d\epsilon_2 L_{\Gamma_s}(\epsilon_2 - \Omega_s) b(\epsilon_2) \int dx \frac{L_\Gamma(x)}{\omega - E - \epsilon_2 + i0^+ - x} \\ &\quad - \{\Omega_s \rightarrow -\Omega_s\}. \end{aligned} \quad (\text{A.0.2})$$

Using the identity  $\int dx L_\Gamma(x) \gamma(z - x) = 1/[z + i\Gamma \text{sign}(\text{Im}z)]$  we have

$$\begin{aligned} B(\omega, E) &= \frac{1}{\omega - E - \Omega_s + i(\Gamma + \Gamma_s)} - \int d\epsilon_1 \frac{L_\Gamma(\epsilon_1 - E) f(\epsilon_1)}{\omega - \Omega_s + i\Gamma_s - \epsilon_1} \\ &\quad + \int d\epsilon_2 \frac{L_{\Gamma_s}(\epsilon - \Omega_s) b(\epsilon_2)}{\omega - E + i\Gamma - \epsilon_2} - \{\Omega_s \rightarrow -\Omega_s\}. \end{aligned} \quad (\text{A.0.3})$$

The remaining integrals can be performed by closing the integration contour in the complex plane. Due to the poles of the Fermi and Bose functions at the frequencies  $i\omega_n$

and  $i\Omega_n$ , respectively, the integrals involve infinite sums of the residue of these poles. These sums can be rewritten in terms of the digamma function

$$\psi(x) = \lim_{N \rightarrow \infty} \left( \ln N - \sum_{n=0}^N \frac{1}{n+x} \right). \quad (\text{A.0.4})$$

We quote only the final result:

$$\begin{aligned} B(\omega, E) = & \frac{1 - f(E_i\Gamma) + b(\Omega_s - i\Gamma_s)}{\omega - E - \Omega_s + i(\Gamma + \Gamma_s)} + \frac{\Gamma}{\pi} \frac{\psi\left(\frac{1}{2} + \frac{\beta\Gamma_s}{2\pi} + \frac{\beta(\omega - \Omega_s)}{2\pi i}\right)}{(\omega - E - \Omega_s + i\Gamma_s)^2 + \Gamma^2} \\ & + \frac{\Gamma_s}{\pi} \frac{\psi\left(\frac{\beta\Gamma}{2\pi} + \frac{\beta(\omega - E)}{2\pi i}\right)}{(\omega - E - \Omega_s + i\Gamma)^2 + \Gamma_s^2} + \frac{1}{2\pi i} \left[ \frac{\psi\left(\frac{1}{2} - \frac{\beta\Gamma}{2\pi} + \frac{\beta E}{2\pi i}\right) + \psi\left(-\frac{\beta\Gamma_s}{2\pi} + \frac{\beta\Omega_s}{2\pi i}\right)}{\omega - E - \Omega_s + i(\Gamma + \Gamma_s)} \right. \\ & \left. - \frac{\psi\left(\frac{1}{2} + \frac{\beta\Gamma}{2\pi} + \frac{\beta E}{2\pi i}\right)}{\omega - E - \Omega_s - i(\Gamma - \Gamma_s)} - \frac{\psi\left(\frac{\beta\Gamma_s}{2\pi} + \frac{\beta\Omega_s}{2\pi i}\right)}{\omega - E - \Omega_s + i(\Gamma - \Gamma_s)} \right] \\ & - \{\Omega_s \rightarrow -\Omega_s\}. \end{aligned} \quad (\text{A.0.5})$$

The function  $B$  simplifies considerably in the case of a sharp mode ( $\Gamma_s = 0^+$ ) and sharp quasiparticles ( $\Gamma = 0^+$ ) as well as zero temperature:

$$B(\omega, E) = \frac{1}{\omega - E - \Omega_s \text{sign}(E) + i0^+} \quad (\Gamma_s = \Gamma = T = 0), \quad (\text{A.0.6})$$

as can be readily deduced from Eq. A.0.1 by replacing the Lorentzians by delta functions.

# Appendix B

## Cross-correlation definition

The cross-correlation between signals  $f(\mathbf{r})$  and  $g(\mathbf{r})$  is defined as

$$C_{fg}(\mathbf{R}) = \frac{\int (f(\mathbf{r}) - \bar{f}) \times (g(\mathbf{r} + \mathbf{R}) - \bar{g}) d^2r}{\sqrt{C_{ff}(\mathbf{0})C_{gg}(\mathbf{0})}}. \quad (\text{B.0.1})$$

The cross-correlation function  $C_{fg}(\mathbf{0})$  yields 1 for identical images  $f(\mathbf{r}) = g(\mathbf{r})$  and  $-1$  for the image and its negative  $f(\mathbf{r}) = -g(\mathbf{r})$ . For non-correlated images  $C_{fg}(\mathbf{0})$  yields 0. The auto-correlation of the signal  $f(\mathbf{r})$  is defined as

$$A_f(\mathbf{R}) \equiv C_{ff}(\mathbf{R}). \quad (\text{B.0.2})$$



# Appendix C

## Fourier Transform definitions and convention

The Fourier Transform of the discrete signal  $X(k)$  (and of its inverse  $x(j)$ ) is defined:

$$X(k) = \sum_{j=1}^N x(j) (e^{i2\pi/N})^{(j-1)(k-1)},$$
$$x(j) = \frac{1}{N} \sum_{k=1}^N X(k) (e^{i2\pi/N})^{-(j-1)(k-1)},$$

To conserve the same energy spectrum, we scale the Fourier transform  $X(k)$  in the following way:

$$M = \frac{1}{N} \sum_{j=1}^N x(j)$$
$$X(k) = \frac{1}{\sqrt{M}} \sum_{j=1}^N x(j) (e^{i2\pi/N})^{(j-1)(k-1)}$$
$$x(j) = \frac{1}{\sqrt{M}} \sum_{k=1}^N X(k) (e^{i2\pi/N})^{-(j-1)(k-1)}$$

Now to avoid the energy dependence of each map, we scale by:

$$M = \frac{1}{\sqrt{N}} \sum_{k=1}^N |X(k)|$$
$$X(k) = \frac{1}{M} \sum_{j=1}^N x(j) (e^{i2\pi/N})^{(j-1)(k-1)}$$

The Normalized Fourier Transform Intensity ( $Norm I_{FT}(E, \vec{q})$ ) is:

$$Norm I_{FT}(E, \vec{q}) = \frac{I_{FT}(E, \vec{q})}{\sum_{\vec{q}} I_{FT}(E, \vec{q})}$$

# Bibliography

- [1] Binnig, G. & Rohrer, H. Vacuum tunnel microscope. *Helv. Phys. Acta* **55**, 128 (1982). (Cited on pages 1, 15 and 17.)
- [2] Binnig, G. & Rohrer, H. Scanning tunneling microscopy—from birth to adolescence. *Rev. Mod. Phys.* **59**, 615–625 (1987). URL <http://dx.doi.org/10.1103/RevModPhys.59.615>. (Cited on pages 1, 15 and 17.)
- [3] Renner, C., Niedermann, P., Kent, A. D. & Fischer, O. A versatile low-temperature scanning tunneling microscope. *Journal of Vacuum Science & Technology A: Vacuum, Surfaces, and Films* **8**, 330–332 (1990). URL <http://dx.doi.org/10.1116/1.577100>. (Cited on pages 2 and 19.)
- [4] Renner, C., Niedermann, P., Kent, A. D. & Fischer, O. A vertical piezoelectric inertial slider. *Review of Scientific Instruments* **61**, 965–967 (1990). URL <http://dx.doi.org/10.1063/1.1141450>. (Cited on pages 2 and 19.)
- [5] Bednorz, J. G. & Müller, J. G. Possible high- $T_c$  superconductivity in the Ba-La-Cu-O system. *Zeitschrift für Physik B Condensed Matter* **64**, 189–193 (1986). URL <http://dx.doi.org/10.1007/BF01303701>. (Cited on pages 3 and 15.)
- [6] Presland, M. R., Tallon, J. L., Buckley, R. G., Liu, R. S. & Flower, N. E. General trends in oxygen stoichiometry effects on  $T_c$  in Bi and Tl superconductors. *Physica C* **176**, 95 (1991). URL [http://dx.doi.org/10.1016/0921-4534\(91\)90700-9](http://dx.doi.org/10.1016/0921-4534(91)90700-9). (Cited on pages 4, 52, 74 and 89.)
- [7] Tersoff, J. & Hamann, D. R. Theory and application for the scanning tunneling microscope. *Phys. Rev. Lett.* **50**, 1998–2001 (1983). URL <http://dx.doi.org/10.1103/PhysRevLett.50.1998>. (Cited on pages 4, 29, 31, 33, 78 and 112.)
- [8] Chen, C. J. Origin of atomic resolution on metal surfaces in scanning tunneling microscopy. *Phys. Rev. Lett.* **65**, 448–451 (1990). URL <http://dx.doi.org/10.1103/PhysRevLett.65.448>. (Cited on pages 4 and 112.)
- [9] Zasadzinski, J. F. *et al.* Correlation of tunneling spectra in  $\text{Bi}_2\text{Sr}_2\text{CaCu}_2\text{O}_{8+\delta}$  with the resonance spin excitation. *Phys. Rev. Lett.* **87**, 067005 (2001). URL <http://dx.doi.org/10.1103/PhysRevLett.87.067005>. (Cited on pages 4, 13, 53, 54, 86, 90, 112 and 114.)
- [10] Rantner, W. & Wen, X.-G. Tunneling density of states of high  $T_c$  superconductors:  $d$ -wave BCS model versus SU(2) slave-boson model. *Phys. Rev. Lett.* **85**, 3692–3695 (2000). URL <http://dx.doi.org/10.1103/PhysRevLett.85.3692>. (Cited on pages 5, 11, 53, 90, 102, 107 and 112.)
- [11] Randeria, M., Sensarma, R., Trivedi, N. & Zhang, F.-C. Particle-hole asymmetry in doped mott insulators: Implications for tunneling and photoemission spectroscopies. *Physical Review Letters* **95**, 137001 (2005). URL <http://dx.doi.org/10.1103/PhysRevLett.95.137001>. (Cited on pages 5, 11, 53, 90, 102, 107 and 112.)

- [12] Anderson, P. W. & Ong, N. P. Theory of asymmetric tunneling in the cuprate superconductors. *J. Phys. Chem. Solids* **67**, 1 (2006). URL <http://dx.doi.org/10.1016/j.jpcs.2005.10.132>. (Cited on pages 5, 11, 53, 90, 102, 107 and 112.)
- [13] Pan, S. H. *et al.* STM studies of the electronic structure of vortex cores in  $\text{Bi}_2\text{Sr}_2\text{CaCu}_2\text{O}_{8+\delta}$ . *Phys. Rev. Lett.* **85**, 1536–1539 (2000). URL <http://dx.doi.org/10.1103/PhysRevLett.85.1536>. (Cited on pages 5, 60 and 63.)
- [14] Hoogenboom, B. W., Renner, C., Revaz, B., Maggio-Aprile, I. & Fischer, Ø. Low-energy structures in vortex core tunneling spectra in  $\text{Bi}_2\text{Sr}_2\text{CaCu}_2\text{O}_{8+\delta}$ . *Physica C* **332**, 440 (2000). URL [http://dx.doi.org/10.1016/S0921-4534\(99\)00720-0](http://dx.doi.org/10.1016/S0921-4534(99)00720-0). (Cited on pages 5, 60 and 63.)
- [15] Matsuba, K., Sakata, H., Mochiku, T., Hirata, K. & Nishida, N. Influence of disorder on superconductivity in  $\text{Bi}_2\text{Sr}_2\text{CaCu}_2\text{O}_x$  studied by low temperature scanning tunneling spectroscopy. *Physica C* **388**, 281 (2003). URL [http://dx.doi.org/10.1016/S0921-4534\(02\)02442-5](http://dx.doi.org/10.1016/S0921-4534(02)02442-5). (Cited on pages 5, 60 and 63.)
- [16] Hoffman, J. E. *et al.* A four unit cell periodic pattern of quasi-particle states surrounding vortex cores in  $\text{Bi}_2\text{Sr}_2\text{CaCu}_2\text{O}_{8+\delta}$ . *Science* **295**, 466–469 (2002). URL <http://dx.doi.org/10.1126/science.1066974>. (Cited on pages 5, 7, 60 and 65.)
- [17] Hoffman, J. E. *et al.* Imaging quasiparticle interference in  $\text{Bi}_2\text{Sr}_2\text{CaCu}_2\text{O}_{8+\delta}$ . *Science* **297**, 1148–1151 (2002). URL <http://dx.doi.org/10.1126/science.1072640>. (Cited on pages 5, 7, 56, 60, 61 and 67.)
- [18] Howald, C., Eisaki, H., Kaneko, N., Greven, M. & Kapitulnik, A. Periodic density-of-states modulations in superconducting  $\text{Bi}_2\text{Sr}_2\text{CaCu}_2\text{O}_{8+\delta}$ . *Phys. Rev. B* **67**, 014533 (2003). URL <http://dx.doi.org/10.1103/PhysRevB.67.014533>. (Cited on pages 5, 57, 60 and 61.)
- [19] Wang, Q.-H. & Lee, D.-H. Quasiparticle scattering interference in high-temperature superconductors. *Phys. Rev. B* **67**, 020511(R) (2003). URL <http://dx.doi.org/10.1103/PhysRevB.67.020511>. (Cited on pages 5 and 60.)
- [20] Vershinin, M. *et al.* Local ordering in the pseudogap state of the high- $T_c$  superconductor  $\text{Bi}_2\text{Sr}_2\text{CaCu}_2\text{O}_{8+\delta}$ . *Science* **303**, 1995 (2004). URL <http://dx.doi.org/10.1126/science.1093384>. (Cited on pages 5, 9, 57, 60, 61, 68 and 125.)
- [21] McElroy, K. *et al.* Coincidence of checkerboard charge order and antinodal state decoherence in strongly underdoped superconducting  $\text{Bi}_2\text{Sr}_2\text{CaCu}_2\text{O}_{8+\delta}$ . *Physical Review Letters* **94**, 197005 (2005). URL <http://dx.doi.org/10.1103/PhysRevLett.94.197005>. (Cited on pages 5, 60, 92 and 106.)
- [22] Hanaguri, T. *et al.* A 'checkerboard' electronic crystal state in lightly hole-doped  $\text{Ca}_{2-x}\text{Na}_x\text{CuO}_2\text{Cl}_2$ . *Nature* **430**, 1001 (2004). URL <http://dx.doi.org/10.1038/nature02861>. (Cited on pages 5, 9, 57, 60 and 68.)
- [23] Renner, C., Revaz, B., Kadowaki, K., Maggio-Aprile, I. & Fischer, O. Observation of the low temperature pseudogap in the vortex cores of  $\text{Bi}_2\text{Sr}_2\text{CaCu}_2\text{O}_{8+\delta}$ . *Phys. Rev. Lett.* **80**, 3606–3609 (1998). URL <http://dx.doi.org/10.1103/PhysRevLett.80.3606>. (Cited on pages 5, 54, 60, 63, 65 and 68.)
- [24] Hoogenboom, B. W. *et al.* Shape and motion of vortex cores in  $\text{Bi}_2\text{Sr}_2\text{CaCu}_2\text{O}_{8+\delta}$ . *Phys. Rev. B* **62**, 9179–9185 (2000). URL <http://dx.doi.org/10.1103/PhysRevB.62.9179>. (Cited on pages 5 and 65.)
- [25] Won, H. & Maki, K. d-wave superconductor as a model of high- $T_c$  superconductors. *Phys. Rev. B* **49**, 1397–1402 (1994). URL <http://dx.doi.org/10.1103/PhysRevB.49.1397>. (Cited on pages 11 and 114.)

- [26] Our theoretical curves in Figs. 8.2.1 and 8.3.2 show the density of states (DOS) corrected by three broadening effects: a constant scattering rate  $\Gamma = 2$  meV, a 2 K thermal smearing, and a gaussian broadening of 4 meV. The latter accounts for the combined experimental uncertainty due to the lock-in ac modulation at  $V_{ac} = 2$  mV, and the averaging of several slightly different spectra. (Cited on pages 11, 13, 114 and 115.)
- [27] Feng, D. L. *et al.* Electronic structure of the trilayer cuprate superconductor  $\text{Bi}_2\text{Sr}_2\text{CaCu}_2\text{O}_{8+\delta}$ . *Phys. Rev. Lett.* **88**, 107001 (2002). URL <http://dx.doi.org/10.1103/PhysRevLett.88.107001>. (Cited on pages 13, 112 and 114.)
- [28] Eliashberg, G. M. ? *Sov. Phys. JETP* **11**, 696 (1960). (Cited on pages 13, 111 and 114.)
- [29] Giaever, I., Hart, H. R. & Megerle, K. Tunneling into superconductors at temperatures below 1K. *Phys. Rev.* **126**, 941–948 (1962). URL <http://dx.doi.org/10.1103/PhysRev.126.941>. (Cited on pages 13, 111 and 114.)
- [30] McMillan, W. L. & Rowell, J. M. Lead phonon spectrum calculated from superconducting density of states. *Phys. Rev. Lett.* **14**, 108–112 (1965). URL <http://dx.doi.org/10.1103/PhysRevLett.14.108>. (Cited on pages 13, 29, 54, 111 and 114.)
- [31] Sandvik, A. W., Scalapino, D. J. & Bickers, N. E. Effect of an electron-phonon interaction on the one-electron spectral weight of a  $d$ -wave superconductor. *Physical Review B (Condensed Matter and Materials Physics)* **69**, 094523 (2004). URL <http://dx.doi.org/10.1103/PhysRevB.69.094523>. (Cited on pages 13 and 114.)
- [32] Devereaux, T. P., Cuk, T., Shen, Z.-X. & Nagaosa, N. Anisotropic electron-phonon interaction in the cuprates. *Physical Review Letters* **93**, 117004 (2004). URL <http://dx.doi.org/10.1103/PhysRevLett.93.117004>. (Cited on pages 13 and 114.)
- [33] Citro, R., Cojocaru, S. & Marinaro, M. Role of electron-phonon interaction on quasiparticle dispersion in the strongly correlated cuprate superconductors. *Physical Review B (Condensed Matter and Materials Physics)* **73**, 014527 (2006). URL <http://dx.doi.org/10.1103/PhysRevB.73.014527>. (Cited on pages 13 and 114.)
- [34] Lee, J. *et al.* Interplay of electron-lattice interactions and superconductivity in  $\text{Bi}_2\text{Sr}_2\text{CaCu}_2\text{O}_{8+\delta}$ . *Nature* **442**, 546 (2006). URL <http://dx.doi.org/10.1038/nature04973>. (Cited on pages 13, 45, 114 and 118.)
- [35] Pilgram, S., Rice, T. M. & Sigrist, M. Role of inelastic tunneling through the insulating barrier in scanning-tunneling-microscope experiments on cuprate superconductors. *Physical Review Letters* **97**, 117003 (2006). URL <http://dx.doi.org/10.1103/PhysRevLett.97.117003>. (Cited on pages 13, 14, 82, 114 and 115.)
- [36] Zhao, G.-m. Strong coupling to multiple phonon modes in high-temperature superconductors. *Physical Review B (Condensed Matter and Materials Physics)* **75**, 214507 (2007). URL <http://dx.doi.org/10.1103/PhysRevB.75.214507>. (Cited on pages 13 and 114.)
- [37] Campuzano, J. C. *et al.* Electronic spectra and their relation to the  $(\pi, \pi)$  collective mode in high- $T_c$  superconductors. *Phys. Rev. Lett.* **83**, 3709–3712 (1999). URL <http://dx.doi.org/10.1103/PhysRevLett.83.3709>. (Cited on pages 13, 103, 111 and 114.)
- [38] Eschrig, M. & Norman, M. R. Neutron resonance: Modeling photoemission and tunneling data in the superconducting state of  $\text{Bi}_2\text{Sr}_2\text{CaCu}_2\text{O}_{8+\delta}$ . *Phys. Rev. Lett.* **85**, 3261–3264 (2000). URL <http://dx.doi.org/10.1103/PhysRevLett.85.3261>. (Cited on pages 13, 37, 39, 40, 112 and 114.)
- [39] Sidis, Y. *et al.* Magnetic resonant excitations in high- $T_c$  superconductors. *Phys. Status Solidi B* **241**, 1204 (2004). URL <http://dx.doi.org/10.1002/pssb.200304498>. (Cited on pages 13 and 114.)

- [40] Hoogenboom, B. W., Berthod, C., Peter, M., Fischer, O. & Kordyuk, A. A. Modeling scanning tunneling spectra of  $\text{Bi}_2\text{Sr}_2\text{CaCu}_2\text{O}_{8+\delta}$ . *Phys. Rev. B* **67**, 224502 (2003). URL <http://dx.doi.org/10.1103/PhysRevB.67.224502>. (Cited on pages 13, 29, 37, 39, 44, 55, 86, 90, 112 and 114.)
- [41] The  $(\pi, \pi)$  resonance was observed by neutron scattering at  $\Omega_s = 42$  meV in a  $T_c = 110$  K Bi2223 sample, and had intrinsic energy and momentum widths of 12 meV and  $0.37 \text{ \AA}^{-1}$ , respectively. S. Pailhès, private communication. (Cited on pages 14, 115 and 116.)
- [42] Zasadzinski, J. F. *et al.* Persistence of strong electron coupling to a narrow boson spectrum in overdoped  $\text{Bi}_2\text{Sr}_2\text{CaCu}_2\text{O}_{8+\delta}$  tunneling data. *Physical Review Letters* **96**, 017004 (2006). URL <http://dx.doi.org/10.1103/PhysRevLett.96.017004>. (Cited on pages 14, 55 and 115.)
- [43] Bardeen, J., Cooper, L. N. & Schrieffer, J. R. Theory of superconductivity. *Phys. Rev.* **108**, 1175–1204 (1957). URL <http://dx.doi.org/10.1103/PhysRev.108.1175>. (Cited on page 15.)
- [44] Schilling, O., Cantoni, M., Guo, J. D. & Ott, H. R. Superconductivity above 130 K in the Hg-Ba-Ca-Cu-O system. *Nature* **363**, 56–58 (1993). URL <http://dx.doi.org/10.1038/363056a0>. (Cited on page 15.)
- [45]  $1 \text{ \AA} = 0.1 \text{ nm} = 10^{-6} \text{ m}$ . (Cited on page 16.)
- [46] Hamers, R. J., Tromp, R. M. & Demuth, J. E. Surface electronic structure of Si (111)-(7×7) resolved in real space. *Phys. Rev. Lett.* **56**, 1972–1975 (1986). URL <http://dx.doi.org/10.1103/PhysRevLett.56.1972>. (Cited on pages 17 and 27.)
- [47] Hess, H. F., Robinson, R. B., Dynes, R. C., Valles, J. M. & Waszczak, J. V. Scanning-tunneling-microscope observation of the Abrikosov flux lattice and the density of states near and inside a fluxoid. *Phys. Rev. Lett.* **62**, 214–216 (1989). URL <http://dx.doi.org/10.1103/PhysRevLett.62.214>. (Cited on pages 17 and 59.)
- [48] Caroli, C., de Gennes, P. G. & Matricon, J. Bound fermion states on a vortex line in a type II superconductor. *Phys. Lett.* **9**, 307 (1964). (Cited on pages 17 and 59.)
- [49] Kitamura, S.-i., Sato, T. & Iwatsuki, M. Observation of surface reconstruction on silicon above  $800^\circ\text{C}$  using the STM. *Nature* **351**, 215–217 (1991). URL <http://dx.doi.org/10.1038/351215a0>. (Cited on page 17.)
- [50] Giambattista, B., Slough, C. G., McNairy, W. W. & Coleman, R. V. Scanning tunneling microscopy of atoms and charge-density waves in 1T-TaS<sub>2</sub>, 1T-TaSe<sub>2</sub>, and 1T-VSe<sub>2</sub>. *Phys. Rev. B* **41**, 10082–10103 (1990). URL <http://dx.doi.org/10.1103/PhysRevB.41.10082>. (Cited on pages 17 and 55.)
- [51] Crommie, M. F., Lutz, C. P. & Eigler, D. M. Imaging standing waves in a two-dimensional electron gas. *Nature* **363**, 524–527 (1993). URL <http://dx.doi.org/10.1038/363524a0>. (Cited on pages 17 and 55.)
- [52] Eigler, D. M., Lutz, C. P. & Rudge, W. E. An atomic switch realized with the scanning tunnelling microscope. *Nature* **352**, 600–603 (1991). URL <http://dx.doi.org/10.1038/352600a0>. (Cited on page 17.)
- [53] Hla, S.-W., Bartels, L., Meyer, G. & Rieder, K.-H. Inducing all steps of a chemical reaction with the scanning tunneling microscope tip: Towards single molecule engineering. *Phys. Rev. Lett.* **85**, 2777–2780 (2000). URL <http://dx.doi.org/10.1103/PhysRevLett.85.2777>. (Cited on page 17.)

- [54] Hahn, J. R., Lee, H. J. & Ho, W. Electronic resonance and symmetry in single-molecule inelastic electron tunneling. *Phys. Rev. Lett.* **85**, 1914–1917 (2000). URL <http://dx.doi.org/10.1103/PhysRevLett.85.1914>. (Cited on page 17.)
- [55] Kugler, M. *A Sub-Kelvin Scanning Tunneling Microscope and its first Application of Spectroscopy on  $\text{Bi}_2\text{Sr}_2\text{CaCu}_2\text{O}_8$  and  $\text{Bi}_2\text{Sr}_2\text{CuO}_6$* . Ph.D. thesis, Facult des Sciences, University of Geneva. (2000). URL [http://dpmc.unige.ch/gr\\_fischer/pdf/phdkugler.pdf](http://dpmc.unige.ch/gr_fischer/pdf/phdkugler.pdf). (Cited on pages 18, 19, 20, 23, 27, 54, 63 and 78.)
- [56] URL <http://dpmc.unige.ch/pdf/RS2003.pdf>. Research Report of the Department of Condensed Matter Physics, University of Geneva, 2003. (Cited on page 18.)
- [57] Cernox sensor CX-1030-SD, LakeShore Cryotronics, Westerwill, Ohio, USA. (Cited on page 19.)
- [58] Caro-Bronze Alloy (91.7 % Cu, 8 % Sn, 0.3 % P), Walter Looser AG, CH-8031 Zurich. (Cited on page 19.)
- [59] UHV and low temperature compatible epoxy glues: Epo-Tek H70E thermally conducting, electrical insulating; Epo-Tek 417 electrically conducting. Polyscience AG, CH-6330 Cham. (Cited on page 19.)
- [60] Ir 005120 Iridium wire Ir 99.9 % ( $\phi = 0.25$  mm, 2m long) GoodFellow, Ermine Business Park, Huntingdon PE 296WR, England. (Cited on page 19.)
- [61] Takagi, A. *Nanolithography on  $\text{YBa}_2\text{Cu}_3\text{O}_{7-\delta}$  single crystals using Scanning Tunneling Microscopy*. Ph.D. thesis, Facult des Sciences, University of Geneva. (2000). (Cited on page 20.)
- [62] Dubois, C. *Scanning Tunneling Spectroscopy on  $\text{PbMo}_6\text{S}_8$  and the Development of a 2D Nanopositioning System*. Ph.D. thesis, Facult des Sciences, University of Geneva. (2005). (Cited on page 20.)
- [63] Pobell, F. *Matter and Methods at Low Temperatures* (Springer, Berlin, 1992). (Cited on page 20.)
- [64] Carbon Glass sensor CGR-1-500, working range from 1.5K to room temperature. LakeShore Cryotronics, Westerwill, Ohio, USA. (Cited on page 22.)
- [65] Generic  $\text{RuO}_2$  sensor, Oxford Instruments, Abingdon, Oxon, UK. (Cited on page 22.)
- [66] DAP5216a/626, Digital Acquisition Processor board, Microstar laboratories, Inc., Bellevue WA 98004 USA. (Cited on page 25.)
- [67] MSXB 022, 16-bits Analog Output Expansion board; MSXB 037, Analog Input Expansion board, MSXB 038, Digital Expansion board, Microstar laboratories, Inc., Bellevue WA 98004 USA. (Cited on page 25.)
- [68] STM control software developed by Alfred A. Manuel, University of Geneva, 2002. (Cited on page 25.)
- [69] Lang, N. D. Apparent barrier height in scanning tunneling microscopy. *Phys. Rev. B* **37**, 10395–10398 (1988). URL <http://dx.doi.org/10.1103/PhysRevB.37.10395>. (Cited on pages 26 and 87.)
- [70] Fischer, Ø., Kugler, M., Maggio-Aprile, I., Berthod, C. & Renner, C. Scanning tunneling spectroscopy of high-temperature superconductors. *Reviews of Modern Physics* **79**, 353 (2007). URL <http://dx.doi.org/10.1103/RevModPhys.79.353>. (Cited on pages 27, 31, 53, 54, 62, 74, 75, 106 and 112.)
- [71] Giaever, I. Energy gap in superconductors measured by electron tunneling. *Phys. Rev. Lett.* **5**, 147–148 (1960). URL <http://dx.doi.org/10.1103/PhysRevLett.5.147>. (Cited on page 29.)

- [72] Bardeen, J. Tunneling into superconductors. *Phys. Rev. Lett.* **9**, 147–149 (1962). URL <http://dx.doi.org/10.1103/PhysRevLett.9.147>. (Cited on page 29.)
- [73] Cohen, M. H., Falicov, L. M. & Phillips, J. C. Superconductive tunneling. *Phys. Rev. Lett.* **8**, 316–318 (1962). URL <http://dx.doi.org/10.1103/PhysRevLett.8.316>. (Cited on page 29.)
- [74] Bardeen, J. Tunnelling from a many-particle point of view. *Phys. Rev. Lett.* **6**, 57–59 (1961). URL <http://dx.doi.org/10.1103/PhysRevLett.6.57>. (Cited on pages 29, 30 and 32.)
- [75] Zypman, F. R. & Fonseca, L. F. Time-independent tunneling current of a tip-sample system in scanning tunneling spectroscopy. *Phys. Rev. B* **51**, 2501–2505 (1995). URL <http://dx.doi.org/10.1103/PhysRevB.51.2501>. (Cited on page 30.)
- [76] Tersoff, J. & Hamann, D. R. Theory of the scanning tunneling microscope. *Phys. Rev. B* **31**, 805–813 (1985). URL <http://dx.doi.org/10.1103/PhysRevB.31.805>. (Cited on page 31.)
- [77] Chen, C. J. Tunneling matrix elements in three-dimensional space: The derivative rule and the sum rule. *Phys. Rev. B* **42**, 8841–8857 (1990). URL <http://dx.doi.org/10.1103/PhysRevB.42.8841>. (Cited on page 32.)
- [78] Bartels, L., Meyer, G. & Rieder, K.-H. Controlled vertical manipulation of single co molecules with the scanning tunneling microscope: A route to chemical contrast. *Applied Physics Letters* **71**, 213–215 (1997). URL <http://dx.doi.org/10.1063/1.119503>. (Cited on page 36.)
- [79] Mahan, G. D. *Many-Particle Physics* (Plenum Publishing Corporation, 2000). URL <http://www.amazon.fr/Many-Particle-Physics-Gerald-D-Mahan/dp/0306463385>. (Cited on pages 38 and 41.)
- [80] Zhu, J.-X. *et al.* Fourier-transformed local density of states and tunneling into a *d*-wave superconductor with bosonic modes. *Physical Review B (Condensed Matter and Materials Physics)* **73**, 014511 (2006). URL <http://dx.doi.org/10.1103/PhysRevB.73.014511>. (Cited on pages 39 and 103.)
- [81] Abanov, A., Chubukov, A. V. & Schmalian, J. Fingerprints of spin mediated pairing in cuprates. *Journal of Electron Spectroscopy and Related Phenomena* **117-118**, 129–151 (2003). URL [http://dx.doi.org/10.1016/S0368-2048\(01\)00251-1](http://dx.doi.org/10.1016/S0368-2048(01)00251-1). (Cited on page 39.)
- [82] Mook, H. A., Yethiraj, M., Aeppli, G., Mason, T. E. & Armstrong, T. Polarized neutron determination of the magnetic excitations in  $\text{YBa}_2\text{Cu}_3\text{O}_7$ . *Phys. Rev. Lett.* **70**, 3490–3493 (1993). URL <http://dx.doi.org/10.1103/PhysRevLett.70.3490>. (Cited on page 40.)
- [83] Fong, H. F. *et al.* Neutron scattering from magnetic excitations in  $\text{Bi}_2\text{Sr}_2\text{CaCu}_2\text{O}_{8+\delta}$ . *Nature* **398**, 588 (1999). URL <http://dx.doi.org/10.1038/19255>. (Cited on page 40.)
- [84] Fong, H. F. *et al.* Spin susceptibility in underdoped  $\text{YBa}_2\text{Cu}_3\text{O}_{6+x}$ . *Phys. Rev. B* **61**, 14773–14786 (2000). URL <http://dx.doi.org/10.1103/PhysRevB.61.14773>. (Cited on page 40.)
- [85] Berthod, C. Private Communication. (Cited on page 40.)
- [86] Schrieffer, J. R., Scalapino, D. J. & Wilkins, J. W. Effective tunneling density of states in superconductors. *Phys. Rev. Lett.* **10**, 336–339 (1963). URL <http://dx.doi.org/10.1103/PhysRevLett.10.336>. (Cited on pages 41 and 54.)
- [87] Ketterson, J. B. & Song, S. N. *Superconductivity* (Cambridge University Press, 2003). URL <http://www.amazon.com/Superconductivity-J-B-Ketterson/dp/0521565626>. (Cited on page 41.)
- [88] Tsuei, C. C. & Kirtley, J. R. Pairing symmetry in cuprate superconductors. *Rev. Mod. Phys.* **72**, 969–1016 (2000). URL <http://dx.doi.org/10.1103/RevModPhys.72.969>. (Cited on page 42.)

- [89] This figure was calculate by Christophe Berthod. (Cited on pages 44 and 46.)
- [90] Damascelli, A., Hussain, Z. & Shen, Z.-X. Angle-resolved photoemission studies of the cuprate superconductors. *Rev. Mod. Phys.* **75**, 473–541 (2003). URL <http://dx.doi.org/10.1103/RevModPhys.75.473>. (Cited on pages 44 and 112.)
- [91] Plate, M. *et al.* Fermi surface and quasiparticle excitations of overdoped  $\text{Tl}_2\text{Ba}_2\text{CuO}_{6+\delta}$ . *Physical Review Letters* **95**, 077001 (2005). URL <http://dx.doi.org/10.1103/PhysRevLett.95.077001>. (Cited on page 44.)
- [92] Pickett, W. E. Electronic structure of the high-temperature oxide superconductors. *Rev. Mod. Phys.* **61**, 433–512 (1989). URL <http://dx.doi.org/10.1103/RevModPhys.61.433>. (Cited on pages 44, 49 and 112.)
- [93] Scalapino, D. J. Singularities in superconducting tunnel junction I-V characteristics. *Rev. Mod. Phys.* **36**, 205–207 (1964). URL <http://dx.doi.org/10.1103/RevModPhys.36.205>. (Cited on page 45.)
- [94] Abanov, A. & Chubukov, A. V. SIN and SIS tunneling in cuprates. *Phys. Rev. B* **61**, R9241–R9244 (2000). URL <http://dx.doi.org/10.1103/PhysRevB.61.R9241>. (Cited on page 45.)
- [95] Yamamoto, A. *et al.* Rietveld analysis of the modulated structure in the superconducting oxide  $\text{Bi}_2(\text{SrCa})_3\text{Cu}_2\text{O}_{8+x}$ . *Phys. Rev. B* **42**, 4228–4239 (1990). URL <http://dx.doi.org/10.1103/PhysRevB.42.4228>. (Cited on page 51.)
- [96] Lindberg, P. A. P. *et al.* Reaction of Rb and oxygen overlayers with single-crystalline  $\text{Bi}_2\text{Sr}_2\text{CaCu}_2\text{O}_{8+\delta}$  superconductors. *Phys. Rev. B* **39**, 2890–2893 (1989). URL <http://dx.doi.org/10.1103/PhysRevB.39.2890>. (Cited on page 51.)
- [97] Uemura, Y. J. *et al.* Universal correlations between  $T_c$  and  $\frac{n_s}{m^*}$  (carrier density over effective mass) in high- $T_c$  cuprate superconductors. *Phys. Rev. Lett.* **62**, 2317–2320 (1989). URL <http://dx.doi.org/10.1103/PhysRevLett.62.2317>. (Cited on page 53.)
- [98] Renner, C., Revaz, B., Genoud, J.-Y., Kadowaki, K. & Fischer, O. Pseudogap precursor of the superconducting gap in under- and overdoped  $\text{Bi}_2\text{Sr}_2\text{CaCu}_2\text{O}_{8+\delta}$ . *Phys. Rev. Lett.* **80**, 149–152 (1998). URL <http://dx.doi.org/10.1103/PhysRevLett.80.149>. (Cited on pages 54, 90 and 91.)
- [99] Proust, C., Behnia, K., Bel, R., Maude, D. & Vedeneev, S. I. Heat transport in  $\text{Bi}_{2+x}\text{Sr}_{2-x}\text{CuO}_{6+\delta}$ : Departure from the Wiedemann-Franz law in the vicinity of the metal-insulator transition. *Physical Review B (Condensed Matter and Materials Physics)* **72**, 214511 (2005). URL <http://dx.doi.org/10.1103/PhysRevB.72.214511>. (Cited on page 54.)
- [100] Basov, D. N. & Timusk, T. Electrodynamics of high- $T_c$  superconductors. *Rev. Mod. Phys.* **77**, 721–779 (2005). URL <http://dx.doi.org/10.1103/RevModPhys.77.721>. (Cited on page 54.)
- [101] Timusk, T. & Statt, B. The pseudogap in high temperature superconductors: an experimental survey. *Rep. Prog. Phys.* **62**, 61 (1999). URL <http://dx.doi.org/10.1088/0034-4885/62/1/002>. (Cited on page 54.)
- [102] Scalapino, D. J., Wada, Y. & Swihart, J. C. Strong-coupling superconductor at nonzero temperature. *Phys. Rev. Lett.* **14**, 102–105 (1965). URL <http://dx.doi.org/10.1103/PhysRevLett.14.102>. (Cited on page 54.)
- [103] Zasadzinski, J. F., Coffey, L., Romano, P. & Yusof, Z. Tunneling spectroscopy of  $\text{Bi}_2\text{Sr}_2\text{CaCu}_2\text{O}_{8+\delta}$ : Eliashberg analysis of the spectral dip feature. *Phys. Rev. B* **68**, 180504 (2003). URL <http://dx.doi.org/10.1103/PhysRevB.68.180504>. (Cited on pages 55 and 83.)

- [104] Cren, T. *et al.* Influence of disorder on the local density of states in high-  $T_c$  superconducting thin films. *Phys. Rev. Lett.* **84**, 147–150 (2000). URL <http://dx.doi.org/10.1103/PhysRevLett.84.147>. (Cited on page 55.)
- [105] Howald, C., Fournier, P. & Kapitulnik, A. Inherent inhomogeneities in tunneling spectra of  $\text{Bi}_2\text{Sr}_2\text{CaCu}_2\text{O}_{8+x}$  crystals in the superconducting state. *Phys. Rev. B* **64**, 100504(R) (2001). URL <http://dx.doi.org/10.1103/PhysRevB.64.100504>. (Cited on page 55.)
- [106] Pan, S. H. *et al.* Microscopic electronic inhomogeneity in the high- $T_c$  superconductor  $\text{Bi}_2\text{Sr}_2\text{CaCu}_2\text{O}_{8+x}$ . *Nature* **413**, 282 (2001). URL <http://dx.doi.org/10.1038/35095012>. (Cited on pages 55, 74, 75 and 92.)
- [107] Lang, K. M. *et al.* Imaging the granular structure of high- $T_c$  superconductivity in underdoped  $\text{Bi}_2\text{Sr}_2\text{CaCu}_2\text{O}_{8+\delta}$ . *Nature* **415**, 412 (2002). URL <http://dx.doi.org/10.1038/415412a>. (Cited on pages 55 and 88.)
- [108] Kinoda, G. *et al.* Observations of electronic inhomogeneity in heavily Pb-doped  $\text{Bi}_2\text{Sr}_2\text{CaCu}_2\text{O}_y$  single crystals by scanning tunneling microscopy. *Phys. Rev. B* **67**, 224509 (2003). URL <http://dx.doi.org/10.1103/PhysRevB.67.224509>. (Cited on pages 55 and 56.)
- [109] McElroy, K. *et al.* Atomic-scale sources and mechanism of nanoscale electronic disorder in  $\text{Bi}_2\text{Sr}_2\text{CaCu}_2\text{O}_{8+\delta}$ . *Science* **309**, 1048 (2005). URL <http://dx.doi.org/10.1126/science.1113095>. (Cited on pages 55 and 74.)
- [110] Hoogenboom, B. W. *Scanning Tunneling Spectroscopy on Vortex Cores in  $\text{Bi}_2\text{Sr}_2\text{CaCu}_2\text{O}_{8+\delta}$* . Ph.D. thesis, Facult des Sciences, University of Geneva. (2002). (Cited on pages 55, 63, 72 and 125.)
- [111] McElroy, K. *et al.* Relating atomic-scale electronic phenomena to wave-like quasiparticle states in superconducting  $\text{Bi}_2\text{Sr}_2\text{CaCu}_2\text{O}_{8+\delta}$ . *Nature* **422**, 592 (2003). URL <http://dx.doi.org/10.1038/nature01496>. (Cited on page 56.)
- [112] Misra, S., Vershinin, M., Phillips, P. & Yazdani, A. Failure of scattering interference in the pseudogap state of cuprate superconductors. *Physical Review B (Condensed Matter and Materials Physics)* **70**, 220503 (2004). URL <http://dx.doi.org/10.1103/PhysRevB.70.220503>. (Cited on page 57.)
- [113] Momono, N., Hashimoto, A., Kobatake, Y., Oda, M. & Ido, M. STM/STS study on  $4a \times 4a$  electronic charge order of superconducting  $\text{Bi}_2\text{Sr}_2\text{CaCu}_2\text{O}_{8+\delta}$ . *J. Phys. Soc. Jpn.* **74**, 2400 (2005). URL <http://dx.doi.org/10.1143/JPSJ.74.2400>. (Cited on page 57.)
- [114] Maggio-Aprile, I., Renner, C., Erb, A., Walker, E. & Fischer, O. Direct vortex lattice imaging and tunneling spectroscopy of flux lines on  $\text{YBa}_2\text{Cu}_3\text{O}_{7-\delta}$ . *Phys. Rev. Lett.* **75**, 2754–2757 (1995). URL <http://dx.doi.org/10.1103/PhysRevLett.75.2754>. (Cited on pages 59 and 60.)
- [115] Wang, Y. & MacDonald, A. H. Mixed-state quasiparticle spectrum for  $d$ -wave superconductors. *Phys. Rev. B* **52**, R3876–R3879 (1995). URL <http://dx.doi.org/10.1103/PhysRevB.52.R3876>. (Cited on page 60.)
- [116] Franz, M. & Tešanović, Z. Quasiparticle spectra in the vicinity of a  $d$ -wave vortex. *Phys. Rev. B* **60**, 3581–3588 (1999). URL <http://dx.doi.org/10.1103/PhysRevB.60.3581>. (Cited on page 60.)
- [117] Berthod, C. & Giovannini, B. Density of states in high- $T_c$  superconductor vortices. *Phys. Rev. Lett.* **87**, 277002 (2001). URL <http://dx.doi.org/10.1103/PhysRevLett.87.277002>. (Cited on page 60.)
- [118] Zhu, J.-X. & Ting, C. S. Quasiparticle states at a  $d$ -wave vortex core in high- $T_c$  superconductors: Induction of local spin density wave order. *Phys. Rev. Lett.* **87**, 147002 (2001). URL <http://dx.doi.org/10.1103/PhysRevLett.87.147002>. (Cited on page 60.)

- [119] Hoogenboom, B. W. *et al.* Linear and field-independent relation between vortex core state energy and gap in  $\text{Bi}_2\text{Sr}_2\text{CaCu}_2\text{O}_{8+\delta}$ . *Phys. Rev. Lett.* **87**, 267001 (2001). URL <http://dx.doi.org/10.1103/PhysRevLett.87.267001>. (Cited on page 60.)
- [120] The sample was grown by Ming Li. Kamerlingh Onnes Laboratory, Leiden University, P.O. Box 9506, 2300 RA Leiden, The Netherlands. The measurements were performed in collaboration with Martin Kugler. (Cited on pages 60 and 72.)
- [121] Hoogenboom, B. W., Kadowaki, K., Revaz, B. & Fischer, Ø. Homogeneous samples of  $\text{Bi}_2\text{Sr}_2\text{CaCu}_2\text{O}_{8+\delta}$ . *Physica C* **391**, 376 (2003). URL [http://dx.doi.org/10.1016/S0921-4534\(03\)01087-6](http://dx.doi.org/10.1016/S0921-4534(03)01087-6). (Cited on pages 61, 74, 75, 77 and 88.)
- [122] Kugler, M., Renner, C., Mikheev, V., Batey, G. & Fischer, Ø. A  $^3\text{He}$  refrigerated scanning tunneling microscope in high magnetic fields and ultrahigh vacuum. *Rev. Sci. Instrum.* **71**, 1475 (2000). URL <http://dx.doi.org/10.1063/1.1150483>. (Cited on pages 61, 72 and 86.)
- [123] Berlinsky, A. J., Fetter, A. L., Franz, M., Kallin, C. & Soininen, P. I. Ginzburg-Landau theory of vortices in *d*-wave superconductors. *Phys. Rev. Lett.* **75**, 2200–2203 (1995). URL <http://dx.doi.org/10.1103/PhysRevLett.75.2200>. (Cited on page 63.)
- [124] Wang, Y. *et al.* Onset of the vortexlike nernst signal above  $T_c$  in  $\text{La}_{2-x}\text{Sr}_x\text{CuO}_4$  and  $\text{Bi}_2\text{Sr}_{2-y}\text{La}_y\text{CuO}_6$ . *Phys. Rev. B* **64**, 224519 (2001). URL <http://dx.doi.org/10.1103/PhysRevB.64.224519>. (Cited on page 68.)
- [125] Zaanen, J. & Gunnarsson, O. Charged magnetic domain lines and the magnetism of high- $T_c$  oxides. *Phys. Rev. B* **40**, 7391–7394 (1989). URL <http://dx.doi.org/10.1103/PhysRevB.40.7391>. (Cited on page 69.)
- [126] Zhang, S.-C. A unified theory based on  $\text{SO}(5)$  symmetry of superconductivity and antiferromagnetism. *Science* **275**, 1089–1096 (1997). URL <http://dx.doi.org/10.1126/science.275.5303.1089>. (Cited on page 69.)
- [127] Emery, V. J. & Kivelson, S. A. Electronic structure of doped insulators and high temperature superconductivity. *J. Low Temp. Phys.* **117**, 189 (1999). URL <http://dx.doi.org/10.1023/A:1022512004119>. (Cited on page 69.)
- [128] Vojta, M. & Sachdev, S. Charge order, superconductivity, and a global phase diagram of doped antiferromagnets. *Phys. Rev. Lett.* **83**, 3916–3919 (1999). URL <http://dx.doi.org/10.1103/PhysRevLett.83.3916>. (Cited on page 69.)
- [129] Wen, X.-G. & Lee, P. A. Theory of underdoped cuprates. *Phys. Rev. Lett.* **76**, 503–506 (1996). URL <http://dx.doi.org/10.1103/PhysRevLett.76.503>. (Cited on page 69.)
- [130] Chakravarty, S., Laughlin, R. B., Morr, D. K. & Nayak, C. Hidden order in the cuprates. *Phys. Rev. B* **63**, 094503 (2001). URL <http://dx.doi.org/10.1103/PhysRevB.63.094503>. (Cited on page 69.)
- [131] Chen, H.-D., Hu, J.-P., Capponi, S., Arrighoni, E. & Zhang, S.-C. Antiferromagnetism and hole pair checkerboard in the vortex state of high  $T_c$  superconductors. *Phys. Rev. Lett.* **89**, 137004 (2002). URL <http://dx.doi.org/10.1103/PhysRevLett.89.137004>. (Cited on page 69.)
- [132] Chen, H.-D., Vafek, O., Yazdani, A. & Zhang, S.-C. Pair density wave in the pseudogap state of high temperature superconductors. *Physical Review Letters* **93**, 187002 (2004). URL <http://dx.doi.org/10.1103/PhysRevLett.93.187002>. (Cited on page 69.)
- [133] Tešanović, Z. Charge modulation, spin response, and dual Hofstadter butterfly in high- $T_c$  cuprates. *Physical Review Letters* **93**, 217004 (2004). URL <http://dx.doi.org/10.1103/PhysRevLett.93.217004>. (Cited on page 69.)

- [134] Anderson, P. W. A suggested  $4 \times 4$  structure in underdoped cuprate superconductors: a wigner supersolid. (2004). URL <http://arxiv.org/abs/cond-mat/0406038>. (Cited on page 69.)
- [135] Renner, C. & Fischer, Ø. Vacuum tunneling spectroscopy and asymmetric density of states of  $\text{Bi}_2\text{Sr}_2\text{CaCu}_2\text{O}_{8+\delta}$ . *Phys. Rev. B* **51**, 9208–9218 (1995). URL <http://dx.doi.org/10.1103/PhysRevB.51.9208>. (Cited on pages 72, 74, 86 and 111.)
- [136] Nunner, T. S., Andersen, B. M., Melikyan, A. & Hirschfeld, P. J. Dopant-modulated pair interaction in cuprate superconductors. *Physical Review Letters* **95**, 177003 (2005). URL <http://dx.doi.org/10.1103/PhysRevLett.95.177003>. (Cited on page 78.)
- [137] Renner, C. *Low temperature Scanning Tunneling Microscopy and Spectroscopy of Layered Superconductors*. Ph.D. thesis, Faculté des Sciences, University of Geneva. (1993). (Cited on page 80.)
- [138] Lang, K. M. *Scanning Tunneling Spectroscopy Study of Inhomogeneity, Granularity, & Segregation in the Electronic Structure of  $\text{Bi}_2\text{Sr}_2\text{CaCu}_2\text{O}_{8+\delta}$* . Ph.D. thesis, University of California at Berkeley. (2001). URL [http://people.ccmr.cornell.edu/~jcdavis/theses/KMLang\\_Thesis.pdf](http://people.ccmr.cornell.edu/~jcdavis/theses/KMLang_Thesis.pdf). (Cited on page 80.)
- [139] Kordyuk, A. A., Borisenko, S. V., Knupfer, M. & Fink, J. Measuring the gap in angle-resolved photoemission experiments on cuprates. *Phys. Rev. B* **67**, 064504 (2003). URL <http://dx.doi.org/10.1103/PhysRevB.67.064504>. (Cited on page 83.)
- [140] Eskildsen, M. R. *et al.* Scanning tunneling spectroscopy on single crystal  $\text{MgB}_2$ . *Physica C* **385**, 169 (2003). URL [http://dx.doi.org/10.1016/S0921-4534\(02\)02301-8](http://dx.doi.org/10.1016/S0921-4534(02)02301-8). (Cited on page 83.)
- [141] Fujii, T., Watanabe, T. & Matsuda, A. Single-crystal growth of  $\text{Bi}_2\text{Sr}_2\text{Ca}_2\text{Cu}_3\text{O}_{10+\delta}$  (Bi-2223) by TSFZ method. *J. Cryst. Growth* **223**, 175 (2001). URL [http://dx.doi.org/10.1016/S0022-0248\(00\)01028-9](http://dx.doi.org/10.1016/S0022-0248(00)01028-9). (Cited on page 85.)
- [142] Giannini, E., Garnier, V., Gladyshevskii, R. & Flükiger, R. Growth and characterization of  $\text{Bi}_2\text{Sr}_2\text{Ca}_2\text{Cu}_3\text{O}_{10}$  and  $(\text{Bi,Pb})_2\text{Sr}_2\text{Ca}_2\text{Cu}_3\text{O}_{10-\delta}$  single crystals. *Supercond. Sci. Technol.* **17**, 220 (2004). URL <http://dx.doi.org/10.1088/0953-2048/17/1/037>. (Cited on page 86.)
- [143] Kugler, M., Fischer, O., Renner, C., Ono, S. & Ando, Y. Scanning tunneling spectroscopy of  $\text{Bi}_2\text{Sr}_2\text{CuO}_{6+\delta}$ : New evidence for the common origin of the pseudogap and superconductivity. *Phys. Rev. Lett.* **86**, 4911–4914 (2001). URL <http://dx.doi.org/10.1103/PhysRevLett.86.4911>. (Cited on page 86.)
- [144] Zandbergen, H. W., Groen, W. A., Mijlhoff, F. C., van Tendeloo, G. & Amelinkx, S. Models for the modulation in  $\text{A}_2\text{B}_2\text{Ca}_n\text{Cu}_{1+n}\text{O}_{6+2n}$ , A, B=Bi, Sr or Tl, Ba and  $n = 0, 1, 2$ . *Physica C* **156**, 325 (1998). URL [http://dx.doi.org/10.1016/0921-4534\(88\)90756-3](http://dx.doi.org/10.1016/0921-4534(88)90756-3). (Cited on page 86.)
- [145] The annealing treatments as well as the determination of the critical temperature  $T_c$  and the transitions width  $\Delta T_c$  deduced from the *ac*-susceptibility measurements were performed by Alexandre Piriou. (Cited on pages 88 and 93.)
- [146] Fujii, T., Terasaki, I., Watanabe, T. & Matsuda, A. Doping dependence of anisotropic resistivities in the trilayered superconductor  $\text{Bi}_2\text{Sr}_2\text{Ca}_2\text{Cu}_3\text{O}_{10+\delta}$ . *Phys. Rev. B* **66**, 024507 (2002). URL <http://dx.doi.org/10.1103/PhysRevB.66.024507>. (Cited on pages 89 and 90.)
- [147] Yamada, Y. *et al.* Interlayer tunneling spectroscopy and doping-dependent energy-gap structure of the trilayer superconductor  $\text{Bi}_2\text{Sr}_2\text{Ca}_2\text{Cu}_3\text{O}_{10+\delta}$ . *Phys. Rev. B* **68**, 054533 (2003). URL <http://dx.doi.org/10.1103/PhysRevB.68.054533>. (Cited on pages 89 and 90.)

- [148] Miyakawa, N., Guptasarma, P., Zasadzinski, J. F., Hinks, D. G. & Gray, K. E. Strong dependence of the superconducting gap on oxygen doping from tunneling measurements on  $\text{Bi}_2\text{Sr}_2\text{CaCu}_2\text{O}_{8-\delta}$ . *Phys. Rev. Lett.* **80**, 157–160 (1998). URL <http://dx.doi.org/10.1103/PhysRevLett.80.157>. (Cited on page 90.)
- [149] Matsuda, A., Fujii, T. & Watanabe, T. Gap inhomogeneity, phase separation and pseudogap in  $\text{Bi}_2\text{Sr}_2\text{CaCu}_2\text{O}_{8+\delta}$ . *Physica C* **388-389**, 207 (2003). URL [http://dx.doi.org/10.1016/S0921-4534\(02\)02378-X](http://dx.doi.org/10.1016/S0921-4534(02)02378-X). (Cited on page 92.)
- [150] URL <http://dpmc.unige.ch/pdf/RS2004.pdf>. Research Report of the Department of Condensed Matter Physics, University of Geneva, 2004. (Cited on page 93.)
- [151] The samples were grown by Enrico Giannini and characterized by Nicolas Musolino at the University of Geneva. (Cited on page 99.)
- [152] The samples coded "PP" were grown by Pablo Pedrazzini and Gladys Nieva at the Low temperature laboratory in Bariloche, Argentina. (Cited on page 99.)
- [153] McElroy, K. *et al.* Coincidence of checkerboard charge order and antinodal state decoherence in strongly underdoped superconducting  $\text{Bi}_2\text{Sr}_2\text{CaCu}_2\text{O}_{8+\delta}$ . *Phys. Rev. Lett.* **94**, 197005 (2005). URL <http://dx.doi.org/10.1103/PhysRevLett.94.197005>. (Cited on page 106.)
- [154] Campuzano, J. C., Norman, M. & Randeria, M. Photoemission in the high- $T_c$  superconductors. In Bennemann, K. H. & Ketterson, J. B. (eds.) *Physics of Superconductors*, vol. II, 167 (Springer, Berlin, 2004). URL [http://www.amazon.com/Physics-Superconductors-K-H-Bennemann/dp/3540442324/ref=sr\\_1\\_1/103-7175489-1220630?ie=UTF8&s=books&qid=1184922165&sr=1-1](http://www.amazon.com/Physics-Superconductors-K-H-Bennemann/dp/3540442324/ref=sr_1_1/103-7175489-1220630?ie=UTF8&s=books&qid=1184922165&sr=1-1). (Cited on page 111.)
- [155] Sato, T. *et al.* Observation of band renormalization effects in hole-doped high- $T_c$  superconductors. *Phys. Rev. Lett.* **91**, 157003 (2003). URL <http://dx.doi.org/10.1103/PhysRevLett.91.157003>. (Cited on page 112.)
- [156] Kouznetsov, K. & Coffey, L. Theory of tunneling and photoemission spectroscopy for high-temperature superconductors. *Phys. Rev. B* **54**, 3617–3621 (1996). URL <http://dx.doi.org/10.1103/PhysRevB.54.3617>. (Cited on page 112.)
- [157] Yusof, Z., Zasadzinski, J. F., Coffey, L. & Miyakawa, N. Modeling of tunneling spectroscopy in high- $T_c$  superconductors incorporating band structure, gap symmetry, group velocity, and tunneling directionality. *Phys. Rev. B* **58**, 514–521 (1998). URL <http://dx.doi.org/10.1103/PhysRevB.58.514>. (Cited on page 112.)
- [158] Harrison, W. A. Tunneling from an independent-particle point of view. *Phys. Rev.* **123**, 85–89 (1961). URL <http://dx.doi.org/10.1103/PhysRev.123.85>. (Cited on page 112.)
- [159] Ouyang, M., Huang, J.-L., Cheung, C. L. & Lieber, C. M. Energy gaps in "metallic" single-walled carbon nanotubes. *Science* **292**, 702 (2001). URL <http://dx.doi.org/10.1126/science.1058853>. (Cited on page 112.)
- [160] Kugler, M. *et al.* Scanning tunnelling spectroscopy on  $\text{Bi}_2\text{Sr}_2\text{Ca}_2\text{Cu}_3\text{O}_{10+\delta}$  single crystals. *J. Phys. Chem. Solids* **67**, 353 (2006). URL <http://dx.doi.org/10.1016/j.jpcs.2005.10.155>. (Cited on page 112.)



# Index

- Apparent barrier height
  - Experimental determination, [87](#)
  - Definition, [26](#)
- Atomic-scale variations of the spectra
  - Energy dependent, [80](#)
  - Energy independent, [78](#)
- Background slope:  $\alpha$ , [92](#)
  - Gap evolution, [103](#), [108](#)
- Band structure
  - DOS relation, [45](#)
  - HTS, [44](#)
- Bi-based compounds
  - Crystal structure, [50](#)
  - Supermodulation, [51](#)
- Bias potential:  $V_s$ , [28](#)
- Coherence peaks
  - Double-peak structure, [80](#)
  - Gap evolution, [77](#), [93](#), [94](#)
  - BCS theory, [43](#)
- Collective mode
  - DOS, effects on the, [115](#), [116](#)
  - Model, [39](#)
- Cryostat Description, [20](#)
- Dip-Hump structure
  - Gap evolution, [107](#)
  - Collective mode relation, [47](#)
- Doping
  - Evolution of the spectra, [90](#), [106](#)
  - Optimal, [52](#)
  - Overdoped regime, [52](#)
  - Underdoped regime, [52](#)
- Electron tunneling in superconductors, [41](#)
- Electronic setup, [24](#)
- Gap
  - $d$ -wave, [42](#)
  - Distribution in Bi2212, [74](#)
  - Distribution in Bi2223, [93](#), [94](#)
  - Evolution of the spectra with the, [121](#)
  - Experimental determination in HTS, [53](#)
- Green's function
  - BCS theory, [38](#)
  - Definition, [37](#)
  - Spectral function relation, [37](#)
- Homogeneity, spectral, [89](#)
- Impurity states, [55](#)
- Lock-in Technique, [27](#)
- Phase diagram of HTS, [52](#)
- Pseudogap, [54](#)
- Quasiparticle interference, [56](#)
- Refrigerator
  - $^3\text{He}$ , [22](#)
  - $^4\text{He}$ , [20](#)
- Spectral Map
  - Definition, [27](#)
- Spectral Trace
  - Definition, [28](#)
- STM
  - Description, [19](#)
  - Materials, [19](#)
- Temperature control, [22](#)
- Tip preparation, [20](#)
- Topography
  - Bi2223, [87](#)

- ILDOS relation, 36
- Bi2212, 61
- Definition, 27
- Tunneling conductance:  $dI/dV$ 
  - Normalization to tunnel resistance, 35
  - Definition, 28
  - LDOS relation, 34
- Tunneling current:  $I$ , 28
- Tunneling Hamiltonian formalism, 30
- Van Hove singularity
  - DOS, effect on the, 114, 116
- Vortex
  - Characteristics, 63
  - Core states, 63
  - Inhomogeneities, effect of, 63
  - Pseudogap relation, 68
  - Spatial distribution, 62
  - Spatial evolution of core states, 67
  - Square modulation, 65

# Acknowledgements

## Remerciements

Je tiens tout d'abord à remercier Prof. Øystein Fischer pour m'avoir reçu dans son groupe. Pendant les cinq années de ma thèse il m'a conseillé et guidé afin de me transmettre son expérience. Il a su combiner les doses adéquates d'indépendances et de supervision afin d'orienter au mieux mon travail.

Je remercie aussi Martin Kugler, qui m'a transmis les secrets et les mystères du STM in UHV. Son excellente méthodologie du travail a développé en moi l'habileté nécessaire afin d'obtenir une précision nanométrique. De plus, sa manière rigoureuse du travail a été un grand avantage pour attaquer le problème du STM en HTS.

Les simulations théoriques détaillées des mesures tunnel dans des supraconducteurs présentés dans cette thèse n'auraient pas été possibles sans l'étroite collaboration avec Christophe Berthod. L'une de ses qualités que j'ai le plus apprécié et qui a grandement bénéficié à ma thèse a été son habileté à expliquer simplement des problèmes et des concepts théoriques d'une apparence compliquée. Je le remercie aussi pour sa prédisposition et sa disponibilité aux échanges d'idées.

Pendant le développement de cette thèse j'ai eu des échanges avec Morten Eskildsen, Bart Hoogenboom, Christian Hess et Ivan Magio-Aprile. Ces échanges ont toujours débouché sur des expériences utiles.

Un élément important pour le développement de cette thèse a été l'usage d'échantillons cristallins de qualité. Je remercie particulièrement les fournisseurs d'échantillons distincts utilisés : Enrico Giannini, Alexandre Piriou, Gladys Nieva, Pablo Pedrazzini et Ming Li. La collaboration avec le groupe de Genève a été particulièrement bénéfique à l'amélioration de la qualité des échantillons.

Durant les dernières années de thèse, la venue de Yanina Fasano dans le groupe du Titanic a permis une meilleure distribution des travaux. Ce qui a contribué à effectuer le travail d'une manière plus efficace. Je lui souhaite bonne chance avec le Titanic dans l'avenir !

Dans le groupe, pendant ces cinq années la continuelle évolution de la technique de mesure STM a permis une amélioration de la qualité des mesures. Deux personnes en ont

été les principaux responsables: Laurent Stark pour le développement de l'électronique et Alfred Manuel pour le développement d'un nouveau système d'acquisition de données.

Pendant ces cinq années il y a toujours eu dans le groupe une excellente ambiance du travail. Je remercie pour cela les différents membres du groupe et spécialement à Cedric Dubois, Silvia Seiro, Olivier Kuffer, Ivan Maggio-Aprile, Isabel Joumard, Alex Petrovic, Nathan Jenkins, Jorge Cors et Nicolas Wanner. Un grand merci à Alex P. qui a contribué à la correction de cette thèse.

Je remercie aussi Paul-Emile Bisson pour l'appui technique qu'il m'a offert ainsi que sa bonne humeur qui m'a toujours aidé à faire passer les orages. Sans oublier l'équipe de cryogénie de l'Université de Genève : Spiros Zanos et Gregory Manfrini qui m'ont fourni l'hélium et l'azote liquide nécessaire aux mesures ici présentées.

Une personne spéciale qui m'a appuyé pendant la réalisation de la thèse a été mon amour Alba. Elle a eu toute la patience et compréhension pour supporter les longues heures dépensées pour le développement de cette thèse.

# Curriculum Vitae

## Personal Information

Name: Francisco Giorgio Levy de Castro  
Date of Birth: May 5<sup>th</sup>, 1977  
Place of Birth: Neuquén, Argentina  
Citizenship: Argentinean  
Civil Status: Single  
Home Address: Rue de Lausanne 55,  
1202 Genève, Switzerland.  
*Phone:* (+41 76) 410 17 68  
Office Address: Department of Condensed Matter Physics,  
Université de Genève  
24, Quai Ernest-Ansermet,  
CH-1211 Geneva 4, Switzerland.  
*Phone:* (+41 22) 379 63 97  
*Fax:* (+41 22) 379 68 69  
<http://dpmc.unige.ch/>  
*E-mail:* giorgio.levy@physics.unige.ch

## Education

- **PhD. in Physics**, University of Geneva, Switzerland (May 2007).  
*Thesis:* Scanning Tunneling Spectroscopy on  $\text{Bi}_2\text{Sr}_2\text{CaCu}_2\text{O}_{6+\delta}$  and  $\text{Bi}_2\text{Sr}_2\text{Ca}_2\text{Cu}_3\text{O}_{10+\delta}$  compounds.  
*Advisor:* Øystein Fischer at the Department of Condensed Matter Physics.
- **M. Sc. in Physics**, Instituto Balseiro, Argentina (December 2001).  
*Thesis:* Studies of the structural, superconducting and magnetic properties in the solid solution  $\text{Y}_{1-x}\text{Pr}_x\text{Ba}_2\text{Cu}_3\text{O}_y$  varying the oxygen concentration.  
*Advisor:* Gladys Nieva at the Low temperature Laboratory.
- **Languages:** Spanish (mother tongue); English (advanced); French (advanced).

## Academic Appointments

- June 2007 - Present: Post-doctoral Assistant, STM Lab, Group of Prof. Ø. Fischer, Department of Condensed Matter Physics, University of Geneva, Switzerland.
- June 2002 - May 2007: Ph. D. in Physics Scholar, STM Lab, Group of Prof. Øystein Fischer, Department of Condensed Matter Physics, University of Geneva, Switzerland.  
[http://dpmc.unige.ch/gr\\_fischer/index.fr.html](http://dpmc.unige.ch/gr_fischer/index.fr.html)
- June 2002 - Present: Under Graduate Teaching Assistant, Department of Condensed Matter Physics, University of Geneva, Switzerland.
- August 1998 - December 2001: M. Sc. in Physics Scholar, Instituto Balseiro, Argentina.  
<http://www.ib.edu.ar/>

## Scholarships

- 1998-2001: Atomic National Comision (Argentina) to attain the M. Sc. in Physics from the Instituto Balseiro. <http://www.cab.cnea.gov.ar>

## Publications

1. 2007: *Preeminent role of the Van Hove singularity in the strong-coupling analysis of scanning tunneling spectroscopy for two-dimensional cuprate superconductors.*  
**Giorgio Levy de Castro**, C. Berthod, A. Piriou, E. Giannini, Ø. Fischer.  
Submitted to Phys. Rev. Letters.  
E-print: <http://arxiv.org/abs/cond-mat/0703131>
2. 2006: *Scanning tunnelling spectroscopy on  $Bi_2Sr_2Ca_2Cu_3O_{10+\delta}$  single crystals.*  
M. Kugler, **Giorgio Levy de Castro**, E. Giannini, A. Piriou, A. A. Manuel, C. Hess, Ø Fischer.  
J. Phys. Chem. Solids **67**, 353 (2006).  
<http://dx.doi.org/10.1016/j.jpcs.2005.10.155>
3. 2005: *Fourfold Structure of Vortex-Core States in  $Bi_2Sr_2CaCu_2O_{8+\delta}$ .*  
**Giorgio Levy**, M. Kugler, M. A. Manuel, Ø Fischer, M. Li.  
Phys. Rev. Lett. **95**, 257005 (2005).  
<http://dx.doi.org/10.1103/PhysRevLett.95.257005>

4. 2003: *Vortex imaging in magnesium diboride with  $H \perp c$* .  
M. R. Eskildsen, N. Jenkins, **Giorgio Levy**, M. Kugler, Ø. Fischer, J. Jun, S. M. Kazakov, J. Karpinski.  
Phys. Rev. B **68**, 100508 (2003).  
<http://dx.doi.org/10.1103/PhysRevB.68.100508>
5. 2003: *Vortex lattice imaging in single crystal  $MgB_2$  by scanning tunneling spectroscopy*  
M. R. Eskildsen, M. Kugler, **Giorgio Levy**, S. Tanaka, J. Jun, S. M. Kazakov, J. Karpinski, Ø. Fischer.  
Physica C **385**, 169 (2003).  
[http://dx.doi.org/10.1016/S0921-4534\(02\)02686-2](http://dx.doi.org/10.1016/S0921-4534(02)02686-2)
6. 2003: *Scanning tunneling spectroscopy on single crystal  $MgB_2$* .  
M. R. Eskildsen, M. Kugler, **Giorgio Levy**, S. Tanaka, J. Jun, S. M. Kazakov, J. Karpinski, Ø. Fischer.  
Physica C **385**, 169 (2003).  
[http://dx.doi.org/10.1016/S0921-4534\(02\)02301-8](http://dx.doi.org/10.1016/S0921-4534(02)02301-8)
7. 2002: *Oxygen overdoping in  $Y_{1-x}Pr_xBa_2Cu_3O_y$  superconducting and non-superconducting compounds*.  
**Giorgio Levy**, B. Maiorov, M. S. Corvalan, A. Fainstein, and G. Nieva.  
Physica B **320**, 333 (2002).  
[http://dx.doi.org/10.1016/S0921-4526\(02\)00741-X](http://dx.doi.org/10.1016/S0921-4526(02)00741-X)

## Research Experience

- **Technical Background:** During my Ph.D. in Øystein Fischer's group, I have measured the tunneling spectroscopic properties of  $Bi_2Sr_2CaCu_2O_{8+\delta}$  (Bi2212) and  $Bi_2Sr_2Ca_2Cu_3O_{10+\delta}$  (Bi2223) compounds. The measurements were performed in a sub-Kelvin STM which operates in a temperature range between 275 mK and room temperature in magnetic fields up to 14 Tesla and in a Ultra High Vacuum (UHV) chamber with *in situ* manipulation capabilities.
- **Sample characterization and preparation:** I have growth  $Y_{1-x}Pr_xBa_2Cu_3O_y$  single crystals by zone melting method during my Master thesis. Their doping concentration was changed by annealing them at high temperatures and in a high oxygen pressure atmosphere. At the beginning of my Ph.D., I also anneal and characterize some  $Bi_2Sr_2CaCu_2O_{8+\delta}$  single crystals.
- **Research achievements:**

1. We have been able to perform single vortex core spectroscopy in  $\text{Bi}_2\text{Sr}_2\text{CaCu}_2\text{O}_{8+\delta}$ . We have related the core states to the four-fold modulation that appears inside the core.
2. We have successfully measured the tunneling spectra of  $\text{Bi}_2\text{Sr}_2\text{Ca}_2\text{Cu}_3\text{O}_{10+\delta}$  single crystals. Furthermore, we have determined the variations of the spectra with doping and compare them with the spectra of its parent compound  $\text{Bi}_2\text{Sr}_2\text{CaCu}_2\text{O}_{8+\delta}$ .
3. Finally, we have developed a computer program to fit the tunneling spectra of high- $T_c$  superconductors. This program includes BCS quasiparticles settled in a two-dimensional tight-binding band and coupled to a collective mode.

## Research Interests

My research interest focus in the microscopic mechanism of high- $T_c$  superconductors. In particular, I am interested in their low-dimensional properties and how the strong electronic correlations affects the superconductivity.

## Teaching Experience

- Teaching Assistant, University of Geneva, Switzerland. Experimental Activities on General Physics III, Scanning Tunneling Microscopy and Spectroscopy experiments (Bachelor in Physics). During the winter semesters, between 2002 and 2005:
- Teaching Assistant, University of Geneva, Switzerland. Introduction to Solid State Physics (Bachelor in Physics). During the summer semesters, between 2004 and 2006.
- Teaching Assistant, University of Geneva, Switzerland. Advanced Physics, Superconductivity and Surfaces. (M. Sc. in Physics). Summer semester 2007.

## Obtained Scholarships

1998-2001: Master and College scholarship from Comisión Nacional de Energía Atómica (National Atomic Energy Agency of Argentina)

## Presentations to Congress

- Talk 2007: *Scanning Tunneling Spectra on HTS: The interplay of the gap, the bosonic mode and the van Hove singularity.* **Giorgio Levy**, Christophe Berthod, Alexandre Piriou, Yanina Fasano, Ivan Maggio-Aprile and Øystein Fischer. SPS '07 - Swiss Physical Society - MaNEP Meeting Zurich, February 21 - 22, 2007.
- Poster 2006: *Four-fold structure of vortex core states in  $\text{Bi}_2\text{Sr}_2\text{CaCu}_2\text{O}_8$ .* **G. Levy**, M. Kugler, A. A. Manuel, and Ø. Fischer. 8-th International Conference on Materials and Mechanisms of Superconductivity and High-Temperature Superconductors. July 9<sup>th</sup> - 14<sup>th</sup>, 2006 Dresden - Germany.
- Poster 2006: *Scanning Tunneling Spectra on HTS: The interplay of the gap, the bosonic mode and the van Hove singularity.* **Giorgio Levy**, Christophe Berthod and Øystein Fischer. Low-Energy Excitations in High-Tc Superconductors Satellite Conference to the M2S-VIII in Dresden. July 5<sup>th</sup> - 7<sup>th</sup>, 2006. Stuttgart, Germany.
- Poster 2005: *Four-fold structure of vortex core states in  $\text{Bi}_2\text{Sr}_2\text{CaCu}_2\text{O}_8$ .* **G. Levy**, M. Kugler, A. A. Manuel, and Ø. Fischer. Nanoscale Fluctuations in Magnetic and Superconducting Systems Workshop: May 10 - 14, 2005. Dresden, Germany
- Poster 2004: *Scanning Tunnelling Microscope measurements in  $\text{Bi}_2\text{Sr}_2\text{Ca}_2\text{Cu}_3\text{O}_{10}$ .* **G. Levy**, M. Kugler, A. A. Manuel, A. Piriou, E. Giannini and Ø. Fischer. SNS'04 - Spectroscopies on Novel Superconductors - July 11- 16, 2004. Sitges, Spain.
- Poster 2004: *Scanning Tunnelling Microscope measurements in  $\text{Bi}_2\text{Sr}_2\text{Ca}_2\text{Cu}_3\text{O}_{10}$ .* **G. Levy**, M. Kugler, A. A. Manuel, A. Piriou, E. Giannini and Ø. Fischer. SPS 04 - 2004 Swiss Physical Society - MaNEP Meeting Neuchtel, March 3 and 4, 2004.
- Poster 2003: *Nanoscale variations of the superconducting density of states of  $\text{Bi}_2\text{Sr}_2\text{CaCu}_2\text{O}_{8+\delta}$ .* **G. Levy**, M. Kugler, A. A. Manuel, B. W. Hoogenboom, M. Li and Ø. Fischer. SWM03 2003 - Swiss Workshop on Materials with novel electronic properties. September 29 - October 1, 2003. Les Diablerets, Switzerland.
- Poster 2003: *Nanoscale variations of the superconducting density of states of  $\text{Bi}_2\text{Sr}_2\text{CaCu}_2\text{O}_{8+\delta}$ .* **G. Levy**, M. Kugler, A. A. Manuel, B. W. Hoogenboom, M. Li and Ø. Fischer. M2S-HTSC RIO 2003 - 7<sup>o</sup> International conference on materials and mechanism of superconductivity and high temperature superconductors. May 25-30, 2003. Rio de Janeiro, Brazil.
- Poster 2001: *Oxygen overdoping in  $\text{Y}_{1-x}\text{Pr}_x\text{Ba}_2\text{Cu}_3\text{O}_y$  superconducting and non-superconducting compounds.* **G. Levy**, B. Maiorov, M. S. Corvalan, A. Fainstein, and G. Nieva. Fifth Latin American Workshop on Magnetism, Magnetic Materials and their Applications. September 3-7 2001 - San Carlos de Bariloche - Argentina

- Poster, 2001: *Sobredopado con oxígeno en  $Y_{1-x}Pr_xBa_2Cu_3O_y$*   
**G. Levy**, B. Maiorov, M.S. Corvaln, A. Fainstein, G. Nieva  
86° Reunión de la Asociación de Física Argentina, Rosario, Argentina.
- Poster, 2000: *Efectos de cambios en el contenido de oxígeno en el superconductor  $YBa_2Cu_3O_y$  dopado con praseodimio*  
J. Lasave, **G. Levy**, B. Maiorov, M. S. Corvalan, G. Nieva  
85° Reunión de la Asociación de Física Argentina, Bs. As., Argentina.

## Extracurricular activities

- Participation to "Course de l'escalade" in 2004 and 2006.
- Participation to the triathlon Nyon, category "Mini-tri, elites hommes" in 2003 and 2004.